SAPIENZA
UNIVERSITÀ DI ROMA

Thermal-hydraulic study and optimization of the DEMO Water Cooled Lithium-Lead Breeding Blanket

Facoltà di Ingegneria Civile e Industriale
Dottorato di Ricerca in Energia e Ambiente - Scuola di Dottorato in Scienze e Tecnologie per l'Innovazione Industriale – XXXIII Ciclo

Candidate

Francesco Edemetti

ID number: 1343253

Thesis Advisor

Prof. Gianfranco Caruso

February 8, 2021

“This page has been intentionally left blank”

ABSTRACT

One of the key components of a nuclear fusion power plant is the Breeding Blanket (BB), in charge of ensuring the essential functions of Tritium production, shield the Vacuum Vessel (VV) and remove the heat generated in the toroidal chamber. Two conceptual designs are currently being studied for the implementation in the DEMOnstration Fusion Reactor (DEMO) in the framework of R&D activities under the coordination of the EUROfusion Consortium. One of these two BB is the Water-Cooled Lithium-Lead (WCLL), which relies on two different fluid: the water, necessary to remove the generated heat in the tokamak and to shield the vacuum vessel from neutrons, and the Lithium-Lead (PbLi) eutectic alloy, adopted as breeder and neutron multiplier, necessary for the Tritium production in order to make the fusion self-sustaining. The first function is fulfilled by two independent cooling systems: the First Wall (FW), that facing the plasma removes the heat flux raised from it, and the Breeding Zone (BZ), that removes the deposited power due to neutron and photon interaction inside the breeder. To guarantee good energy conversion efficiencies, these two systems must operate under certain conditions, and pressurized water at the typical pressure of the nuclear Pressurized Water Reactor (PWR) is adopted.

The Ph.D. work has been developed in collaboration with ENEA Brasimone Research Center, under the coordination of the EUROfusion Consortium in the task of the Work Package Breeding Blanket.

The aim of this Ph.D. thesis is to contribute to the development of the conceptual design of the WCLL breeding blanket, in order to design an efficient and reliable system, demonstrating the capability to fully withstands the DEMO requirements in normal and off-normal conditions. The activity has been focused on the thermal-hydraulic of the system; specifically, the analyses were performed on one single elementary cell, that compose the WCLL due to its periodicity. To perform realistic analyses, multiple factors have taken into account: engineering aspects, neutronic and thermo-mechanic. This has been pursued through the engineering approach and with the application of the numerical CFD code to represent the behaviors of the different analyzed models.

The first part of this study (Chapter 3) starts from the WCLL design review, which is described in Section 3.1. This section concerns the previously studied and developed configurations of the WCLL. Four different configurations (T01.A, T01.B, T02 and T03) have been studied in a comparative analysis, evaluating the main advantages and issues, that have led to the

development of the WCLL 2018 V0.2 configuration. The WCLL 2018 V0.2 is the starting point of this research activity. The elementary cell is fully described in Section 3.2, where all the components have been expounded, concluding the introductory part of this Ph.D. work.

Subsequently, in Chapter 4, different thermal-hydraulic analyses have been performed through numerical simulations, where a complete three-dimensional finite volume model of the WCLL elementary cell has been set-up in each analysis, using the commercial CFD code ANSYS CFX v18.2. Several steady-state analyses have been performed in order to optimize the BZ tubes layout, the FW cooling system, the BZ manifold layout and to evaluate the impact of the heat transfer modelling approach through the PbLi modelling and its properties. Once the CAD has been defined, the thermal power and the related cooling systems, FW and BZ, have been set through an analytical approach, in order to guarantee compliance with the main DEMO requirements design. The numerical model includes fluid and solid domains, representing in detail the WCLL elementary cell with its different structures and fluids. The Section 4.3 has the aim of optimizing the arrangement of the BZ pipes, guaranteeing a Eurofer temperature below the imposed limit of 550°C, and water at certain conditions in compliance with the thermodynamic cycle assumed for the electricity production. Several configurations have been analyzed to identify a promising BZ coolant system layout, which satisfies the DEMO requirements. The CFD analyses have been carried out investigating the temperature field of the solid structures, Eurofer and Tungsten, and also the thermal-hydraulic performances of the water-cooling systems and PbLi. These optimization analyses led to the V0.6 configuration, which has set the minimum number of BZ tubes to 22 and ensuring a symmetric temperature field in the toroidal direction in the BZ and FW systems and concerning the FW also in poloidal direction, a maximum temperature of the Eurofer structures of around 500°C, which not exceeds the imposed limit of 550°C.

In the next paragraph, the Section 4.4, a FW water channels optimization has been achieved, reducing the channels number from 10 up to 4. This channels reduction has been pursued thanks to the fact that the FW temperature was considerably below the imposed limit of 550°C, and to a DEMO's thermal load review that has led to a modification on the imposed heat flux on the FW from 0.5 MW/m^2 to 0.32 MW/m^2. The optimization has returned a greater homogeneity of the temperature field between BZ and FW systems, reducing the passive heat removal of the FW system from the BZ system. Although the pressure drops strongly increase, it has resulted in a decrease in the volume of water present in the first centimeters of the cell which positively affects the Tritium Breeding Ratio (TBR), the fundamental parameter for the Tritium production. The V0.6 configuration with 4 water channels (named V0.6_FW4), fully

withstands the DEMO thermal loads not exceeding the Eurofer temperature limit of 550°C. Another important parameter that has been affected by this reduction is the FW water velocity that has been strongly increased, enhancing the water thermal-hydraulic performances.

In Section 4.5, the results from the analysis of the V0.6_FW4_R model have highlighted that the recirculation manifold have to be adopted to guarantee large and safety margins from a thermal crisis. The recirculation ensures a lower wall temperature in all the BZ tubes, especially in the tubes near the FW which are subjected to greater power deposition. In addition, a greater flow of water flow rate, guarantee a large and safety margin from the possibility of thermal crisis.

The second part of the activity, reported in Section 4.6, concerns the assessment of the assumption made in the numerical model development. Since the PbLi thermal conductivity deeply affects the elementary cell temperature field, due to its huge thermal inertia, a study was also conducted on it. Two different PbLi thermal conductivity have been chosen to evaluate the temperature field of the cell, the suggested Mogahed correlation and the conservative IAEA correlation. The analyses have also been performed with the PbLi domain set as liquid and solid, evaluating the impact of this assumption on the numerical prediction. It has been evaluated that the PbLi modelling approach does not affect the results, increasing the temperature field by only a few degrees in the model with solid PbLi. In addition, simulations with liquid PbLi in forced convection and absence of buoyancy forces and magneto-hydrodynamics effects, have demonstrated that the convective contribution to the heat exchange is actually negligible. The PbLi has, in both cases with forced convection and in the absence of buoyancy effects, a laminar flow. Moreover, to evaluate the liquid metal behavior the Prandtl number has been analytically evaluated. The dimensionless number has shown that the thermal diffusivity, which is related to the rate of heat transfer by conduction, unambiguously dominates prevailing on convection, that can be neglected. Instead, what significantly affects the model is the adopted PbLi thermal conductivity correlation, that with the IAEA causes the Eurofer temperature limit to be exceeded and the hot-spots onset. Due to the choice of setting as reference property, for the PbLi thermal conductivity, the IAEA correlation, the analyses on the updated configuration returns an Eurofer temperature field which exceeds the imposed Eurofer temperature limits in different areas.

The analyses, reported in Section 4.7, have led to a further set of simulations to find out a BZ tubes layout in order to guarantee the respects of the requirements, even in the worst conservative conditions. The second BZ optimization has carried out an alternative BZ tubes disposal, which has resulted in a configuration named WCLL 2018 V0.6_B. These

modifications have not led to major changes in the BZ water domain, keeping almost unchanged the relevant thermal-hydraulic parameters, as velocity, pressure drops and temperature. However, they have involved the PbLi and structures temperature field reaching a Eurofer temperature slightly below the imposed limit of 550°C, extinguishing the structures hot-spots. The V0.6_B has been chosen as final configuration, able to cope with the operative DEMO thermal loads, guaranteeing the respect of the DEMO Eurofer temperature limit and its related requirements.

The last part of this work (Chapter 5) has been focused on the operational phases of the WCLL breeding blanket. One of the main functions of the BB is the conversions of the thermal energy from the fusion reaction in energy suitable for the power generation. The pulsed nature of the DEMO fusion reactor divides the operative phase in two main phases: pulse where the Deuterium and Tritium are burnt and energy is produced for 120 min, and dwell estimated to be 10 min where the central solenoid is recharging, and decay heat is removed. This research activity has been pursued to verify if the selected V0.6_B design is able to face the DEMO operational phases, investigating the response of the systems from the thermal-hydraulic point of view. In Section 5.1, a three-dimensional model has been reproduced according to the main outcomes of the previous Chapter. Different CFD transient analyses have been performed to verify if the selected design is suitable with the DEMO constrains and requirements, investigating different thermal behaviors. Transient thermal-hydraulic analyses have been set-up to simulate the burning phase, composed by ramp-up and ramp-down, after which steady state conditions of full power and dwell are reached respectively. Moreover, power fluctuation analyses have been performed to investigate the plasma instabilities caused by the pellets injection during the normal operation, this causes peaks of over or under power. In addition, a further analysis focused on the evaluation of the effect of the PbLi thermal inertia has been performed. This analysis it does not represent any realistic behavior of the reactor, as the previous ones, but it serves to investigate the ideal behavior that would occur in PbLi in case of constant cooling.

Unfortunately, the transient analyses require a significantly higher computational cost, and this implies that in order to obtain results in a reasonable time, it is mandatory to reduce the number of elements in the numerical model. Although it is interesting to obtain extremely accurate output values of the model, the main goal of these analyses is to investigate the global performances of the cooling systems, therefore, in Section 5.2 a mesh sensitivity has been performed in order to reduce the high number of elements without losing accuracy in the obtained results.

To perform the transient analyses different time-dependent thermal loads have been considered. The operational phases of DEMO have been characterized by different power contributions which vary in space and time. These thermal loads have been widely discussed in Section 5.3, identifying the power contribution curves to adopt for the model. In particular, in Section 5.4, the model solver settings and boundary conditions have been set-up per each run.

In Section 5.5, the results have been described and differentiated by steady-state and transient analyses. The first part (Section 5.5.1) concerns the steady-state analyses performed to impose the initial conditions for the transient, and in the second part (Section 5.5.2), the transient analyses have been widely discussed. In particular, in sub-sections 5.5.2.1 and 5.5.2.2, the fast ramp-up and ramp-down phases are respectively analyzed. Both show how the PbLi thermal inertia plays a key role in the rise and fall of the temperature of the structures, ensuring to the systems a slowly gradual trend. The FW system promptly reacts to the power variation, showing a temperature trend similar to the power one. Instead, the BZ system slowly reacts to power variations. It depends on the PbLi thermal inertia, which strongly slows down the temperature trend, causing a considerable delay in reaching steady-state conditions. In both simulations, the Eurofer temperature is below the limit and the operative water constrains are respected and guaranteed.

The study of the power fluctuations has been reported in sub-sections 5.5.2.3 and 5.5.2.4, where the V0.6_B layout has been subjected to different power oscillation. These analyses have been performed for the purpose of studying if the PbLi thermal inertia can mitigate these oscillations, continuing to operate within the required requirements. The thermal-hydraulic goal is that the elementary cell continues to supply water to the Primary Heat Transfer System (PHTS) at the required conditions for the electricity production. In addition, it has been highlighted that, in the remote case of an overpower peaks series, the huge PbLi thermal inertia absorbs these oscillations not provoking a temperature build-up. The same cannot be stated regarding the FW systems where a slight temperature build-up has been evidenced.

In sub-section 5.5.2.5, an unrealistic study has been performed to evaluate the PbLi thermal inertia. The system has been subjected to a step-down ramp, passing from the nominal power to a zero-power condition. The analysis is aimed at identifying the characteristic time trend of both systems. A strong cooling time differentiation, between FW and BZ system, has been highlighted, where the cooling time of the PbLi has different order of magnitude compared with the FW.

In conclusions, different numerical simulations have been performed to fully evaluate the thermal behavior of the WCLL elementary cell, within steady-state and transient analyses. The

first part of the Ph.D. research activity has focused in the development of a WCLL elementary cell design that satisfies the DEMO requirements, optimizing the BZ tubes and the FW water channels. The analyses have led to choose a final design the V0.6_B layout, since it withstands the normal operative thermal loads. The second part, instead, has demonstrated that the selected design is able to withstand all the operational phases of the DEMO fusion reactor, confirming the choice made in the first part. The final design has been selected to comply with the DEMO requirements, withstanding the thermal loads, and guaranteeing adequate water conditions for the electricity production during all the reactor phases.

“This page has been intentionally left blank”

LIST OF CONTENTS

“This page has been intentionally left blank”

LIST OF ABBREVIATIONS

BB	Breeder Blanket
BC	Boundary Condition
BoP	Balance of Plant
BP	Back Plate
BSS	Back Supporting Structure
BZ	Breeding Zone
CAD	Computer Aided Design
CANDU	CANadian Deuterium Uranium reactor
CB	Ceramic Breeder
CEA	Commissariat à l'Energie Atomique et aux Energies Alternatives
CFD	Computational Fluid Dynamics
COB	Central Outboard Blanket
CP	Cooling Plate
CR	Research Center
CS	Central Solenoid
D	Deuterium
D-T	Deuterium-Tritium (nuclear reaction)
DB	Dittus-Boelter correlation
DCLL	Dual Coolant Lithium Lead (Blanket)
DEMO	Demonstration fusion power plant
DIAEE	Department of Astronautic Electric and Energetic Engineering
DIV	Divertor
DWT	Double Wall Tube
ECH	Electron Cyclotron Heating
EFDA	European fusion development agreement
ENEA	Italian National Agency for New Technologies, Energy and Sustainable Economic Develpment
ESS	Energy Storage System
FEM	Finite Element Method
FPP	Fusion Power Plant
FW	First Wall
HC	Helical
HCLL	Helium Cooled Lithium Lead (Blanket)
HCPB	Helium Cooled Pebble Bed (Blanket)
He	Helium
HF	Heat Flux
HSP	Horizontal Stiffener Plate
HTC	Heat Transfer Coefficient
IB	Inboard Blanket
ICH	Ion Cyclotron Heating
IHTS	Intermediate Heat Transfer System
IHX	Intermediate Heat Exchanger
ITER	International Thermonuclear Experimental Reactor
LIB	Left Inboard Blanket
LOB	Left Outboard Blanket
LOCA	Loss of Coolant Accident
LOFA	Loss of Flow Accident
MHD	Magneto Hydro Dynamic
MFR	Mass Flow Rate
MMS	Multi-Module Segment
MS	Magnet System
NBI	Neutral Beams Injection
NMM	Neutron Multiplier
OB	Outboard Blanket

PbLi	Lithium Lead
PCS	Power Conversion System
PFC	Plasma Facing Component
PFC	Poloidal Field Coil
PHTS	Primary Heat Transfer System
PPPT	Power Plant Physics & Technology
PWR	Pressurized Water Reactor
R&D	Research and Development
RAFM	Reduced Activation Ferritic/Martensitic (Eurofer)
RELAP	Reactor Loss of Coolant Analysis Program
RIB	Right Inboard Blanket
ROB	Right Outboard Blanket
SMS	Single-Module Segment
SW	Side Wall
T	Tritium
TBM	Test Blanket Module
TBR	Tritium Breeding Ratio
TES	Tritium Extraction System
TFC	Toroidal Field Coil
TR	Tie Rods
TRS	Tritium Removal System
VSP	Vertical Stiffener Plate
VV	Vacuum Vessel
WC	Water Cooled
WCLL	Water Cooled Lithium Lead (blanket)
WP	Work Package
WPBB	Work Package Breeding Blanket
WPBoP	Work Package Balance Of Plant

LIST OF FIGURES

LIST OF TABLES

“This page has been intentionally left blank”

1. INTRODUCTION

From a technical and economic perspective, energy is the commodity that allows a society to progress and develop. Nowadays, the development of a robust and reliable energy sector, able to promote a sustainable and secure energy solution is pivotal to every economic, environmental and developmental issue. The energy demand is expected to be more than double in 2050 [1], this will be caused by a constant increase of population and increasing use of energy per capita due to the use of products that are increasingly running on electricity and increasingly connected. Moreover, considering the progressive reduction of the use of fossil fuels, to mitigate the increase in greenhouse gases emission, as the CO2, as well as the necessity of cleaner ways to produce energy, the world population is forced to invest in the research for alternative power sources that can provide them a long-term sustainability, reliability and security. In compliance with this background, nuclear energy has become a considerable solution to solve the energy problem. Nuclear energy provides a large amount of energy in a comparative manner with fossil fuels, is carbon-free and with low variable costs. However, nuclear energy still has to solve problems as nuclear waste management, proliferation risks and safety during the severe accident. In this framework, nuclear fusion has several advantages over nuclear fission, if the technology will be successfully developed, so it has been selected as a research field where to make large investments. It has been considered as the most suitable solution to the energy problem. It will ensure sustainability and security of supply: fuels are widely available and virtually unlimited since they are processed from water; no production of greenhouse gases; intrinsically safe, as no chain-reaction is possible; environmentally responsible, with a proper choice of materials for the reaction chamber, radioactivity decays in a few tens of years and at around 100 years after the reactor shutdown all the materials can be recycled in a new life cycle. However, efforts still need to be done to engineer a system that can sustain the plasma for a period sufficient to reach very high temperatures and density and use materials that withstand to this particular environment.

During 2012, the EUROfusion's previous organization [2], the European Fusion Development Agreement (EFDA), has published a roadmap which outlines hot to supply fusion electricity by 2050. The "Roadmap to the realization of fusion energy" [1] breaks the quest for fusion energy down into eight missions. For each mission, it reviews the current status of research, identifies open issues, proposes a research and development programme and estimates the

required resources. It points out the needs to intensify industrial involvement and to seek all opportunities for collaboration outside Europe.

These eight missions can briefly resume in:

1) Demonstrate plasma regimes of operation with ITER (based on the tokamak configuration);
2) Demonstrate a heat exhaust system capable of withstanding the large load of DEMO;
3) Develop materials that withstand large 14 MeV neutron fluence without degrading their physical properties;
4) Ensure tritium self-sufficiency through a technological solution for the breeding blanket; which will have to be made consistently with the choice of the components for the transformation of the high-grade heat into electricity (the so-called Balance of Plant).
5) Implement the intrinsic safety features of fusion into the design of DEMO following the experience gained with ITER;
6) Combining all the fusion technologies into an integrated DEMO design; e.g. exploiting a complete BoP including the heat transfer and associated electrical generation systems;
7) Ensure the economic potential of fusion by reducing the DEMO capital costs and developing long-term technologies;
8) Bring the stellarator line to maturity.

From an initial roadmap of 2012 where some dates were provided and foreseen, considerable technological challenges had to be faced, and for this reason, the roadmap has evolved in a new one, scheduled with: short, medium and long term. Precisely in 2018, a new "European Research Roadmap to the realization of fusion energy" [3] has been published, where ITER has been identified as the facility that will have to provide the greatest number of answers regarding the feasibility of fusion, and DEMO has been identified as the power plant reactor which will pave the way for commercial reactors. In addition, a characterization was given to the three main phases, where, the end of the short-term will be identified with the ITER first plasma ignition, the medium-term will end with the DEMO commence construction and it is where the long-term will starts, until the electricity production will be achieved.

The DEMO reactor must demonstrate the possibility of generating electricity through nuclear fusion reactions, although not in a cost-effective way as the commercial power plants.

Moreover, it must operate with technologies able not only to control the plasma but also to generate electricity as a safe and reliable power plant. The main challenge of the DEMO power plant will be to create and sustain a long-lasting plasma with a power 25 time higher than ITER, and moreover to maintain its stability to demonstrate the feasibility of the electricity production [4].

1.1. Framework of the activity

The Ph.D. research activity has been performed in the framework of a cooperation between the University of Rome – DIAEE (Department of Astronautic, Electrical and Energetic Engineering) and the ENEA Brasimone Research Center – Experimental Engineering Division (FSN-ING), under the coordination of the European Consortium for the Development of Fusion Energy (EUROfusion).

Since 2014, the EUROfusion Consortium manages and coordinates fusion research activities and it was established to succeed the European Fusion Development Agreement (EFDA). It has been funded by the Euratom agency, to pursue the stated goal of an operative DEMOnstration Fusion Power Plant (DEMO) in accordance with the roadmap for the realization of the fusion energy, in the frame of the Horizon2020 programme. In this context, the development of two alternative blanket designs is being studied in the DEMO pre-conceptual phase: the Helium Cooled Pebble Bed (HCPB), based on solid breeder technology, and the Water-Cooled Lithium Lead (WCLL), based on liquid breeder technology.

The EUROfusion Consortium agreement has been signed by thirty members research organizations and universities from 26 European Union countries plus Switzerland. Italy is one of the signatory members of EUROfusion Consortium and ENEA is the national Research&Development (R&D) agency that leads and coordinates the activities. This programme involves several universities and industries, one of these is the Sapienza University of Rome which is involved in different research activities. ENEA actively participates to the conceptual development of the DEMO power plant. In particular, at Experimental Engineering Division (FSN-ING) of ENEA C.R. Brasimone, R&D activities are pursued to develop the WCLL design in the framework of the Work Package Breeding Blanket (WPBB) project of the EUROfusion Power Plant Physics & Technology (PPPT) Programme.

In particular, Sapienza University of Rome is the third linked part of ENEA, and one of the commissioned activities is precisely the study of the WCLL thermal-hydraulic by means of CFD code.

1.2. Objectives of the thesis

The objectives of this thesis is to develop a conceptual design that can safely operate and satisfy the multiple DEMO requirements, which is also one of the open fields in the WCLL breeding blanket research activities. The BB is one of the key components of a nuclear fusion power plant, is in charge of ensuring the essential functions of Tritium production, generating the fuel necessary for the plant self-sustainment; shield the Vacuum Vessel (VV) from nuclear radiation that may impact essential reactor systems and personnel and superconducting coils in order to avoid quenching; remove the heat generated in the toroidal chamber by photons and neutrons interaction, converting in energy suitable for the electricity production.
This research activity has focused on developing the conceptual design of the WCLL from a thermal-hydraulic point of view, demonstrating the capability to fully satisfy the DEMO requirements. The goal is to be able to identify a configuration of the elementary cell that has to satisfy several design requirements concerning the structures and both cooling systems, the First Wall (FW) and the Breeding Zone (BZ). The requirements are listed below:

- Temperature symmetry in toroidal direction;
- Maximized cooling performances enhancing the water heat transfer coefficient;
- Structures temperature below the imposed limit;
- Optimized number of BZ tubes reducing the amount of Eurofer into the BZ increasing the breeder volume which affect the Tritium production performances;
- Optimized number of FW channels reducing the amount of Eurofer and water into the FW which affect the Tritium production performances;
- Enhancing manufacturability avoiding pipes crossing structural stiffeners.

Based on these points, a preliminary review of the previous WCLL configurations has been studied, highlighting the advantages and issues of the different configurations. Both have shown achieved goals but in conflict with other points. It was necessary to study these results and to engineer them, even if taken individually they seemed disparate, to analytically develop an elementary cell which can satisfy all these requirements. This process led to the creation of a

layout named WCLL 2018 V0.2. To better understand the feasibility of this innovative layout, a three-dimensional finite volume model of the elementary cell has been set-up, using the CFD code ANSYS CFX v18.2. The model fully reproduces in detail the WCLL elementary cell, composed of solid and fluid domains. From this CFD model, the optimization process of the BZ and FW systems has begun. Several analyses have been performed to investigate thermal and fluid-dynamic behavior of the breeding cell, to optimize and evaluate the efficiency of the FW and BZ water cooling systems, and to verify if the maximum temperature of solid structures were in the allowed limits. Moreover, after each analysis, key issues and areas of improvements are highlighted for further optimization. Once the number of tubes and channels has been optimized, efforts have been made to improve the efficiency of the cooling system, optimizing temperature distribution, reducing the tubes wall temperature to avoid thermal crisis and enhancing the water thermal-hydraulic performances.

This process has led to obtaining the WCLL 2018 V0.6 layout, which operates with twenty-two BZ tubes with an alternative manifold that adopts the recirculation and four FW channels in alternate and opposite flows. In order to verify the effective efficiency of the systems, conservative boundary conditions have been implemented in CFX, so as to confirm the choice made and the solutions adopted. These analyses led to further optimization of the layout, modifying the layout of the tubes due to the hot-spots onset into the structures exceeding the imposed limit. The final selected design has been confirmed through the numerical simulation, returning a model that faces the imposed requirements. The configuration is named WCLL V0.6_B.

The second part of the activity has the objectives to verify if the elementary cell WCLL V0.6_B is able to withstand the postulated operational phases of the DEMO power plant. In this part, transient CFD analyses have been performed, which require a significantly higher computational cost. This implies that in order to obtain results in a reasonable time, it has been deemed mandatory to reduce the number of elements in the numerical model. The main goal of these analyses has been switched in investigating the global performances of the elementary cell with its related cooling systems and the temperature field of the structures. The pulsed nature of the DEMO fusion reactor divides the operative phase in two main phases: the Pulse where the Deuterium and Tritium are burnt and energy is produced for 120 min, and the Dwell estimated to be 10 min where the central solenoid is in recharge and the decay heat is removed. Transient thermal-hydraulic analyses have been set-up to simulate the Pulse-Dwell phase,

composed by ramp-up and ramp-down, after which steady state conditions of full power and dwell are reached, respectively. In addition, power fluctuation analyses have been performed to investigate the plasma instabilities caused by the pellets injection during the normal operation, this causes peaks of over or under power. In addition, a comparison between the obtained data and the data provided by the analysis done in the Balance of Plant Work Package (WPBoP), has been done. The comparison laying the basis to understand the commercial feasibility of the reactor with the postulated off-reactor systems necessary to produce and provide electricity to the grid.

The research activity has led to the development of a complete conceptual design of WCLL breeding blanket elementary cell, that fully satisfy the DEMO design requirement. Moreover, the configuration fully withstands the DEMO thermal-loads postulated in normal and off-normal operation and deals with the pulse nature of the reactor with its plasma instabilities.

1.3. Thesis structures

This Ph.D. thesis is structured in six sections. The first section includes a brief introduction, the framework and objectives of the research activity, whereas the sixth section presents the conclusions and perspectives.

An overview of the nuclear fusion technologies, DEMO reactor with its components, fuel cycle and breeding blanket concepts are described in the second section.

The third section describes in detail the Water-Cooled Lithium Lead Breeding Blanket. It starts with a brief review of the previously analyzed blanket concepts, which led to the development of the actual configuration. In the subsections, the actual WCLL configuration is described, with its main functions, requirements and limits. In addition, FW, BZ and Manifold regions are widely discussed, describing their functions and design. In the last part the main achievement and issues of the WCLL 2018 V0.2 are pointed out.

In the fourth section, the first part of the numerical simulations is reported. Thermal-hydraulic steady state analyses are performed starting from the elementary cell layout described in the previous section (WCLL 2018 V0.2). The three-dimensional finite volume model of the

elementary cell has been developed to perform the CFD simulation. Several studies are carried out regarding: the optimization of the BZ tubes layout and FW channels; evaluation of the impact of an alternative BZ manifold; investigation of the PbLi modelling impact with its related thermal properties; realization of a design that meets all DEMO requirements during the normal operation. The last subsection showed an elementary cell design (V0.6_B) which is able to face the steady state operational phase of the DEMO reactor.

Then, in the second numerical part (fifth section), a validation of the selected design is performed through transient thermal-hydraulic analyses. The different operational phases of the reactor are analyzed to verify if the selected design can sustain the operative pulsed behavior of DEMO reactor, evidencing peculiarities or issues.

2. NUCLEAR BACKGROUND

The current nuclear power plants produce energy with a process in which a heavy nucleus, mainly uranium, collides with a subatomic particle, neutron, producing new lighter nuclei and subatomic particles. This process is called nuclear fission, and when one single nuclear reaction causes other subsequent nuclear reactions, thus leads to a self-propagation through a chain process. The opposite process, that allows two light nuclei to collide and fuse together into a heavier nucleus, is the nuclear fusion. In both case, nuclear reactions, in accordance with the mass-energy conservation principle, are accompanied by a net energy release; thus, the missing mass is transformed into energy, in accordance with the famous Einstein's equation $E = mc^2$ formulated in 1905. The energy release depends on the type of the nucleus/nuclei and, therefore, on the type of performed reaction. Since the nuclei, lighter than iron, have an energy release with fusion reactions and heavier than iron release energy with fission reactions.

2.1. Nuclear fusion technology

Fusion reaction is the process that powers the stars, it occurs spontaneously, given the reached very high temperatures [5]. To originate a nuclear fusion reaction, two nuclei have to collide with enough energy to overcome the mutual repulsive Coulombian force acting between them, approaching each other sufficiently close that the short-range attractive nuclear force becomes dominant. In order to provide enough energy to the nuclei, to approach and fuse together, overcoming the Coulombian force, kinetic energy is increased by heating up to temperatures around 100 millions of degrees [6]. At these temperatures, the matter is no longer in a gaseous state but in a plasma state. Once temperature reaches the order of 10000 degrees, the electrons detach from nuclei forming an ionized gas where naked charged nuclei and free electrons move independently, being so energized that they don't combine, this state of matter is called plasma.

The reaction identified as the most suitable for fusion reactors involves two heavy hydrogen isotopes, Deuterium (D) and Tritium (T), described by the expression:

$$D_1^2 + T_1^3 \rightarrow He_2^4\ (3.5\ MeV) + n\ (14.1\ MeV)$$

which produce a total amount of energy of 17.6 MeV. This reaction is characterized by the highest reactivity at the lowest temperature of all relevant reactions [6]. In order to be able to obtain this reaction, the fuel (i.e. Deuterium and Tritium) must be heated to temperature over $5 \cdot 10^7$ degrees before achieving a significant fusion rate.

Since fusion has been discovered in the 30s of the past century, the hardest challenge was to be able to create a machine capable of reaching such temperatures to heat the fuel and to confine it for a sufficiently long time, enough to produce through fusion reactions, more energy than was spent on heating the plasma [6]. During these years various types of machine have been studied to heat and confine the plasma, which differs by the types of confinement. Two of these have gathered the greatest interest and are the inertial and the magnetic confinement. In the former, a small pellet of D-T fuel is subjected to a high pulse flow of highly powerful laser that creates a high-density plasma instantly increasing the temperature of the pellet providing a favorable fusion reaction rate for few nanoseconds. The second approach, which is the one on which the investments are focusing, uses strong magnetic fields to confine the plasma in a vacuum environment with a toroidal shape, named tokamak [7].

2.1.1. Magnetic confinement

In a fusion reactor, which works with a tokamak magnetic confinement, the reactions take place inside the plasma, confined in the toroidal chamber. The charged particles are subjected to the magnetic field by Lorentz force, which determines their trajectory. Imposing a magnetic field to the torus chamber, the particles start to orient with the magnetic field line and move with a path, in accordance with the field lines, in the toroidal chamber with no escapes. However, the motion will tend to diverge to the outer plasma edge escaping from the plasma; this is due to the centrifugal force, which must be balanced with the Lorentz one. To ensure that all forces are balanced, two different magnetic fields are applied: toroidal and poloidal; this establishes a helical path, perpendicular to the torus axis, avoiding that charged particles escape from the plasma. In addition, a central solenoid coil is placed in the central hole of the tokamak to induce the plasma current which acts as a starter for the plasma's ignition. In Fig. 2.1 a schematic diagram showing the working principles of the tokamak magnetic configuration is shown.

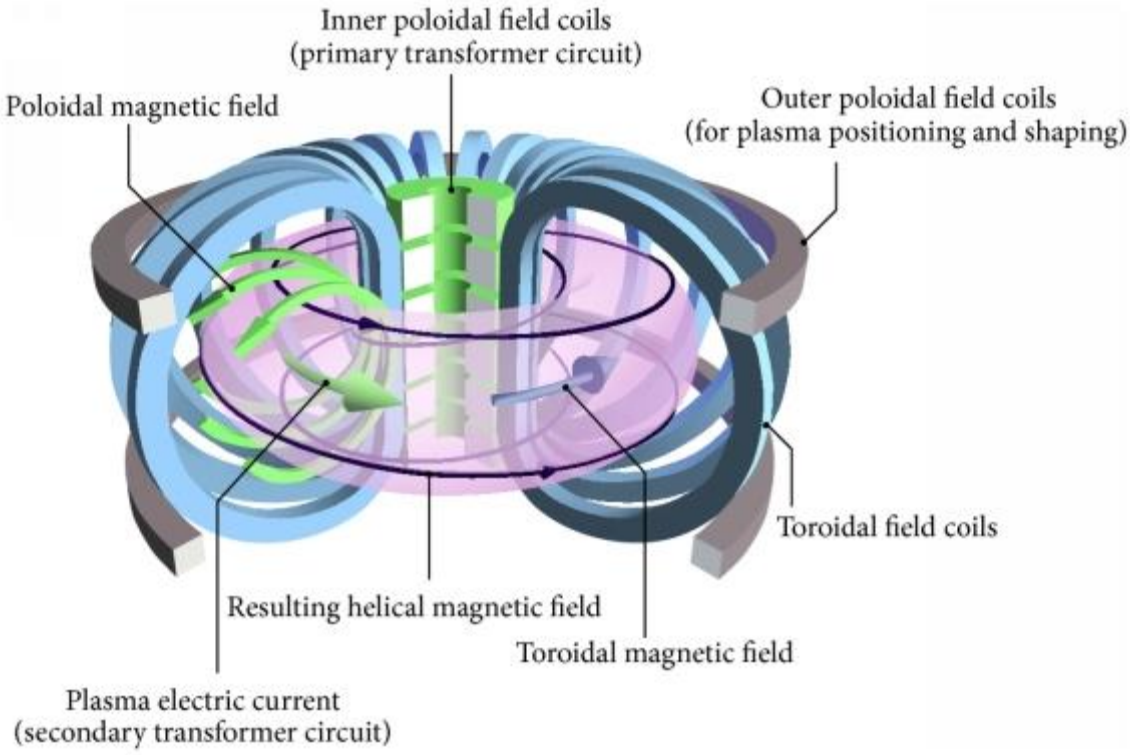

Fig. 2.1 – Tokamak magnetic confinement working principles [8]

To reach the sufficient conditions to obtain fusion reactions, the plasma current is not enough, and even if the Helium produced by the D-T reaction remain in the plasma transferring its energy to it, additional systems are necessary to heat the plasma and balance the thermal losses, such as: neutral beam injection, radiofrequency heaters and current drive.

Currently, the largest European tokamak is the Joint European Torus JET [9], which has reached the breakeven point with a gain factor of Q=1, where the energy spent is equal to the energy produced. The demonstration of high-power fusion reactor with a $Q \geq 10$ is the main mid-term goal, which will have to be proved by the International Thermonuclear Experimental Reactor ITER [3][8], which is actually under construction in France and will be the first large scale reactor. Once ITER will demonstrate the feasibility of a sustainable fusion reactor [10], the construction of the DEMOnstration Fusion Power Plant DEMO will begin to demonstrate the successive steps: the electricity supply to the grid and the realization of a closed fuel cycle [2][3].

2.2. DEMO reactor and components

The DEMO reactor relies on the tokamak magnetic confinement, with Deuterium and Tritium as fuel. The hot plasma, where the D-T reaction occurs, is held in a thermally insulated chamber, the Vacuum Vessel (VV). As described in the section above, the D-T reaction has, as reaction product, Helium and neutron; the Helium heats the plasma, but neutron is intensely energetic and it is very difficult to contain into the plasma or even in the VV, it bombards the structural components and causes severe damages and activation products. Neutrons are essentials for the reactor operation, due to their high energy that can be extracted and the possibility to close the fuel cycle with a breeding operation.

To obtain a lasting fusion reaction, different systems are necessary to create, control and monitor the plasma. These systems must also provide a protection and mitigation for human and plant safety, containing the reaction products, radionuclides and thermal power. Different and structured confinement are adopted, ensuring an adequate shielding. These containments can be identified in three main groups, where, within them contain multiple systems [11]. The principal three confinement and their related systems of DEMO are described in the following [10]-[14]:

- Vacuum Vessel (VV): is a torus-shaped double-walled pressure vessel. It encloses the plasma chamber, and provides a high-vacuum environment, with very high purity, which improves the plasma stability, must withstand high temperature to shield and maintain radionuclides and neutron inside the reactor. It also shields the Magnets System. The VV houses the in-vessel components and systems:
    - Breeding Blanket (BB): DEMO is subdivided into 16 sectors with two inboard (IB) and three outboard (OB) segments each. Each segment is composed by the First Wall (FW) that is a plasma-facing component integrated with the blanket. It must withstand to high heat loads and radiation that arise from the plasma, is actively cooled to refrigerate the structures and to transfers the heat loads for the electricity production;

      and the Breeding Zone (BZ), placed behind the FW, it contains Lithium to breed into Tritium due to the neutron radiation, ensuring the reactor fuel self-sufficiency. It is refrigerated by one coolant that can be Helium or water, to cool down the internal structures and extracts the thermal power for electricity

production. In addition, it must ensure an adequate thermal and neutron shielding;

- Divertor: is placed at the bottom of the BB. The magnetic topology of the plasma causes that the field lines impact the Divertor targets, collecting and removing the spent Helium ashes and impurities from plasma. Is subjected to the highest heat loads and the particle impact causes the most severe erosion.

- Magnets System (MS): is an assembly of superconducting coils (SC) which provide the magnetic field to confine the plasma, driving its current and defining its poloidal structure. The magnets are composed by Low-Temperature Super Conducting Nb_3Sn, and are divided in three different coils group:
  - Toroidal Field Coils (TFC): powered by a constant current which provides the toroidal field;
  - Poloidal Field Coils (PFC): powered by a current that change over the plasma operation, they provide the poloidal and radial magnetic field and improve the plasma stability;
  - Central Solenoid (CS): is a stack of coils in the hole of the torus, it induces the plasma current by discharging itself;

- Cryostat: is a large single-walled, passively cooled vacuum vessel at the ambient temperature, placed outside the VV and MS, containing them. It provides the high-vacuum and very low-temperature environment necessary for the magnets and the plasma chamber.

The general DEMO layout is shown in Fig. 2.2.

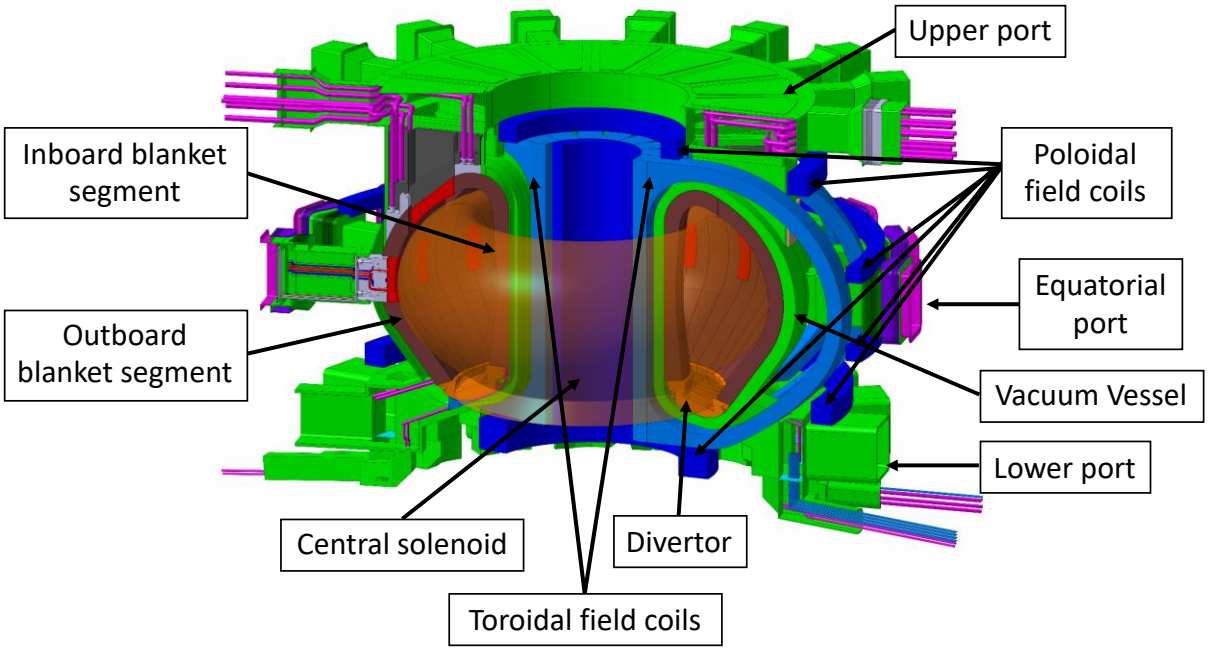

Fig. 2.2 – DEMO reactor general layout [12]

Several other relevant systems are necessary to obtain a fusion reaction. External heating systems are necessary to reach the high plasma temperature, employing: injection of neutral beams (NBI) into the plasma, transferring their energy to it; electromagnetic waves, Electron Cyclotron Heating (ECH) and Ion Cyclotron Heating (ICH). These three systems also provide additional functions as control and current drive. Another fundamental system is the Tritium Extraction System [14], that is tasked for the removal of the Tritium from the breeder, which aims at the tritium self-sufficiency, to restore in the reactor as fuel supplies.

Two different structural materials are adopted in DEMO [13], the first one is employed for the in-vessel components, is named Reduced Activation Ferritic Martensitic (RAFM) steel Eurofer, which must be refrigerated below temperatures of 550°C in order to ensure adequate thermo-mechanical properties. The second one is the AISI ITER-grade 316 stainless steel that is adopted for the VV.

Due to the necessity to provide a long-lasting plasma current, to guarantee the plasma stability, the DEMO fusion reactor works with two different phases alternate, being a pulsed regime machine. The first phase is the burning phase, is when the plasma is generated and the fuel is burnt inside the chamber producing nuclear reactions, thus energy. The second phase is the dwell phase, during which the CS is in recharge, preparing for the next pulse. In DEMO, the

pulse is assumed to be around 2 hours, followed by a dwell of around 10 minutes [12]. With these assumptions, the thermal fusion power is estimated to be 2000 MW_{th} resulting in a net electrical power of 500 MW_e [13]. The pulsed nature of the reactor poses a further challenge in building a grid-connected plant. The turbines, for electricity production, work in a continuous regime, and this pulsed behavior is deleterious to their life. To address this problem, a complex system's chain, which is devoted to the power extraction from the plasma and its conversion into electricity to deliver to the grid, has been adopted. The chain has, as first, the Primary Heat Transfer System (PHTS), that is responsible of converting the energy collected in the blanket by both cooling systems. The PHTS, followed by the Power Conversion System (PCS), ensure the electricity production during the burning phase. An Intermediate Heat Transport System (IHTS), which is placed between the PHTS and the PCS, operates in both phases, pulse and dwell. The IHTS is provided by an Energy Storage System (ESS), which accumulates energy during the pulse phase and releases during the dwell, to smooth the pulsed behavior producing a continuous conversion/production of electricity [15][16].

There are still many engineering and physical challenges that will have to be faced, more information on the open issues can be found in Refs. [17][18].

2.3. Fuel cycle

The D-T fusion reaction has been selected as a characteristic reaction on which tokamaks are based, due to its highest reactivity at the lowest temperature and to the availability of the fuel supply. Deuterium is the second most abundant hydrogen isotope, it exists in seawater at 0.0153% and can be extracted from it, a source with availability practically inexhaustible. Tritium, instead, is radioactive and undergoes beta decay in ^{3}He with a half-life of 12.5 yr, following the reaction:

$$T_1^3 \rightarrow He_2^3 + \beta^- + \bar{v}_e + 18.6\ keV$$

Its short half-life makes Tritium extremely rare on Earth and no industrial exploitation from a natural source is economically feasible. Achieving the Tritium self-sufficiency is a key issue in the development of a self-sustaining fusion reactor which operates with D-T fuel.
Actually, Tritium is artificially produced as product of the CANDU fission reactor operations, where it is generated by the irradiation of the moderator, which is heavy water (D_2O). Moreover,

the quantity produced is useless for a large-scale reactor as DEMO, and in addition, a closed fuel cycle is one of the key points of the fusion realization roadmap; thus, the supply of Tritium cannot be dependent on the CANDU operations.

The chosen option to face this problem is to generate Tritium in the reactor through the breeding blanket, exploiting the high energy neutrons (14MeV), which derive from the fusion reactions, via capture reaction with Lithium, which is the breeder, as reported in the reactions below:

$$n^0 + Li_3^6 \rightarrow He_2^4 + T_1^3 + 4.8\ MeV$$
$$n^0 + Li_3^7 \rightarrow He_2^4 + T_1^3 + n^0 - 2.5\ MeV$$

The first reaction has a large cross section for thermal neutron, while the second reaction is more probable with fast neutrons. For this purpose, the breeder must be enriched up to 90% of ^{6}Li. Unfortunately, the fusion reactions have a low neutron production rate (1 per reaction), this implies that a neutron multiplier is necessary to face the neutron losses, due to capture or absorption, and to obtain a self-sufficient Tritium production. Therefore, the blanket is filled with the breeder and the neutron multiplier. The latter can be Beryllium or Lead, depending on which BB concepts is adopted. The R&D activities are actually focused on two different breeding blanket concepts: the Helium Cooled Pebble Bed (HCPB), based on solid breeder technology, and the Water Cooled Lithium Lead (WCLL), based on liquid breeder technology.

The realization of a closed fuel cycle passes through another engineering challenge: a highly efficient Tritium production in order to generate a surplus of it in a reasonable time to start a new reactor [19]. The reasonable time is expected to be around 5 years; in this regards it has been defined an important parameter, the Tritium Breeding Ratio (TBR). It is the ratio between the Tritium generated into the breeder and the Tritium burnt in the D-T reaction. The TBR is a complex parameter, composed by different and many reactor variables, which include radioactive decay, losses due to Tritium permeation, accumulation for a new reactor, failure of an extraction system. Concerning these uncertain variables, it has been set for DEMO a TBR ≥ 1.15 to achieve the tritium self-sufficiency [20].

2.4. Breeding blanket concepts

The breeding blanket is a key component in charge of ensuring the Tritium production, shield the VV from neutron and radiation and accumulates energy, generated into the plasma via thermal radiation and neutrons interactions, transforming into thermal energy. The latter is removed by means of cooling systems, which convey this energy to the PHTS, where is converted into electricity through a turbine.

Different blanket concepts are and have been studied in the last years, but they can be classified in two different main categories, solid breeder and liquid breeder, which still remains Lithium. Since 2014, four different blanket concepts have been selected to address the role of breeding blanket in the DEMO reactor [21]: the Helium Cooled Pebble Bed (HCPB), the Helium Cooled Lithium Lead (HCLL), the Dual Coolant Lithium Lead (DCLL) and the Water Cooled Lithium Lead (WCLL). The former and the last are the more promising two blanket concepts, currently under study, one with a solid breeder and other with a liquid one respectively. Therefore, the EUROfusion consortium has decided to continue to develop only the HCPB and the WCLL, to the detriment of the HCLL and DCLL. These blanket concepts will be outlined in Sections 2.4.1 and 2.4.2, and regarding the WCLL it will be outlined in Section 3.

The two blanket concepts, the HCPB and the WCLL, have a similar architecture and design features, imposed by the use of a common DEMO 2017 baseline [10]. They are both characterized by 16 sectors, each including two inboard and three outboard BB segments. They also adopt Eurofer as a structural material. Given the advantages obtained for the WCLL [22], both designs have been developed on the basis of the Single-Module-Segment (SMS) approach. Each segment consists of a long continuous Eurofer chase external box, composing the FW system, which develops along the entire poloidal length with a bottom and a top cap. In addition, both have provided a Back Plate (BP), which divide the BZ system with the manifold region. Each segment is supported by a Back Supporting Structure (BSS), which connects the BB to the VV [14].

2.4.1. Overview of the previous blanket concepts

The HCLL and the DCLL relied on liquid Lithium-Lead eutectic alloy (PbLi) as breeder, neutron multiplier and regarding the DCLL also as coolant, instead of HCLL which used the Helium gas as coolant.

The HCLL blanket concept was based on the Multi-Module-Segment (MMS) approach with Eurofer as structural material, PbLi was adopted as breeder, neutron multiplier and tritium carrier and Helium gas as coolant [23]. The coolant thermodynamic cycle was supposed to be 300°C – 500°C, at 8 MPa. The modules were attached to the BSS with Tie Rods (TR) forming a segment which could be easily removed from the upper port. The BSS was supposed to work as manifold, collecting and distributing PbLi and He to the different blanket modules. Horizontal stiffener plates (hSPs) had cooling and structural tasks. The PbLi was flowing in a "snake-like" path through the module, passing between two hSPs in a radial path toward the FW, flowing to the slice above through holes, designed one out of two hSPs, then radially flowing back until it was collected in the BSS. The resulting described design is shown in Fig. 2.3.

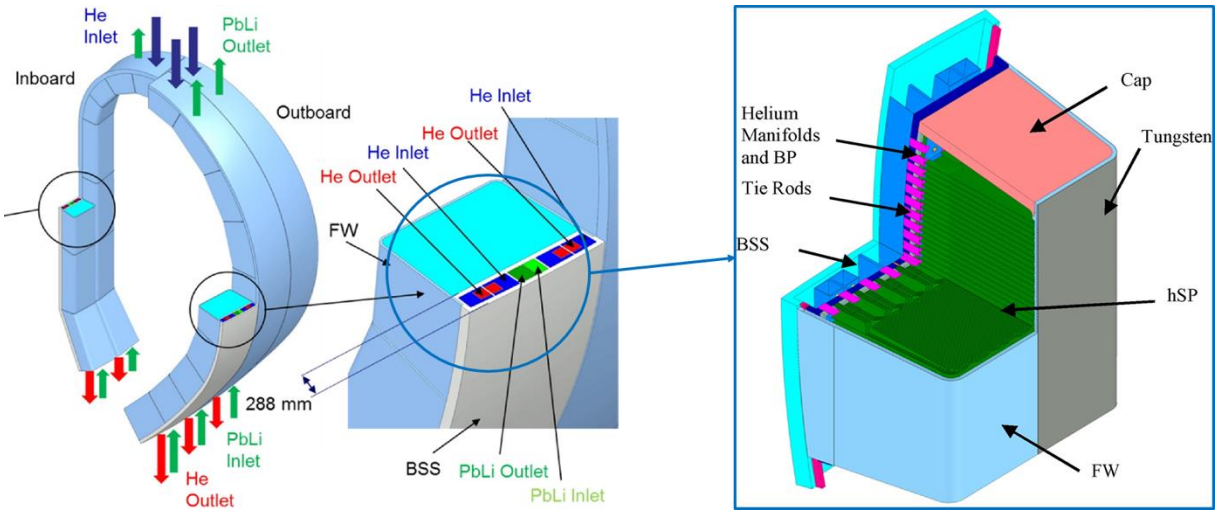

Fig. 2.3 – HCLL breeding blanket design concept (left) and equatorial outboard module (right) [23]

The DCLL blanket concept was based on the MMS approach, with Eurofer as structural material, where modules were joined to the BSS, which also accomplishes functions of manifold and shield. The PbLi was adopted as breeder, neutron multiplier, tritium carrier and BZ coolant; Helium gas was also adopted as FW coolant [24]. The PbLi was flowing mainly in poloidal direction through an array of 8 parallel circuits disposed along the toroidal direction. The FW system, covered by a 2mm Tungsten layer, was cooled by He, which was flowing in rectangular channels in alternate and opposite flow along the toroidal direction. Afterwards, He was circulating through the top wall, the radial stiffening plates and the bottom wall. The different flows were finally collected into a common manifold to leaving the module. The PbLi and He thermodynamic cycle was limited by the Eurofer operating temperature and it was supposed to be 300°C – 500°C~530°C depending on the module. The described blanket concept is shown in Fig. 2.4, where can be appreciated the blanket design and the PbLi flow path.

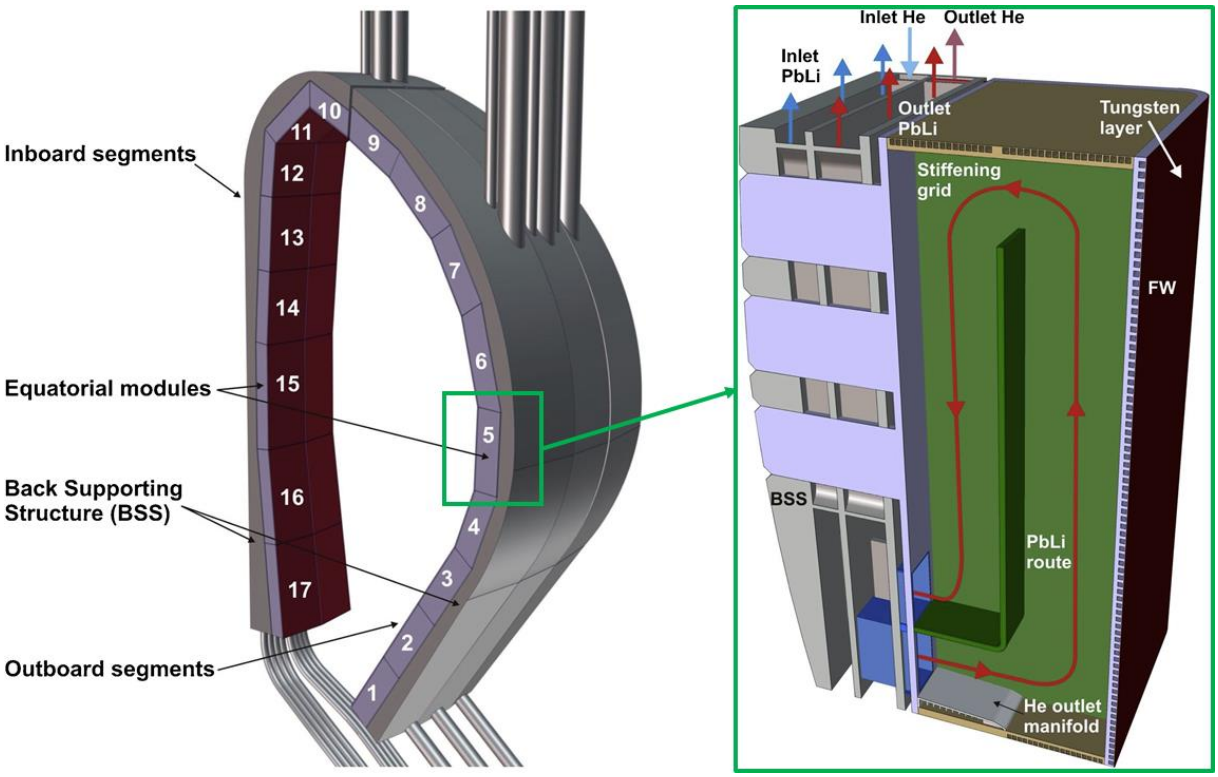

Fig. 2.4 – DCLL breeding blanket design concept (left) and equatorial outboard module and PbLi flow path (right) [24]

2.4.2. The Helium-Cooled Pebble Bed

The European HCPB architecture, proposed for the DEMO 2017 baseline [10], is based on an arrangement of the so-called fuel-breeder pins, where there are two concentric tubes, forming the inner and outer cladding. The blanket adopts a solid breeder with a fission-like architecture [25].

The BZ system starts from the BP until the internal part of the FW. It is filled with bundles of radial pressurized tubes, having external diameter d_{ext}=78 mm with a thickness of 4 mm. These pressurized tubes, which join the FW with the BZ BP, also act as radial stiffeners against pressurization during an accidental coolant ingress inside the BZ. The fuel-pins are inserted into these pressurized tubes and are connected to the BP. The fuel-breeder pin has been designed as a "pen-like" shape, with two concentric cylinders which are joined at the front of the pin (near the FW) by a reversed funnel. The outer cylinder has an internal diameter of 60mm with a thickness of 3 mm, the internal cylinder, instead, has an internal diameter of 16 mm with a thickness of 6 mm [26]. The resulting volume is filled with a Ceramic Breeder (CB), which is a mixture of silicate Li_4SiO_4 and titanate Li_2TiO_3 in the form of a pebble bed (pebble size 250 μm to 1250 μm) named KALOS [27][28]. To ensure a sufficient neutron production, a neutron multiplier is provided. The chosen material is the $Be_{12}Ti$ [29], which wrap the pressurized tubes (1 mm of gas gap) with a prismatic hexagonal geometry and radial elongation. The hexagonal blocks have between them a gas gap of 10 mm. This geometry is reproduced among the central region of the BZ, for the region adjacent to the Side Wall (SW) the prismatic block is missing due to problems of space and geometry [30]. The Tritium is extracted and transported by the Helium purge gas, which it enters firstly in the prismatic blocks and sweeps them from the top down, while in a second step, it enters into the pins. The FW system is a 20mm U-shaped chase, which is coated with 2mm of Tungsten that faces the plasma, actively cooled by several square channels, with side 11x11 mm, in opposite and alternate flow. The channels are equally divided among the poloidal length and varying their orientation to avoid uncooled regions [31]. The reference HCPB design can be appreciated in Fig. 2.5.

Helium gas, at 8 MPa, is adopted as coolant due to its neutronic and chemical inertness, providing an excellent neutron economy and very good compatibility with the involved structural materials (no exothermic chemical reactions at high temperature). The coolant thermodynamic cycle is set to 300°C – 520°C [26]. It enters at 300°C from the FW inlet

manifold flowing into the FW cooling channels, which are in the opposite and alternate flow. Then, is collected into a manifold that has the double function of FW outlet manifold and BZ inlet manifold, where then is distributed into the fuel pins. After cooling the pins, it is finally collected in the BZ outlet manifold at approximately 520°C. The main drawback of gas cooling is its compressibility and low density, which can result in high-pressure drop (Δp) and can limit its heat transfer capability. The Helium flowing scheme and the thermodynamic cycle are shown in Fig. 2.6.

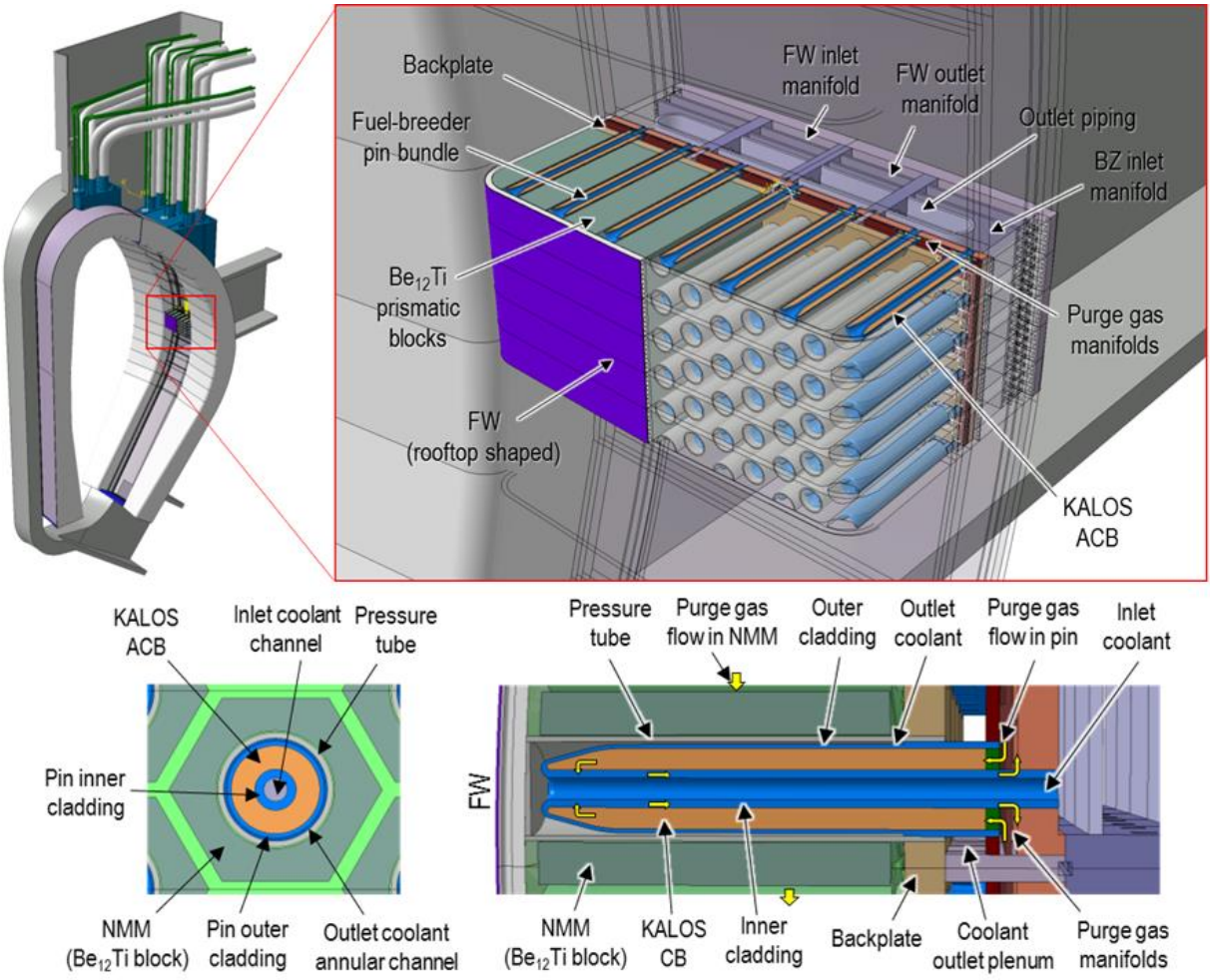

Fig. 2.5 – HCPB breeding blanket reference design [26][31]

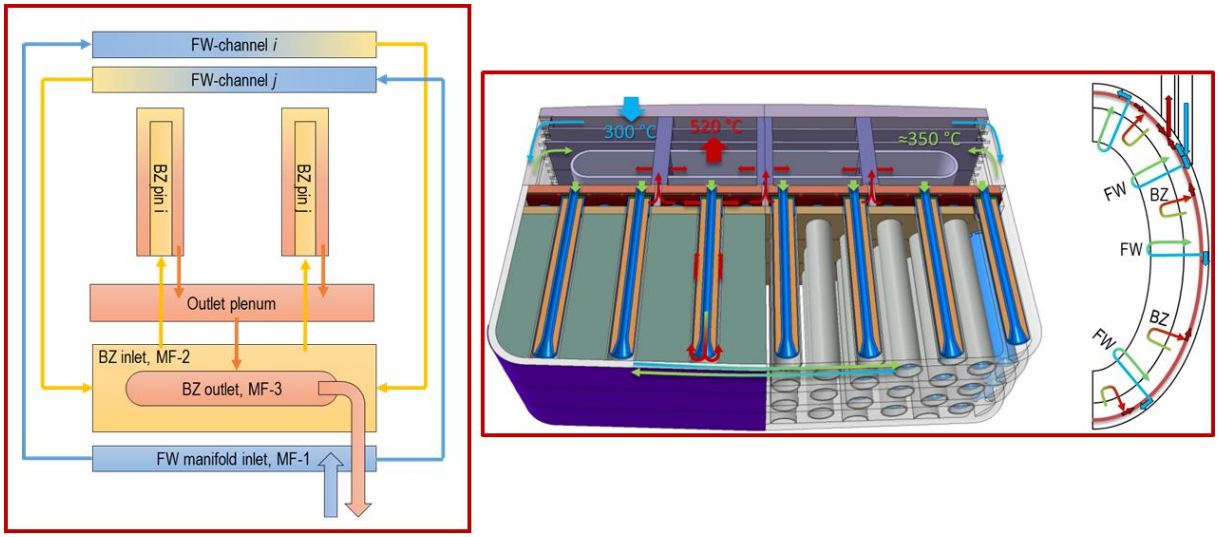

Fig. 2.6 – HCPB coolant system: schematic flow scheme (left), flow scheme and temperature (right) [26][31]

3. DEMO WCLL BREEDING BLANKET

The European breeding blanket concept, named Water-Cooled Lithium Lead, is currently studied in the framework of the R&D activities coordinated by the EUROfusion Consortium. In accordance with the DEMO 2017 baseline [10], the WCLL is composed by 16 sectors, covering 22.5° per each sector, with 2 inboard segments: left and right (LIB and RIB respectively) and 3 outboard segments: left, central and right (LOB, COB and ROB respectively). The IBs are located in the inner part of the torus, close to the central solenoid, and the OBs are placed near the external radius of the vacuum vessel. The BB is a key component in charge of ensuring Tritium production, shield the vacuum vessel and remove the heat generated by plasma thermal radiation and nuclear reactions. Is based on a liquid breeder technology, it relies on the PbLi eutectic alloy, enriched at 90% in ^{6}Li, adopted as breeder, neutron multiplier and Tritium carrier. Since the PbLi does not have the task to refrigerate structures, its velocity is extremely reduced to avoid corrosions. In addition, the velocity is also limited since the liquid metal is subjected to the magnetic field due to its electrical conductivity. The magnetic field of the plasma confinement strongly modifies the liquid metal flow behavior inside the reactor, causing huge pressure drops by means of magnetohydrodynamics (MHD). To have an idea of the effects that the MHD causes on the WCLL blanket performances the evaluation of the dimensionless Hartmann number, $Ha = B \cdot L\sqrt{\sigma/\mu}$, where B represents the magnetic field intensity, L is the characteristic length, σ and μ are the electrical conductivity and the dynamic viscosity of the PbLi respectively; provides a first indication of the effects of the magnetic field. Since Ha provides the ratio of the electromagnetic forces to the viscous forces, in the DEMO reactor it has been evaluated around 10^4, resulting in a strong deviation from the ordinary hydrodynamic behavior. In addition, evaluating the dimensionless Lykoudis number $Ly = {Ha^2}/{Gr^{0.5}}$, which characterize the balance between the electromagnetic forces (Ha) and the buoyancy forces (Gr), it returns that the electromagnetic forces drive the PbLi flow almost suppressing the natural convection, since typical value of the Gr number for the WCLL are estimated around 10^{10}. For the sake of completeness, more information regarding the MHD effects can be found in Refs. [32][33][34]. The WCLL is refrigerated with pressurized water at the typical Pressurized Water Reactor (PWR) conditions. The breeding blanket layout is shown in Fig. 3.1.

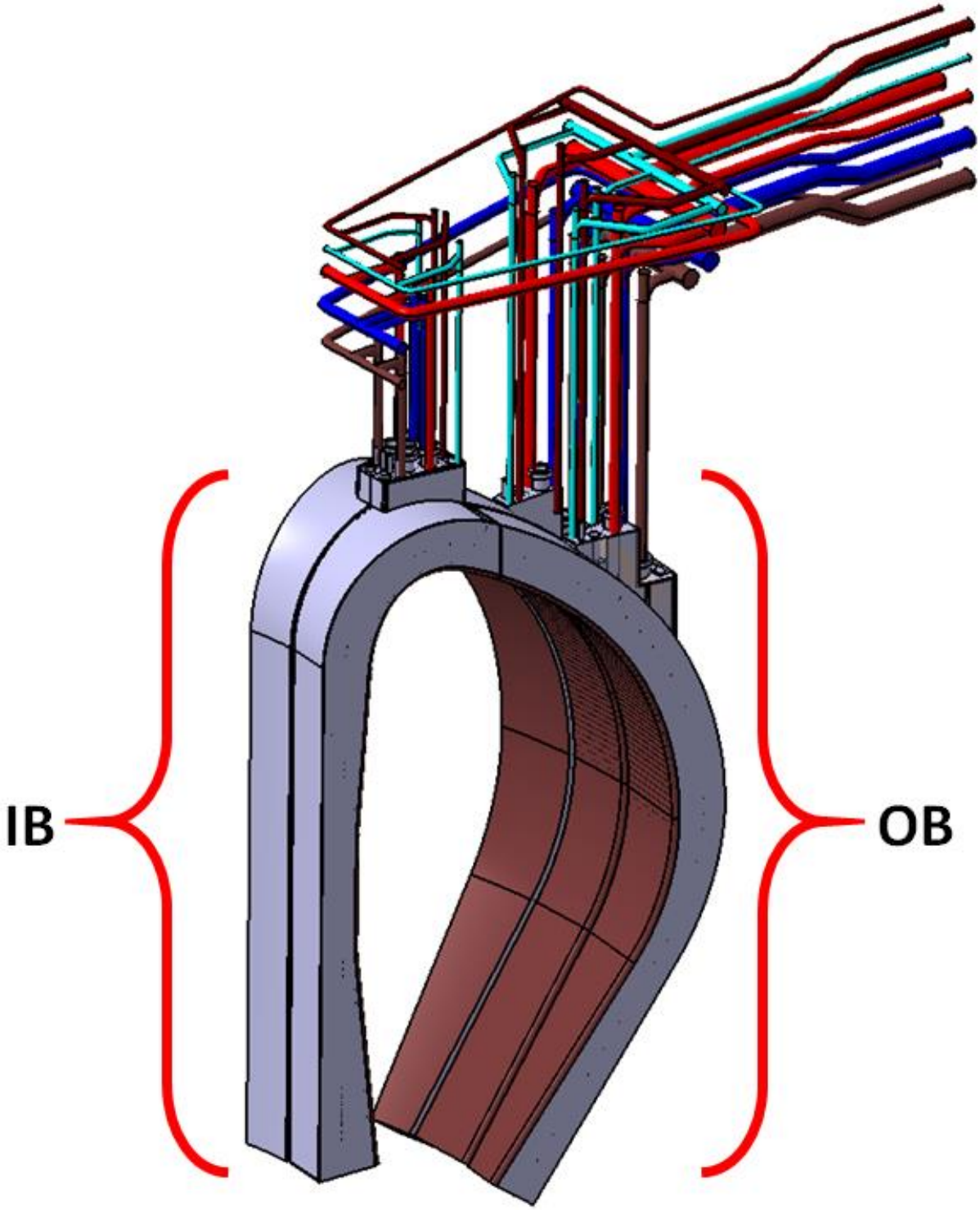

Fig. 3.1 – WCLL blanket design with IB and OB sector and feeding pipe

Since 2017, the WCLL adopts the SMS approach; this choice has been demonstrated by several blanket analyses, reported in Refs. [22], [36] and [37]. The SMS has demonstrated that, compared with the MMS, the PbLi drainage and the Helium bubbles removal from the segment are facilitated. Moreover, it provides better thermo-mechanical performances during the operational phases. The WCLL adopts Eurofer as structural material for different components: First Wall, internal structures and back supporting structure. The FW system is coated with a Tungsten layer, which provides a shield from the high plasma temperature and radiations. The operating window temperature of Eurofer, for the safe operation, is set between $T \geq 350°C$, where brittle transition due to irradiation occurs, and $T \leq 550°C$, beyond which there are strong degradations of the thermo-mechanical properties [38]. The Tungsten, instead, has a superior limit of 1300°C [36].

The water coolant, employed for the refrigeration of the BZ and FW systems, operates with a nominal pressure of 15.5 MPa, inlet temperature equal to 295°C, and outlet at 328°C. Regarding the FW cooling system, water flows in alternate and opposite flow into square channels, built inside the FW Eurofer chase, for all the linear extension. The BZ cooling system is immersed into the breeder. It is composed by different tubes with several possible arrangements, which must provide: a temperature field toroidally symmetric; the lowest amount of structural material to reduce the neutronic parasitic capture; to avoid to across the internal structures in order to reduce the possibility of corrosions and vibrations and therefore possible breakage. Nevertheless, to reduce the risk of a tube rupture, thus, a lithium-water chemical reaction into the breeder, which is highly exothermal and with hydrogen production, the BZ tubes are Double Wall Tubes (DWTs).

3.1. Previously studied layout

The WCLL recent design starts from a review of the previously performed designs in order to identify strengths and weakness.

The first configuration had been developed in 1995 [40][41], pioneering studies on a water-cooled blanket concept had performed, for the development of a European blanket on a fusion power plant. The design had been developed assuming a single segment box, providing one box for the inboard and one box for the outboard. This configuration had based on the concept of steam generator. Each segment was essentially a PbLi container, actively cooled by a FW cooling system and a DWTs bundle, poloidally immersed in the liquid metal. The box was reinforced by radial-poloidal and toroidal-poloidal stiffeners, reproducing a “beer-box like” geometry, ensuring the PbLi circulation. The BZ water was flowing downward in the front part of the box and upward in the rear part. The PbLi, instead, was flowing downward in the back part and upward in the front. This design had the manifold at the top of the module, allowing the maintenance of the whole module from the top. The configuration and the operating scheme are shown in Fig. 3.2.

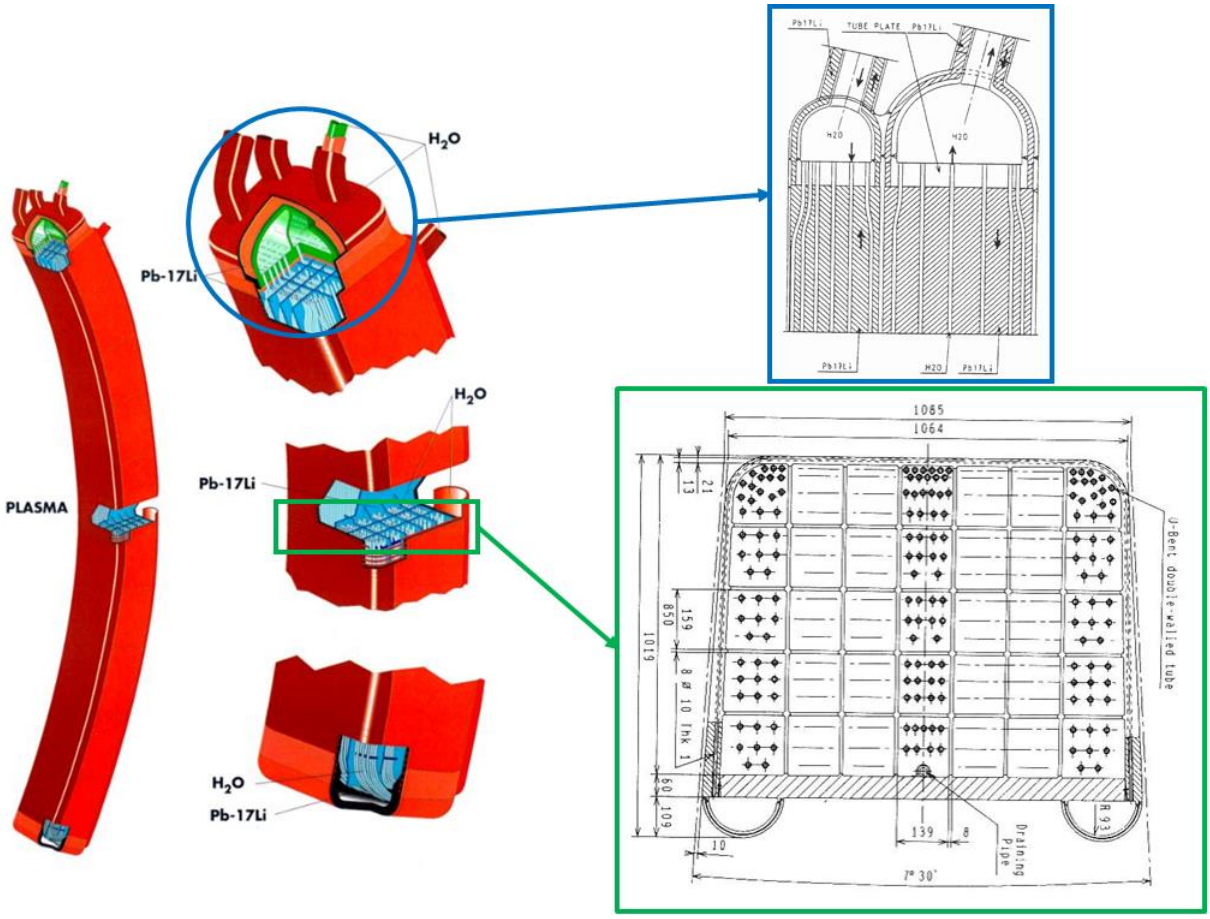

Fig. 3.2 – WCLL blanket concept outboard segment box 1995; manifold section (blue box) and equatorial radial-toroidal view (green box) [40] – (color online version)

Further studies have been performed in 2004, in which the reactor had been segmented into several modules, defining the MMS approach [42][43].

Starting from 2012, CEA developed an innovative design, based on the MMS approach. This design was constituted by different modules with different sizes, all attached along the poloidal length of the BSS and fed with pipes in the rear part of the modules. The module was constituted by radial-poloidal stiffeners for structural function and toroidal-poloidal stiffeners to define the PbLi flow path that was predominantly poloidal. The BZ cooling system was composed by several vertical DWTs, having a radial-poloidal-radial path. The water was flowing from the upper part of the module to the bottom part. The PbLi had the inlet in the rear and bottom part; then it had to radially flow frontward toward the FW in the bottom part of the module, where it was conveyed upward into square channels identified by the stiffeners, then radially exit going backward in the top part of the module. Unfortunately, only the equatorial outboard module was developed in detail and it is shown in Fig. 3.3.

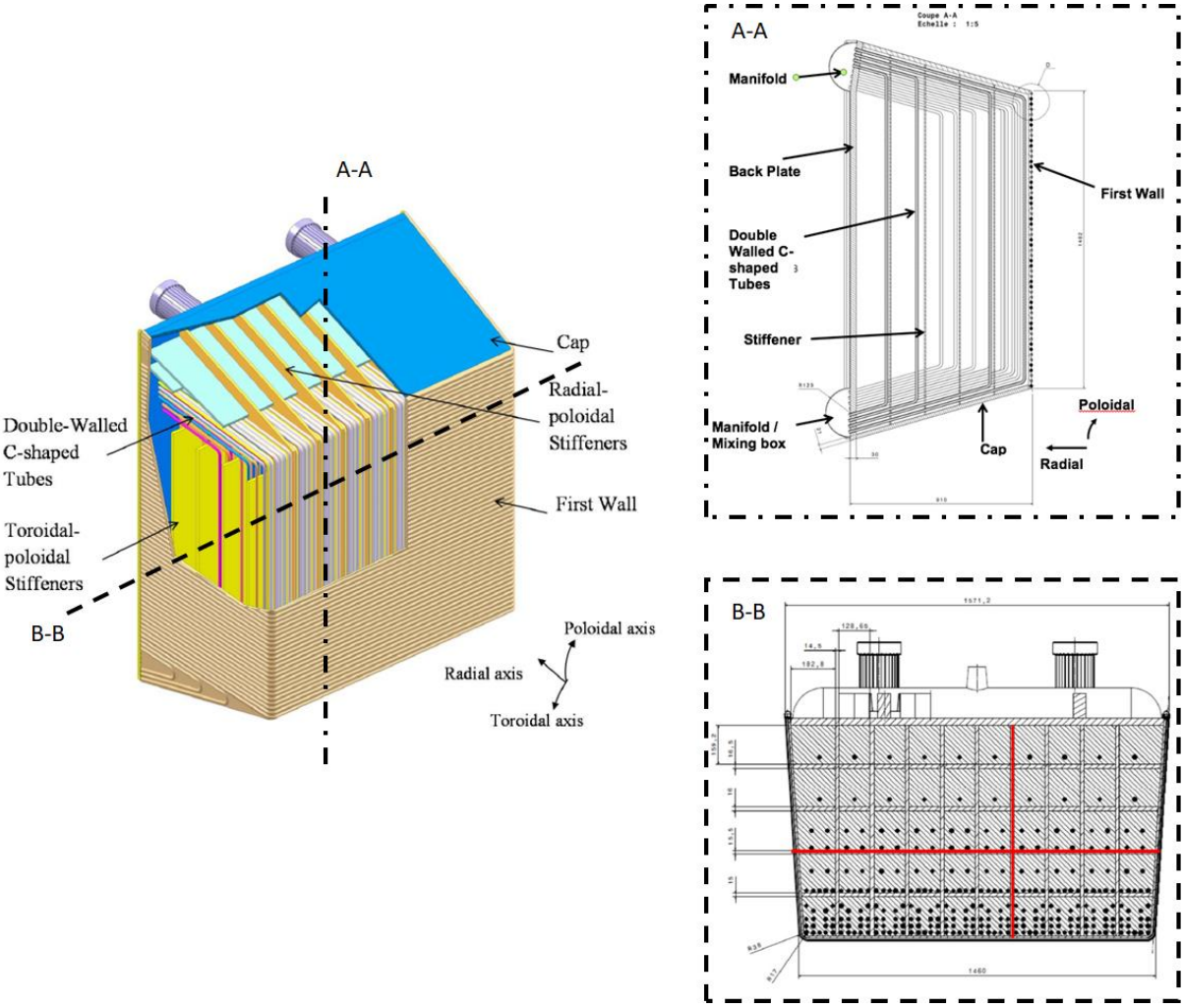

Fig. 3.3 – WCLL blanket concept equatorial outboard module 2012 (CEA), different view [44]

Since 2014, ENEA and its third linked parties started to develop an innovative concept, still based on the MMS approach, but with different BZ tubes orientation (horizontal). The module, shown in Fig. 3.4, externally very similar to the configuration of the CEA, had a different internal structure, being composed of 16 horizontal elementary cells. The units were formed by poloidal-radial stiffeners (vertical plates) and toroidal-radial stiffeners (horizontal plates) which had the structural function, and toroidal-radial baffle plates placed in the middle of two horizontal plates which had to guide the PbLi flow. In this concept, both fluids, had a predominantly radial flow path, as shown in Fig. 3.5. With this configuration, the number of FW channels necessary to refrigerate the unit cell was set equal to 10. Moreover, the rationale of the FW coolant flow path was consolidated as alternate and opposite flow to obtain a symmetric temperature field on the FW and Tungsten layer.

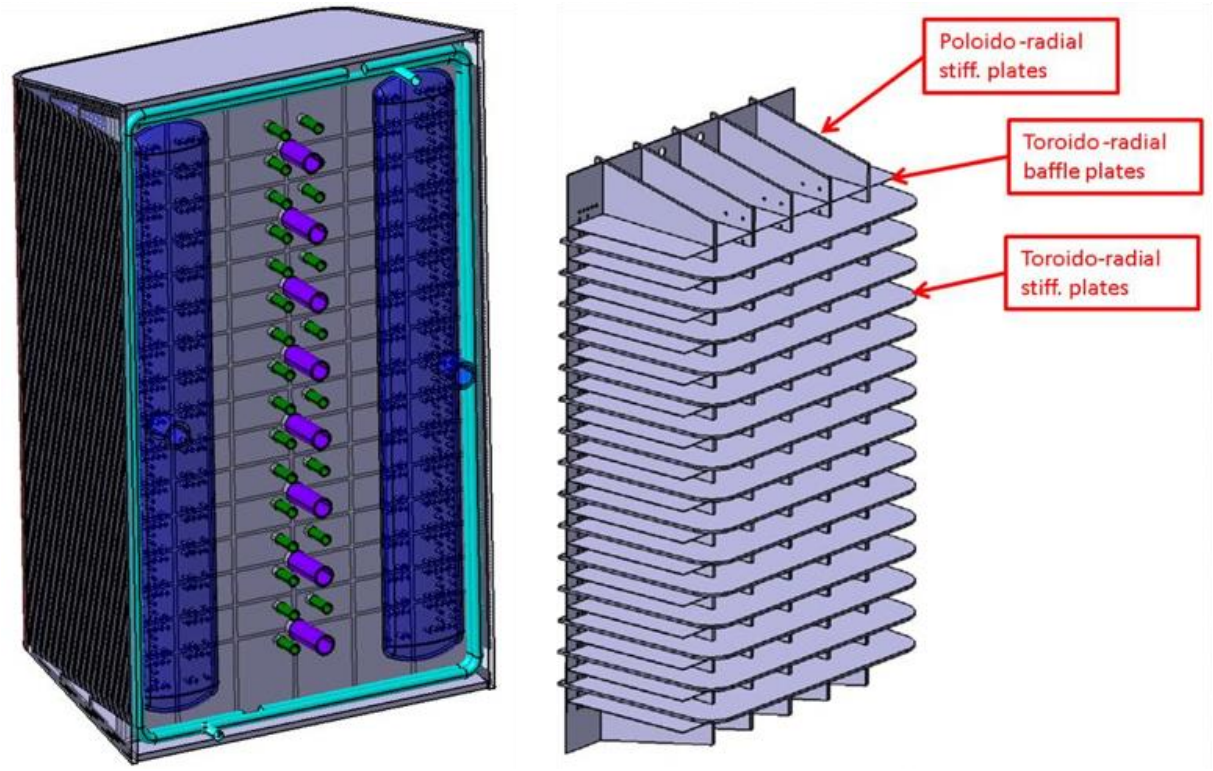

Fig. 3.4 – WCLL blanket concept equatorial outboard module 2015 (ENEA), different view [39]

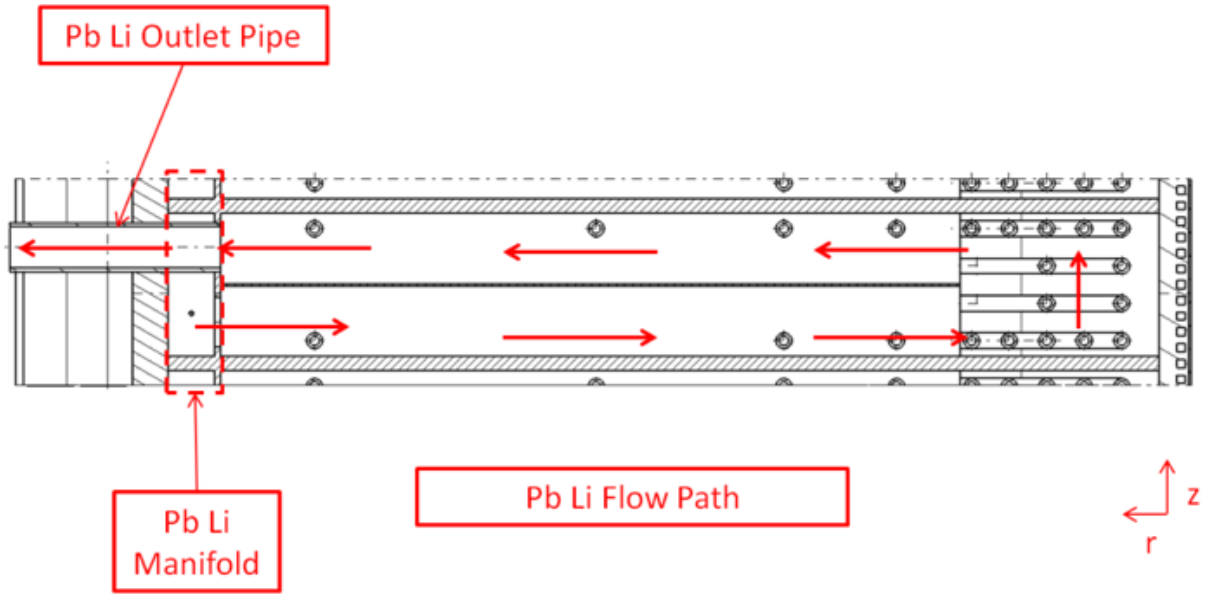

Fig. 3.5 – WCLL blanket concept 2015 (ENEA), PbLi flow path, DWTs and FW channels distributions [39]

On the basis of the main outcomes obtained from WCLL 2015 analyses [39], the design was further optimized in 2016 [45]. The main improvement was the development of a WCLL blanket design based on the SMS approach, but conserving the same internal structures. This was chosen to facilitate the PbLi drainage and the Helium bubbles removal from the segment.

In addition, a reference thermo-dynamic cycle was set in 2016 to improve the efficiency of PHTS and the BoP. Thus, the water, at 15.5 MPa, enters in the BZ and FW systems at 295°C and exits at 328°C [15][46]. The 2016 design rationale is shown in Fig. 3.6.

In order to avoid the stiffeners crossing, during 2017, a new BZ layout system was developed. It was constituted by a simpler configuration in which the DWTs were assembled without crossing the stiffeners. In addition, the baffle plate was removed due to its no-structural function. The elementary cell was made up of six sub-elementary cells formed by the radial-poloidal stiffeners arrangement. The vertical plates were lengthened up to the FW composing these six sub-cells; thus, the BZ tubes were placed in these sub-cells refrigerating structures and breeder avoiding the stiffeners crossing. Several BZ tubes layouts have been studied, with U-shape, helical-shape and wave-shape (Fig. 3.7), but only a few were able to guarantee the fulfillment of the Eurofer temperature requirement (temperature limit of 550°C) [48][49]. During the cell analyses, the manufacturing work package added as a requirement, the impossibility of making tubes with more than two bends, by dropping the choice, in a forced manner, on the U-tubes.

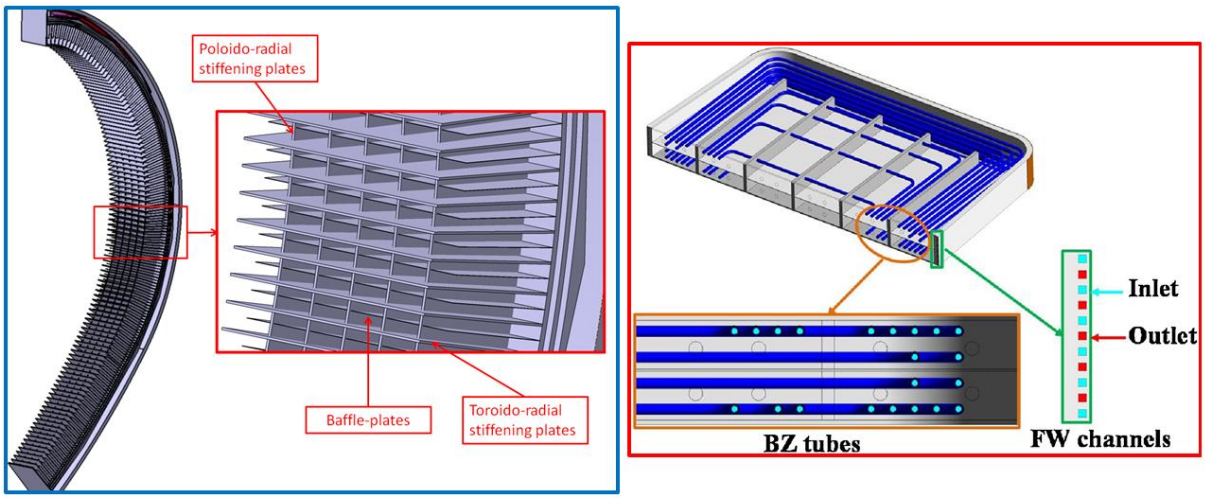

Fig. 3.6 – WCLL blanket concept COB (left) and equatorial elementary cell (right), 2016 (ENEA) [45]

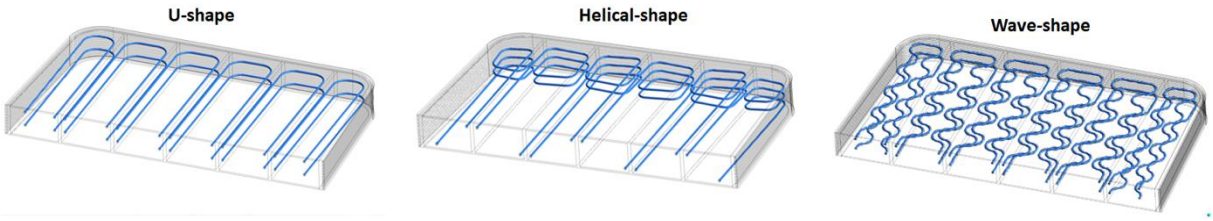

Fig. 3.7 – WCLL blanket concept 2017 (ENEA) – three different BZ tubes layout [48][49]

At this point, towards the end of 2017, several activities were launched in parallel to identify a promising design that would satisfy all the above-mentioned requirements. Even the blanket structure was involved in this process, obtaining two different models: the reviewed horizontal plates layout [50] and a "newer" vertical plates layout, as known as beer-box [51] (Fig. 3.8). Having changed the internal structure, the PbLi flow path also underwent modifications. The beer-box concept foresaw a poloidal path, how was the 1995's concept; conversely, the concept of the horizontal plate envisaged two different paths, both mainly radial. The first path concerned the elementary cell only (as in Fig. 3.5,) and the second envisaged a flow path along the whole segment in a "snake-like" mode through all the cells of the segment. With these two different layouts, four different BZ design options were considered having the following main features:

- WCLL BB v2017.t01.A: Horizontal plates. PbLi flow path mainly in radial direction as configuration 2016. Horizontal BZ cooling tubes. PbLi manifold placed between the BZ and the water manifold;
- WCLL BB v2017.t01.B: Horizontal plates. PbLi flow path mainly in radial direction as snake-like. Horizontal BZ cooling tubes. PbLi manifold integrated in the BZ;
- WCLL BB v2017.t02: Vertical plates. PbLi flow path mainly poloidal direction. PbLi manifold integrated in the BZ. Horizontal BZ cooling tubes;
- WCLL BB v2017.t03: Vertical plates. PbLi flow path mainly poloidal direction. PbLi manifold integrated in the BZ. Poloidal BZ cooling tubes.

Of these four configurations, the v2017.t01.B was immediately discarded due to the high pressure drops of the PbLi covering the entire segment [35]. The remaining three configurations were analyzed and compared from the thermo-hydraulic, thermo-mechanical and magnetohydrodynamic points of view [35][50][54][55]. The BZ tubes rationale of the three analyzed layout is shown in Fig. 3.9. From this comparison, it has been highlighted that the layout of the tubes is significantly simplified by using horizontal tubes. Concerning the

stiffeners approach, the arrangement of the horizontal plates has been selected as reference, due to the lower volume of Eurofer into the cell and with the baffle plate reintroduction in the layout to facilitates the PbLi flow. As a result of this comparison, the WCLL 2018 V0.2 configuration has been designed and analyzed [55]. Its description is presented in the next Subsection (3.2).

For a complete evaluation of the pressure drops of the four "2017 models" listed above, which is beyond the scope of this thesis, Ref. [35] can be consulted.

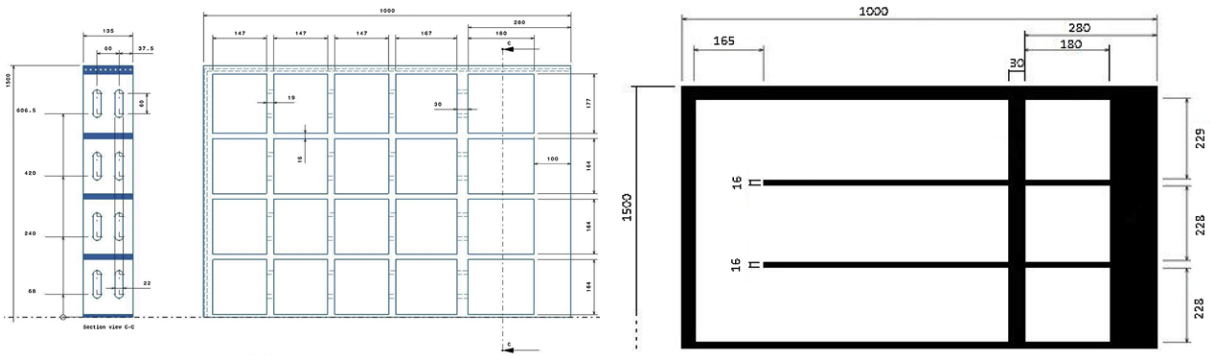

Fig. 3.8 – WCLL blanket concept 2017 half equatorial elementary cell geometry: vertical stiffeners (left) and horizontal stiffeners (right) [55]

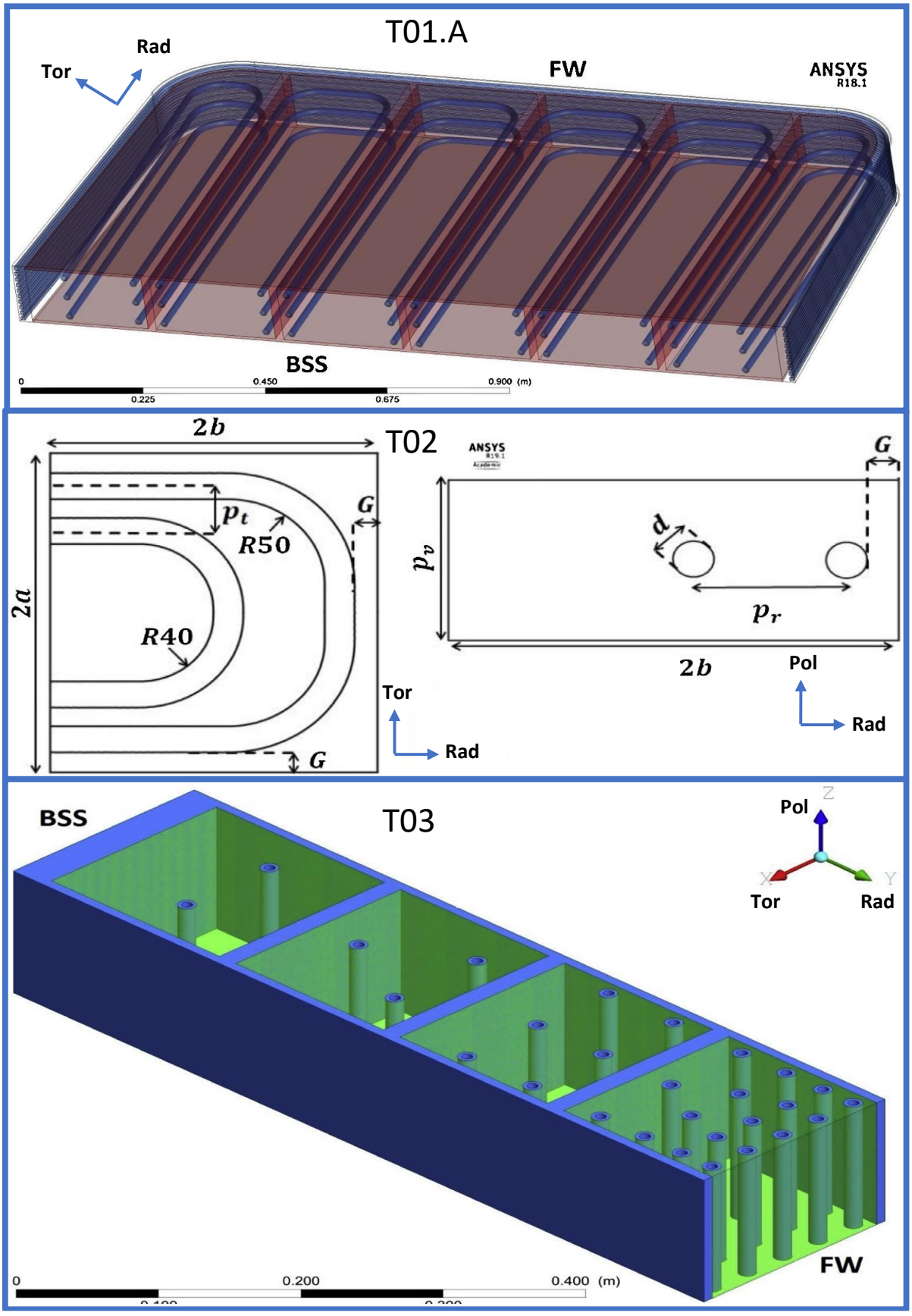

Fig. 3.9 – WCLL blanket concept 2017 – different elementary cell configurations and BZ tubes layout (ENEA) [55]

3.2. WCLL 2018 configuration

The innovative blanket layout [52][53], with its related elementary cell named WCLL 2018 V0.2, has been carried out after a thorough review of previous layouts, as described above and reported in Ref. [56]. The WCLL 2018 layout is based on DEMO 2017 baseline [10] and relies on the SMS approach. It is composed by several elementary cells (i.e. COB~105) repeated along the poloidal direction of the segment. Compared with the 2017's concept, the radial length allocated for the BB has been reduced by 300 mm; thus, it has been enhanced the compactness in the radial direction. The rationale for this concept is based on different considerations:

- Different design option are allowed: stiffeners approach [50], BZ tubes arrangement [54][55][57], and PbLi manifold [35];
- Maximized the TBR performances [58]: reduced Eurofer percentage in the inner part of the cell, PbLi manifold located in the BZ;
- Enhanced shielding performance;
- Facilitated PbLi filling and draining procedures; allows He bubble removal from the BZ [59].

The blanket is enclosed within the FW and the BSS. It is strengthened by internal structural components that must ensure the blanket thermo-mechanical seal; these components are called stiffeners. In Fig. 3.10 their arrangement inside the cell is represented: two horizontal plates of 10 mm, anchored with the FW and the BSS, determine cell's poloidal height; five vertical plates (i.e. ribs) of 12 mm thickness, anchored to the BSS run along the entire blanket poloidal length, radially elongated up to a distance of 175 mm from the FW; and a 2 mm thickness baffle plate, welded to the manifold region and with a radial length equal to the five ribs, which ensures an appropriate PbLi flow. The assessment of the structural components is conducted according to the RCC-MRx standard [50][60].

The WCLL elementary cell V0.2 is composed by five vertical stiffeners, which divide the cell into six sub-unit; two horizontal stiffeners, which act as a cell cover; and a baffle plate, placed in the middle of the poloidal height dividing the cell in upper and lower part with no structural function. The cell has a toroidal length of 1500 mm and an overall radial dimension of 1000

mm. Its poloidal height is constrained by the two horizontal plates. The cell can be divided in three different systems/areas: the First Wall, the Breeding Zone and the Manifold.

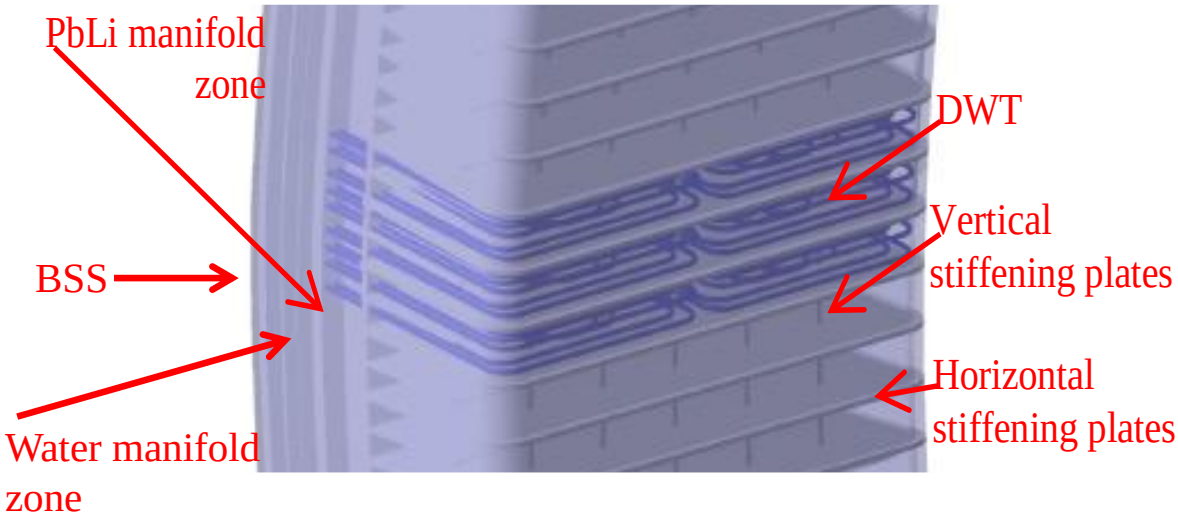

Fig. 3.10 – WCLL 2018 V0.2 outboard segment internal structures [52]

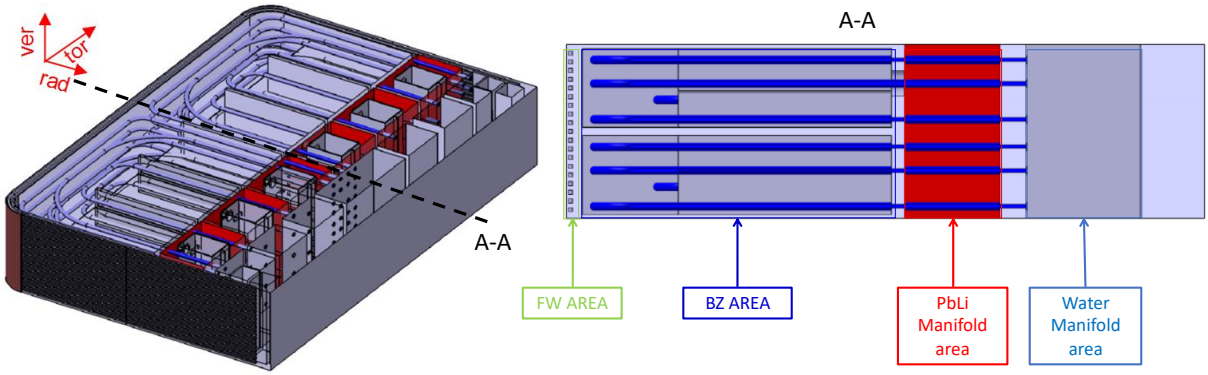

Fig. 3.11 – WCLL 2018 V0.2 COB elementary cell isometric view (left), radial division of the areas (right) [53]

3.2.1. FW system

The part of the blanket that faces the plasma is the First Wall system. It is composed by a C-shaped Eurofer structure 25 mm thick, bent in the radial direction, while the plasma-facing surface is coated with a 2 mm Tungsten armor. The coating covers the plasma-facing surface (toroidal length of 1300 mm) and the elbows. The FW is actively cooled by an independent water system. The coolant flows in alternate and opposite flow inside square channels (l = 7 mm). These channels are arranged in poloidal direction equally distributed among the whole

poloidal height with a pitch of 13.5 mm. Each elementary cell is cooled by 10 water channels, which cover the entire length extension of the component (radial-toroidal-radial). The FW system layout and the cooling scheme is shown in Fig. 3.12. The FW system has the following tasks: to deliver coolant to the PHTS at the design temperature (i.e. 328°C at 15.5 MPa), to remove the volumetric deposited power into the system, not exceeding the Eurofer temperature limit of 550°C and Tungsten temperature limit of 1300°C, and also to remove the surface heat load related to the plasma operation that directly impacts the Tungsten armor. During the normal operation, the central outboard equatorial FW system must withstand a maximum surface heat load of 0.5 MW/m^2, plus the contribution due to the volumetric deposited power, according to the design requirement. In addition, to reduce the water corrosion, the water flow velocity is limited to 7 m/s [52]. The FW is one of the most thermally stressed components due to its proximity to the plasma.

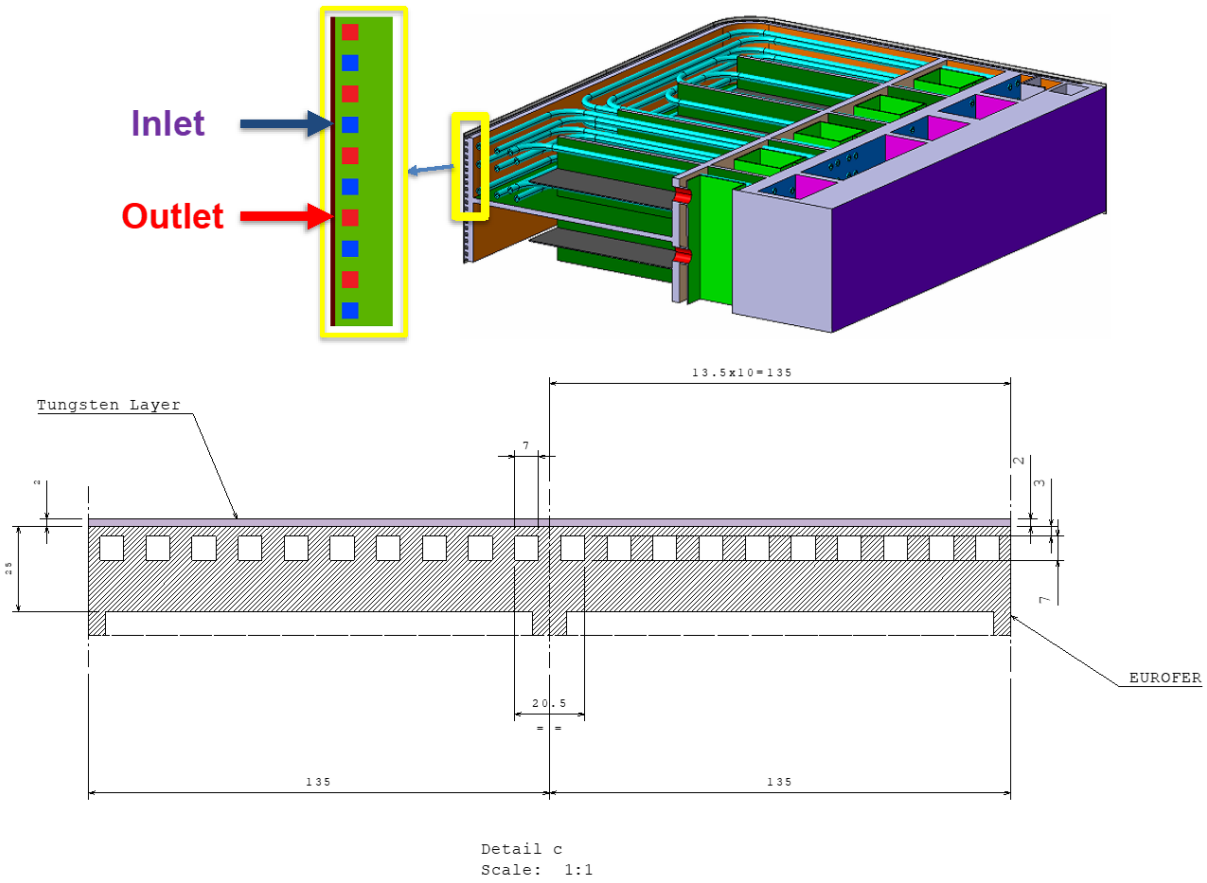

Fig. 3.12 – WCLL 2018 V0.2 FW system: cooling channels scheme (up) and geometrical parameters (down) [53]

3.2.2. BZ system

The internal box filled with liquid PbLi eutectic alloy, enclosed between FW and Manifold, is the Breeding Zone system. The PbLi, which acts as: breeder, neutron multiplier, and Tritium carrier, flows into the cell in a radial-poloidal-radial path. Its circulation is ensured by the stiffeners grid, it enters from the lower part of the cell through dedicated holes, flows along the radial length up to the end of the baffle plate, which acts as separator between inlet and outlet channels, there it poloidally develops and turns, following back in the upper part and exiting through holes in the PbLi outlet manifold. Since it has no coolant function, its velocity is extremely reduced to avoid large pressure drops, being inside the cell around 0.2 mm/s. Thanks to the Eurofer reduction in the inner part of the BZ, due to the stiffeners grid, the TBR undergoes a considerable increase, reaching a value of 1.119, where the 94% of Tritium is produced in this zone.

The BZ refrigeration is ensured by an independent coolant system, composed by several DWTs immersed in the liquid metal alloy, whose must guarantee that the temperature of Eurofer structures does not exceed 550°C. The DWTs have an internal diameter of 8 mm and a thickness of 2.75 mm. Even in this cooling system the flow velocity is limited to 7 m/s [52]. The elementary cell is based on twenty C-shaped DWTs, toroidally symmetric and characterized by a simpler configuration without crossing vertical stiffeners. The tubes are grouped in three different arrays. The first has 6 tubes with the longest linear length, poloidally located one above the other. They start from the mid toroidal length of the cell and radially run toward the FW, then curving (i.e. curvature radius 50 mm) in toroidal direction to then bend again in a radial direction near the sidewall. The second array is composed by 6 tubes with different curvature radius (i.e. curvature radius 50 and 200 mm), but with a comparable overall length, the path is similar to the first array but with a greater FW detachment, thus, a shorter radial and toroidal path. The third array is composed by 8 tubes that are the shortest, poloidally alternated as a “chessboard”, and have a considerably short toroidal length, almost equivalent to a U-tube. All the inlets are located in the central toroidal part of the cell to obtain a toroidal symmetry, and the outlets are respectively placed in the opposite side, near the SWs. The BZ elementary cell cooling scheme and tubes displacement of the V0.2 layout is shown in Fig. 3.13.

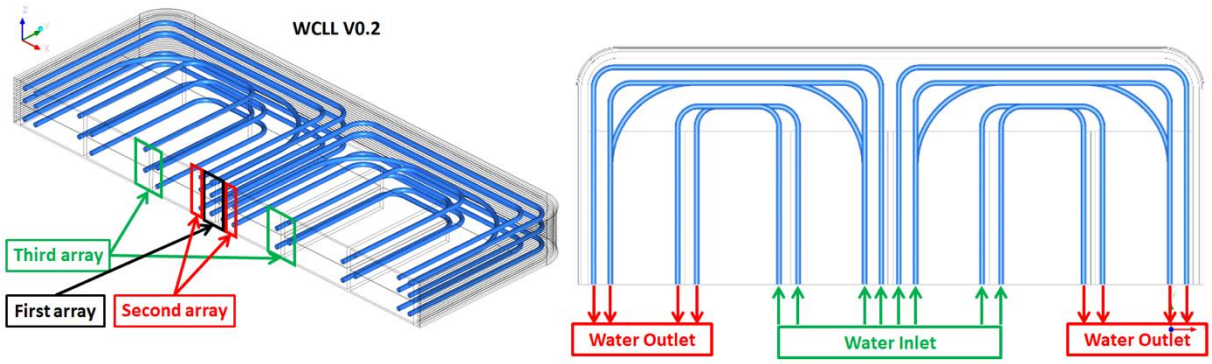

Fig. 3.13 – WCLL 2018 V0.2 BZ system: tubes isometric view (left), cooling scheme (right) [53]

3.2.3. Manifold system

The SMS approach relies on a segment attached to the vacuum vessel through the BSS. This is a plate 215 mm thick, which has to sustain the weight of the segment. Placed in the back part of the segment, between the BZ system and the BSS, there is the manifold region, which fed both cooling systems and the PbLi. The manifold region is composed by three independent systems: the PbLi manifold, which can be said to belong to the zone of BZ; the BZ and the FW manifolds (Fig. 3.14).

The PbLi manifold is separated from the BZ by a thin plate of 20 mm, passively cooled by the DWTs passing through it radially before being collected in the related manifold. The liquid metal is distributed to the BZ elementary cells through a compact poloidal manifold, which fulfills both tasks: distribution and collection. The PbLi flows in poloidal direction through the manifold from the bottom to the top of the segment. The manifold is composed by 6 rectangular channels, in which 6 co-axial channels reside, covering the entire poloidal length of the blanket. The 6 external boxes are rectangular annulus that has the task to distribute the PbLi into the BZ through holes placed in the lower part of the elementary cell. The 6 rectangular co-axial channels, on the other hand, have the collecting task. The PbLi exits from the cells through holes placed in the upper part of the elementary cell, one per single sub-unit (Fig. 3.14). This manifold rationale contributes to the TBR performances, providing about 6% of the total Tritium production. The PbLi inlet and outlet manifold holes layout of the V0.2 configuration is shown in Fig. 3.15.

Concerning the FW and BZ water manifolds, separated from the PbLi manifold by a plate 40 mm thick, both are connected with the related cooling system. In both, the coolant flows at 295°C in the inlet manifold, whereas 328°C is the manifold outlet temperature in accordance with the BoP and PHTS requirements. The BZ manifold system provides two different inlet systems so called “high-pressure” and “low-pressure”. This choice is foreseen to take into account the different DWTs length providing an optimal flow distribution into the tubes. In particular, the high-pressure feeds the first and the second tubes array, which has a comparable length, and the low-pressure provides water to the third ones. The absolute pressure is almost the same; the difference between high and low resides in compensating the different pressure drops that would occur in the case of parallel channels. The FW manifold system instead, consists of two inlet-outlet pairs, positioned at the toroidal ends of the cell. The inlet water flows inside the two square channels placed in the opposite toroidal side, to ensure the alternate and opposite flow characteristic of the FW. The same happens for the outlet manifold, which collects the water coming out of the FW circuit from both sides. Both water manifold layouts are shown in Fig. 3.14.

The two water manifolds reside Inside the BSS, creating a “wall” of water between the cell and the end of the BSS. This choice is to ensure adequate refrigeration of the structure, which must be below 550°C, especially regarding the IB segments. As regards the OB, this manifold is sufficient to guarantee compliance with this temperature requirement, conversely, the IB, due to the limited available space, cannot be taken for granted that it meets this requirement. Moreover, the water wall enhances the neutron shielding performance, ensuring adequate protection for the VV and the toroidal field coils from the neutronic flux.

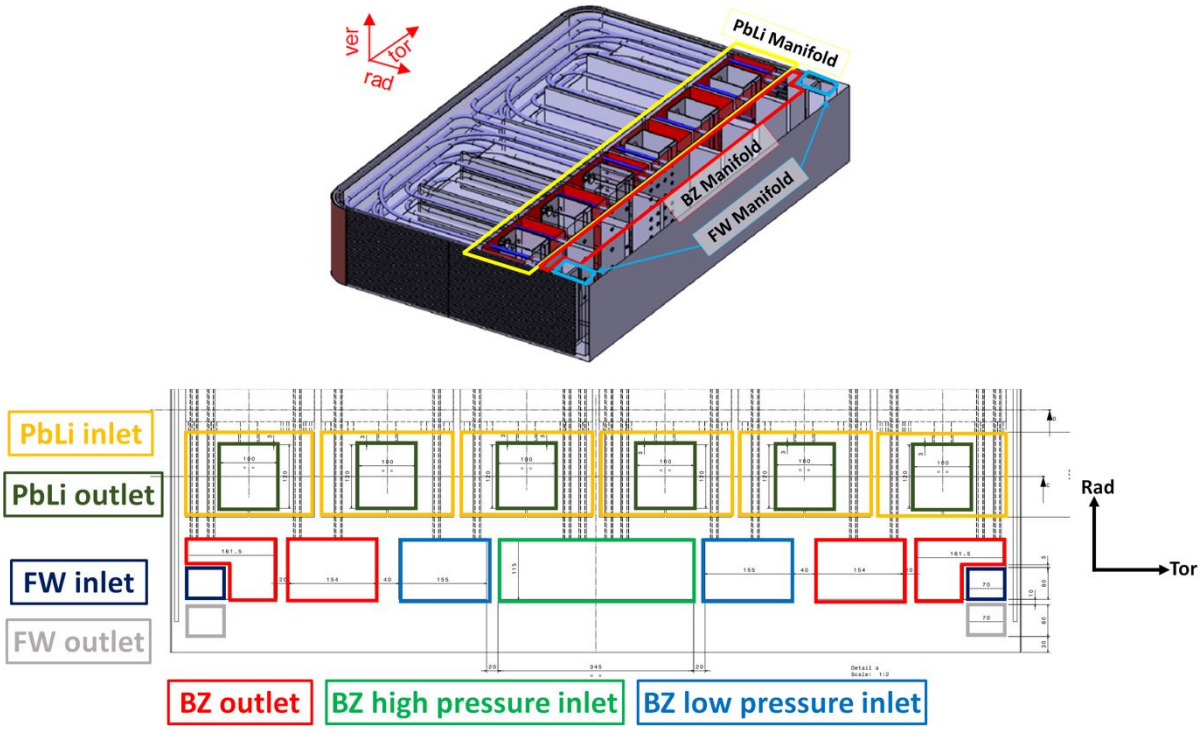

Fig. 3.14 – WCLL 2018 V0.2 COB elementary cell manifold layout: isometric view (up), radial-toroidal cut (down)

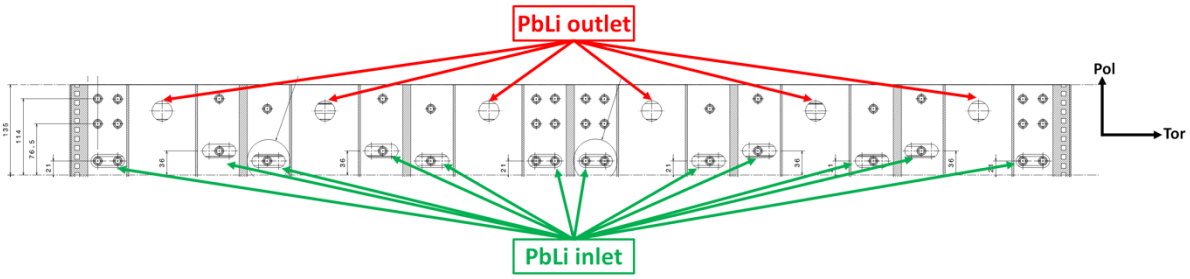

Fig. 3.15 – WCLL 2018 V0.2 PbLi manifold, inlet and outlet layout holes

3.3. Main achievement and issue

The WCLL 2018 design has shown positive features, accounting the parameters of the new DEMO 2017 baseline, characterized by a remarkable radial reduction of the space allocated in the BB. Nevertheless, drawbacks and areas for improvements have been identified.

Concerning the SMS approach and the BSS design, with its integrated water manifold, it can be stated that the choices made are consolidated. As regards the BSS of the IB segment, the temperature requirement must be checked to affirm that the configuration guarantees adequate refrigeration and not requires an additional cooling system. On the other hand, the innovative PbLi manifold system, integrated into the BZ, is proposed and shall be further investigated evaluating if the He bubbles are dissolved in the liquid metal flow. In addition, the MHD effects have to be evaluated with detailed analyses to assess the flow distribution and the effect of the electromagnetic coupling of the co-axial channels; and exploiting if the electrical insulation of inlet and outlet channels can be considered. In addition. The realization of this PbLi manifold is challenging, as it shall withstand a maximum pressure of 18.6 MPa in accidental conditions of an in-box LOCA and shall ensure a uniform PbLi distribution in the elementary cell ensuring an adequate recirculation in the BZ; succeeding in guaranteeing a pressure drops of the whole PbLi loop system less than 5 MPa. The reference PbLi in-vessel loop pressure losses has not yet been defined in the EUROfusion project but it is reasonable for it to be significantly lower than 5 MPa for safety reasons, which is assumed as the theoretical upper limit for MHD pressure losses in the loop, allowing that the actual limit could be lowered by the maximum head available from the pumping system and plant economy considerations [61].

As regard the BZ cooling system an innovative and simplified layout has been proposed in the 2018, which fully satisfy the requirements of temperature symmetry in toroidal direction, not crossing the stiffeners and not exceeding the Eurofer temperature limit. Nevertheless, further improvements are needed to enhance the cooling performances (i.e. increase water velocity, outlet water temperature distribution). Although, in the preliminary analysis the buoyance forces of the PbLi have been suppressed and only forced convection has been considered, this implies that the flow of PbLi, that is also affected by MHD, could significantly change the Eurofer thermal field. Efforts are needed to calculate the thermal and the flow fields through the MHD analysis.

As regard the stiffeners grid, the 2018's layout, is characterized by a meaningful Eurofer reduction, especially in the frontal part of the BB, which is derived from the thermo-mechanics and thermo-hydraulics studies. This reduction, about 12% less in the BZ, has led to a TBR enhancement. This layout is to be considered verified and validated, given its versatility, which allows different tubes orientations (i.e. horizontal and vertical), different PbLi flow path and an acceptable margin from the RCC-MRX design criteria.

As regard the FW system, studies have confirmed the cooling performances, highlighting a significant margin available to optimize the number of channels, thus, the pitch. Having reliable and accurate thermal loads of the FW in all poloidal positions and operative conditions, this will allow to select the pitch of the appropriate channels as the poloidal position changes. The pitch optimization is a key aspect in order to further enhance the TBR performances. In addition, the coolant velocity can be enhanced to further optimize the cooling performances. Nevertheless, the passive cooling of the BZ from the FW cooling system will need to be analyzed in more detail, since two separate cooling systems are provided for the PHTS, to not over dimensioning it.

4. THERMAL-HYDRAULIC ANALYSES IN STEADY-STATE CONDITIONS

The main objective of these bench of analyses is to evaluate, optimize and defining an innovative COB equatorial elementary cell layout from the thermal-hydraulic point of view. The starting point for these numerical simulations is the WCLL 2018 V0.2 elementary cell, described in Section 3.2.

The thermal-hydraulic analyses are performed in support of the design R&D activities of the EUROfusion Consortium, verifying if the selected design is able to satisfy the multiple requirements listed below:

- Temperature symmetry in toroidal direction;
- Eurofer temperature below the limit requirements (550°C);
- Enhance the cooling performances;
- Optimize the number of DWTs;
- Optimize the number of FW channels;
- Alternative coolant manifold.

The activities are constituted by investigating the thermal-hydraulic of WCLL BB elementary cell and the related temperature field of the solid structures. This is pursued through the ANSYS CFX v18.2 CFD code by means of steady-state analysis.

For each steady-state analysis, a 3D finite volume model has been set up with a simplified geometry. As mentioned above, the COB equatorial blanket has a toroidal length of 1500 mm and radial dimension of 1000 mm. In the present analysis, the poloidal dimension of the model is clipped to a height of 135 mm, considering only half-thickness (5 mm) of the horizontal plates, which is representative of a single elementary cell. Moreover, the model radial dimension is reduced to 567 mm, thus neglecting the section covering the manifold and back supporting structure, where heat loads are foreseen to be negligible.

The different 3D finite volume models have been set-up to realistically reproduce the geometry and flow features of WCLL COB equatorial elementary cell and to obtain a complete and

detailed temperature distribution, both in the fluid and the solid domains. The solid properties are specified in terms of density, specific heat and thermal conductivity, while fluids also require the dynamic viscosity. In these analyses, the fluid domains have been modelled for BZ and FW water, as regards the PbLi it has been modeled as both fluid and solid; the solid domains have been set for Eurofer structures, FW Eurofer chase and Tungsten armor.

4.1. Material properties

The thermo-physical properties of water coolant, PbLi, Eurofer and Tungsten have been implemented in the CFX commercial code with a constant value or temperature-dependent function using a polynomial fitting of data ([47][64]). The properties of the different materials have been summarized in Table 4.1, Table 4.2, Table 4.3 and Table 4.4, respectively. As regards the Tungsten thermo-physical properties, fixed values have been imposed, since its properties do not have a significant variation over an extended temperature range (327-727 °C), as reported in ANNEX A: Materials properties. In addition, the typical temperature range has been is 400-600 °C, where the variation from the imposed value is less than the 2%. Regarding the PbLi thermo-physical properties, for the density, heat capacity, and dynamic viscosity have been used the recommended properties of Ref. [64], instead, for the thermal conductivity, two different equations have been taken into account, the Mogahed [65], which is recommended, and the IAEA correlation [66]. This option finds its foundation, firstly, in the possibility to further perform conservative analyses verifying if the design guarantees the temperature requirement, due to a mean percentage difference of 32% from the Mogahed recommended correlation, and secondly, in the fact that during the research activity, the IAEA correlation has become the reference property for the PbLi thermal conductivity.

The thermo-physical properties table are reported in ANNEX A: Materials properties.

Value	Unit
$\rho = 19300$	kg/m^3
$c_p = 145$	J/(kg K)
$\lambda = 125$	W/(m K)

Table 4.1 – Tungsten thermo-physical properties [47]

Equation	Unit
$\rho = 7874.3 - 0.361 \cdot T$	kg/m^3
$c_p = -438.83 + 4.9838 \cdot T - 8.7371 \cdot 10^{-3} \cdot T^2 + 5.3333 \cdot 10^{-6} \cdot T^3$	J/(kg K)
$\lambda = 60.915 - 9.081 \cdot 10^{-2} \cdot T + 6.5 \cdot 10^{-5} \cdot T^2$	W/(m K)

Table 4.2 – Eurofer thermo-physical properties (T in K) [47]

Equation	Unit
$\rho = 10520.35 - 1.19051 \cdot T[K]$	kg/m^3
$c_p = (0.195 - 9.116 \cdot 10^{-6} \cdot T[K]) \cdot 10^3$	J/(kg K)
$\lambda_{Mogahed\ [65]} = 0.1451 + 1.9631 \cdot 10^{-4} \cdot T[°C]$	W/(cm K)
$\lambda_{IAEA\ [66]} = 11.9 + 1.96 \cdot 10^{-2} \cdot (T[°C] - 235)$	W/(m K)
$\mu_d = 0.187 \cdot e^{\left(11640/R \cdot T[K]\right)}$	mPa s

Table 4.3 – PbLi thermo-physical properties [64]

Equation	Unit
$\rho = -1.4226 \cdot 10^{-2} \cdot T^2 + 14.122 \cdot T - 2693$	kg/m^3
$c_p = 9.8485 \cdot 10^{-3} \cdot T^3 - 16.39861 \cdot T^2 + 9118.681 \cdot T - 1.6882247 \cdot 10^6$	J/(kg K)
$\lambda = -1.2024 \cdot 10^{-5} \cdot T^2 + 1.1846 \cdot 10^{-2} \cdot T - 2.2804$	W/(m K)
$\mu_d = (-8.095238 \cdot 10^{-4} \cdot T^2 + 0.5722429 \cdot T + 29.67213) \cdot 10^{-6}$	kg/(m s)

Table 4.4 – Water thermo-physical properties (T in K) [47]

4.2. WCLL Thermal loads

The thermal loads in the WCLL BB are mainly caused by two sources: the neutron flux generated by the fusion reaction and thermal radiation between plasma and facing materials, both can be assumed constant during these analyses. These phenomena can be represented with a volumetric power density into materials, and heat flux (HF) applied to the Tungsten armor to simulate the total power deposition in the WCLL.

According to Ref. [58], which provides the nuclear heating data of the WCLL 2018 breeding blanket, the elementary cell under analysis has its own power curves, that radially decrease moving from the Tungsten to the BSS. The structural material power curve reaches its maximum in the Tungsten layer, and the PbLi curve has its maximum at the FW-BZ interface, both radially decrease. To realistically reproduce the radial power deposition trend into PbLi and solid structures, multiple curves have been created to obtain an appropriate power deposition trend into the cell. Two different sets of equations have been implemented in the models, which represent the Eurofer and the PbLi power deposition trend, shown in Fig. 4.1.

The Tungsten layer, which faces the plasma and located in front of the FW, is subjected to a heat flux composed of charged particles and thermal radiation. According to Refs. [39][62][63], two different maximum nominal heat fluxes have been evaluated during these years, and thus imposed onto the straight surface of the Tungsten. Initially, the maximum HF was equal to 0.5 MW/m^2, after that, more recent studies have demonstrated that, as regards the COB equatorial elementary cell, the maximum heat flux is assumed 0.32 MW/m^2 onto the straight surface of the Tungsten armor. Concerning the elbows, a decreasing linear trend equation with radial direction is implemented, this to take into account the decrease in the normal component of the heat flux, due to the variation of the incidence angle, $q''_{SW}(y) = \left[1 - \frac{(y_0 - y)}{y_{tot}}\right] \cdot q''_{max}$.

Although the implemented power curves are linear functions, the total deposited power varies depending on the run. The variation is because changing the cell layout the amount of Eurofer in the model is different, and the same occurs for the PbLi, leading to a variation in the volume occupied by PbLi and Eurofer in the specific radial position.

The deposited power removal is ensured by the FW and BZ water coolant circuit. For each steady-state analysis, the reference water thermodynamic cycle is assumed by the BoP requirements [37][46] for the PHTS. The cycle, based on PWR conditions, foresees water coolant entering at 295°C and exiting at 328°C, at 15.5 MPa. The imposed water mass flow rate varies in each run and it is evaluated with the enthalpy balance ($\Delta h = 193.6\ kJ/kg$) using RELAP5/Mod3.3 water properties [67][68], obtaining in all the analyses the required water outlet temperature of 328°C. This version of RELAP5/Mod.3.3 was developed at the Department of Astronautical, Electrical and Energy Engineering (DIAEE) "Sapienza" University of Rome in collaboration with ENEA [68], improving the code modelling capability for fusion reactors and their primary cooling systems.

The thermal loads equations are reported in ANNEX B: Steady-state and transient thermal loads.

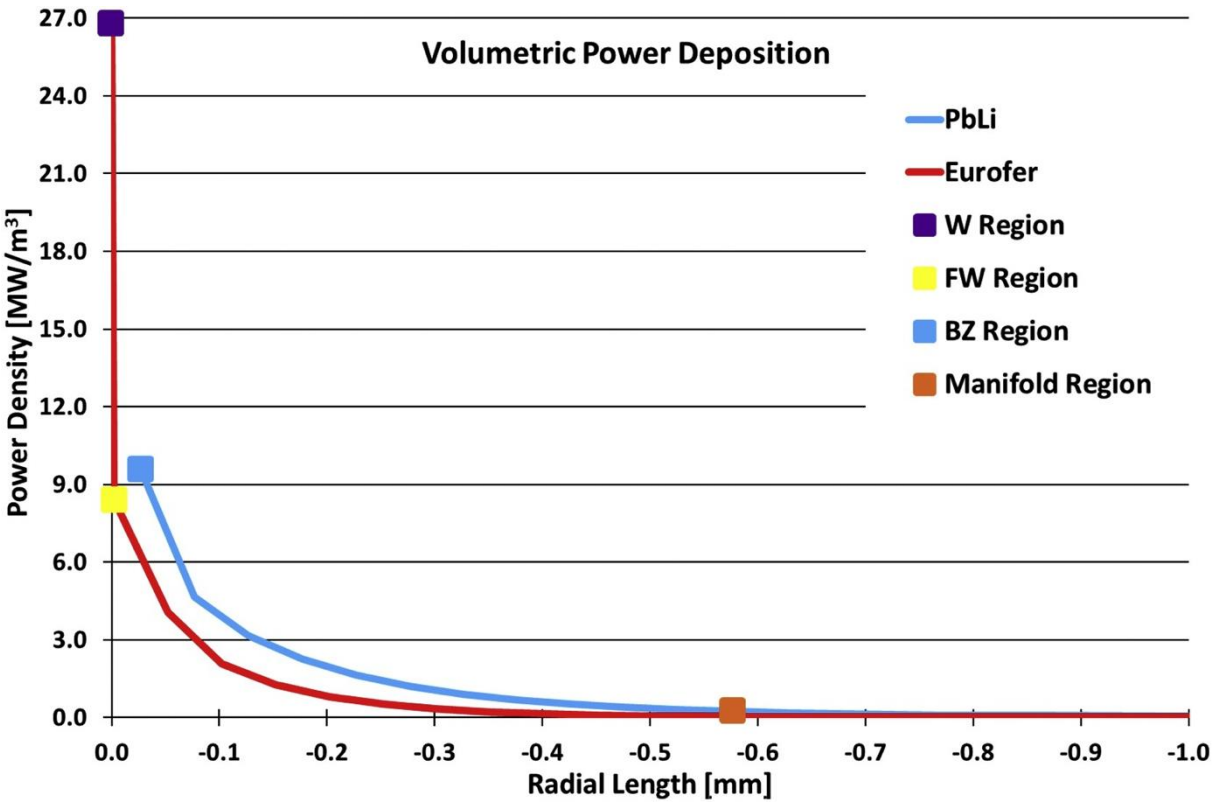

Fig. 4.1 – WCLL BB COB equatorial cell volumetric power deposition in the radial length

4.3. BZ system analyses – From WCLL V0.2 to V0.6

This first set of analyses concerns the optimization of the BZ cooling system verifying if the DEMO 2017 baseline requirements are met. To optimize the BZ cooling system, several DWTs arrangements have been investigated. Five different analyses have been performed to find out an adequate BZ tubes layout, taking into account the following main requirements [52]:

- Maximum temperature of Eurofer structural components below 550°C [38];
- DWTs minimum curvature radius equal to 3 times of the external diameter;
- Minimum distance between DWTs axes of 26 mm;
- Maximum number of DWTs curves limited to 2;
- Temperature toroidal symmetry into the BZ;
- No stiffeners crossing.

4.3.1. Numerical models and mesh

The first numerical model has been performed on the WCLL 2018 V0.2 configuration, composed by 20 C-shaped tubes and 10 FW cooling channels, as reported in Section 3.2. The second configuration, the V0.3, has the same number of BZ tubes but with different displacement, indeed, all the tubes arrays have a modified radial elongation and enhanced distance from the FW system. The V0.3 layout consolidates the geometric layout of the first tube array, fixing the FW distance at 20 mm and a minimum number of 6 tubes, 3 per side.

The other three systems, V0.4, V0.5 and V0.6 respectively, have an additional pair of tubes, one per side. The added tubes have been placed in the second array, thus, becoming a 22 C-shaped DWTs configuration. From the V0.4 layout, the additional pair has been inserted in the second array, with relative modification of the poloidal pitch between the tubes, in fact, the second array has the same poloidal pitch as the third array but placed one above the other. Moreover, the additional pair has a curvature radius of 200 mm alternating with the 50 mm curvature radius. The V0.5 also features a layout change of the second array, modifying the tubes pair with a curvature radius of 50 mm to 100 mm, remaining alternated with the 200 mm curve radius. The final layout, V0.6, foreseen a differentiation between the radial extension of the tubes of the second array, where tubes with a curvature radius of 200 mm reduce the FW

detachment, and those with a curvature radius of 100 mm, instead increase the same detachment. In addition, also the third array provides a modification on the radial extensions, it has been lengthened about 10 mm, reducing the FW distance.

The different BZ tubes layouts are shown in Fig. 4.2, and an overview of the geometrical parameters of the five numerical models is reported in Table 4.5. To facilitate the analysis and the recognition of the different tubes they have been numbered, only one half of the cell is reported given the toroidal symmetry. Starting from the first array, the tube 1 is located in the lower part, and the tube 3 is adjacent to the upper plate. Concerning the second array, the numbering of the tubes follows the poloidal direction; therefore, tube 4 is adjacent to the lower plate and tube 6 or 7 (depending on the configuration) is located at the top of the cell. To differs the tubes of the 2nd array with different curvature radius, they have also been named as "2nd array L", the tubes with the lower curvature radius (i.e. 50 or 100 mm), and "2nd array C" with the higher ones (i.e. 200 mm). The tubes of the last array have been named accordingly to the poloidal and also toroidal orientation. The first tube is in the lower plate near the central part of the cell, and the second is above the baffle plate in the same toroidal position. It follows that the third and fourth are next to these, but one is positioned just below the baffle, and the other is adjacent to the upper plate.

The different 3D finite volume models have been modelled with fluid domains for BZ water, FW water and PbLi; and solid domains for Eurofer structures, FW Eurofer chase and Tungsten armor.

WCLL 2018 V0.2				
Arrays	**N° Tubes**	**Curve Rad. [mm]**	**FW Dist. [mm]**	**Tube Length [mm]**
1st array	Tube 1	50.0	15.0	1682.58
	Tube 2	50.0	15.0	1682.58
	Tube 3	50.0	15.0	1682.58
2nd array	Tube 4	50.0	52.5	1527.58
	Tube 5	200.0	52.5	1398.82
	Tube 6	50.0	52.5	1527.58
3rd array	Tube 7	50.0	108.25	1050.08
	Tube 8	50.0	108.25	1050.08
	Tube 9	50.0	108.25	1050.08
	Tube 10	50.0	108.25	1050.08

WCLL 2018 V0.3				
Arrays	**N° Tubes**	**Curve Rad. [mm]**	**FW Dist. [mm]**	**Tube Length [mm]**
1st array	Tube 1	50.0	20.0	1682.58
	Tube 2	50.0	20.0	1682.58
	Tube 3	50.0	20.0	1682.58
2nd array	Tube 4	50.0	63.0	1527.58
	Tube 5	200.0	63.0	1398.82
	Tube 6	50.0	63.0	1527.58
3rd array	Tube 7	50.0	138.25	1050.08
	Tube 8	50.0	138.25	1050.08
	Tube 9	50.0	138.25	1050.08
	Tube 10	50.0	138.25	1050.08

WCLL 2018 V0.4				
Arrays	**N° Tubes**	**Curve Rad. [mm]**	**FW Dist. [mm]**	**Tube Length [mm]**
1st array	Tube 1	50.0	20.0	1672.58
	Tube 2	50.0	20.0	1672.58
	Tube 3	50.0	20.0	1672.58
2nd array	Tube 4	50.0	63.0	1506.58
	Tube 5	200.0	63.0	1377.82
	Tube 6	50.0	63.0	1506.58
	Tube 7	200.0	63.0	1377.82
3rd array	Tube 8	50.0	138.25	990.08
	Tube 9	50.0	138.25	990.08
	Tube 10	50.0	138.25	990.08
	Tube 11	50.0	138.25	990.08

WCLL 2018 V0.5				
Arrays	**N° Tubes**	**Curve Rad. [mm]**	**FW Dist. [mm]**	**Tube Length [mm]**
1st array	Tube 1	50.0	20.0	1672.58
	Tube 2	50.0	20.0	1672.58
	Tube 3	50.0	20.0	1672.58
2nd array	Tube 4	100.0	63.0	1463.66
	Tube 5	200.0	63.0	1377.82
	Tube 6	100.0	63.0	1463.66
	Tube 7	200.0	63.0	1377.82
3rd array	Tube 8	50.0	138.25	990.08
	Tube 9	50.0	138.25	990.08
	Tube 10	50.0	138.25	990.08
	Tube 11	50.0	138.25	990.08

WCLL 2018 V0.6				
Arrays	**N° Tubes**	**Curve Rad. [mm]**	**FW Dist. [mm]**	**Tube Length [mm]**
1st array	Tube 1	50.0	20.0	1672.58
	Tube 2	50.0	20.0	1672.58
	Tube 3	50.0	20.0	1672.58
2nd array	Tube 4	100.0	73.0	1443.66
	Tube 5	200.0	53.0	1397.82
	Tube 6	100.0	73.0	1443.66
	Tube 7	200.0	53.0	1397.82
3rd array	Tube 8	50.0	128.25	1010.08
	Tube 9	50.0	128.25	1010.08
	Tube 10	50.0	128.25	1010.08
	Tube 11	50.0	128.25	1010.08

Table 4.5 – WCLL 2018 equatorial elementary cell geometrical parameters

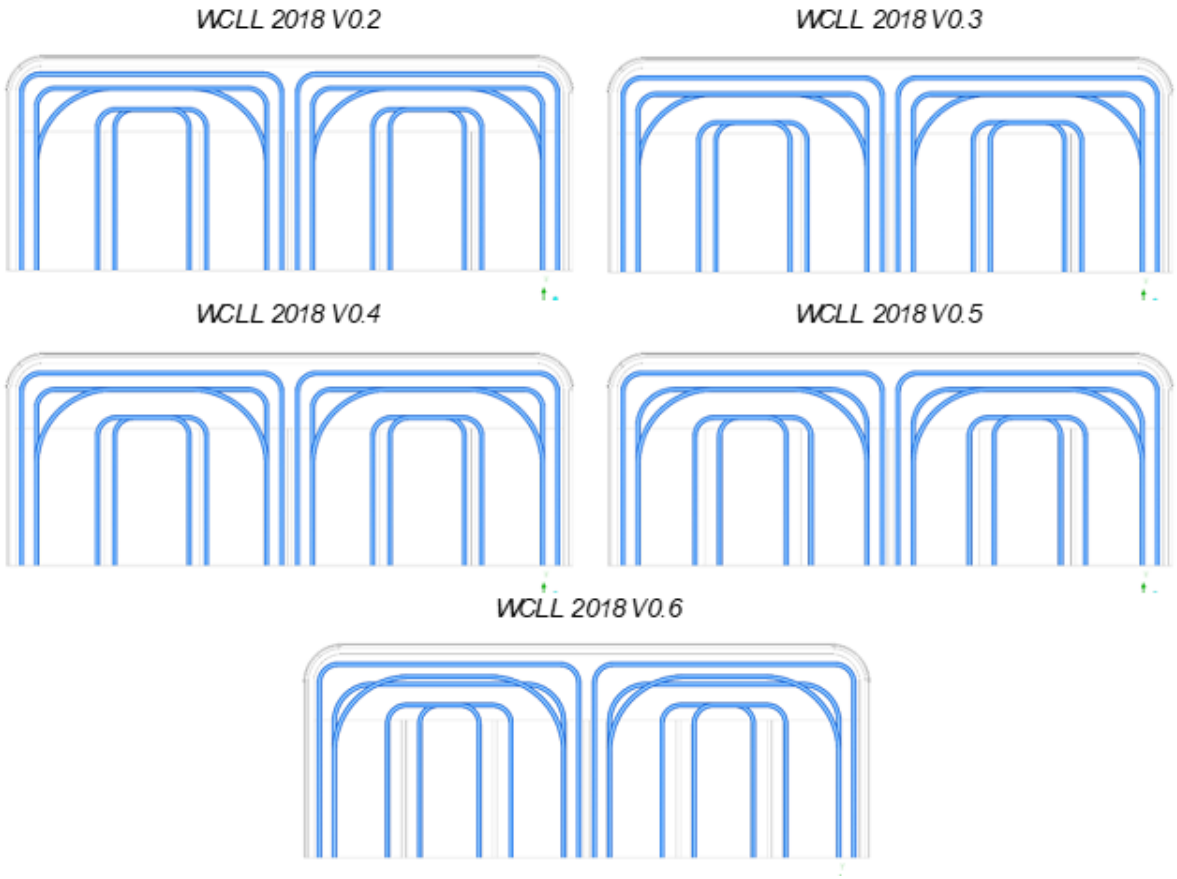

Fig. 4.2 – WCLL 2018 Numerical models BZ tubes arrangement

A mesh independence analysis has been performed, allowing accurate results and reasonable calculation time, using meshes with different degree of detail. All the geometrical models are developed as a single part, to simulate the heat transfer between the multiple components, solids and fluid, using a conformal mesh between domains. Hexahedral and tetrahedral elements were adopted in the models, considering the geometrical features of the domains, many and different local controls are inserted to define the complex geometry of the cell properly. For this purpose, different code tools were exploited, such as sizing control, sweep method, mapped face, and the inflation control near the solid walls for the resolution of the viscous sub-layer (y^+=1) of the water, based on a maximum velocity of 7 m/s.

The analysis was conducted to establish the independence of results from the grid and to optimize the number of elements in the model. The simulations have been reported and proved in Ref. [47] for a COB equatorial elementary cell with the same geometry and a similar DWTs distribution. A mesh detail is shown in Fig. 4.3, and the mesh statistics of each numerical models are reported in Table 4.6.

Parameters	**Models**				
	V0.2	***V0.3***	***V0.4***	***V0.5***	***V0.6***
N° Nodes	14.0 M	14.4 M	14.3 M	14.3 M	14.3 M
N° Elements	27.1 M	27.1 M	27.6 M	28.0 M	27.7 M
Ave Orth Qual	0.814	0.818	0.817	0.816	0.817
Ave Skewness	0.208	0.202	0.206	0.207	0.206

Table 4.6 – WCLL 2018 V0 numerical models mesh statistics

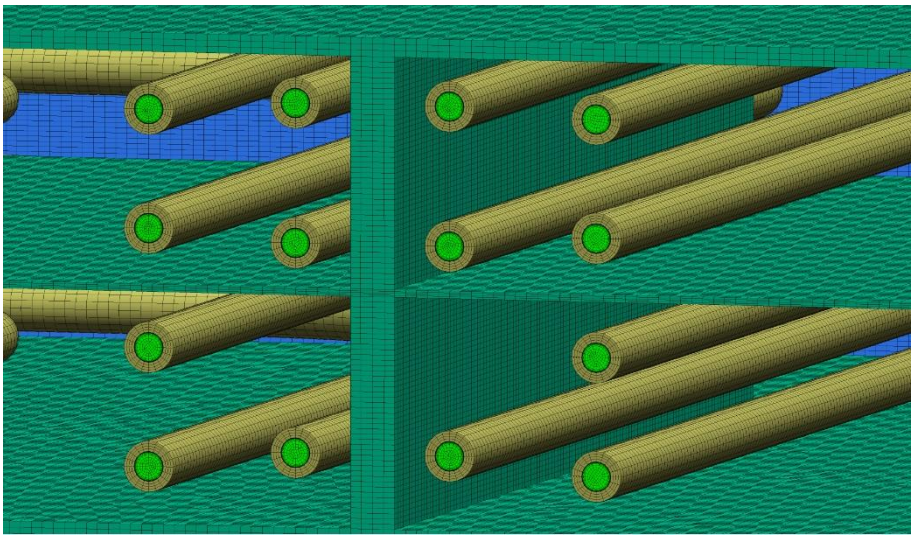

a) Detail of BZ tubes and stiffeners mesh

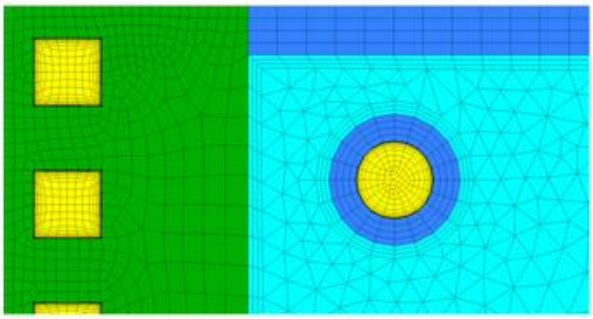

b) Detail of FW tubes and plate mesh

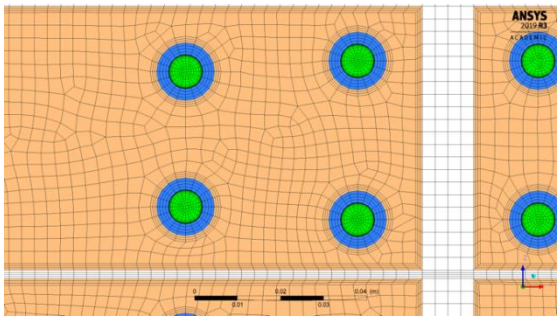

c) Detail of BZ mesh

Fig. 4.3 – WCLL BB 2018 V0.6 mesh: detail of fluid and solid domains

4.3.2. Solver settings and boundary conditions

To evaluate the Eurofer temperature field obtaining proper refrigeration not exceeding the imposed limit of 550°C, and the thermal-hydraulic behaviour of the elementary cell focussing on the water coolant performances, verifying the reliability to deliver the coolant at the design temperature imposed by the PHTS (i.e. water outlet temperature at 328°C), for each configuration steady-state analysis has been performed to assess the coolant systems efficiency by removing the total deposited power, as well as sensitivity analyses to optimize the BZ DWTs layout.

As regards the thermophysical properties of the materials, they have been implemented into the CFX code with the temperature dependent function and fixed value reported in Sect. 4.1.

Concerning the thermal loads, two main contributions have been implemented into the codes to reproduce the deposited power: the HF, with a nominal maximum value of 0.5 MW/m^2 onto the straight Tungsten surface; and two radial volumetric power depositions, one into the solid structures and the other into the PbLi domain. These heat loads have been implemented with several functions depending on the radial position according with Sect. 4.2.

In Table 4.7 are reported the deposited power divided per models and domains, necessary to calculate the water mass flow needed to obtain an average temperature of 328°C at both systems water outlets and to dissipate the produced thermal power. Thus, the total mass flow varies according with the deposited power. The BZ cooling system has an imposed water mass flow equally divided by the total number of tubes, which is 51% of the total water mass flow rate. The FW, instead, has 49% of the total water, equally distributed on the ten water channels. Given the heat exchange between FW and BZ, the percentages considered do not correspond to the value that would be obtained from the actual power deposited within the single systems. This uncertainty has already been found and investigated by several CFD analyses (Ref. [36]) which show the limits of the water mass flow rate enthalpy balance method.

As regards the PbLi, forced circulation is assumed and no buoyancy forces are considered. Inlet mass flow rate of 0.16521 kg/s equally distributed on the six sub-channels, temperature of 327°C and reference pressure of 100 kPa have been set [59] as boundary conditions. In these analyses, the Mogahed thermal conductivity [65] has been set in the PbLi domain.

The other boundary conditions adopted for all the models are:

- Periodic boundary conditions on the upper and lower surfaces of upper and lower stiffening plates, FW and Tungsten layer, in poloidal direction, to simulate the presence of adjacent elementary cell;
- Adiabatic condition to back walls of FW, stiffeners, Tungsten layer and FW side walls;
- Mass flow rate and static pressure imposed in the fluid domain at inlet and outlet sections, respectively;
- No-slip condition at the interface between coolant and the circuit steel walls.

To choose the appropriate resolutive method, the Reynolds number $\left(Re = \frac{\rho \cdot \bar{v} \cdot D_h}{\mu}\right)$ is calculated to evaluate whether the fluids were in laminar or turbulent motion. It returns that into the water domains, the Reynolds number is above 35,000 in all the BZ system layout and above 140,000 in all FW system, resulting in turbulent flow for both systems and all models. The two-equations k-ω Shear Stress Transport (SST) model has been selected as an appropriate method to simulate the turbulence effects of water because it is able to solve the viscous sublayer explicitly with y+≤1 without losing accuracy in the free stream of the channels, as reported in Ref. [69]. Moreover, it has been applied to a large variety of similar turbulent flows (Refs. [47][55]). In addition, the model represents an acceptable compromise between accuracy and robustness [70]. Regarding the PbLi, given the very slow velocities reached in the cells, resulting in a Reynolds number of around 40, the laminar model has been set to solve the Navier-Stokes equations in this domain.

A detailed set of the imposed boundary conditions are shown in Fig. 4.4 and the related numerical values are reported Table 4.8.

System	**Region**	**Models**					**Unit**
		V0.2	***V0.3***	***V0.4***	***V0.5***	***V0.6***	
BZ	*PbLi*	170.296	171.093	170.357	170.468	170.387	kW
	Tubes	3.327	3.000	3.229	3.186	3.214	kW
	Stiffeners	7.937	7.937	7.937	7.937	7.937	kW
	BZ Total	*181.560*	*182.030*	*181.522*	*181.592*	*181.538*	*kW*
FW	*FW*	31.156	31.156	31.156	31.156	31.156	kW
	Tungsten	6.694	6.694	6.694	6.694	6.694	kW
	Tung HF	87.750	87.750	87.750	87.750	87.750	kW
	Tung HF$_{SW}$	13.767	13.767	13.767	13.767	13.767	kW
	FW Total	*139.363*	*139.363*	*139.363*	*139.363*	*139.363*	*kW*
Total		***320.929***	***321.396***	***320.888***	***320.958***	***320.904***	**kW**

Table 4.7 – WCLL 2018 design: power distribution divided by models and domains

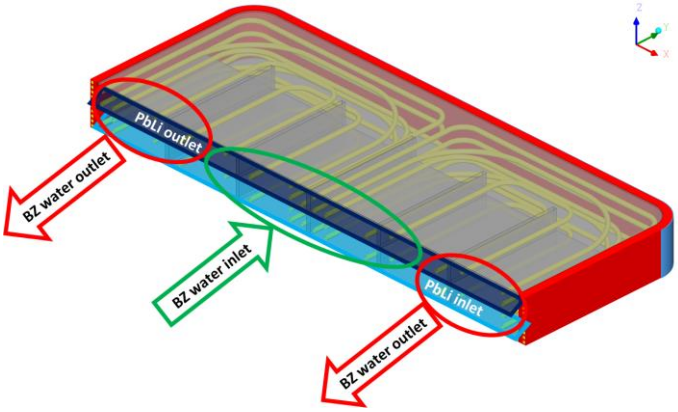

a) BZ water and PbLi inlet and outlet BCs

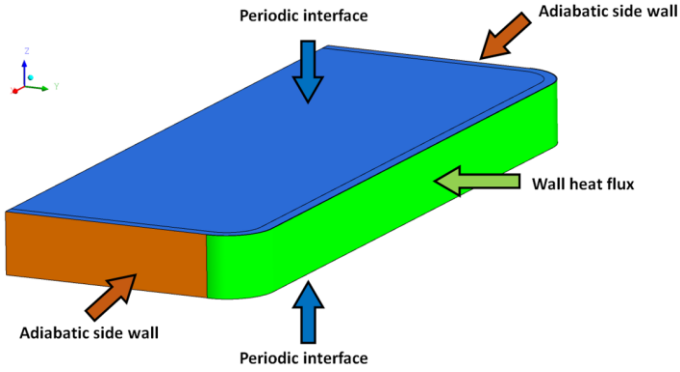

b) Different domain BCs

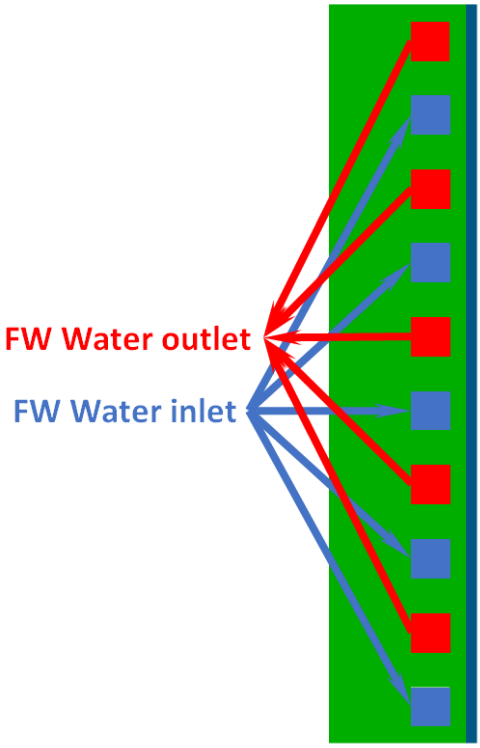

c) FW water inlet and outlet BCs

Fig. 4.4 – WCLL COB equatorial elementary cell boundary conditions

#	Parameters	Models					Unit
		V0.2	***V0.3***	***V0.4***	***V0.5***	***V0.6***	
1	FW HF_{max}	0.5	0.5	0.5	0.5	0.5	MW/m^2
2	Water (BZ-FW) T_{inlet}	295.0	295.0	295.0	295.0	295.0	°C
3	Water (BZ-FW) Pressure	15.5	15.5	15.5	15.5	15.5	MPa
4	FW MFR	0.81223	0.81345	0.81217	0.81232	0.81217	kg/s
5	BZ MFR	0.84547	0.84665	0.84533	0.84548	0.84533	kg/s
6	Total water MFR	1.6577	1.6601	1.6575	1.6578	1.6575	kg/s
7	PbLi T_{inlet}	327.0	327.0	327.0	327.0	327.0	°C
8	Total PbLi MFR	0.16521	0.16521	0.16521	0.16521	0.16521	kg/s

Table 4.8 – WCLL 2018 V0 analyses boundary conditions

4.3.3. Results

The results of the five runs performed are discussed below. The models differ by positions and number of the BZ DWTs. The analyses have been performed in steady-state conditions to optimize the layout of the tubes, obtaining a detailed temperature map of the Eurofer structures and evaluating the water thermal-hydraulic conditions.

The relevant parameters of the steady-state runs are reported in Table 4.9, where, it is clearly shown that the Eurofer temperature exceeds the maximum allowable value of 550°C in the V0.2 and V0.3 configurations in the stiffeners domain. From V0.4, with the addition of the pair of tubes, the maximum temperature drops in the former model by about 36 degrees, achieving the temperature requirement. The V0.5 optimization causes the Eurofer stiffeners temperature to drop by a further 18 degrees and the last V0.6 reaches 505.2°C due to its optimized layout.
From the table arise that the first tube array influences the temperature of the FW, in fact, from the V0.3, where the distance from the FW is fixed at 20mm, there is no temperature variation as the other arrays layout changes, although decreasing the detachment of the second array in V0.6. In addition, the Tungsten layer is only affected by the FW cooling channels, since its temperature has no significative variation, being always within the limit, with temperatures around 425°C. The same temperature decrease is noted in PbLi domain, which, however, did not show the marked reduction as in the stiffeners domain. The PbLi has reduced its temperature by around 49 degrees from the V0.2 to the V0.6 layout.

All the configurations provide as water average outlet temperature, for both BZ and FW cooling systems, temperatures around 328°C. It should be noted that PbLi, as a fluid in forced convection, contributes to the energy balance inside the cell, so that the water temperatures slightly varies from the hypothesized value. Considering the water average outlet velocity in both BZ and FW systems, it is deemed necessary to increase the thermal-hydraulic performances of water, since there are margins for improvement.

#	Parameters	Models					Unit
		V0.2	***V0.3***	***V0.4***	***V0.5***	***V0.6***	
1	Tungsten T_{max}	424.5	425.1	424.9	425.0	424.9	°C
2	FW T_{max}	441.2	447.2	447.2	447.7	448.5	°C
3	Stiffeners T_{max}	573.7	570.2	534.0	516.0	505.2	°C
4	Tubes T_{max}	412.1	411.2	396.6	404.1	401.3	°C
5	PbLi T_{max}	579.3	575.8	537.1	532.3	530.8	°C
6	BZ Water $T_{out\ ave}$	328.3	327.7	327.9	327.8	328.0	°C
7	FW Water $T_{out\ ave}$	328.9	329.5	329.5	329.7	329.6	°C
8	BZ Water $v_{out\ ave}$	1.291	1.283	1.166	1.165	1.166	m/s
9	FW Water $v_{out\ ave}$	2.539	2.550	2.546	2.549	2.548	m/s

Table 4.9 – WCLL 2018 V0 analyses: main output parameters

Concerning the structural materials, in all configurations the temperature toroidal symmetry has been achieved in Eurofer structures, and as regards the FW system also the poloidal symmetry at the Tungsten interface, due to the opposite and alternated water flow and the pitch of the constant channels, as shown in Fig. 4.5 and Fig. 4.6. From the latter figure, it is clear that the hotter part of the FW resides in the inner part, at the FW-BZ interface, due to a higher temperature of the PbLi compared with the FW. This phenomenon implies that the FW-BZ interface is subjected to passive heat removal by the FW; this explains why a higher percentage of water is required by this system to obtain 328°C. In fact, if the two systems were adiabatic between them, the FW would require approximately 43% of the total water mass instead of 49%, as set in the BCs.

Since the V0.2 and V0.3 (Fig. 4.5 a and b) did not meet the Eurofer temperature requirements, they were discarded as eligible configuration. The first promising solution has been carried out from the V0.4, which represents the configuration that sizes the minimum number of DWTs necessary to refrigerate the cell. Already in the V0.4 (Fig. 4.5c), it can be noted that all the hot spots have been successfully extinguished. Both grey areas, previously presented in the V0.3 configuration in the proximity of the second array, have been spent. In the V0.5, where the curvature radius has been increased up to 100mm, the hotter regions have been reduced (black circle in Fig. 4.5 d), and in addition, the regions in proximity of the end of baffle plate greatly reduce their temperature. The same phenomenon is not noted in the FW (Fig. 4.6 d), which increases the temperature of the internal corners compared with V0.4 FW system (Fig. 4.6 c).

In the V0.6, with the differentiation of the radial length of the second array, the temperature field has shown a hot spots area reduction near the side walls (black circle in Fig. 4.5 e). As a result of this optimization, it has returned a more homogeneous temperature field of the Eurofer structures than the previous layout. Even the FW system has benefited from the radial differentiation; in fact, the inner temperature field is very similar to the V0.4 layout (Fig. 4.6 e).

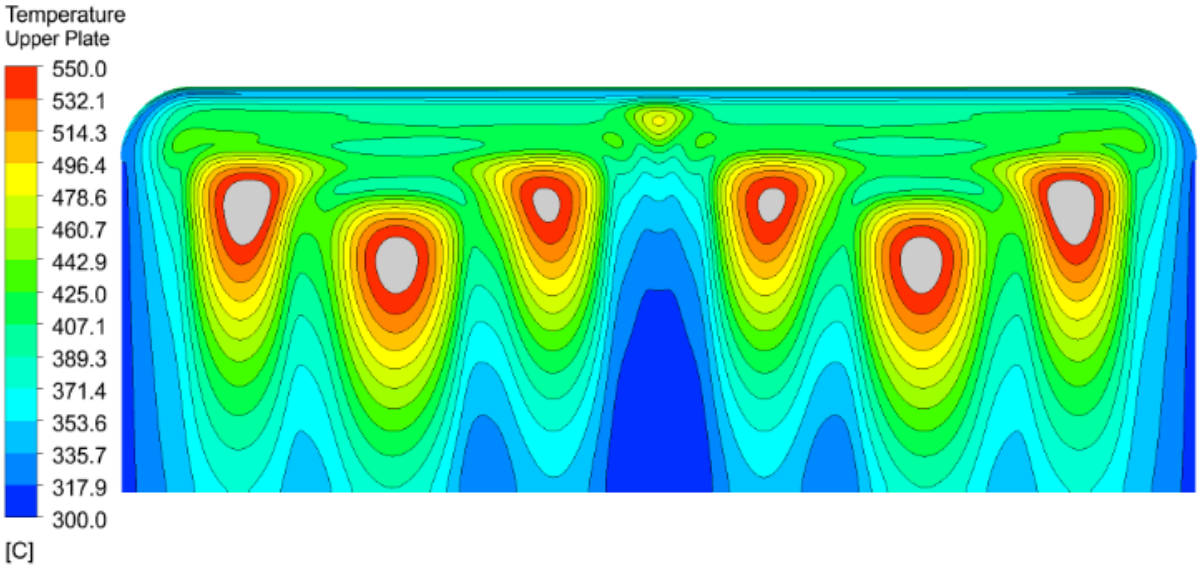

a) V0.2 Eurofer upper plate

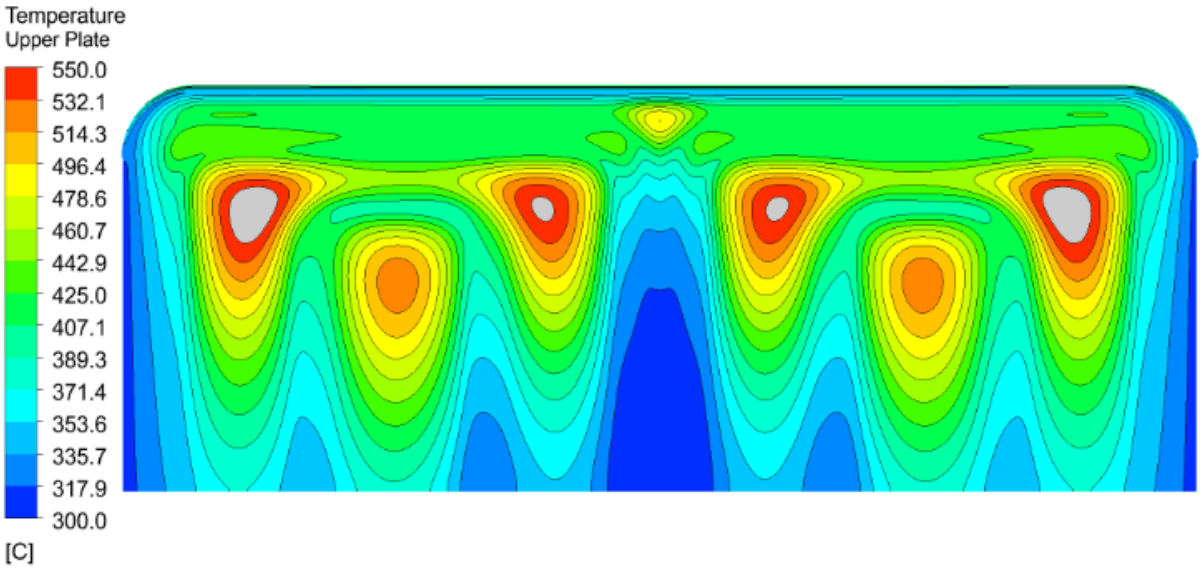

b) V0.3 Eurofer upper plate

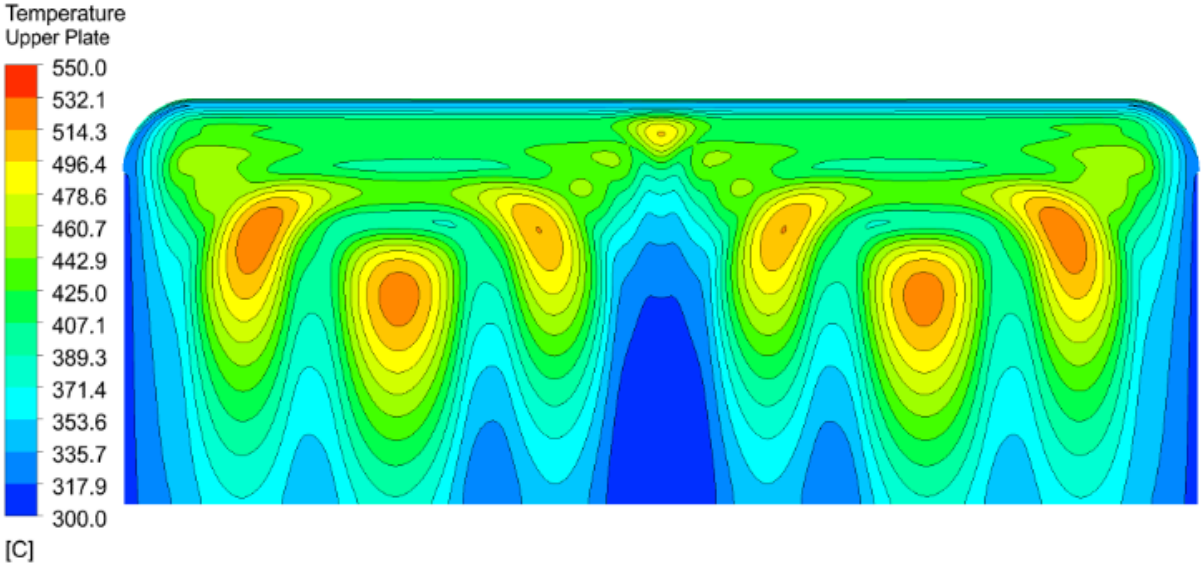

c) V0.4 Eurofer upper plate

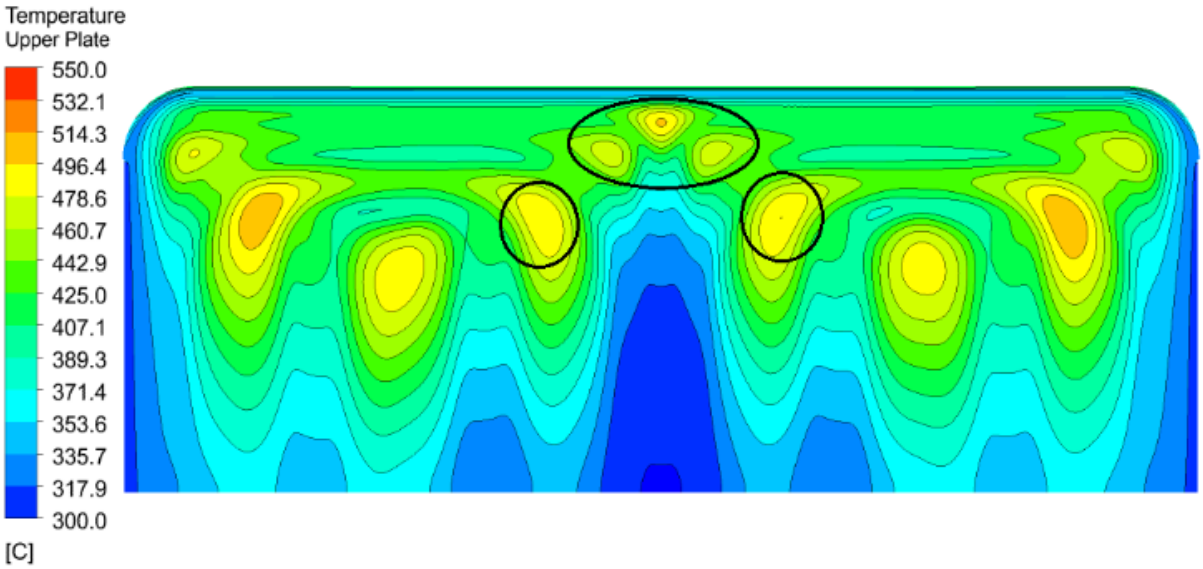

d) V0.5 Eurofer upper plate

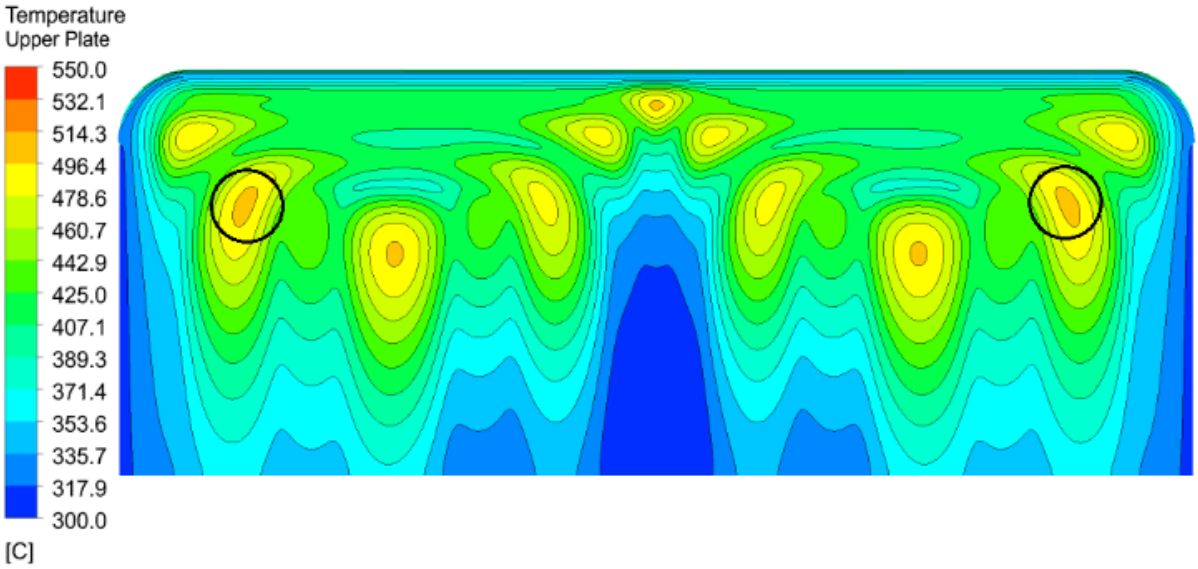

e) V0.6 Eurofer upper plate

Fig. 4.5 – WCLL 2018 V0 Eurofer upper plate temperature distribution

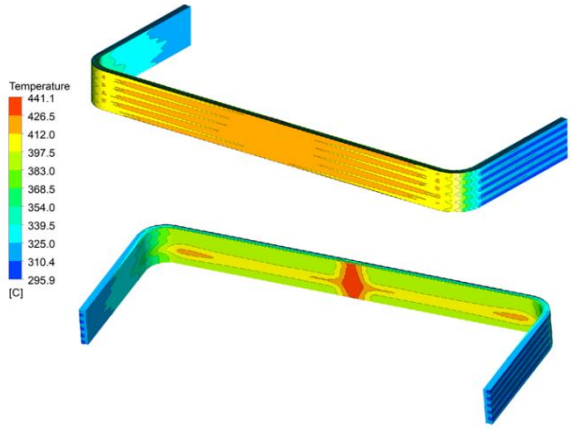

a) V0.2 FW Eurofer

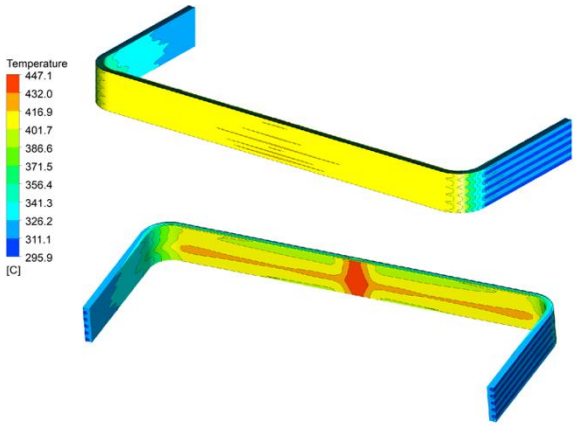

b) V0.3 FW Eurofer

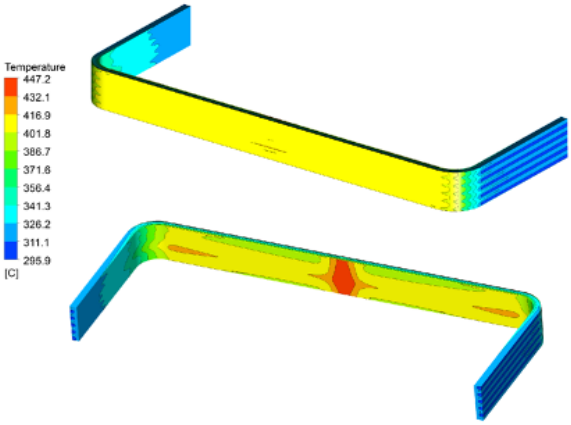

c) V0.4 FW Eurofer

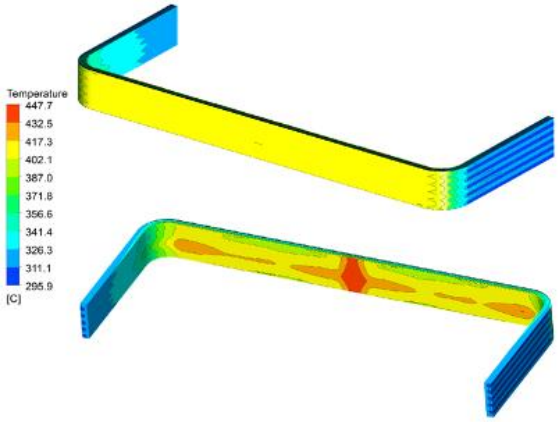

d) V0.5 FW Eurofer

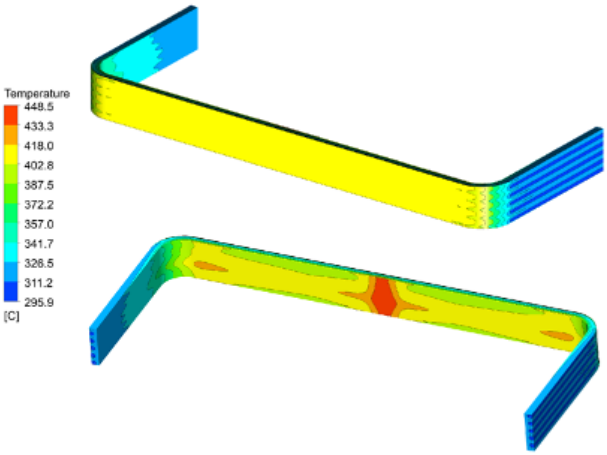

e) V0.6 FW Eurofer

Fig. 4.6 – WCLL 2018 V0 FW Eurofer chase temperature distribution

Focusing on the V0.6 configuration, the PbLi temperature field is shown in Fig. 4.7, where the hot spots are located at the PbLi-Stiffeners interface. Despite being in forced convection, from the poloidal-toroidal cut placed after the baffle plate, returns an almost symmetric temperature field in the poloidal direction, due to the very low velocity of the PbLi. The plane has been placed at 160mm from the FW, to analyze the possibility of PbLi stratification in that area, which does not occur. The Fig. 4.8 shows the PbLi velocity profile where three different regions are highlighted: the square channel, where the flow is predominantly radial and the velocity profile clearly returns the parabolic trend in both directions inlet and outlet; the end of the baffle plate, which returns higher velocity turning in the upper part, immediately after the end of the baffle; and the tubes zone, where the PbLi is almost stationary. In addition, swirling areas can be noted in the upper part of the cell near the end of the baffle, and in the lower part of the cell between the third and second array of DWTs.

As regards the BZ and FW coolant systems, the average outlet temperature is 328.0°C and 329.6°C, respectively. The equal division of the mass flow rate makes causes an inhomogeneous BZ outlet temperature distribution. Thus, the first array has the highest outlet temperature, exceeding by 8 degrees from the required value, and the third array has a temperature of about 10 degrees lower. Due to the decreasing radial power trend, the first tube array is significantly more thermally stressed than the remaining ones reaching a maximum temperature at the coolant-tube interface, near the side walls, at around 364.6°C exceeding by around 20 degrees the saturation temperature, resulting in a local boiling. The BZ water-tubes interface and the outlet temperature is shown in Fig. 4.10. The FW cooling system, on the other hand, thanks to its alternating and opposite flow, shows a regular temperature trend into the channels, as demonstrated by Fig. 4.11. Even in this system, the hottest regions are near the SWs, exceeding the saturation temperature by 16 degrees.

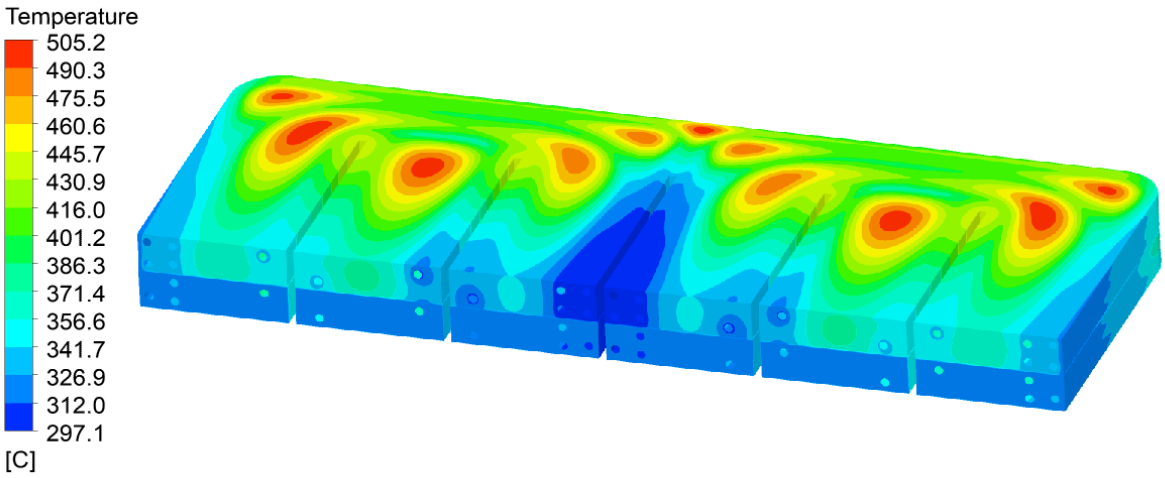

a) Isometric view of PbLi domain

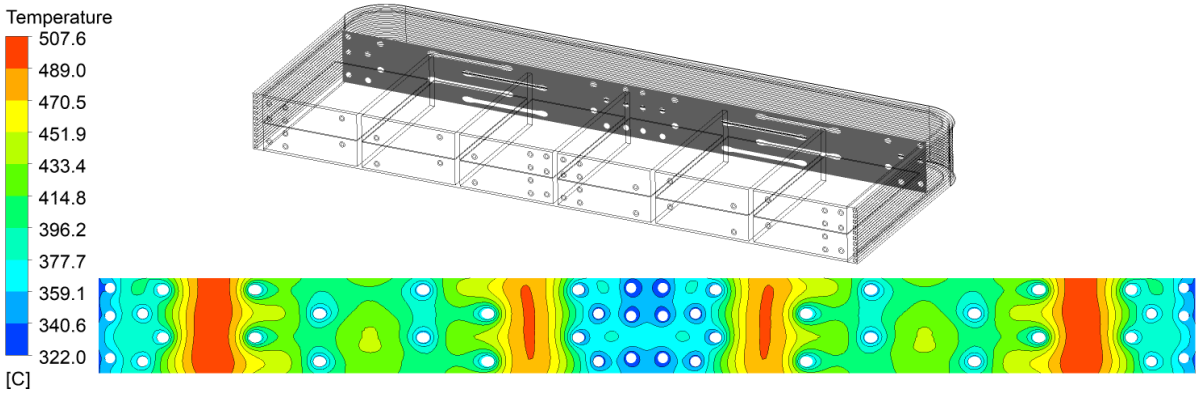

b) Poloidal-toroidal view of PbLi domain at 160 mm from FW

Fig. 4.7 – WCLL 2018 V0.6 layout: PbLi temperature field

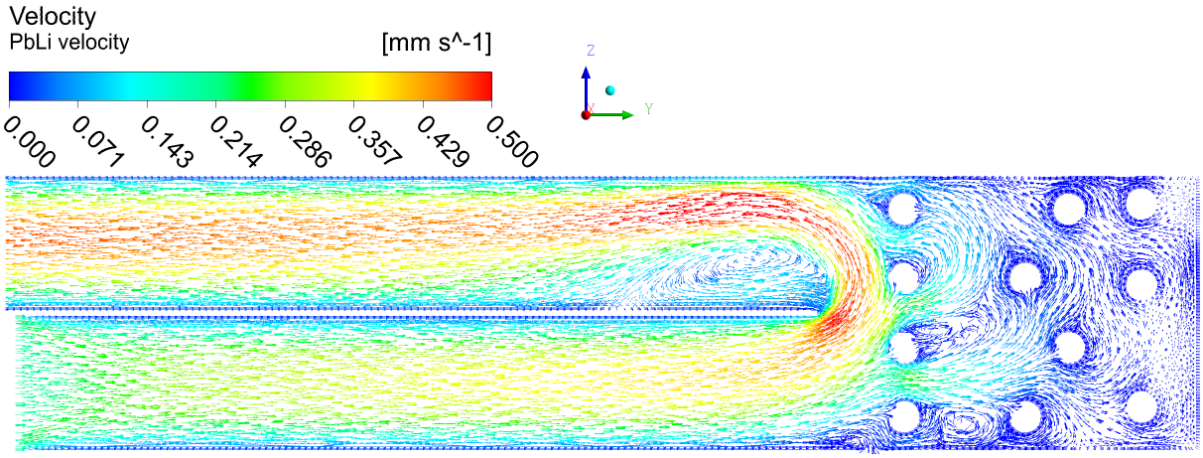

Fig. 4.8 – WCLL 2018 V0.6 layout: PbLi velocity profile

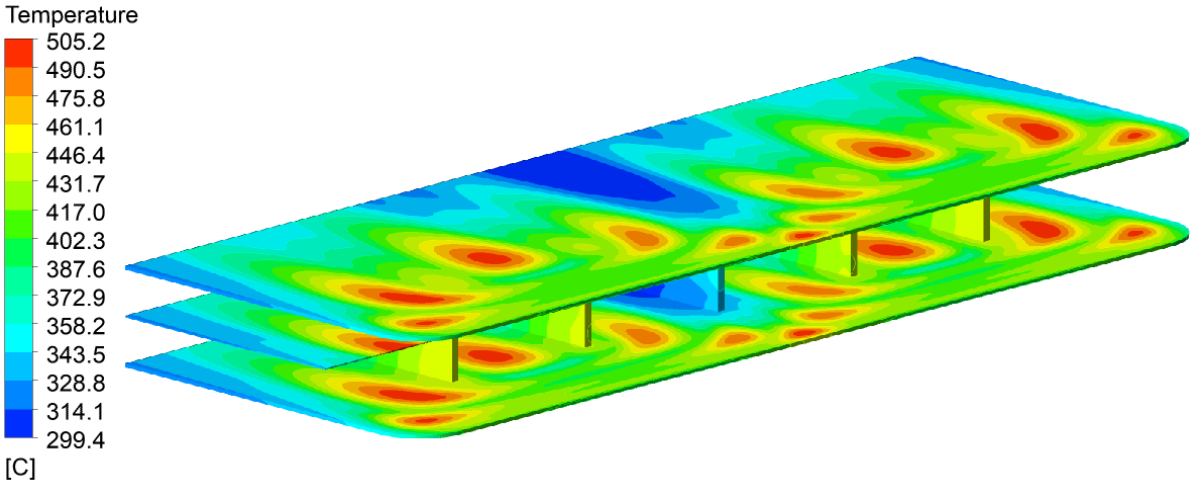

Fig. 4.9 – WCLL 2018 V0.6 layout: Eurofer structures temperature field

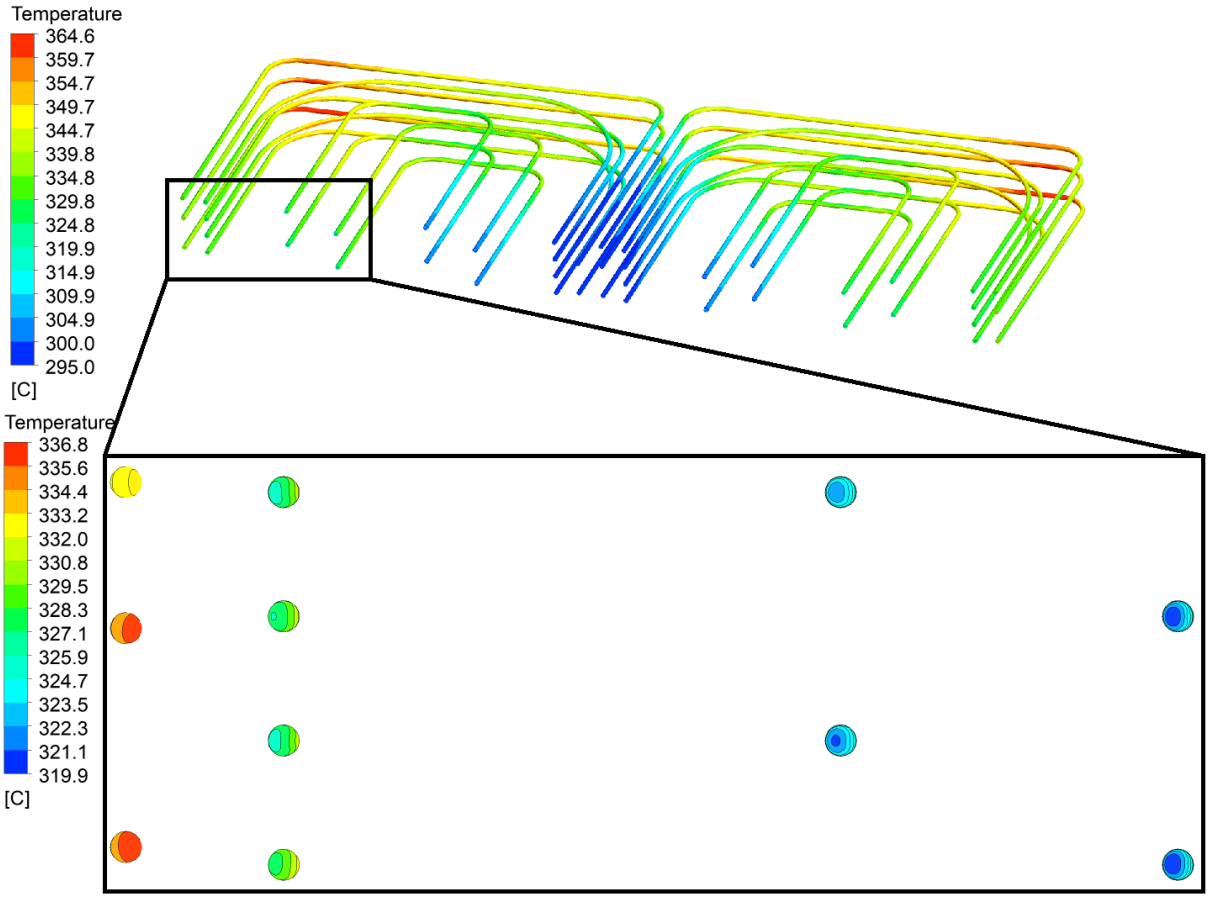

Fig. 4.10 – WCLL 2018 V0.6 layout: DWTs water interface and outlet temperature focus

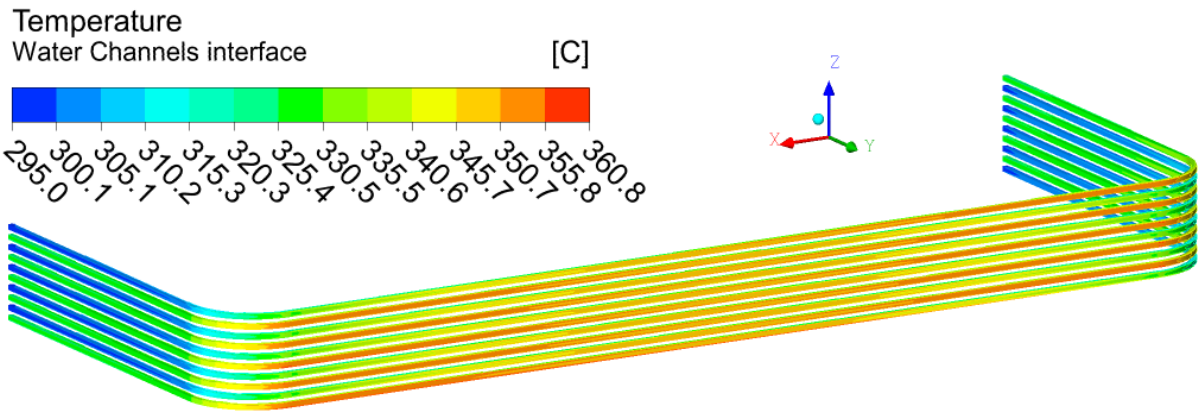

Fig. 4.11 – WCLL 2018 V0.6 layout: water channels interface temperature

4.3.4. Summary

The cooling performance of the WCLL 2018 elementary cell has been investigated using a CFD approach, with the aim of its BZ tubes optimization. The analyses based on the WCLL 2018 design focused on five different BZ tubes layout.

The simplified BZ layout, with the C-shaped orientation, has made possible to achieve the goal of a symmetric temperature field in the toroidal direction for all configurations. In addition, avoiding vertical stiffeners crossing due to the manufacturing requirement has been respected.

As to optimize the BZ tubes number, from the analyses on the different layouts is it clear that a configuration with 20 C-shaped BZ tubes does not meet the Eurofer temperature requirement, exceeding it. The V0.2 and V0.3 BZ layout have highlighted large temperature hot spots into the plates. On the other hand, a configuration with 22 DWTs ensures an adequate Eurofer temperature, which is below the limit, being the most promising solution. The addition of one pair of tubes causes a marked temperature decrease, although also the BZ water velocity decreases considerably, being around 1.16 m/s. The configuration V0.4 has returned a stiffeners domain characterized by a marked temperature reduction without changing the geometrical arrangement of the tubes. In the V0.5 layout, the increase in the curvature radius, the hot spots into the plates have been reduced but have been increased the temperature at the FW interface near the SWs, although the latter is well below the Eurofer limit. The last analyzed configuration, the V0.6, has turned out to be the most promising configuration, which has reached the lowest Eurofer temperature in the stiffeners domain. From the V0.6 result, it has

been evaluated that the PbLi velocity, even in forced convection, does not exceed 0.5 mm/s. In addition, it has shown that in forced convection there is no thermal stratification, showing a homogeneous temperature distribution in the poloidal direction, further analyses considering buoyancy forces and/or MHD have to be performed to evaluate the real motion of the fluid inside the cell.

Concerning the V0.6 cooling systems, FW and BZ, they have presented excellent cooling performances. Both systems have returned a water velocity well below the imposed limit (7 m/s); thus, solutions to enhance the cooling performances should be considered. In addition, the equal distribution of the BZ mass flow rate has demonstrated a strong imbalance concerning both outlet and tubes wall temperature exceeding the saturation temperature at the wall interface and providing an inhomogeneous water outlet temperature distribution. The FW system instead, due to its alternate and opposite flow, has an optimal water outlet distribution. It also exceeds the saturation temperature inside the water channels in limited regions, which results in located sub nucleate boiling. The analysis has demonstrated that the BZ and FW systems are related to each other, being a heat exchange between the PbLi and FW interface. This phenomenon entails in an over mass flow rate required from the FW system, compared to the power generated in it.

The V0.6 layout has been selected as a promising layout to further analyze and optimize in compliance with the EUROfusion R&D activities. The main points of interest highlighted are: optimization of the number of FW channels given the high-temperature margin; study of an alternative manifold to increase the BZ water velocity ensuring a more uniform temperature distribution and a lower wall temperature in order to avoid the possibility of thermal crisis; and investigation of the PbLi heat transfer modelling impact.

4.4. FW system optimization

The analyses are focused on the WCLL COB FW cooling system of the V0.6 elementary cell. A detailed three-dimensional model of the FW has been developed, analyzing three different FW cooling layout adaptable to the V0.6. In particular, the equatorial COB has the highest volumetric power deposition and a lower HF on the plasma-facing surface.

The main objective of this study is to optimize the channels layout by reducing the number of channels and, indeed, the amount of water in the first centimeters of the elementary cells, that affects in a negative way the TBR, because of neutrons thermalization and the consequent reduced interaction with the breeder, but ensuring adequate refrigeration of the Eurofer structures. Moreover, the analysis is aiming to increase water performance in order to obtain adequate thermodynamic conditions for the PHTS heat exchanger.

The analyses have been pursued through a preliminary optimization of the FW system modelled stand alone, and a parallel analysis on the elementary cell to evaluate the effect of the channels reduction. In addition, in this activity the imposed HF has been reduced from 0.5 MW/m^2 to 0.32 MW/m^2 as mentioned in Sect. 4.2 and Refs. [62][63]. The stand-alone modelling analysis has been carried out from a research activity fully described in Ref. [71], where different FW systems, not only concerning the COB equatorial system, have been analyzed.

4.4.1. Numerical models and mesh

Three stand-alone FW systems with different channels layout are evaluated for steady-state analyses, varying the number of the channels and their pitch. The first numerical model is based on the reference layout of the FW system, with 10 square channels arranged along the poloidal direction and a uniform pitch of 13.5 mm, previously analyzed with the entire cell but with a lower HF on the Tungsten armor. The second and third configurations foresee 6 and 4 channels, with a constant pitch of 22.5 mm and 33.75 mm respectively. In Fig. 4.12 the three different configurations of the COB equatorial cell are reported. The complete V0.6 elementary cell has been modelled only with the six and four channels systems.

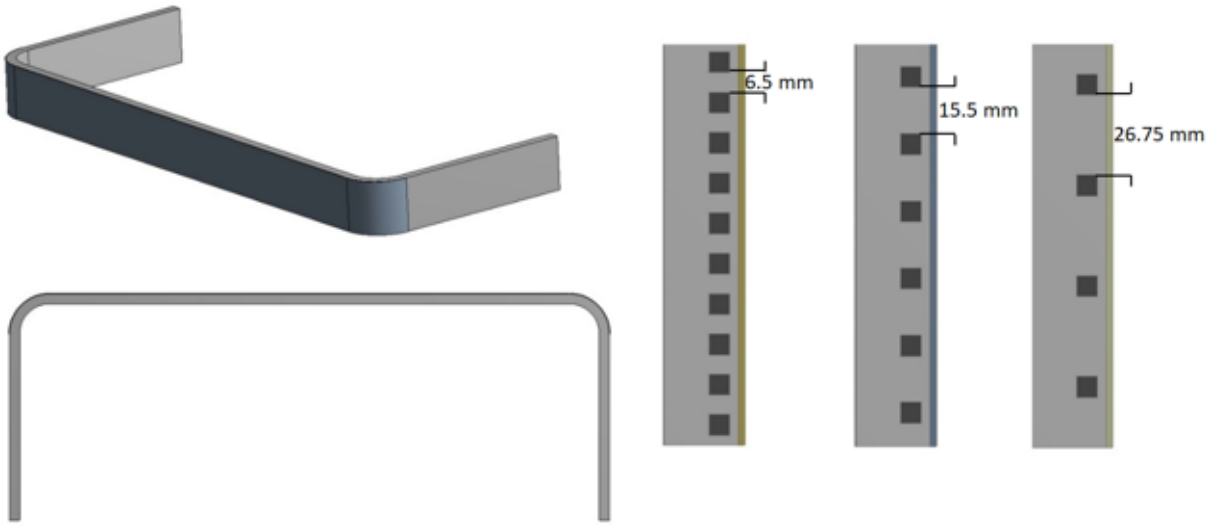

Fig. 4.12 – WCLL FW system COB equatorial model with different number of channels [71]

For the stand-alone calculations, a mesh independence study has been performed, using meshes with different degree of detail. The analysis was conducted to establish the independence of results from the grid and to optimize the number of elements of the model. The mesh independence analyses have been performed and proved in [71], where it is widely discussed. In Table 4.10 are summarized the main outcomes of the independence analyses with four different meshes, where, the "C" model has been adopted have reasonable computational costs. The mesh statistics of each numerical models have been reported in Table 4.11.

Mesh	**Elements**	**T_{out} Water [°C]**	**T_{max} Eurofer [°C]**	**T_{max} Tungsten [°C]**
A	0.71 M	326.50	389.78	396.09
B	1.56 M	327.42	392.91	397.86
C	3.87 M	327.48	393.89	398.90
D	6.21 M	327.48	393.96	398.92

Table 4.10 – WCLL stand-alone optimized FW system mesh independence analyses

Parameters	**Models**				
	FW 10	***FW 6***	***FW 4***	***V0.6_FW6***	***V0.6_FW4***
N° Elements	19.8 M	15.0 M	13.3 M	26.6 M	25.3 M
Ave Orth Qual	0.780	0.749	0.788	0.833	0.836
Ave Skewness	0.307	0.266	0.240	0.196	0.191

Table 4.11 – WCLL FW systems optimization analyses mesh statistics

4.4.2. Solver settings and boundary conditions

To evaluate the thermal-hydraulics performance of the FW cooling system, verifying the reliability to deliver the coolant at the design temperature of 328°C to the PHTS, and to optimize the number of the water channels not exceeding the imposed Eurofer temperature limit of 550°C, different models of the FW system have been set up, firstly stand-alone and secondly in the WCLL V0.6 layout, for the CFD analysis.

The 3D finite volume models have been reproduced according to Sect. 4.4.1, using ANSYS CFX v18.2 code, to realistically reproduce the geometry and flow features of WCLL FW cooling system and to obtain a complete and detailed temperature distribution both in the fluids (i.e. water coolant and PbLi) and the solid domains (i.e. FW, Tungsten layer and Stiffeners). For each configuration, thermal-hydraulic steady-state analyses to assess the coolant systems efficiency by removing the total power, as well as sensitivity analyses to reduce the number of water channels, and the PbLi-FW interaction, have been performed.

To reproduce the thermal behavior of the systems, materials thermophysical properties of water, Eurofer, PbLi and Tungsten have been implemented in the commercial code as reported in Sect. 4.1. In addition, thermal loads have been imposed into the models to reproduce the total deposited power. A maximum heat flux has been imposed on the Tungsten layer with a value switched to 0.32 MW/m2 accordingly with the most updated data (Refs. [62][63]). Volumetric power deposition curves, depending on the radial dimension and materials, have been imposed as reported in Sect. 4.2, based on Ref. [58].

The water mass flow rate has been evaluated with the enthalpy balance on the total deposited power, which varies according with the materials volume variation. In Table 4.12 the total deposited powers divided by run are reported. Concerning the first three runs with the stand-alone systems, the total water mass flow corresponds at the FW water, and it has been imposed at the inlet. Regarding the elementary cell models, have been divided by FW and BZ in percentage to guarantee 328°C at the outlets, as in the previous cases. The V0.6 FW system with 6 and 4 channels has 43.5% and 43% of the total water mass flow, respectively.

In the V0.6 models, the PbLi forced convection has been set, with an inlet mass flow rate of 0.16521 kg/s equally distributed on the six sub-channels and a temperature of 327°C. The reference pressure has been imposed at 100 kPa [59]. Even in these analyses the Mogahed thermal conductivity [65] has been adopted in the PbLi domain. As in the previous case no buoyancy forces have been considered.

The other boundary conditions adopted for all the models are:

- Periodic boundary conditions on the upper and lower surfaces of upper and lower stiffening plates, FW and Tungsten layer, in poloidal direction, to simulate the presence of adjacent elementary cell;
- Adiabatic condition to back walls of FW, stiffeners, Tungsten layer and FW side walls;
- Mass flow rate and static pressure imposed in the fluid domain at inlet and outlet sections, respectively;
- No-slip condition at the interface between coolant and the circuit steel walls.

The two-equations k-ω Shear Stress Transport (SST) model has been selected as an appropriate method to simulate the turbulence effects of water, and regarding the PbLi, the laminar model has been set to solve the Navier-Stokes equations in this domain, as explained in Sect.4.3.2. As regards the water Reynolds number, with the reduced number of channels the total mass flow rate increase and this leads to an increase in velocity of the fluid. For the stand-alone systems, it has been analytically evaluated that the Reynolds number passes from 85,000, of the 10 channels, to 217,000 of the 4's channels design. While, for the complete systems it has been calculated that the BZ is around 67,000 and the FW passes from 170,000 up to 250,000 of the optimized configuration.

A detailed set of the imposed boundary conditions are shown in Fig. 4.4 and the related numerical values are reported Table 4.13.

System	Region	Models					Unit
		FW 10	***FW 6***	***FW 4***	***V0.6_FW6***	***V0.6_FW4***	
BZ	*PbLi*				170.387	170.387	kW
	Tubes				3.214	3.214	kW
	Stiffeners				7.937	7.937	kW
	BZ Total				*181.538*	*181.538*	*kW*
FW	*FW*	31.156	33.486	34.656	33.486	34.656	kW
	Tungsten	6.694	6.694	6.694	6.694	6.694	kW
	Tung HF	56.160	56.160	56.160	56.160	56.160	kW
	Tung HF_{SW}	8.810	8.810	8.810	8.810	8.810	kW
	FW Total	*102.820*	*105.150*	*106.320*	*105.150*	*106.320*	*kW*
Total		***102.820***	***105.150***	***106.320***	***286.688***	***287.858***	***kW***

Table 4.12 – WCLL V0.6 FW optimization power distribution divided by models and domains

#	Parameters	Models					Unit
		FW10	***FW6***	***FW4***	***V0.6_FW6***	***V0.6_FW4***	
1	FW HF_{max}	0.32	0.32	0.32	0.32	0.32	MW/m^2
2	Water (BZ-FW) T_{inlet}	295.0	295.0	295.0	295.0	295.0	°C
3	Water (BZ-FW) P	15.5	15.5	15.5	15.5	15.5	MPa
4	FW Water MFR	0.5311	0.54315	0.54918	0.6440	0.63784	kg/s
5	BZ Water MFR	-	-	-	0.8366	0.84896	kg/s
6	Total MFR	0.5311	0.54315	0.54918	1.4806	1.4868	kg/s
7	PbLi T_{inlet}	-	-	-	327.0	327.0	°C
8	PbLi MFR	-	-	-	0.16521	0.16521	kg/s

Table 4.13 – WCLL V0.6 FW optimization analyses boundary conditions

4.4.3. Results

The results of the five performed simulations are discussed below. They differ in terms of FW number of channels and imposed boundary conditions. The first three runs have been performed with a stand-alone system in steady-state conditions to optimize the channels layout. The last two has been performed with the optimized FW system integrated into the V0.6 cell, to evaluate the impact of this reduction on the PbLi and Stiffeners temperature fields and the passive heat removal from the FW to the BZ.

The relevant parameters of the runs are reported in Table 4.14 and Table 4.15, where the configuration of each model satisfied the Eurofer temperature requirement and adequate water condition for the PHTS. The obtained results are hereafter discussed, divided by models and type of run.

#	**Parameters**	**Models**			**Unit**
		FW 10	***FW 6***	***FW 4***	
1	Tungsten T_{max}	398.7	418.2	468.0	°C
2	FW T_{max}	393.6	413.7	463.9	°C
3	FW Water $T_{ave\ out}$	327.7	327.8	327.8	°C
4	FW Water T_{max}	357.9	360.7	364.8	°C
5	FW Water $v_{ave\ out}$	1.651	2.815	4.269	m/s
6	FW Water v_{max}	2.006	3.362	5.05	m/s
7	FW Water Press drop	5.850	15.097	31.898	kPa
8	FW Fr Number	48.50	140.70	323.60	-
9	FW CHF	2.250	2.660	3.150	MW/m^2
10	FW q''_{max}	0.596	0.793	1.100	MW/m^2

Table 4.14 – WCLL V0.6 FW optimization analyses: stand-alone main output parameters

#	Parameters	Models		Unit
		V06_FW6	***V06_FW4***	
1	Tungsten T_{max}	422.5	485.3	°C
2	FW T_{max}	467.4	502.9	°C
3	Stiffeners T_{max}	513.0	531.4	°C
4	PbLi T_{max}	541.0	558.5	°C
5	FW Water $T_{ave\ out}$	328.2	328.1	°C
6	FW Water T_{max}	358.2	357.5	°C
7	BZ Water $T_{ave\ out}$	327.6	327.8	°C
8	BZ 1st array T_{max}	371.8	373.8	°C
9	BZ 2nd arrayL T_{max}	358.2	357.5	°C
10	BZ 2nd arrayC T_{max}	363.5	362.9	°C
11	BZ Water 3rd array T_{max}	351.7	350.9	°C
12	FW Water $v_{ave\ out}$	3.343	4.964	m/s
13	FW Water v_{max}	3.987	5.873	m/s
14	BZ Water $v_{ave\ out}$	1.165	1.191	m/s
15	BZ Water v_{max}	1.444	1.471	m/s
16	FW Water P drop	20.462	41.788	kPa
17	BZ Water P drop	1.573	1.636	kPa
18	FW Fr Number	197.79	436.56	-
19	BZ Fr Number	20.64	21.26	-
20	FW CHF	2.880	3.430	MW/m^2
21	BZ 1st array CHF	2.290	2.300	MW/m^2
22	BZ 2nd arrayL CHF	2.380	2.390	MW/m^2
23	BZ 2nd arrayC CHF	2.400	2.400	MW/m^2
24	BZ 3rd array CHF	2.550	2.560	MW/m^2
25	FW q''_{max}	0.870	1.056	MW/m^2
26	BZ 1st array q''_{max}	0.655	0.703	MW/m^2
27	BZ 2nd arrayL q''_{max}	0.496	0.502	MW/m^2
28	BZ 2nd arrayC q''_{max}	0.405	0.409	MW/m^2
29	BZ 3rd array q''_{max}	0.493	0.494	MW/m^2

Table 4.15 – WCLL V0.6 FW optimization analyses: complete system main output parameters

4.4.3.1. Stand-alone FW optimization

The first part of this activity regards the COB equatorial FW system stand-alone; three configurations have been investigated: FW10, FW6 and FW4, with 10, 6 and 4 channels, respectively. Considering all the runs, as expected, the water outlet temperatures, obtained from the CFD-Post as the temperature averaged on the mass flow rate and the overall outlet tube sections, are very similar: 327.7°C, 327.8°C and 327.8°C, respectively.

The pressure drops increases as the number of channels present in the FW decreases, going from 5.85 kPa of run FW10 to 15.097 kPa of FW6 and up to 31.898 kPa of the FW4. This marked variation is also because the average outlet water velocity increases from 1.651 m/s, 2.815 m/s and 4.269 m/s, respectively. This increase in pressure drops can be considered negligible, compared with the pressure drops of the entire FW circuit, as demonstrated in [72].

Analyzing the maximum water temperature, it exceeds the saturation temperature (344.8°C at 15.5 MPa), which should result in a local boiling but, in the CFX numerical model, the phase change is not considered. The possibility of thermal crisis occurrence has been then evaluated. For horizontal tubes and high flow rates, according to Ref. [73], the Critical Heat Flux (CHF) can be predicted using the correlation $q''_{CHF,Hor} = k * q''_{CHF,Ver}$. The parameter k varies with the Froude number $Fr = {G^2}/{(\rho_L^2 g D)}$, where G is the total mass flux (kg/m^2 s), ρ_L is the density of the saturated liquid at 15.5 MPa (kg/m^3), g is the gravity acceleration (m/s^2) and D corresponds to the diameter of the tube (m); $q''_{CHF,Ver}$ is the correlation for the vertical channels subjected to the same heat flux. The value of "k" is calculated in term of Fr number as $k = 0.725 * Fr^{0.082} \leq 1$. Thus, if k is greater than 1, k=1 is adopted and also k=1 at Fr number greater than 50. Regarding the three cases, Fr = 48.5, 140.7 and 323.6 are obtained, thus is imposed k=0.996 for the first case, and k=1 for the remaining two cases. The Tong's correlation [74] has been adopted to evaluate the $q''_{CHF,Ver}$, obtaining $q''_{CHF,Hor}$ = 2.25 MW/m^2, 2.66 MW/m^2 and 3.15 MW/m^2 for 10, 6 and 4 channels layout. The portion of the FW channels affected by the highest HF is the front-toroidal part of the channels, in which the maximum HFs are 0.596 MW/m^2, 0.793 MW/m^2 and 1.10 MW/m^2, respectively. Therefore, no thermal crisis within the FW channels occurs, but it is likely that limited areas of the channel wall can exist where subcooled nucleate boiling is the dominant heat transfer regime.

Regarding the solid materials, all the three runs return a symmetrical temperature field both in toroidal and poloidal direction, due to the opposite and alternate flow and the poloidal periodicity. The three configurations result widely below the required limits of 1300°C for the Tungsten and a largely below of 550°C for the FW Eurofer chase. Reducing the number of channels, the maximum temperature in the Eurofer increases from the value of the reference layout (393.6°C) by 20.1 degrees for 6 channels and 70.3 degrees for 4 channels. The configuration with 4 channels returns a maximum temperature of 463.9°C that is around 86 degrees below the imposed limit. Regarding the Tungsten domain, with the reduction of the channel number, it follows the same temperature trend as the Eurofer, increasing by 19.5 degrees from FW10 (398.7°C) to FW6 and 69.3 degrees from FW10 to FW4. The case FW4 returns a maximum temperature of 468.0°C, widely below the limit. In Fig. 4.13, Fig. 4.14 and Fig. 4.15 the characteristic temperature fields of the FW Eurofer structures with 10, 6 and 4 channels, respectively, and the radial-poloidal cuts at the middle of the FW toroidal length are presented. From the figures, it is clear how the temperature contour of the reference FW system is the lowest compared with the other two systems. From the radial-poloidal cuts, it is noted that the influence of the backside of the 10 FW channels is extremely reduced after around 13 mm from the facing plasma surface, where the front side of the channels acts as a thermal sink. This phenomenon is reduced in the 6 channels layout but still present, and the 4 channels layout returns a higher temperature field in the back part, which can reduce the BZ passive cooling. The results summarized in Table 4.14 show that the configuration with 4 water channels returns Eurofer and Tungsten structures not exceeding the temperature limits, enhanced water performances ensuring outlet water conditions suitable for the PHTS and a reduction of the amount of water in the first centimeters of the elementary cell, that positively influences the TBR.

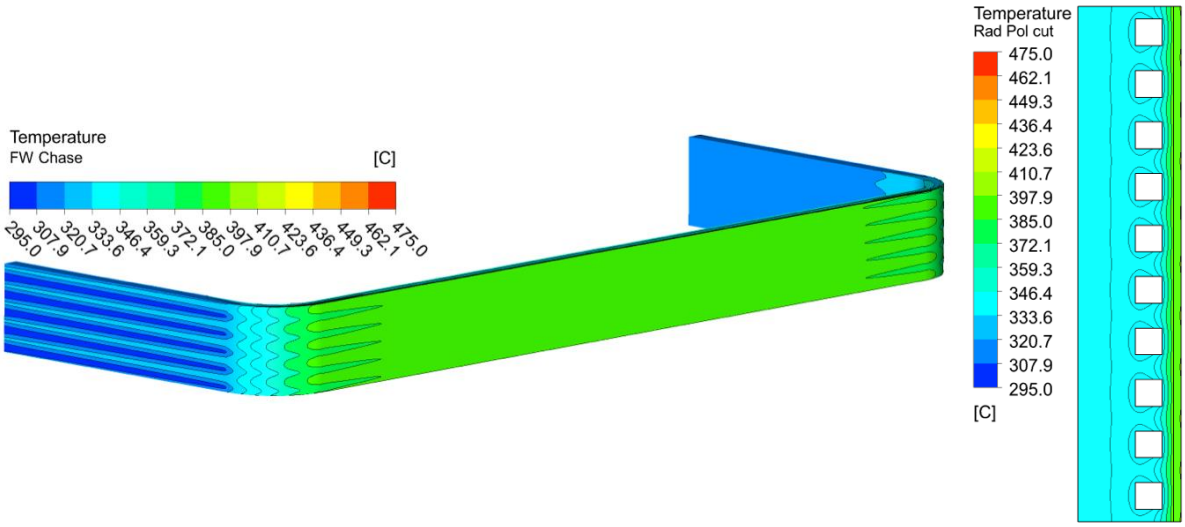

a) FW domain

b) Radial-poloidal plane

Fig. 4.13 – WCLL FW 10 stand-alone system: temperature contours

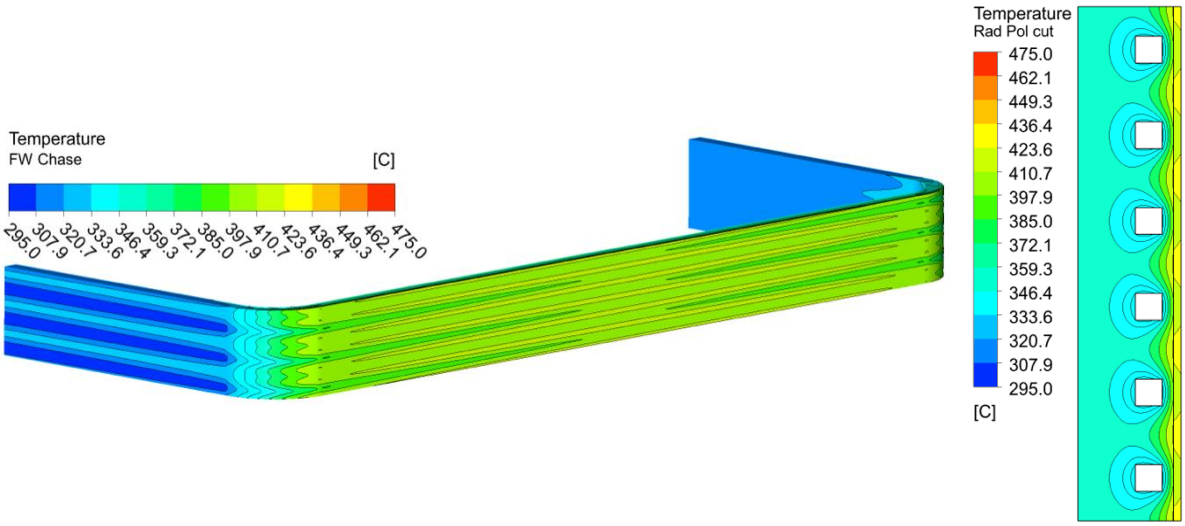

a) FW domain

b) Radial-poloidal plane

Fig. 4.14 – WCLL FW 6 stand-alone system: temperature contours

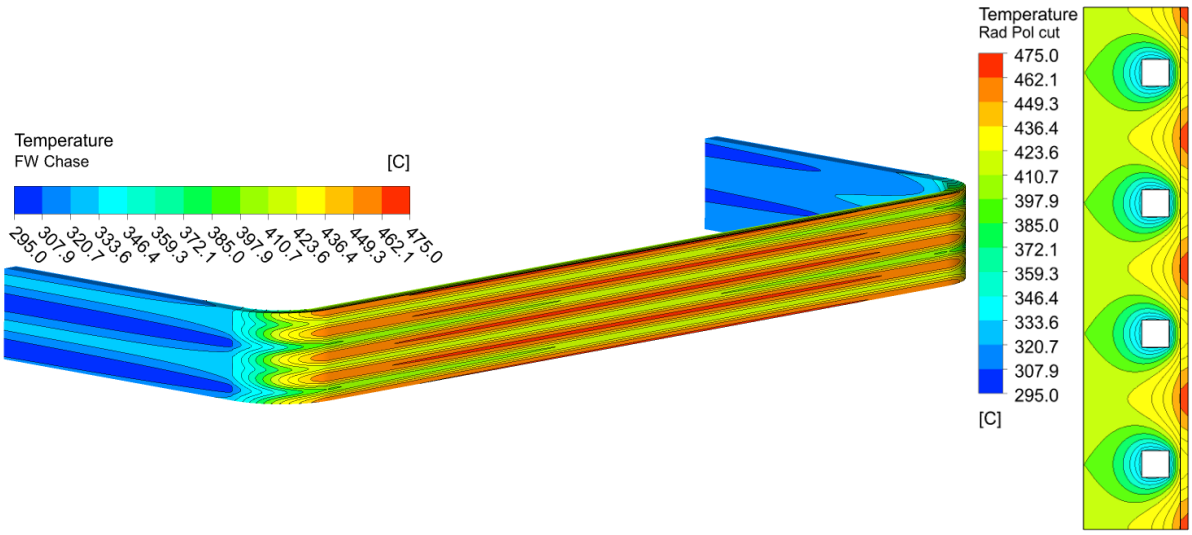

a) FW domain b) Radial-poloidal plane

Fig. 4.15 – WCLL FW 4 stand-alone system: temperature contours

4.4.3.2. V0.6 layout FW optimization

As regards the second part of the activity, with the entire V0.6 and optimized FW system modelled, two configurations with 6 and 4 FW channels have been investigated. Considering both runs, as a consequence of the imposed boundary conditions, the water outlet temperatures averaged on the mass flow rate, and the overall outlet tube sections have been returned close to 328°C. The BZ water coolant has reached 327.6°C and 327.8°C, where, the FW coolant reached 328.2°C, 328.1°C, respectively in V0.6_FW6 and V0.6_FW4. Due to the different Eurofer percentage in the models, the required mass flow is higher in the V0.6_FW4 layout, resulting in different pressure drops in both systems. Concerning the FW, it increases as the number of channels present in the FW decreases, going from 20.462 kPa of run V0.6_FW6 up to 41.788 kPa of the V0.6_FW4. This variation is 2.03 times higher and not 2.11, as discussed in Sect. 4.4.3.1, where, unlike the previous case, the water needed in the FW4 case is greater than in the FW6 case, as opposed to this where the percentage has been decreased from 43.5% of the V0.6_FW6 to 43% of the V0.6_FW4. The average outlet water velocity also undergoes the same increase, less than stand-alone analysis, but still increased by 1.48, reaching 4.964 m/s in the V0.6_FW4.

The BZ cooling system is also affected by the channels decrease, given that the increase in the total mass flow of water has been allocated to the BZ system. Although not a considerable

increase in the thermal-hydraulic performances, the average water outlet velocity switched from 1.165 to 1.195 m/s, with a consequent pressure drops increasing from 1.573 to 1.636 kPa. Even in this case, the increase of the pressure drops is negligible, as mentioned in the section above, having an order of magnitude of 10 kPa.

As reported in Table 4.14, the maximum water temperature exceeds the saturation temperature in both cases and in both systems. The channels reduction has caused a maximum temperature variation of tenths of a degree, both in BZ and in FW. The maximum channels temperature decreases from V0.6_FW6 to V0.6_FW4, instead of the BZ, which has a mixed variation, where, the maximum temperature increases in the 1st tube array, being the most influenced by the near FW system, and the other three decrease their maximum temperature. Similarly to the previous paragraph, the CHF has been evaluated with the same correlation used in the stand-alone systems in terms of Fr number, k and $q''_{CHF,Ver}$. As regards the V0.6_FW6 configuration, the maximum FW heat flux is 3.31 times lower than the CHF, and the tube arrays have margins of 3.5, 4.8, 5.93 and 5.17 times from the first to the third array, where 4.8 and 5.93 regard the 100mm and 200mm curvature radius tubes respectively. The optimized configuration has a higher FW critical heat flux due to the higher water velocity (3.43 MW/m^2), but a lower margin of 3.25 from the maximum obtained q''. The BZ first and second arrays highlight a margin reduction, resulting 3.27, 4.76 and 5.86; except for the third array, which results in 5.18.

Concerning the solid structures, with the reduced number of channels, the temperature increases in all the solid domains. It should be noted that the FW maximum temperature is considerably higher, compared with the stand-alone system; this is caused by the interaction with the PbLi. As shown in Fig. 4.16, in the internal part, in the mid toroidal length at the PbLi interface, the temperature of the 4 channels layout rises up to 514°C zone, reaching its maximum at 502.9°C. The FW chase, although its temperature increases, remains within the limit of 550°C. Comparing the two systems, it seems that the first array has a lower influence on the four channels layout, resulting in lower passive heat removal from the FW to the PbLi, as shown in Fig. 4.17, where the central region has been segmented in different heat transfer zone, and the lateral areas have a lower value. The averaged value of the passive heat removal has been reduced from 87.224 kW/m^2 of the 6 channels layout to 69.707 kW/m^2 of the optimized configuration, thus increasing the independence between the two systems.

In Fig. 4.18 the Eurofer upper plates are shown; both temperature distributions are very similar, except for the hot spot onset in the front part at the mid toroidal length of the V0.6_FW4 cell, as a consequence of the passive cooling reduction. The optimized cell still has a margin of about 20 degrees in the Eurofer plates and around 47 degrees in the FW chase.

It has deemed appropriate investigating the PbLi temperature field in correspondence of the plates hotter zone, with a radial-poloidal cut (Fig. 4.19 a). As evaluated previously (Sect. 4.3), the PbLi, despite being in forced circulation, in that area has a very low velocity (averaged on that area 0.06 mm/s), and this results in a behavior similar to a solid PbLi causing a hot spot column which impacts the upper and lower stiffeners. In particular, as shown in Fig. 4.19 a and b, the V0.6_FW6 has a small region with PbLi temperature within 550°C located below the half poloidal height; instead of the V0.6_FW4, that has a larger hot spot region around 550°C almost in touch with the plates and an area which exceeds 550°C oriented towards the lower plate. These regions may cause the hot spots onset into the Eurofer structures. Regarding the PbLi domain, as expected, even if the total deposited power decrease as reported in Table 4.12, the maximum temperature raises from 530.8°C of the V0.6 with 10 channels layout (Table 4.9) to 558.5°C of the configuration V0.6_FW4.

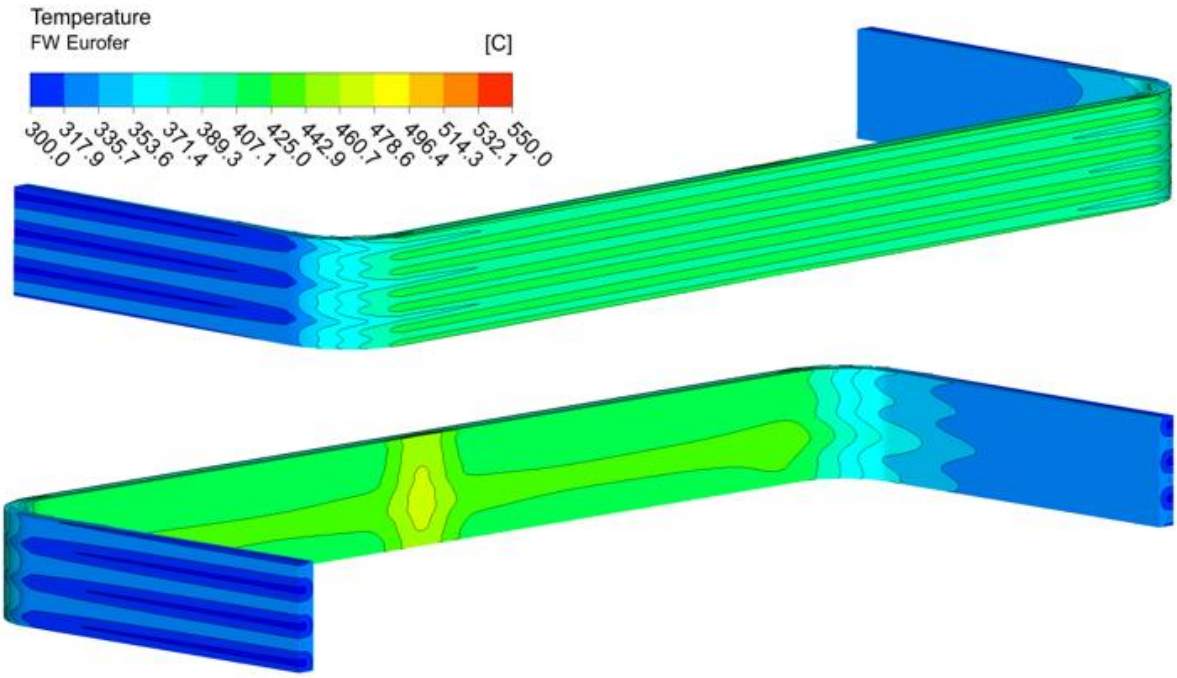

a) V0.6_FW6 model

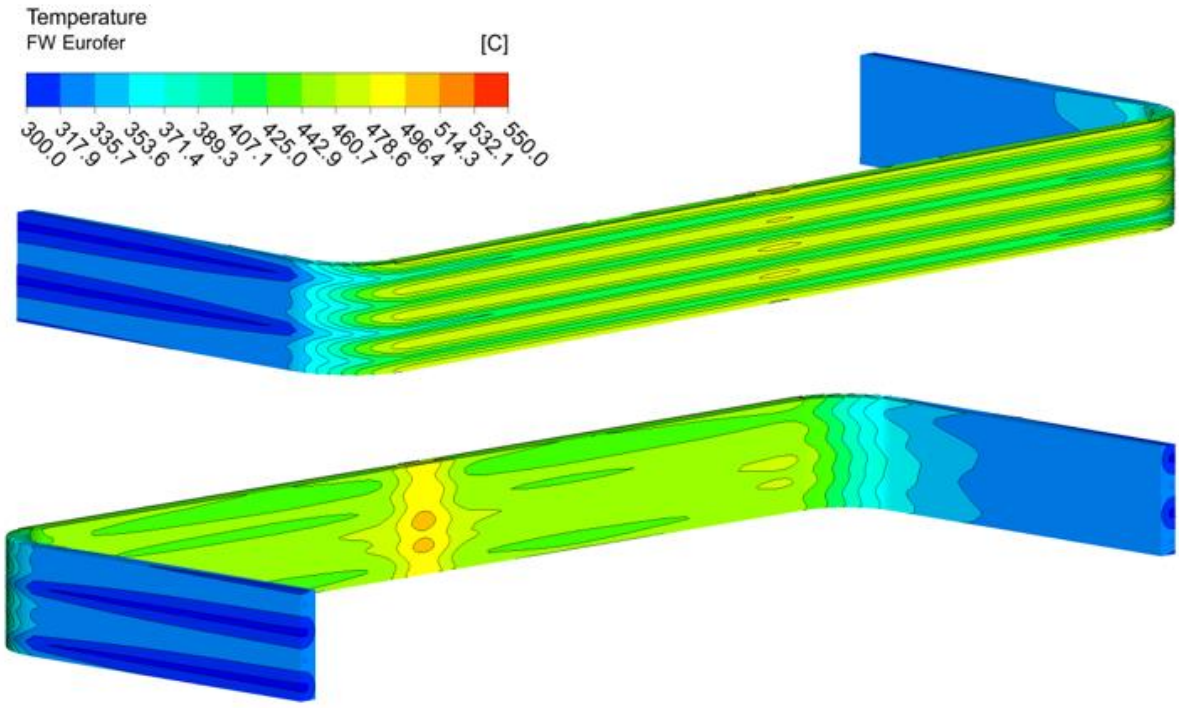

b) V0.6_FW4 model

Fig. 4.16 – WCLL V0.6 FW optimization: FW systems temperature distributions

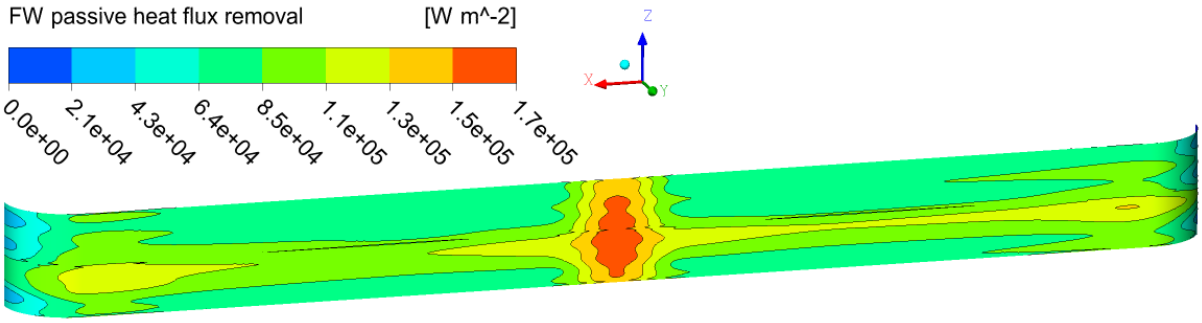

a) V0.6_FW6 model

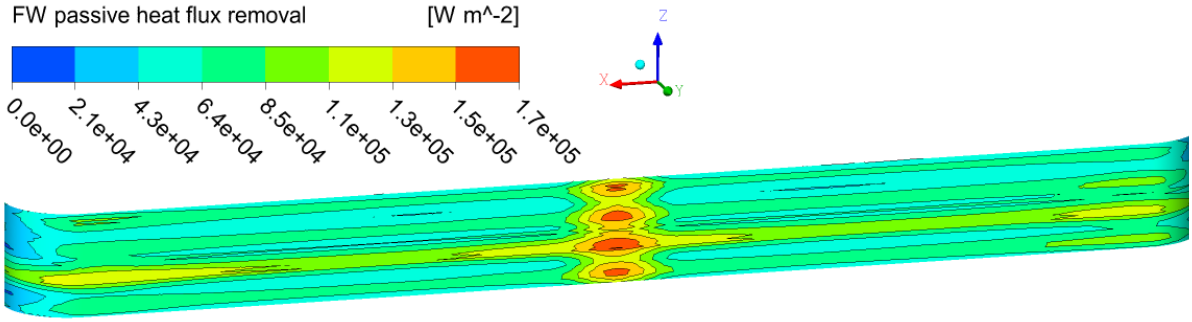

b) V0.6_FW4 model

Fig. 4.17 – WCLL V0.6 FW optimization: BZ-FW interface passive heat flux removal

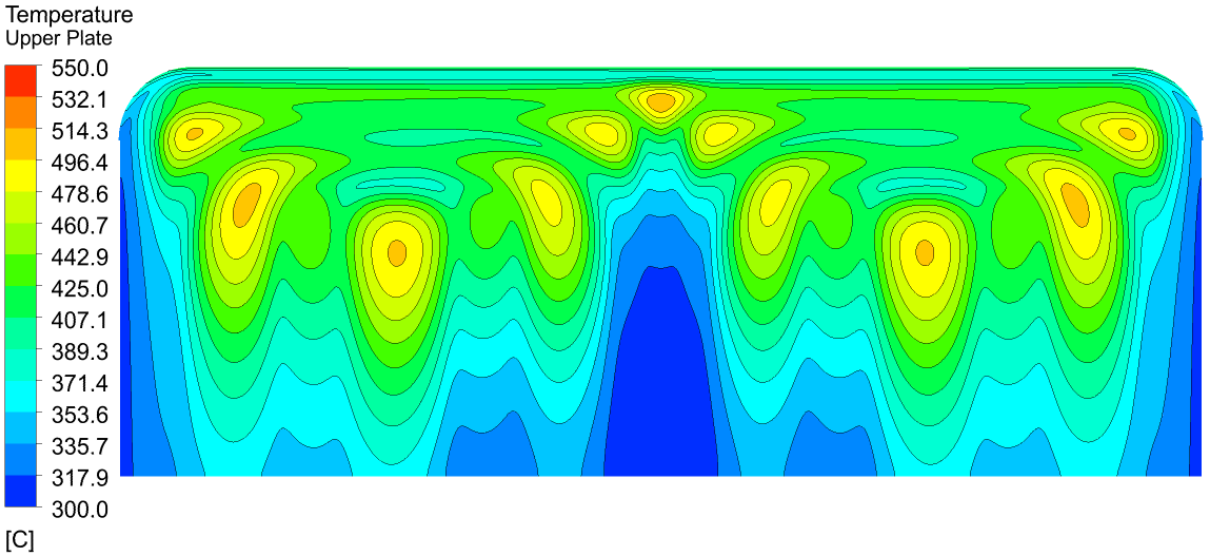

a) V0.6_FW6 upper plate

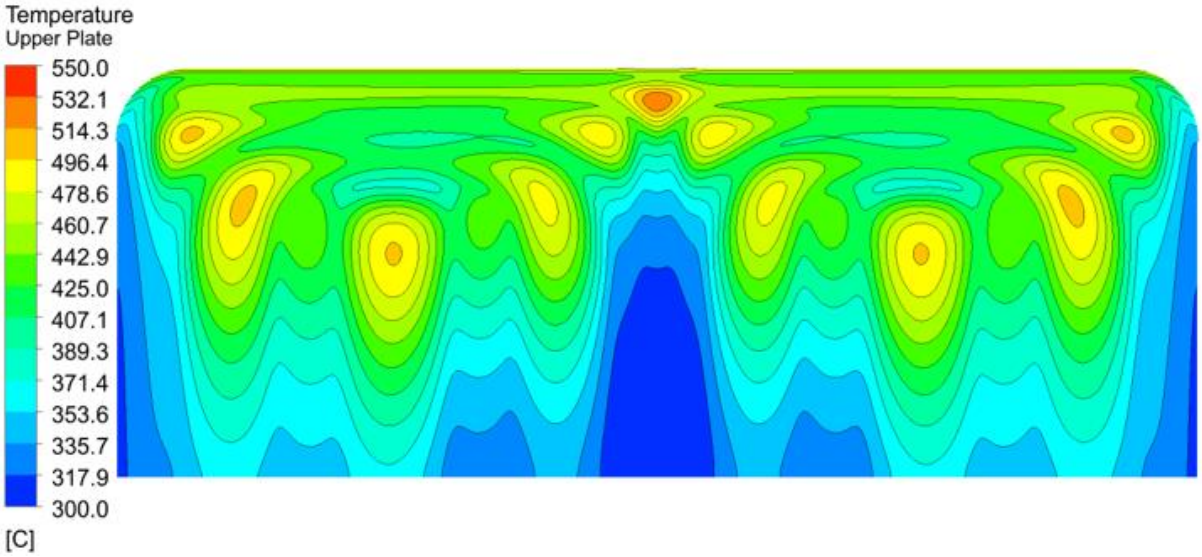

b) V0.6_FW4 upper plate

Fig. 4.18 – WCLL V0.6 FW optimization upper plate temperature distribution

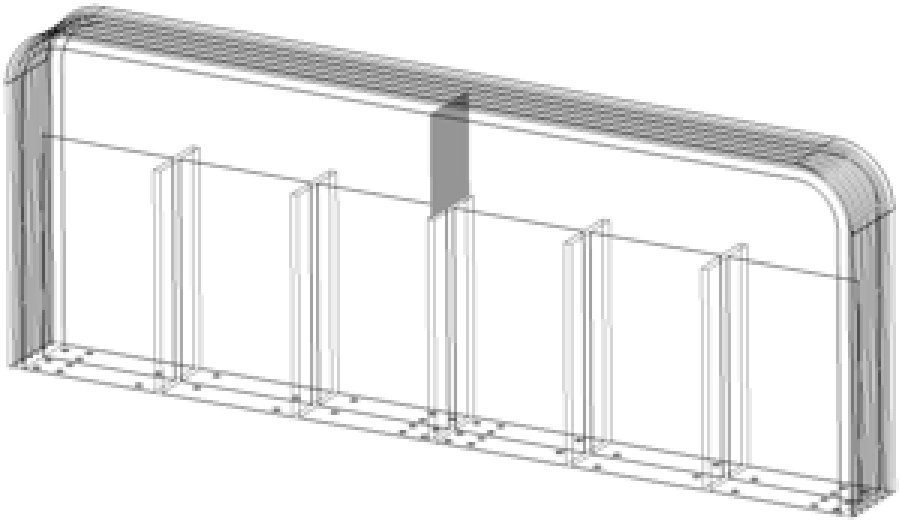

a) PbLi radial poloidal plane

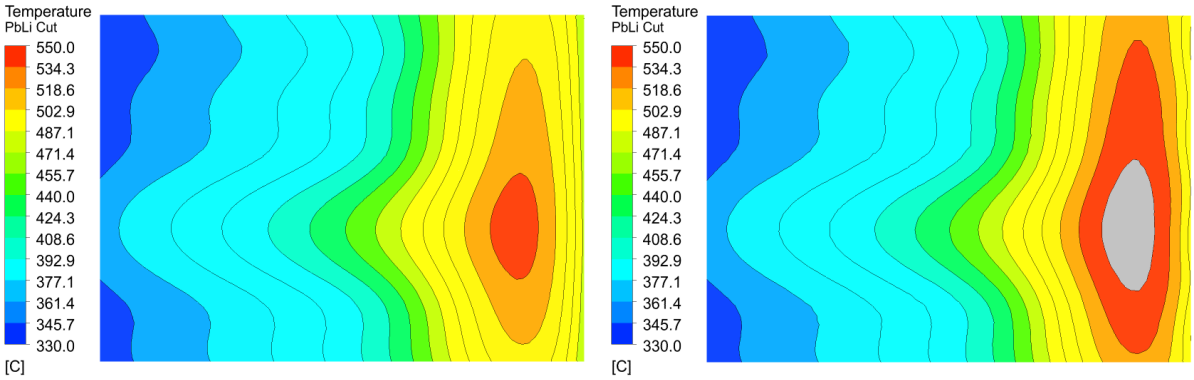

b) V0.6_FW6 PbLi rad-pol temperature c) V0.6_FW4 PbLi rad-pol temperature

Fig. 4.19 – WCLL V0.6 FW optimization PbLi radial-poloidal temperature distribution

4.4.4. Summary

The cooling performances of the WCLL central outboard FW have been investigated using a CFD approach. The analyses, based on the WCLL 2018 design, focused on three different channels layout: ten, six and four channels. The COB equatorial elementary cell, which is subjected to the maximum outboard volumetric deposited power and low heat flux has been optimized. A computational thermal and fluid-dynamic models of these five models have been developed using the commercial CFD code ANSYS CFX v18.2. The heat loads adopted for the analyses are based on the most updated data, to return the thermal field for the most recent design.

The study, aimed to optimize the number of FW channels, has demonstrated that with a different layout, firstly the stand-alone system, and after the whole cell, can withstand the imposed heat loads and meet the DEMO design requirements.

For the stand-alone equatorial system, the configuration that features only 4 FW channels is able to keep the structural materials well below their temperature limits and decrease the volume of water in the first centimeters of the cell, a fundamental parameter for a good yield of the TBR. Large and safety margins are present to avoid the arising of thermal crisis, even if subcooled nucleate boiling is expected to happen in limited regions of the cooling system. Furthermore, configuration with 4 channels increases the thermo-hydraulic performance, enhancing the average velocity of the water circuit.

Concerning the entire models, both configurations met the Eurofer temperature requirement. The channels reduction causes a slight temperature increases into the Eurofer structures but within the limit. Except for the hot spot located in the middle of the toroidal length in the frontal part of the cell, the PbLi has not undergone any significant variation in the temperature field. In addition to the TBR increase, the 4 channels layout has significantly reduced the BZ passive cooling of the 20.1%, reducing the amount of water mass flow necessary to guarantee 328°C, as required by the PHTS, value however overestimated compared to the actual deposited power into the FW system. The BZ cooling system has not undergone any significant variation of the thermal-hydraulic performances, returning comparable values in both cases with the previously analyzed model.

Both cooling systems have large and safety margins to avoid the possibility of thermal crisis, even if subcooled nucleate boiling is expected in limited regions. Furthermore, with the BZ passive cooling reduction, the tubes arrays have an increased maximum temperature which is caused by the equally mass flow rate division inside the tubes. An alternative BZ manifold should be considered to enhance the thermal-hydraulic performances, having drastically reduced the dependence of this system from the FW.

The V0.6_FW4 layout has been selected as a remarkable improvement of the FW layout, as it is able to guarantee an excellent TBR yield, considerably increase of the thermal-hydraulic performances of the FW cooling system guaranteeing a Eurofer temperature within the limit.

4.5. BZ recirculation manifold

To further optimize the BZ temperature field and to enhance the thermal-hydraulic features of its cooling system, and to affirm the V0.6 BZ layout with 4 FW channels as reference configuration, an alternative BZ manifold has been investigated. The heat transfer inside BZ is strongly dependent upon the coolant flow path and, also, on DWTs distribution as demonstrated by several analyses reported in Refs. [54][55][57][75][76]. The proposed alternative layout has been conceived on the main outcomes of Ref. [77], where the manifold layout has been defined. The analysis has been focused on the BZ coolant flow path, assuming a water double-pass flow inside the BZ. The first inlet water manifold is located at the central region and includes the DWTs of the first and second arrays, the water enters into the tubes and exits near the sidewalls, where a recirculation area has been provided to makes the recirculation occur before re-entering. For the second pass in the third tube array, the water flows in the opposite direction, from the side walls to the central region being collected in the outlet water manifold. The manifold rationale is shown in Fig. 4.20.

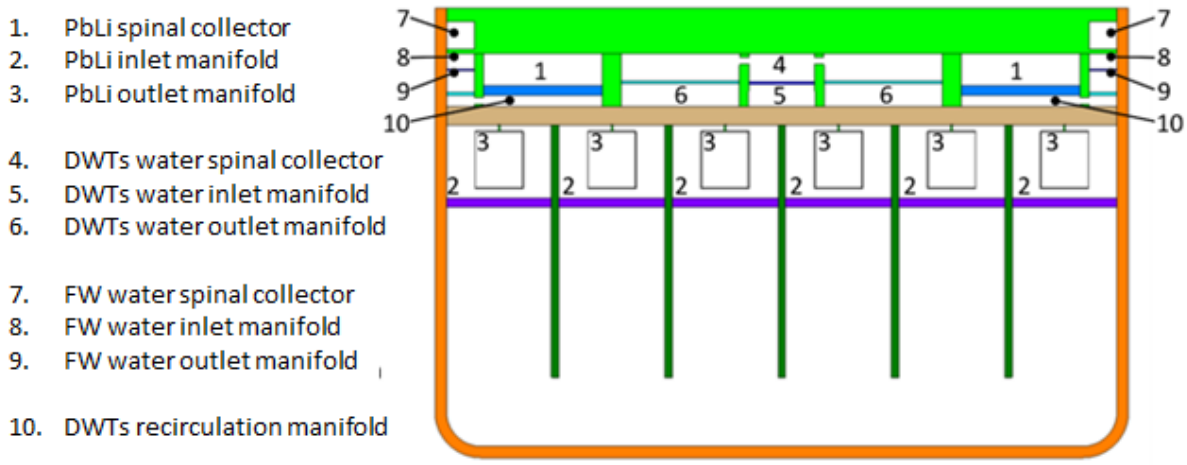

Fig. 4.20 – WCLL COB equatorial elementary cell manifold rationale [77]

4.5.1. Numerical model and mesh

To investigate the effect of the alternative BZ manifold on the elementary cell temperature field and the related flow features of PbLi and coolant systems, a three-dimension finite volume model has been developed for a CFD steady-state analysis, using ANSYS CFX v18.2 code.

The model has been developed according with the main outcomes of Sects. 4.3 and 4.4. As in the previous cases, the configuration consists of the FW, an external Eurofer structure coated by a Tungsten layer that faces the plasma and water-cooled by 4 square channels with opposite and alternate flow direction, and the BZ, an internal box filled with liquid PbLi actively cooled by 22 C-shaped DWTs. Regarding the BZ, presents internal Eurofer structures, which have been represented with horizontal plates, vertical ribs and a baffle plate. Even in this case, the modeled poloidal height is clipped to 135 mm and the radial dimension reduced to 567 mm. In this analysis, fluid domains for PbLi, BZ and FW water, and solid domains for Eurofer structures, FW Eurofer chase and Tungsten armor have been modelled. The developed model is shown in Fig. 4.21. Concerning this analysis, the model has been named as V0.6_FW4_R, to avoid confusion with the previous model.

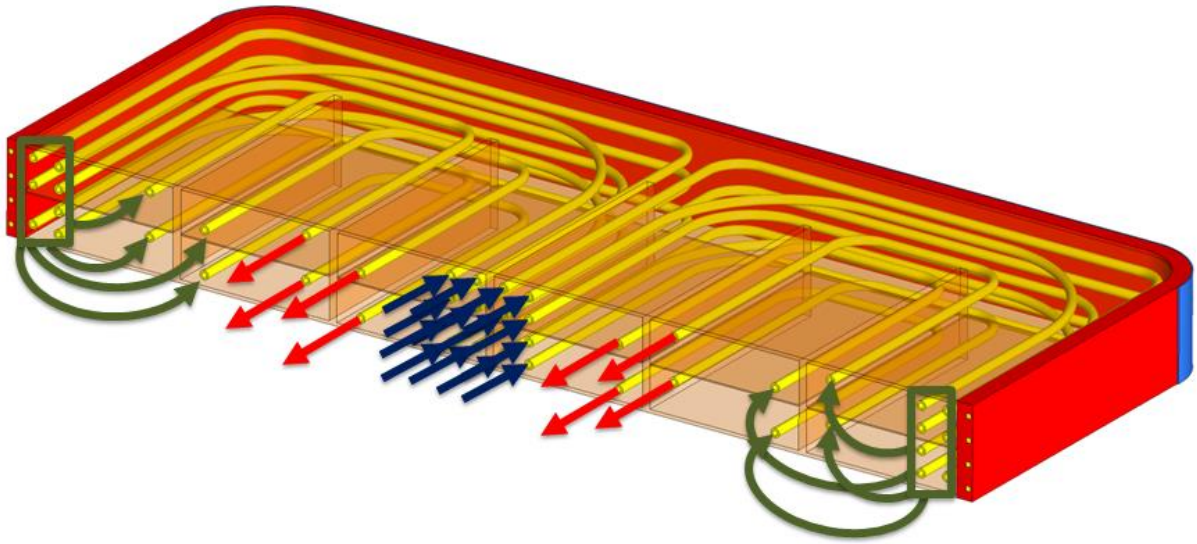

Fig. 4.21 – WCLL V0.6_FW4_R model and BZ recirculation system

To perform the analysis, an appropriate mesh has been defined, allowing accurate results and reasonable calculation time, in accordance with the mesh independence study performed and proved in Ref. [47]. Nevertheless, the model has been better defined with several bodies of FW and PbLi domains, to find the best geometry discretization optimizing the number of the elements. The numerical model has been developed as a single part, to simulate the heat transfer between the multiple components, solids and fluids, using a conformal mesh. The model has been meshed using tetrahedral and hexahedral elements, considering the geometrical features of the domains. In addition, many and different local controls have been inserted to define the

complex geometry of the cell properly. For the resolution of the viscous sub-layer (y^+=1) of the water, the inflation layer has been set, based on a maximum water velocity of 7 m/s.
In Fig. 4.22 are shown the FW and PbLi domain divided into several bodies, highlighted with different colors, and a mesh detail of the upper corner of the model. The mesh statistics of the numerical model are reported in Table 4.16.

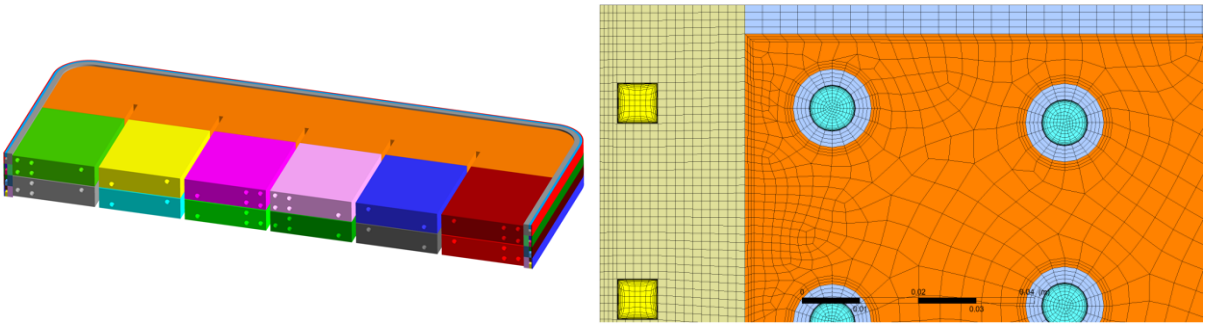

a) Domains body divisions b) New mesh detail

Fig. 4.22 – WCLL V0.6_FW4_R model details: fluids and solids new domain division; new mesh detail

Parameters	**Value**
N° Nodes	13.7 M
N° Elements	19.8 M
Ave Orth Qual	0.842
Ave Skewness	0.180

Table 4.16 – WCLL V0.6_FW4_R mesh statistic

4.5.2. Solver settings and boundary conditions

To evaluate the thermal-hydraulics performance of the BZ cooling system, verifying the reliability to deliver the coolant at the design temperature of 328°C to the PHTS, and to homogenize the outlet water temperature reducing the maximum water temperature into the tubes, not exceeding the imposed Eurofer temperature limit of 550°C, different boundary conditions have been set up for the CFD analysis to simulate the alternative manifold.

The numerical model has been conceived according to Sect. 4.5.1, by means of the ANSYS CFX v18.2 code. To obtain a complete and detailed temperature distribution both in fluids and solid domains, a thermal-hydraulic steady-state analysis assessing the system efficiency by

removing the total power and investigating the impact of the alternative manifold on the BZ water maximum temperature and PbLi-FW interaction, has been performed.
To realistically reproduce the solids and fluids behavior, the materials thermophysical properties of water, Eurofer, PbLi and Tungsten have been implemented in the commercial code as reported in Sect. 4.1. Concerning the PbLi, Mogahed's thermal conductivity [65] has been adopted.

Since the present configuration (V0.6_FW4_R) is the same as analyzed in Section 4.4 (V0.6_FW4), the total deposited power is unvaried. Thus, the total water mass flow rate has been previously calculated with the enthalpy balance as 1.4868 kg/s, respectively divided into 42.5% for the FW and 57.5% for the BZ. The FW system still has an equal mass flow division into the channels with a temperature of 295°C, the BZ, instead, has a new boundary condition. In the present analysis, the total amount of the BZ water mass flow rate has been firstly equally divided by fourteen tubes of the 1st and 2nd array inlets, secondly has been equally divided by eight tubes of the 3rd array, which are now located near the side walls. The water enters for the first passage in the 1st and 2nd array with an inlet temperature of 295°C, then re-enters into the eight tubes for the second passage with an imposed inlet temperature averaged on the 1st and 2nd array outlets temperatures. This boundary condition simulates a perfect mixing into the recirculation manifold. The water cooling systems have a reference pressure imposed at 15.5 MPa.

Regarding the PbLi, no changes have been done from the previous versions: mass flow of 0.16521kg/s, inlet temperature of 327°C, reference pressure of 100 kPa [59] and no buoyancy forces considered.

The heat loads adopted for the analysis are based on the most updated data, as described in Sect. 4.2, with an imposed maximum HF onto the straight Tungsten surface of 0.32 MW/m^2, to obtain an updated thermal field.

As in the previous cases, a periodic and adiabatic surface has been set and also no-slip condition at the fluid-solid interfaces has been imposed. The two-equations k-ω Shear Stress Transport (SST) model has been selected as an appropriate method to simulate the turbulence effects of water due to the high Reynolds number in both systems (i.e. Re_{FW}~250,000–275,000 ;

Re_{BZ}~110,000–210,000). The laminar model has been chosen for the PbLi (Re~40), to solve the Navier-Stokes equations in this domain, as widely discussed in Sect. 4.3.

A complete set of the imposed boundary conditions is reported below in Table 4.17.

#	**Parameters**	**Value**	**Unit**
1	FW HF_{max}	0.32	MW/m^2
2	Water (BZ-FW) T_{inlet}	295.0	°C
3	Water (BZ-FW) Pressure	15.5	MPa
4	FW MFR	0.63189	kg/s
5	BZ MFR	0.85491	kg/s
6	Total MFR	1.4868	kg/s
7	PbLi T_{inlet}	327.0	°C
8	PbLi MFR	0.16521	kg/s

Table 4.17 – WCLL V0.6_FW4_R BZ recirculation manifold boundary conditions

4.5.3. Results

The results of the performed analysis are discussed below. The model differs from the previous ones in the imposed BZ water boundary conditions. The run has been performed with an alternative manifold, simulating a perfect mixing in the recirculation manifold, to evaluate the impact of this feature on the water thermal-hydraulic performances and on the elementary cell thermal field.

As shown in Table 4.18, the FW structures seem not affected from the alternative manifold, even though, the FW water maximum temperature has enhanced by around 5 degrees, attributable to the 0.5% reduction of the mass flow rate. The BZ system, instead, clearly shown different variations: a slight temperature decrease has been noted in the Stiffeners and PbLi domains, by around 5 degrees; and a marked variation into the water tubes resulting in an average decrease of 20 degrees for the 1st and 2nd arrays, and 10 degrees for the 3rd ones. The adopted recirculation manifold of the BZ cooling system guarantees a maximum water temperature below the saturation temperature, exceeding it only into the first tubes array.

#	Parameters	Value	Unit
1	Tungsten T_{max}	486.4	°C
2	FW T_{max}	501.7	°C
3	Stiffeners T_{max}	526.6	°C
4	PbLi T_{max}	552.9	°C
5	FW Water T_{max}	362.4	°C
6	BZ Water 1st array T_{max}	353.5	°C
7	BZ Water 2nd arrayL T_{max}	338.6	°C
8	BZ Water 2nd arrayC T_{max}	343.6	°C
9	BZ Water 3rd array T_{max}	341.1	°C

Table 4.18 – WCLL V0.6_FW4_R BZ recirculation manifold: maximum temperature

The main water parameters have been reported in Table 4.19, where, as expected, the water outlet temperatures, obtained from the temperature averaged on the mass flow rate and the overall outlet tube sections, are very close to 328°C, being 327.7°C and 328.3 at the FW and BZ outlets respectively. The BZ double pass flow significantly increases the water outlet velocities, where in the first and second array have been enhanced up to 1.8 m/s and almost doubled (3.3 m/s) in the third. The increase in water velocity causes the corresponding enhancing of pressure drops into the BZ system, however negligible if compared with the FW system. The CHF for FW channels and first DWTs array has been analytically evaluated with Shah [73] and Tong [74] correlations, resulting 3.42 and 2.77 MW/m^2, respectively. While, the highest heat flux, which the water channels and first array are subjected, correspond to 1.09 and 0.727 MW/m^2, ensuring safety margins from the thermal crisis for both systems.

#	Domain	$T_{ave\ out}$ [°C]	$v_{ave\ out}$ [m/s]	v_{max} [m/s]	Press Drops [kPa]
1	FW Water	327.7	4.910	5.802	41.463
2	BZ Water 1st array	324.1	1.850	2.175	4.509
3	BZ Water 2nd arrayL	317.2	1.798	2.111	3.825
4	BZ Water 2nd arrayC	316.6	1.794	2.104	3.722
5	BZ Water 3rd array	328.3	3.298	3.981	7.925

Table 4.19 – WCLL V0.6_FW4_R BZ recirculation manifold: water relevant parameters

The table show the pressure drops for each group of arrays, which serves to provide an order of magnitude. A preliminary analytical evaluation of the pressure drops of the elementary cell

is performed considering the sudden expansion and contraction of the water into the manifold. According with Ref. [78], the concentrated pressure drops have been estimated with the following equation $\Delta p_{irr} = K \cdot {}^{1}/_{2} \cdot \bar{\rho} \cdot \overline{v^2}$, where K is a numerical parameter, $\bar{\rho}$ the average density averaged on the fluid temperature (kg/m^3) and $\bar{v}$ is the average velocity of the fluid. The parameter K varies accordingly with the area ratio, resulting $K_{con} = 0.5 \cdot (1 - A_{min}/A_{max})$ for the contraction and $K_{exp} = (1 - A_{min}/A_{max})^2$ for the expansion. If $A_{min} \ll A_{max}$, the two coefficients tend respectively to K_{con}=0.5 and K_{exp}=1. Regarding the present analysis, K_{con}=0.5 and K_{exp}=1 have been assumed. In Table 4.20, the results of the pressure drop at the manifold have been reported for both systems.

Parameters	**System**		**Unit**
	BZ	***FW***	
Inlet manifold	0.511	3.500	kPa
Flow path	4.509 + 7.925	41.463	kPa
Recirculation	1.123 + 1.706	-	kPa
Outlet manifold	3.562	7.900	kPa
Total	***19.336***	***52.864***	***kPa***

Table 4.20 – WCLL V0.6_FW4_R BZ recirculation manifold pressure drops analytical estimation

Regarding the structural materials, the Eurofer upper plate temperature contour returns a similar temperature field of the previous model, where no temperature exceeds the limit; even the FW has a very similar temperature distribution. Eurofer plate and FW radial poloidal cut are shown in Fig. 4.23. With the increased mass flow rate into the first array, the hot spots near the side walls corners have decreased their temperatures (black circles). In addition, the higher water velocity has caused a further reduction of the passive heat removal at the FW-PbLi interface as shown in Fig. 4.24, where, the zones between 43 and 64 kW/m^2 have considerably increase their areas. This has been numerically evaluated, resulting in an average heat passive removal of 60.765 kW/m^2 on the entire surface, which corresponds to 12.8% less than the configuration without the BZ recirculation manifold.

To compare both analyses, a radial poloidal plane has been set to evaluate the PbLi temperature field at the plate hotter region (Fig. 4.19 a). As seen previously, the present analysis has a higher flow of water in the first array which generates a greater heat removal in the nearby areas, thus,

is noted that the hot spot in the PbLi is significantly reduced, as well as its maximum temperature decreased by 5.6 degrees (Fig. 4.25).

As regards the BZ water, the areas that exceed the saturation temperature are limited in the lateral corners near the side walls (Fig. 4.26). The lower tube has the largest area, and the upper has the smallest, this is mainly caused by the poloidal asymmetry of the tubes, which have been placed in this way to mitigate the stratification effects on the upper part, that would be driven by the buoyancy forces as reported in Refs. [36].

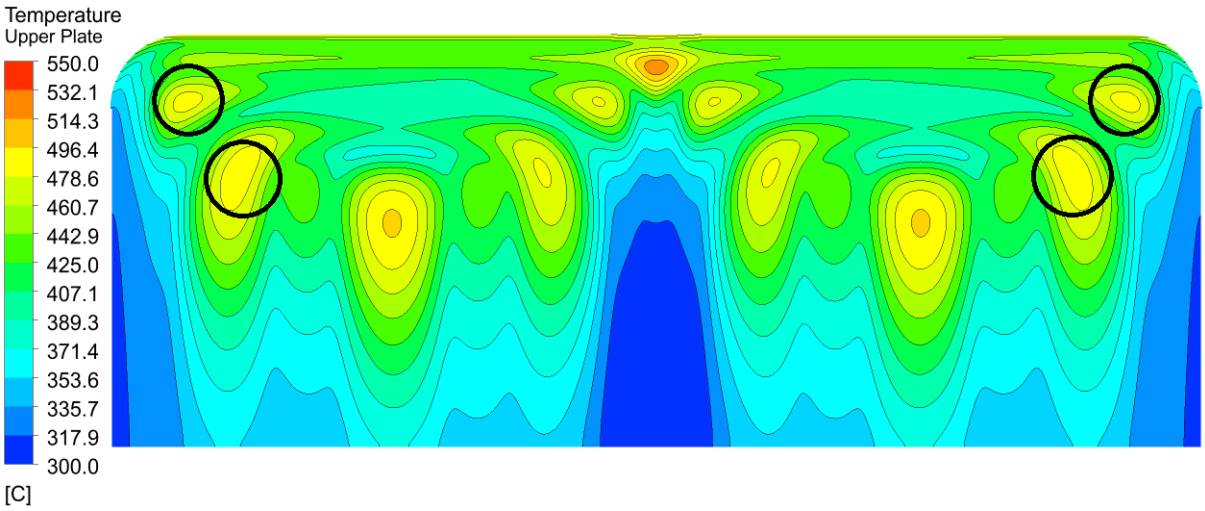

a) Eurofer upper plate

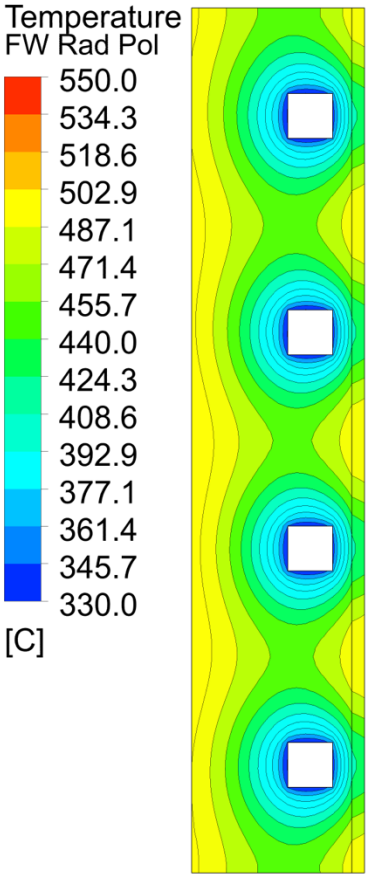

b) FW radial poloidal cut

Fig. 4.23 – WCLL V0.6_FW4_R BZ recirculation manifold: Eurofer structures temperature distribution

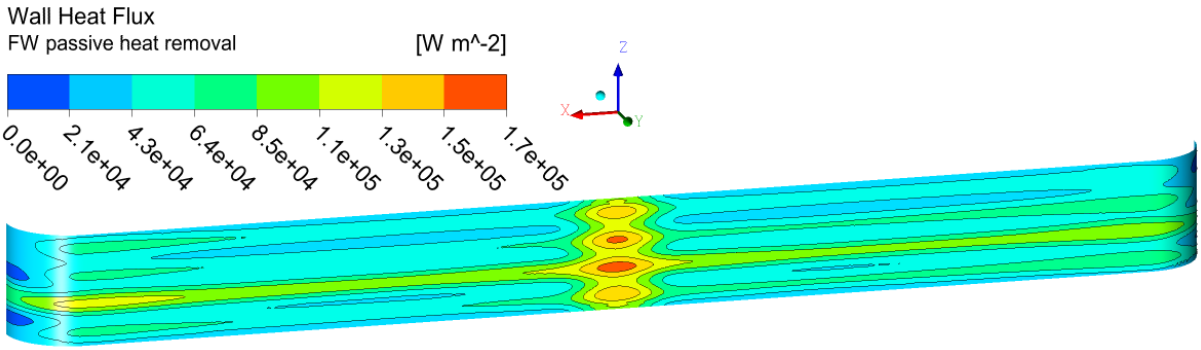

Fig. 4.24 – WCLL V0.6_FW4_R BZ recirculation manifold: BZ-FW interface wall heat flux removal

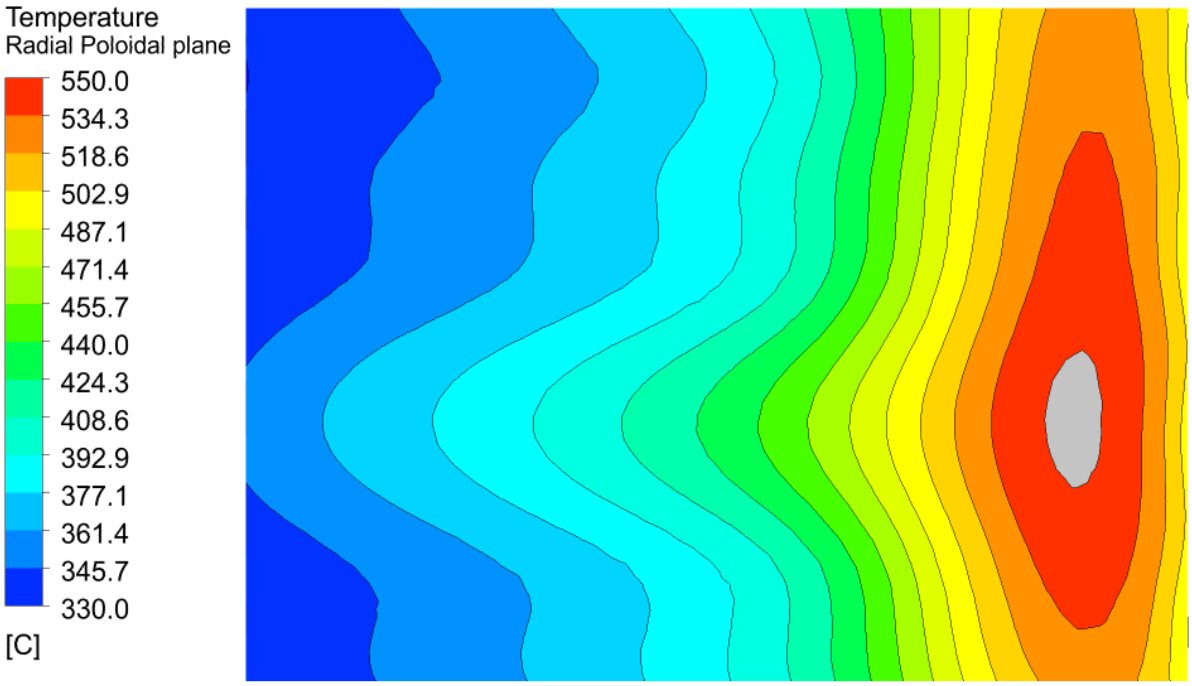

Fig. 4.25 – WCLL V0.6_FW4_R BZ recirculation manifold: PbLi temperature radial poloidal cut

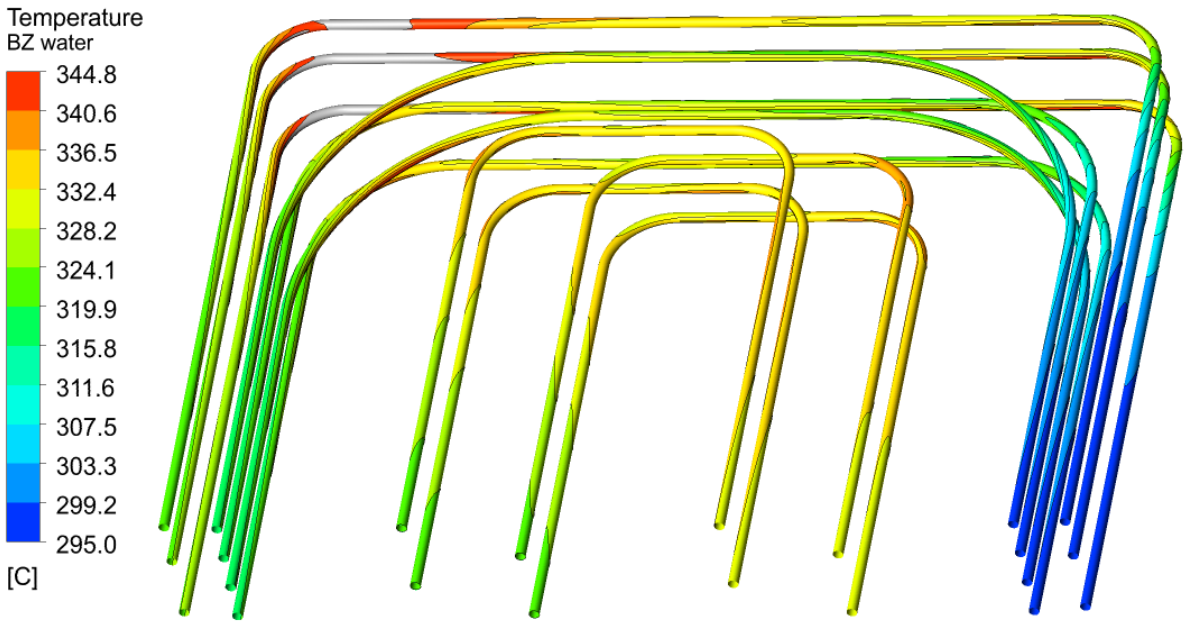

Fig. 4.26 – WCLL V0.6_FW4_R BZ recirculation manifold: water tubes temperature distribution

4.5.4. Summary

The cooling performance of the BZ recirculation manifold has been investigated through the CFD analysis of the WCLL V0.6_FW4_R elementary cell. The analysis, aimed to enhance the thermal-hydraulic performances of the BZ water, providing a water double-pass into the DWTs by means of a simulation of a recirculation manifold, has been performed. The three-dimensional model has been shaped using the ANSYS CFX v18.2 commercial code, material properties and heat loads have been set up on the most recent values, to obtain detailed thermal-hydraulic features.

The research activity, focused on increasing the BZ water performances, has demonstrated that with a recirculation manifold, the advantages are multiple. In fact, the PbLi strongly influences the elementary cell thermal field, which directly depends on the characteristics of the water into the tubes. The configuration, which has previously demonstrated that withstands the imposed heat loads guaranteeing a Eurofer temperature below the limit of 550°C, has obtained a lower temperature field compared with the same without recirculation.

It can be stated that the FW system is not affected by this change, where the Eurofer and Tungsten maximum temperatures are lower and higher, respectively, by only 1 degree. The BZ

internal structures, instead, have reported a slightly lower maximum temperature of 4.8 degrees and a reduced hotter region into the plate near the side walls corner. It can be affirmed that these are secondary effects on the Eurofer structures.

The main aspect of this manifold is the increased thermal-hydraulic performances of the BZ water due to the double-flow pass. The BZ coolant has strongly increased its velocity with a consequent increase in pressure drops, which remain negligible. The BZ water has widely reduced its maximum temperature into all the arrays, exceeding the saturation temperature only in the first ones, in limited regions near the side walls. Due to the higher velocity in this latter, the CHF has been enhanced by the 20%, ensuring a larger margin from a thermal crisis. Moreover, the passive BZ heat removal from the FW has been furthermore decreased as a consequence of a more homogeneous temperature near the interface. In addition, less FW water is required from the system to achieve 328°C at the outlet, making systems more independent of each other. However, it should be noted that 42.5% and 57.5% are still far from the hypothetical values of 37% and 63% obtained considering the actual deposited power, into FW and BZ, respectively. The PbLi hot spot in the mid toroidal length, highlighted in the previous analysis, has reduced its area as an effect of the higher water performances.

A preliminary evaluation of the pressure drops, taking into account the concentrated pressure drops into the manifold, has been carried out, obtaining into the FW a value 2.7 times higher than the BZ, mostly due to the high velocity of the fluid.

Several positive aspects have been verified using the recirculation manifold. It can be affirmed that the recirculation is a valid and suitable method to strongly enhance the thermal-hydraulic performances of the BZ coolant system. Moreover, it has multiple secondary effects, which improve the Eurofer structures temperature field and reduce the BZ passive heat removal. On these main outcomes, the recirculation manifold has been considered as an improvement to be implemented in the WCLL design.

4.6. Heat transfer modelling approach

These analyses have been carried out to evaluate the impact on the numerical model of the heat transfer modelling approach. This research activity is divided in two different parts. The first part concerns the comparison between two modelling methods and the adoption of two different PbLi thermal conductivity; it has been performed with WCLL 2018 V0.6 layout with 10 FW channels and an imposed HF of 0.5 MW/m^2. While, the second part, has been performed on the optimized WCLL configuration, V0.6_FW4_R with the BZ recirculation and the most updated heat flux on the Tungsten layer, regarding a comparison between the PbLi modelling state and also its thermal conductivity.

4.6.1. V0.6 modelling approach comparison

Two different modelling methods have been considered to simulate the heat transfer between structures and fluids, and also the impact in the adoption of a different material thermo-physical property, in particular, the PbLi thermal conductivity. An approach is based on the simulation of convective and diffusive heat transfer processes taking place within the liquid metal by means of a CFD tool based on the Finite Volume Method (FVM). Conversely, the other approach has roughly assumed a pure diffusive heat transfer mechanism within the breeder, due to the very low velocities envisaged for its flow field and has been assessed by means of a commercial code based on the Finite Element Method (FEM).

4.6.1.1. Numerical model

The present analysis has been performed on the WCLL 2018 V0.6 layout. The elementary cell V0.6 has a toroidal length of 1500 mm, the radial dimension is reduced to 567 mm and total height clipped to 135 mm. Its FW includes ten equidistant horizontal coolant channels. Its BZ presents the previously described structural design (Sect. 3.2): radial-poloidal stiffening plates detached from the FW by 175 mm, with a total radial length of 365 mm; a radial-poloidal baffle plate placed at mid-height of the cell allowing PbLi to flow in radial-poloidal-radial direction, forming twelve breeder channels, divided in 8 central (231×61,5 mm) and 4 side channels (233×61,5 mm) elongated for 365mm, after which, there is the “free stream” region where the PbLi flows in poloidal direction. The PbLi enters from the bottom part and exits from the top

part of the cell; the BZ is refrigerated by 22 DWTs, arranged as demonstrated in Sect. 4.3. The BZ water coolant, equally divided between the 22 tubes, enters from the central region and exits near the side walls. The FW water, equally distributed into the 10 channels, has an alternate and opposite flows. The water coolant scheme is shown in Fig. 4.27, and the main geometrical parameters of both cooling circuits are reported in Table 4.21.

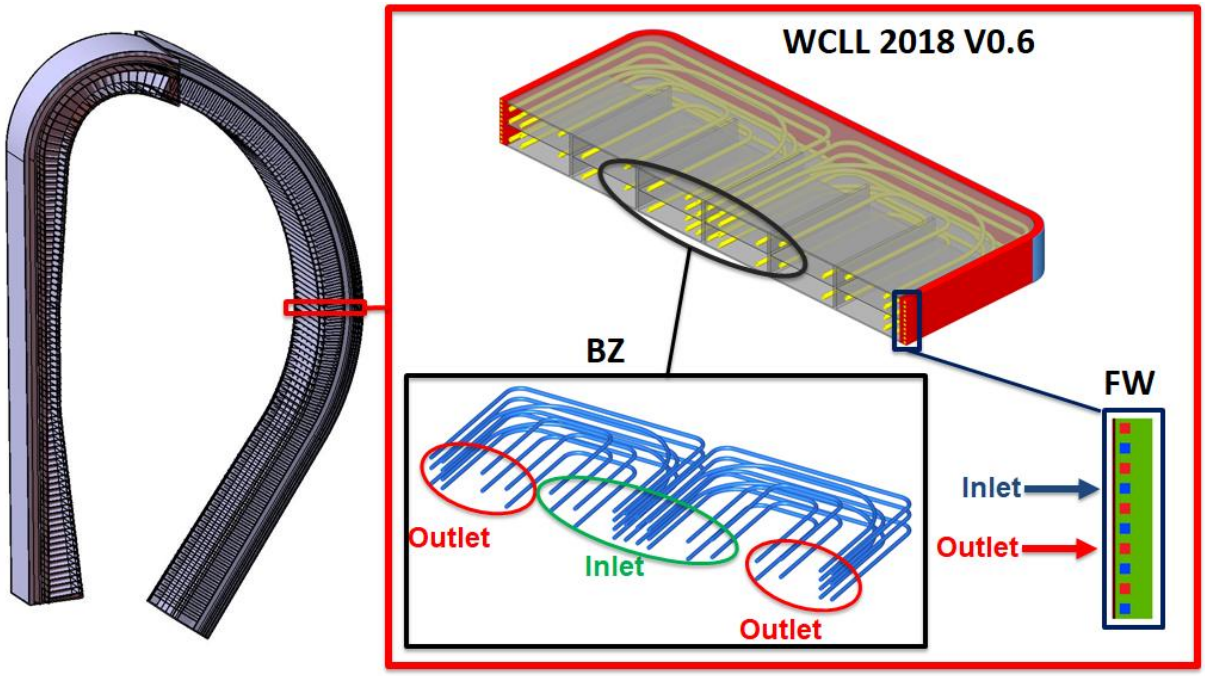

Fig. 4.27 – WCLL 2018 V0.6 layout water coolant schemes

WCLL 2018 V0.6			
Water domain	**Curve Rad. [mm]**	**FW Dist. [mm]**	**Tube Length [mm]**
1st array	50.0	20.0	1672.58
2nd array L	100.0	73.0	1443.66
2nd array C	200.0	53.0	1397.82
3rd array	50.0	128.25	1010.08
FW channel	93.5	-	2417.00

Table 4.21 – WCLL V0.6 BZ and FW water main geometrical parameters

4.6.1.2. Solver settings and boundary conditions

For this study, to mark up the thermal-hydraulics advantage and disadvantage focusing on the impact of the numerical prediction, different approaches to the numerical modelling are analyzed and compared. Four different models have been set up, to compare and evaluating the thermal field of the WCLL 2018 V0.6 elementary cell.

Two of these models use an approach based on a pure conductive analysis that roughly neglects the simulation of convective phenomena between the steel structure and the fluids (i.e. water and PbLi). The water domains are not modeled, both in BZ and FW systems, and their effects are simulated by means of proper convective boundary conditions analytically calculated. While, the PbLi is modelled as a solid domain.

It has been evaluated, by simulations with liquid PbLi, that the convective contribution to the heat exchange is almost irrelevant. The PbLi reaches, in the case with forced convection and in the absence of buoyancy effects, average velocities in the range of v~0.1-0.15 mm/s, resulting in a laminar flow, as the Reynolds number is Re~40. Moreover, the Prandtl number was calculated to evaluate how much the convective contribution affects the heat transmission $\left(Pr = \frac{\mu \cdot c_p}{\lambda}\right)$. Due to the average temperature, the thermo-physical properties have been evaluated, resulting in Pr~0.02, a typical value for liquid metals. This means that the thermal diffusivity, which is related to the rate of heat transfer by conduction, unambiguously dominates prevailing on convection, that can be neglected. Moreover, also the MHD effects strongly reduce the contribution of the convection, suppressing the buoyancy forces. These aspects have been widely discussed and demonstrated by several CFD simulations considering both diffusive and convective contributions, as reported in Refs. [35][54].

The other two models adopt an approach based on a convective-diffusive analysis that might also consider the convective phenomena due to the fluids (i.e. water and PbLi). In particular, in one case water coolant is modelled as a fluid, keeping the PbLi domain as solid, to assess the influence of the water modeling instead of the conductive boundary condition. While, in the other case, both water and breeder are modeled as fluids. This comparison allows to highlight the main discrepancies between the different heat transfer modelling approaches as well as between the different numerical methods and, hence, codes adopted. To this purpose, the ABAQUS v6.14 commercial FEM code is adopted to simulate one of two pure diffusive

models, while, the ANSYS CFX v18.2 FVM commercial code is used to run the remaining three models.

To compare the models in a proper way, the same material thermo-physical properties have been implemented in both commercial codes. The solid structures properties of Eurofer and Tungsten have been specified in terms of density, specific heat capacity and thermal conductivity. The fluids, on the other hand, also require the dynamic viscosity, which is neglected in the cases where the PbLi is modelled as a solid domain. These properties are represented with fixed values or temperature dependent function, as reported in Sect. 4.1. To fully evaluate the effect of the PbLi heat transfer, both PbLi thermal conductivity models have been adopted, the Mogahed [65], which is recommended, and the IAEA correlation [66].

To evaluate the WCLL 2018 V0.6 elementary cell temperature field with the aforementioned FEM and FVM codes, 8 simulations are performed, as schematically represented in Fig. 4.28, and reported in Table 4.22. These are divided into two groups, each of which is composed of four different models, as described above. The two groups, however, differ only in the thermal conductivity adopted to simulate PbLi, since, in the first the Mogahed one is adopted, and in the second the IAEA. Two of these eight simulations, in particular the FEM, have been performed and investigated by the University of Palermo [79].

Two different thermal loads have been imposed to realistically reproduce the power deposition into the elementary cell. According to Sect. 4.2, the curves related to the radial volumetric power density have been set into the Eurofer, Tungsten and PbLi domain; while, a maximum heat flux of 0.5 MW/m^2 has been imposed onto the Tungsten facing plasma surface.

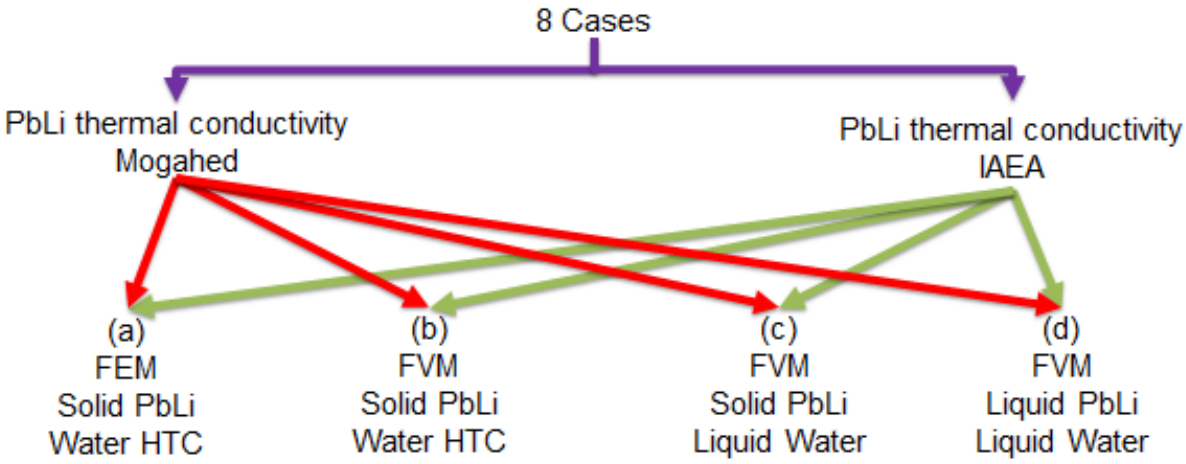

Fig. 4.28 – Analyses performed divided by thermo-physical properties, approach and models

#	Model	ID	Description	Note
1	a – FEM	V0.6_HTC_FEM_M	• FEM approach • Solid PbLi • $\lambda_{Mogahed}$	Water not modelled; HTC boundary condition imposed
2	b – FVM	V0.6_HTC_FVM_M	• FVM approach • Solid PbLi • $\lambda_{Mogahed}$	Water not modelled; HTC boundary condition imposed
3	c – FVM	V0.6_Solid_FVM_M	• FVM approach • Solid PbLi • Fluid Water • $\lambda_{Mogahed}$	
4	d – FVM	V0.6_Fluid_FVM_M	• FVM approach • Fluid PbLi • Fluid Water • $\lambda_{Mogahed}$	No buoyancy forces considered for PbLi
5	a – FEM	V0.6_HTC_FEM_I	• FEM approach • Solid PbLi • λ_{IAEA}	Water not modelled; HTC boundary condition imposed
6	b – FVM	V0.6_HTC_FVM_I	• FVM approach • Solid PbLi • λ_{IAEA}	Water not modelled; HTC boundary condition imposed
7	c – FVM	V0.6_Solid_FVM_I	• FVM approach • Solid PbLi • Fluid Water • λ_{IAEA}	
8	d – FVM	V0.6_Fluid_FVM_I	• FVM approach • Fluid PbLi • Fluid Water • λ_{IAEA}	No buoyancy forces considered for PbLi

Table 4.22 – WCLL 2018 V0.6 layout heat transfer modelling approach: performed simulations

As imposed from the DEMO 2017 baseline, the thermodynamic cycle of the water is 295°C–328°C at 15.5 MPa. In order to provide suitable water to the PHTS and to obtain 328°C at both water cooling systems outlet, an enthalpy balance on the total deposited power has been performed. This leads to the total amount of water mass flow necessary to guarantee an adequate outlet water temperature, within the limits of the thermodynamic cycle. Based on the results obtained in Sect. 4.3, the water mass flow has been equally divided between both systems, 50% per each.

Concerning the boundary conditions of the models without the water fluid domains, a heat transfer coefficient (HTC) has been imposed on the internal surface of the breeding zone DWTs and first wall channels. It has deemed appropriate to impose, as water bulk temperature, the average temperature of the water thermodynamic cycle (311.5°C). The HTC has been calculated through the empirical correlation of Dittus-Boelter, which has gained widespread acceptance for prediction of the Nusselt number with turbulent flow [80], where, in a heated channel, corresponds to $Nu = 0.023 \cdot Re^{0.8} \cdot Pr^{0.4}$. The Nusselt number, which expresses the ratio of convective to conductive heat transfer at a boundary in a fluid, can also be expressed with $Nu = \frac{HTC \cdot D_h}{\lambda}$. Using the two formulas, the HTC values, to impose on the internal surfaces of the BZ DWTs and FW channels, is extrapolated, obtaining 11,175 and 22,012 W/m^2 K for BZ tubes and FW channels respectively.

The model with PbLi modelled as fluid, forced convection is assumed. Inlet mass flow rate of 0.16521 kg/s equally distributed on the six sub-channels, temperature of 327°C and reference pressure of 100 kPa have been set [59] as boundary conditions.

The other boundary conditions adopted for all the models are:

- Periodic boundary conditions on the upper and lower surfaces of upper and lower stiffening plates, FW and Tungsten layer, in poloidal direction, to simulate the presence of adjacent elementary cell;
- Adiabatic condition to back walls of FW, stiffeners, Tungsten layer and FW side walls;
- Static pressure imposed in the fluid domain at the outlet sections;
- No-slip condition at the interface between coolant and the circuit steel walls.

The thermal energy model has been set up to solve the conductive heat transfer equations for "a" and "b" models. The two-equations k-ω Shear Stress Transport (SST) model has been selected to simulate the turbulence effects of water for "c" and "d" model, while for "d" also a laminar model has been chosen to solve the Navier-Stokes equations in the PbLi.

A detailed set of the imposed boundary conditions are shown in Table 4.23.

#	**Parameters**	**Models**				**Unit**
		a - FEM	***b - FVM***	***c - FVM***	***d - FVM***	
1	FW HF_{max}	0.5	0.5	0.5	0.5	MW/m^2
2	Water (BZ-FW) T_{inlet}	295.0	295.0	295.0	295.0	°C
3	Water (BZ-FW) P	15.5	15.5	15.5	15.5	MPa
4	FW MFR	-	-	0.8285	0.8285	kg/s
5	BZ MFR	-	-	0.8285	0.8285	kg/s
6	Total MFR	-	-	1.6570	1.6570	kg/s
7	FW HTC	22,012	22,012			W/m^2 K
8	BZ HTC	11,175	11,175			W/m^2 K
9	PbLi T_{inlet}	-	-	-	327.0	°C
10	PbLi MFR	-	-	-	0.16521	kg/s

Table 4.23 – WCLL 2018 V0.6 layout heat transfer modelling approach: boundary conditions

4.6.1.3. Mesh independence

For the models, a mesh independence analysis has been performed, allowing accurate results to be obtained in reasonable calculation time, using meshes with different degree of detail. As to the FVM models, all the geometrical models are developed as a single part, to simulate the heat transfer between the multiple components, solids and fluid using a conformal mesh. Hexahedral and tetrahedral elements were adopted in the models, considering the geometrical features of the domains, many and different local controls are inserted to define the complex geometry of the cell properly. For this purpose, different code tools were exploited, such as sizing control, sweep method, mapped face, and the inflation control near the solid walls for the resolution of the viscous sub-layer (y^+=1) of the water, based on a maximum velocity of 7 m/s.

The analysis was conducted to establish the independence of results from the grid and to optimize the number of elements in the model. The simulations have been reported and proved in Ref. [47] for a COB equatorial elementary cell with the same geometry and a similar DWTs distribution.

Concerning the FEM model, a dedicated mesh independence analysis is performed varying the sizing of the grid elements with a spatial discretization. In addition, a radially uniform nuclear power deposition is assumed to avoid the misleading effects of its variation due to the change of the adopted mesh. The performed calculations are summarized in Table 4.24 and the results are shown in Fig. 4.29. They show that the finer mesh (D) provides significant improvements compared with others. There are significant variations from (B) to (A), and computational costs are not so wasteful compared with (C). Therefore, the (D) mesh is adopted.

A complete list of the mesh statistics of each numerical model is reported in Table 4.25.

Model	**Nodes**	**Elements**	**Eurofer T_{max} [°C]**	**PbLi T_{max} [°C]**
A	1.71 M	3.72 M	516.0	517.6
B	1.92 M	4.93 M	519.2	519.8
C	2.21 M	6.53 M	519.8	520.3
D	2.49 M	8.10 M	520.2	520.6

Table 4.24 – WCLL 2018 V0.6 FEM model: mesh independence

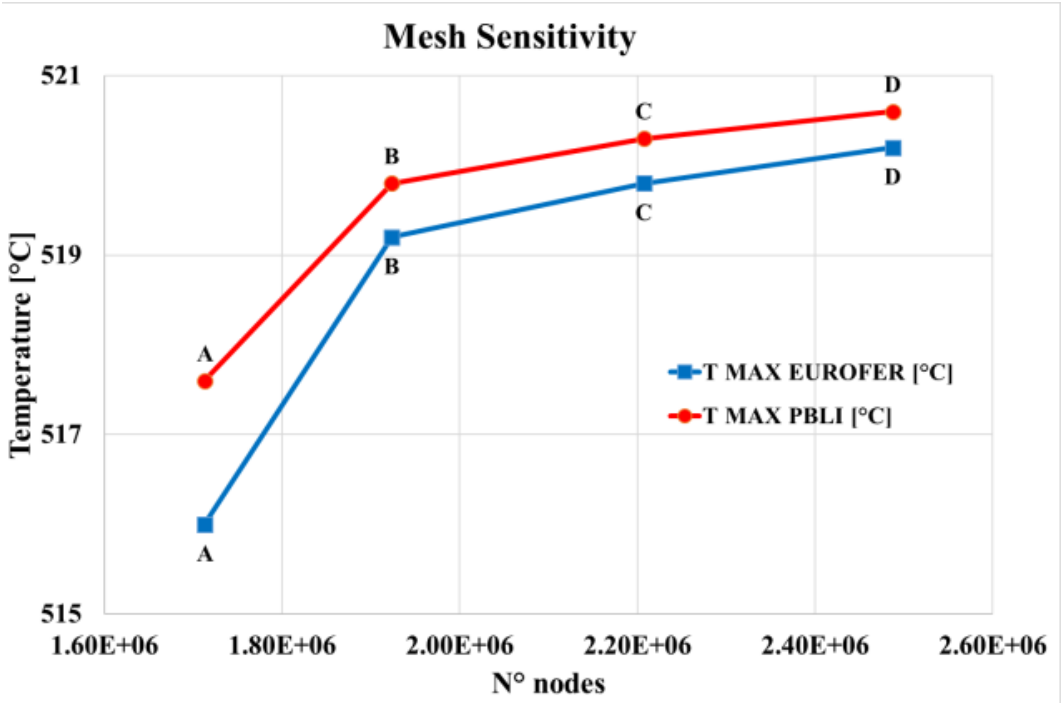

Fig. 4.29 – WCLL 2018 V0.6 FEM model mesh sensitivity temperature results

Parameters	**Models**			
	a - FEM	***b - FVM***	***c - FVM***	***d - FVM***
N° Nodes	2.49 M	9.3 M	14.3 M	14.3 M
N° Elements	8.10 M	21.2 M	27.7 M	27.7 M
Ave Orth Qual	-	0.822	0.817	0.817
Ave Skewness	-	0.198	0.206	0.206

Table 4.25 – WCLL 2018 V0.6 layout heat transfer modelling approach: mesh statistics

4.6.1.4. Results

The results of the analyzed models are hereafter discussed. The four models differ by approach, method and thermophysical properties. To evaluate the effect on the numerical prediction of the model approach and thermo-physical properties, steady-state analyses have been performed. Each model has been simulated once with the Mogahed and secondly with the IAEA PbLi thermal conductivity correlation.

All the eight performed runs return a toroidally symmetric temperature field, which is provided by the DWTs distribution. They mainly differ by the maximum reached temperature. The Eurofer plate and maximum temperatures of the performed analyses are collected in Table 4.26.

Regarding the FEM analyses, as expected, the results show a similar spatial distribution of the thermal field that deeply differ as to their temperatures maximum values of ≈60°C. In the case where IAEA correlation is adopted, results indicate that the maximum temperature of 571.0°C is reached at the baffle plate while the stiffening plates experience a temperature of 562.7°C (Fig. 4.30), both exceeding the imposed limit of 550°C. This calculation turns out to be very conservative due to the absence of the convective contribution and to the underestimation of thermal conductivity due to the IAEA correlation with respect to the Mogahed's one (mean percentage difference around 32%). Conversely, Fig. 4.31 shows the results obtained with Mogahed correlation, which predict a temperature limit of 509.3°C in the upper plate and a maximum temperature of 513.4°C in the baffle plate.

The FVM analyses in a purely conductive model, where solid PbLi and HTC boundary conditions on the DWTs and FW square channels have been assumed, return almost identical results to the FEM ones. The upper plate presents the same hot spots locations as the FEM cases, with both PbLi thermal conductivities. In Fig. 4.32 is reported the temperature field of the upper plate obtained with the Mogahed correlation, where, the maximum temperature predicted is 505.6°C. Moreover, the Eurofer T_{max} is 510.6°C, about 3 degrees less than the FEM case. Regarding Fig. 4.33, related to IAEA correlation, even in this case the upper plate reaches temperatures above the limit (558.7°C), resulting 4 degrees less than that predicted by the FEM analysis. The T_{max}, as highlighted previously, is located in the baffle plate and amounts to 568.1°C.

The third set of analyses presents the integration of the water as a fluid domain into the DWTs and the FW channels. For these analyses, the FVM model is used. In these two cases, thanks to the improved modelling of water convective heat transfer the Eurofer temperature slightly decreases and a more realistic spatial distribution of the thermal field is obtained due to the increase of water coolant bulk temperature along the channels path calculated by the code; in the Mogahed case the maximum temperature continues to stay below the imposed limit, reaching 504.4°C in the upper plate (Fig. 4.34) and 509.8°C in the baffle plate. Despite the predicted temperature increases of the IAEA case, the limit of 550°C is not overcome; it can be seen from Fig. 4.35 that the maximum temperature of the upper plate is 556.9°C while the baffle plate reaches at most 566.4°C.

The last set of analyses, where also the PbLi is modeled as a fluid domain, are performed with the FVM model. For the heat transfer, in addition to the convective contribution of water, there is also that of liquid PbLi, which contributes to a further reduction of the temperature field. In the analysis with Mogahed's correlation, the contribution of the PbLi convection causes the temperature to decrease to 502.4°C in the upper plate (Fig. 4.36), and the Eurofer maximum temperature to be reduced down to 505.6°C, even in this case located in the baffle plate. Regarding the IAEA correlation analysis, the predicted temperature of the upper plate decreases to 548.5°C (Fig. 4.37), slightly satisfying the temperature requirement, even if in the baffle plate this limit is exceeded, as the temperature amounts to 559.6°C.

Focusing on the Eurofer obtained data (Table 4.26), it is shown in Fig. 4.38 that by refining the analysis and going gradually considering the convective heat transfer of the fluid domains into the models, the maximum Eurofer temperature of the model slightly decreases, like that of the stiffening plates. In both cases, the water convective contribution provides a lowering of less than two degrees. This because the Eurofer maximum temperature is located in the baffle plate in the middle of the toroidal halves of the cell and is weakly affected by the presence of the tubes in that region, thus, from the convective contribution of water. Instead, as can be seen, the convective contribution of PbLi has a more marked influence on the maximum temperature of the Eurofer, decreasing by 4.2 and 6.8 degrees in the Mogahed and IAEA respectively.

As expected, FEM model is a more conservative approach, returning higher temperatures of 1.5% in case of Mogahed PbLi thermal conductivity and 2% in the IAEA case, than the corresponding FVM model with PbLi and water modelled as fluid. Moreover, the impact of the correlation adopted for the PbLi thermal conductivity is significant, as results obtained with IAEA and Mogahed, but with the same model, differ on average by 56 degrees, reaching the maximum discrepancy for the FEM analysis (57.6°C) and a minimum difference for the FVM analysis (54°C) with the fluid domains of water and PbLi.

Model	**Eurofer temperature**			
	λ Mogahed		***λ IAEA***	
	$T_{Upper\ Plate}$ [°C]	T_{max} [°C]	$T_{Upper\ Plate}$ [°C]	T_{max} [°C]
a – FEM	509.3	513.4	562.7	571.0
b – FVM	505.6	510.6	558.7	568.1
c – FVM	504.4	509.8	556.9	566.4
d – FVM	502.4	505.6	548.5	559.6

Table 4.26 – WCLL 2018 V0.6 layout heat transfer modelling approach: Eurofer temperature

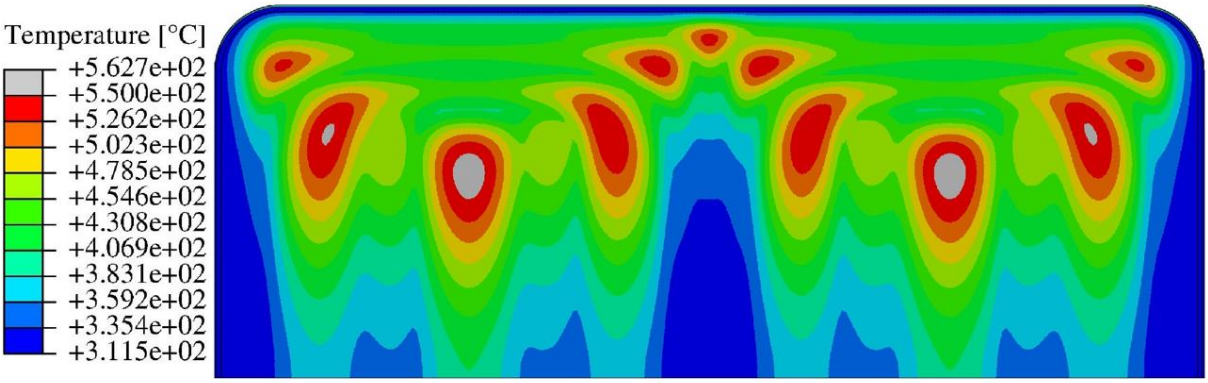

Fig. 4.30 – FEM analysis upper plate temperature field – IAEA correlation

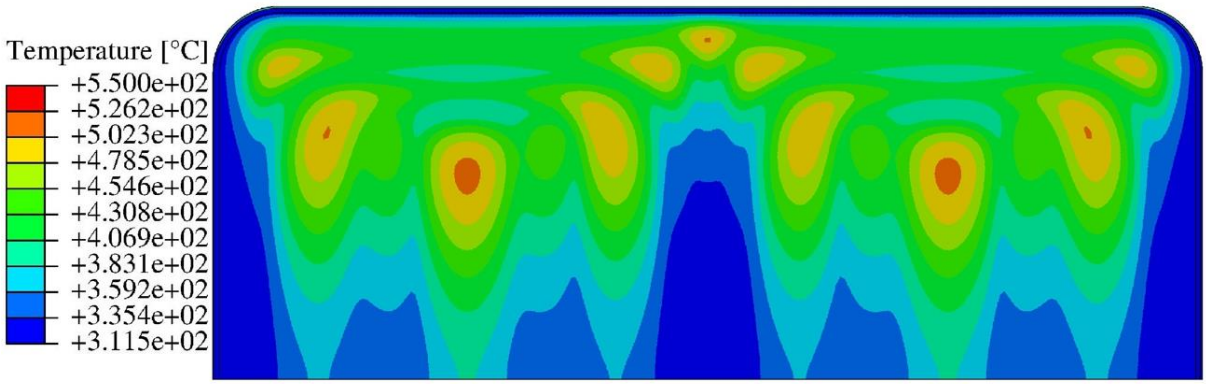

Fig. 4.31 – FEM analysis upper plate temperature field – Mogahed correlation

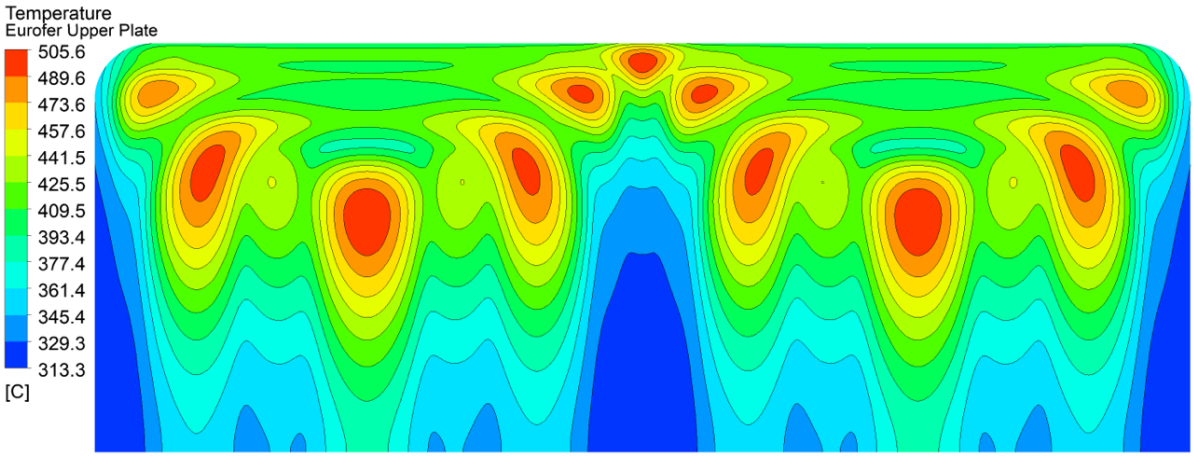

Fig. 4.32 – FVM purely conductive analysis upper plate temperature field – Mogahed correlation

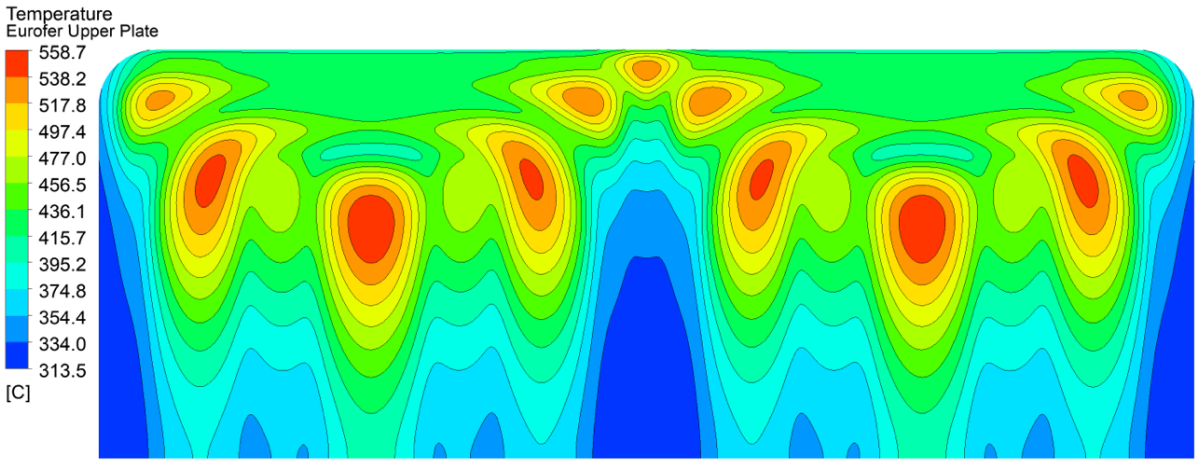

Fig. 4.33 – FVM purely conductive analysis upper plate temperature field – IAEA correlation

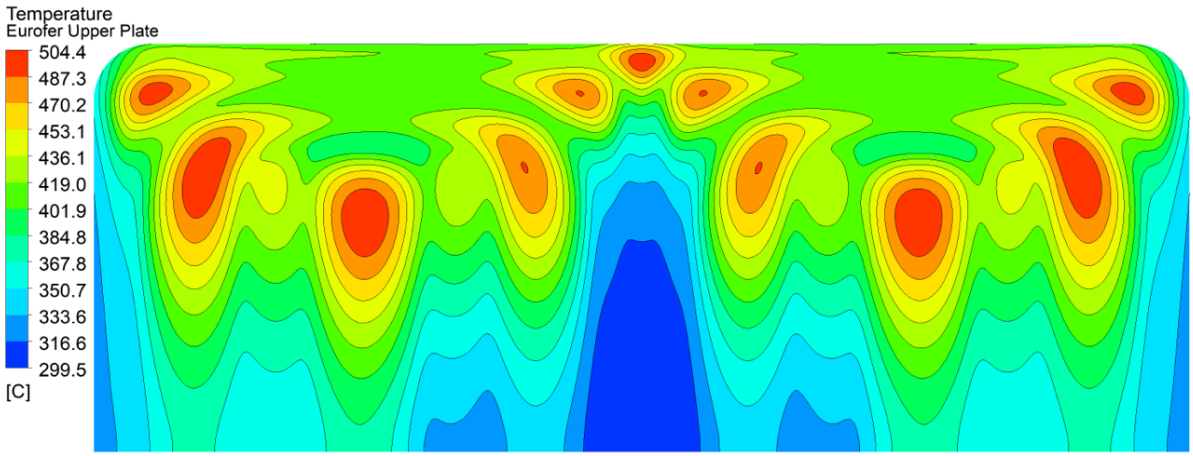

Fig. 4.34 – FVM with fluid water and PbLi solid domains upper plate temperature field – Mogahed correlation

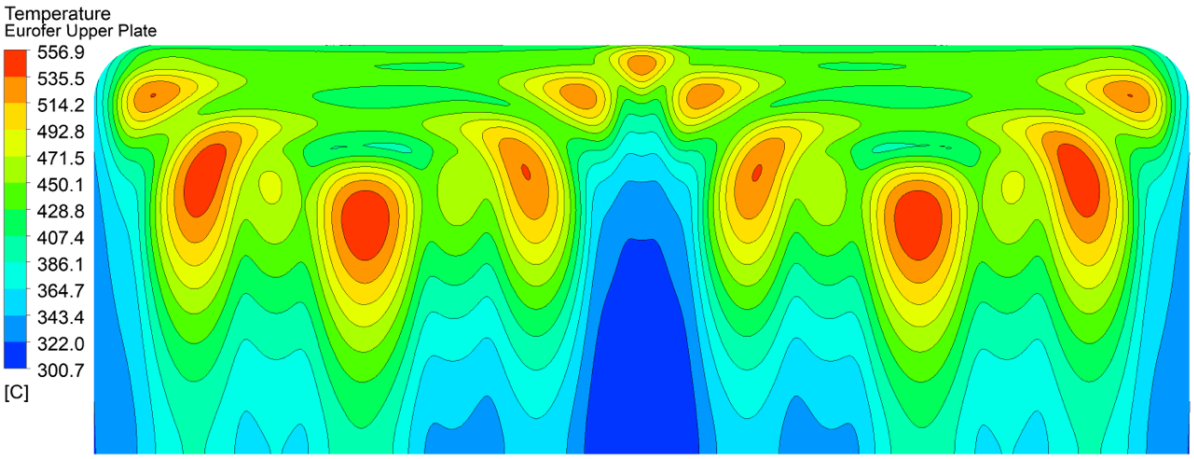

Fig. 4.35 – FVM with fluid water and PbLi solid domains upper plate temperature field – IAEA correlation

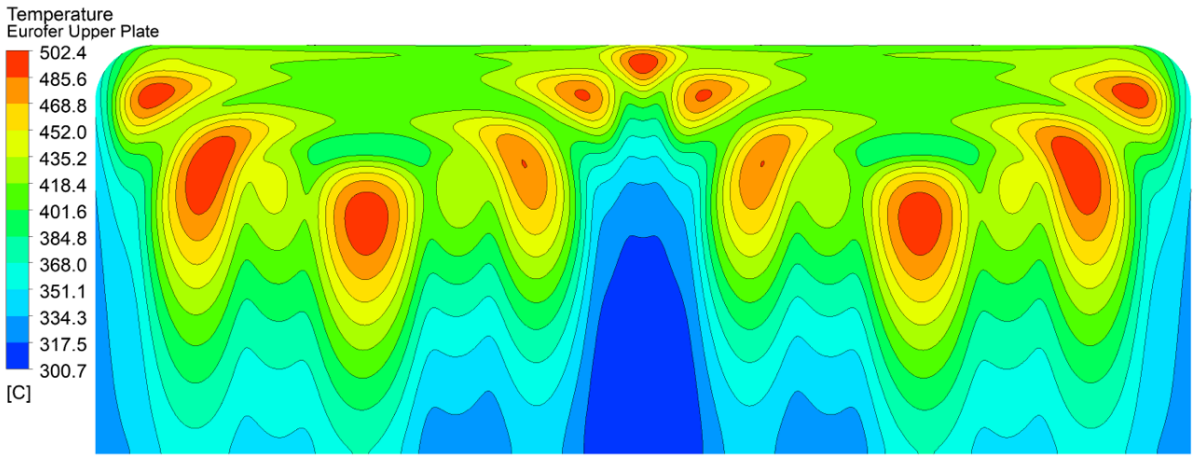

Fig. 4.36 – FVM with fluid water and PbLi domains upper plate temperature field – Mogahed correlation

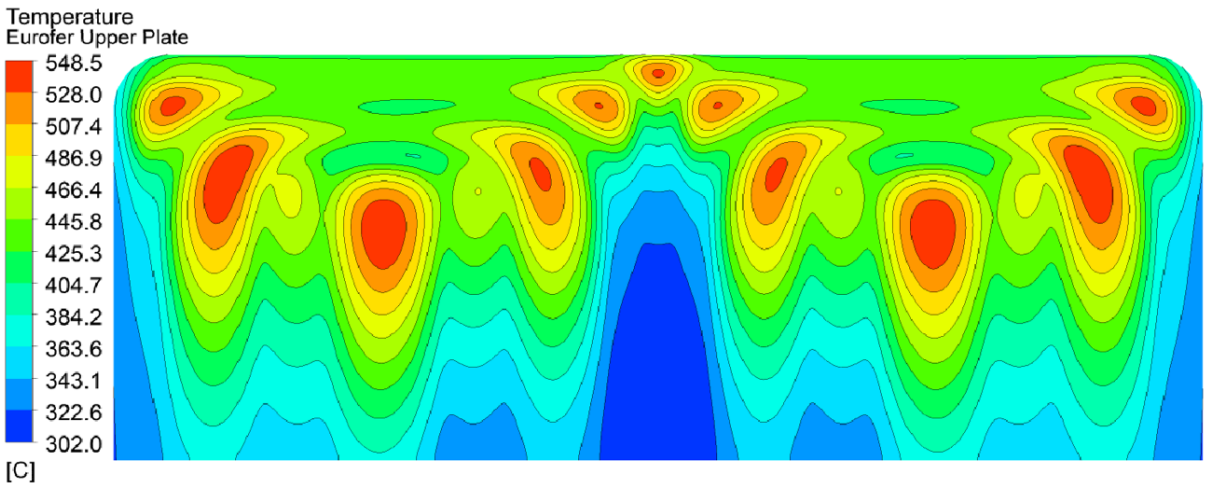

Fig. 4.37 – FVM with fluid water and PbLi domains upper plate temperature field – IAEA correlation

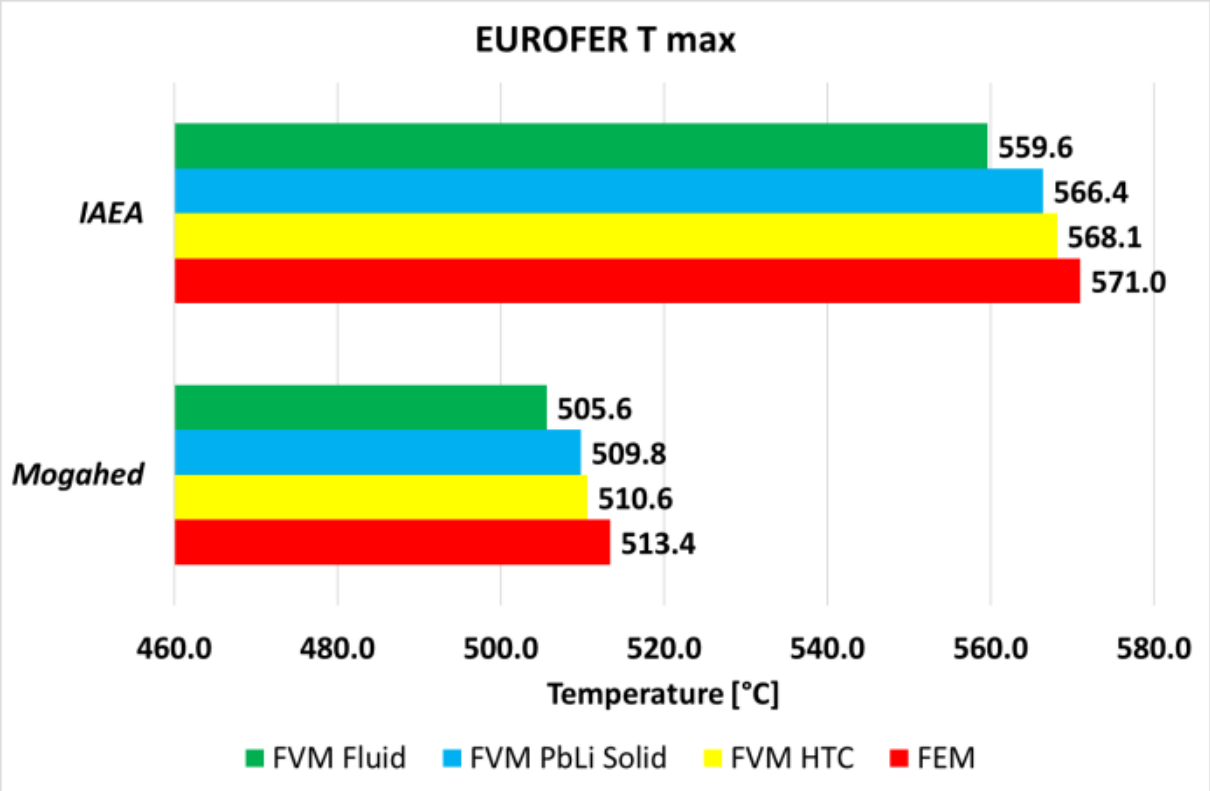

Fig. 4.38 - WCLL 2018 V0.6 layout heat transfer modelling approach: Eurofer maximum temperature trend

4.6.2. V06_FW4_R modelling comparison

The analyses have been performed to investigate the temperature field variations into the Eurofer structures and PbLi domain, due to the adoption of IAEA's PbLi thermal conductivity as reference. Furthermore, a sensitivity assessment on the PbLi modelling has been investigated to highlight the differences into the thermal field caused by a solid PbLi domain instead of a fluid one. The simulations have been performed on the most updated WCLL design and heat loads data, verifying, even in conservative conditions, if the optimized and updated layout can be confirmed as a consolidated design.

4.6.2.1. Numerical model and mesh

To investigate the effect of the modelling approach on the V0.6_FW4_R and the related features of the new reference PbLi thermal conductivity and its impact on the Eurofer plates and coolant systems, a three-dimension finite volume model has been developed for CFD steady-state analyses, using ANSYS CFX v18.2 code. The numerical model, which is fully described in Sect. 4.5, is briefly summarized in the following. It has a toroidal length of 1500 mm, radial extension of 1000 mm, where only 567 mm are modelled, neglecting the manifold region where the power contributions are foreseen negligible, and a poloidal height, constrained from the horizontal plates, of 135 mm. Two independent systems: the FW, an external Eurofer structure, 25 mm thick and bent in the radial direction, coated by a 2 mm of Tungsten layer that faces the plasma and actively water-cooled by 4 square channels with opposite and alternate flow direction; the BZ, an internal box reinforced with Eurofer structures, elongated from the BP for 365 mm, and filled with PbLi, actively cooled by 22 C-shaped DWTs. The internal solid Eurofer structures are represented with horizontal plates, vertical ribs and a baffle plate. The model, being the V0.6_FW4_R, adopts the same mesh previously seen in the related paragraph, where, the mesh statistics are reported in Table 4.16.

4.6.2.2. Solver settings and boundary conditions

The activity focuses on the impact of the PbLi modelling domain and its thermal conductivity, which affects the thermal field. Four different runs have been performed and compared, based on the V0.6_FW4_R model, verifying if the Eurofer temperature requirement is achieved and highlighting the main differences between the assumption made. In the present analyses, the

models have been reproduced with a different PbLi domain: one group modelled as liquid and the others as solid. As previously demonstrated, the assumption of modeling the PbLi as a solid domain is not invalidating for the calculation purposes; on the contrary, a conservative run is obtained. In each model the same thermo-physical properties for Eurofer, Tungsten and water coolant has been set, on the contrary, as regards the PbLi, two models have been set with the Mogahed correlation and the others two with the new reference property, the IAEA. The adopted thermo-physical properties of Tungsten, Eurofer, PbLi and water, are reported in Table 4.1, Table 4.2, Table 4.3 and Table 4.4, respectively. A complete list of the performed runs is shown in Table 4.27.

Thermal heat loads and water mass flow rate have been imposed as in the recently performed analysis for the alternative BZ manifold (Sect. 4.5), thus, calculated with the most updated data of power deposition and heat flux. On the upper and lower surfaces of Tungsten, FW and stiffeners plates, a periodic condition has been imposed. Moreover, adiabatic surfaces have been set for the external side of the side walls and the back part of the solid domains. In addition, a no-slip condition at the fluid-solid interfaces has been imposed. As regards the turbulence effect, the two-equations k-ω Shear Stress Transport (SST) model has been selected in all the simulations. A laminar model, instead, has been chosen for runs where a fluid domain is modelled for the PbLi. A complete set of the imposed boundary conditions is shown in Table 4.28 divided by run.

Model	**Run**	**Description**	**Note**
V0.6_FW4_R	#1	• Fluid PbLi • $\lambda_{Mogahed}$	Buoyancy forces not considered
V0.6_FW4_R	#2	• Solid PbLi • $\lambda_{Mogahed}$	-
V0.6_FW4_R	#3	• Fluid PbLi • λ_{IAEA}	Buoyancy forces not considered
V0.6_FW4_R	#3	• Solid PbLi • λ_{IAEA}	-

Table 4.27 – WCLL V0.6_FW4_R PbLi modelling comparison: performed analyses

#	Parameters	Runs				Unit
		#1	***#2***	***#3***	***#4***	
1	FW HF_{max}	0.32	0.32	0.32	0.32	MW/m^2
2	Water (BZ-FW) T_{inlet}	295.0	295.0	295.0	295.0	°C
3	Water (BZ-FW) Pressure	15.5	15.5	15.5	15.5	MPa
4	FW MFR	0.63189	0.63189	0.63189	0.63189	kg/s
5	BZ MFR	0.85491	0.85491	0.85491	0.85491	kg/s
6	Total MFR	1.4868	1.4868	1.4868	1.4868	kg/s
9	PbLi T_{inlet}	327.0	-	327.0	-	°C
10	PbLi MFR	0.16521	-	0.16521	-	kg/s

Table 4.28 – WCLL V0.6_FW4_R PbLi modelling comparison: boundary conditions divided by runs

4.6.2.3. Results

The results of PbLi modelling approach is hereafter discussed. The four models differ by the PbLi, in terms of thermal conductivity and modelling state. The first two runs have been performed with the Mogahed's thermal conductivity correlation and with two different PbLi state domain, fluid and solid; the others two, also one with PbLi as fluid and one as solid, with the IAEA's correlation. The analysis is aimed to verify if the selected design respects the main Eurofer temperature requirement, first of all with the old thermal conductivity and solid PbLi, and secondly, check if even with the new reference property the requirement is met in both cases.

The relevant outputs parameters of the performed runs are reported in Table 4.29.

#	Parameter	Run				Unit
		#1	*#2*	*#3*	*#4*	
1	Tungsten T_{max}	486.4	486.4	488.8	488.8	°C
2	FW T_{max}	501.7	501.5	514.0	513.8	°C
3	Stiffeners T_{max}	526.6	530.6	559.8	566.2	°C
4	PbLi T_{max}	552.9	551.8	602.2	600.7	°C
5	Stiffeners T_{ave}	388.6	389.9	408.2	410.5	°C
6	PbLi T_{ave}	395.9	397.3	416.9	419.4	°C
7	FW Water T_{max}	362.4	362.4	363.0	363.0	°C
8	BZ Water 1st array T_{max}	353.5	353.5	352.6	352.7	°C
9	BZ Water 2nd arrayL T_{max}	338.6	338.5	338.5	338.5	°C
10	BZ Water 2nd arrayC T_{max}	343.6	342.2	344.4	342.3	°C
11	BZ Water 3rd array T_{max}	341.1	341.3	341.0	341.2	°C
12	FW Water $T_{ave\ out}$	327.7	327.7	328.2	328.2	°C
13	BZ Water 1st array $T_{ave\ out}$	324.1	324.0	323.4	323.3	°C
14	BZ Water 2nd arrayL $T_{ave\ out}$	317.2	317.3	316.9	317.0	°C
15	BZ Water 2nd arrayC $T_{ave\ out}$	316.6	316.8	316.3	316.4	°C
16	BZ Water 3rd array $T_{ave\ out}$	328.3	328.5	327.8	328.1	°C
17	FW Water $v_{ave\ out}$	4.910	4.910	4.923	4.923	m/s
18	BZ Water 1st array $v_{ave\ out}$	1.850	1.850	1.844	1.844	m/s
19	BZ Water 2nd arrayL $v_{ave\ out}$	1.798	1.799	1.796	1.797	m/s
20	BZ Water 2nd arrayC $v_{ave\ out}$	1.794	1.795	1.792	1.793	m/s
21	BZ Water 3rd array $v_{ave\ out}$	3.298	3.300	3.291	3.294	m/s
22	FW Water v_{max}	5.802	5.802	5.817	5.817	m/s
23	BZ Water 1st array v_{max}	2.175	2.175	2.167	2.167	m/s
24	BZ Water 2nd arrayL v_{max}	2.111	2.111	2.111	2.111	m/s
25	BZ Water 2nd arrayC v_{max}	2.104	2.104	2.104	2.104	m/s
26	BZ Water 3rd array v_{max}	3.981	3.983	3.973	3.975	m/s

Table 4.29 – WCLL V0.6_FW4_R PbLi modelling comparison: main outputs parameters

As regards the water domains of FW and BZ water coolant, from the table is highlighted that both domains do not show any significant variations, returning comparable values for velocities and temperatures in each run. As expected, the outlet water temperatures, averaged on the mass flow rate and the overall outlet tube sections, are very similar and close to 328°C. In each model, and for both systems, the water outlet conditions are satisfied, providing adequate water conditions for the PHTS and not exceeding the maximum allowable velocity of 7 m/s. As seen previously, the maximum water temperature exceeds the saturation temperature at 15.5 MPa into FW channels and BZ first tubes array, but no thermal crisis occur ensuring adequate and safety margins, as demonstrated in Section 4.5.3.

Focusing on the structures, the temperature fields of Tungsten and FW are slightly affected by the newer PbLi thermal conductivity. The former return temperature 2.4 degrees higher with the IAEA correlation, reaching 488.8. Moreover, the PbLi modelling approach does not impact on this domain, since the temperatures differ only by the adopted PbLi thermal conductivity. Conversely, the FW Eurofer chase, shows a greater difference according to the adopted PbLi property, in fact, maximum temperature increases by around 12 degrees for both models. A very slight temperature decrease is noted from the fluid PbLi model to the solid ones, which can be considered negligible.

Concerning the BZ system, its Eurofer internal structures have returned an increasing temperature trend. As highlighted in Sect. 4.6.1, as the modeling of PbLi changes from fluid to solid, the temperature increases regardless of the adopted thermal conductivity. On the other hand, if the newer thermal conductivity is considered, the increase is considerably more marked than the older Mogahed. In the case of Mogahed's correlation, the Eurofer temperature requirement is met in both cases with an increase of the maximum temperature of 4 degrees from the fluid version (526.6°C) to the solid (530.6°C), but still below the limit. Contrariwise, concerning the IAEA's models, the Eurofer maximum temperature is above the limit even in the model where the PbLi is modelled as a fluid domain. It exceeds by nearly 10 degrees in the fluid model and more than 16 in the solid one, reaching respectively 559.8°C and 566.2°C.

Fig. 4.39, Fig. 4.40, Fig. 4.41 and Fig. 4.42 shown, respectively, the Eurofer upper plate as the model changes from run #1 to run #4. From the four plates two particularly critical areas can be noted, the first is the frontal area, already analyzed, in the middle of the toroidal length,

which is affected from the DWTs first array distance and from the water h the second is positioned in the middle of the halves at about 230 mm from the FW.

To evaluate the elementary cell behavior and the internal temperature distribution at the hot spots, two different radial poloidal cuts have been chosen in the models, as shown in Fig. 4.43. The plane A, shown in Fig. 4.44, returns, in the cases where Mogahed's correlation is adopted, two hot spots located inside the PbLi domain, very far from the plates; and in the case with IAEA PbLi thermal conductivity two similar hot spots are highlighted, which, from the PbLi domain, are elongated towards the plates impacting them exceeding the temperature limit by 7 and 8 degrees, respectively. Both cases do not show striking differences comparing the PbLi fluid model with the solid domain.

As regards the plane B, there are considerable temperature field differences between one model and another, due to the motion of the fluid, which significantly changes the isothermal lines in the figure. Run #1 and #2 (Fig. 4.45 a, b), do not show any hot spot onset, confirming the temperature distribution of the upper plate previously shown. The solid model has an extended and large column at the end of the baffle plate, which impacts the upper and lower plates with a larger surface than the fluid model, in addition, it also runs over the baffle. The IAEA models, in both cases, show a thermal field which considerably exceeds the limits. Run #3 (Fig. 4.45 c) shows a central hot spot that does not impact the plates thanks to the motion of the fluid. Unfortunately, the baffle plate, being immersed for the front part in the large gray hot spot, exceeds the temperature limit by more than 8 degrees. The Run #4 (Fig. 4.45 d), which is the more conservative analysis, shows a hot spot column that impacts both plates and baffle, widely exceeding the temperature limit by more than 16 degrees. From these images, it can be seen that PbLi, albeit with minimal velocity, contributes with a greater hot spot mitigation, moving and reducing hot areas, especially in the middle of the halves.

Another phenomenon, caused by the average PbLi temperature increase, due to the IAEA thermal conductivity, is the new rise in the passively removed power by the FW onto the BZ system, which has been increased by 20%, returning to a value comparable with a configuration without the BZ recirculation manifold, even if the required water to provide suitable water for the PHTS is unchanged.

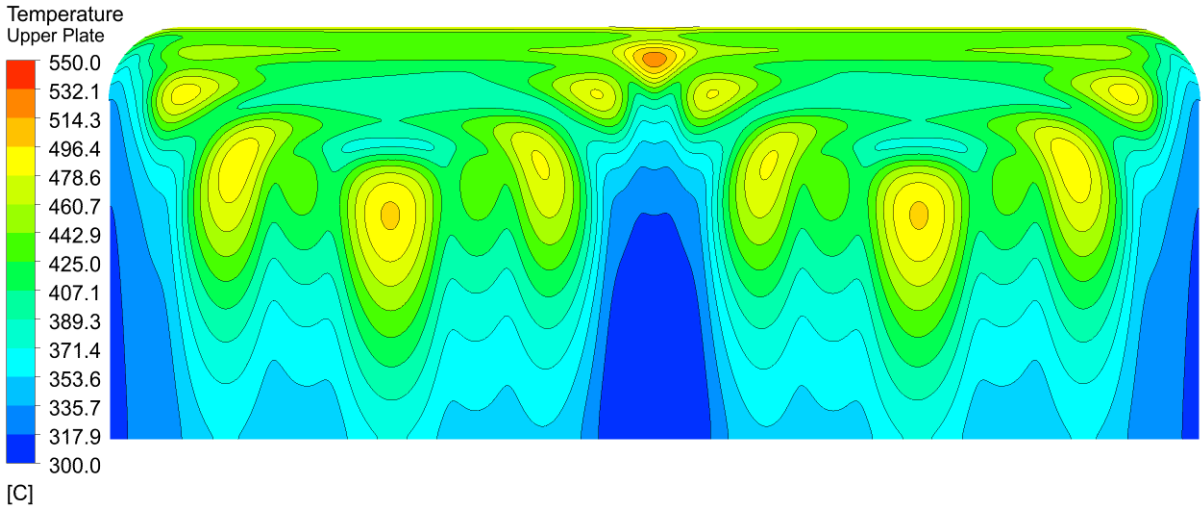

Fig. 4.39 – WCLL V0.6_FW4_R case #1 Eurofer upper plate temperature distribution

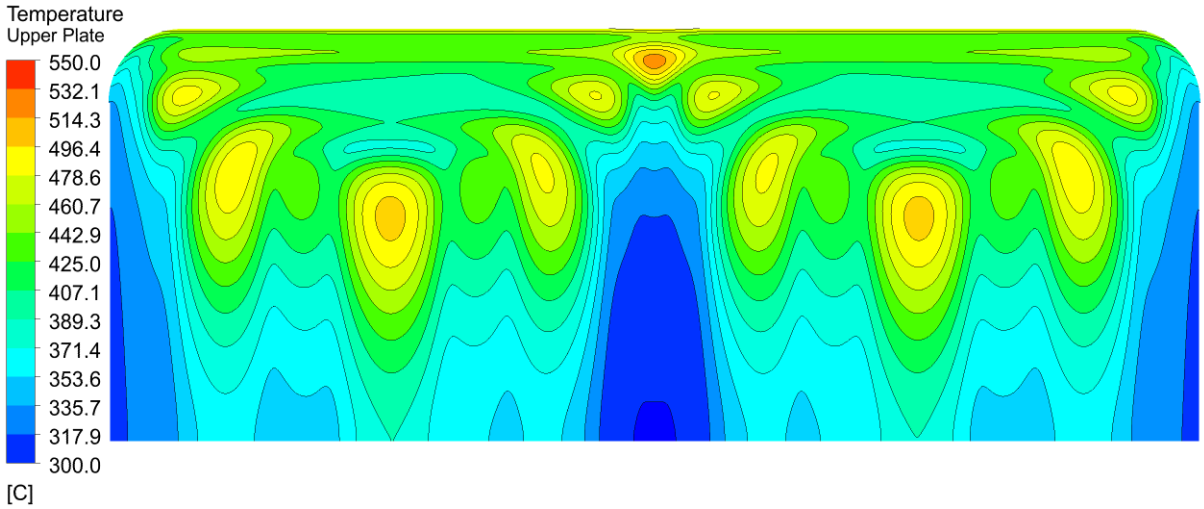

Fig. 4.40 – WCLL V0.6_FW4_R case #2 Eurofer upper plate temperature distribution

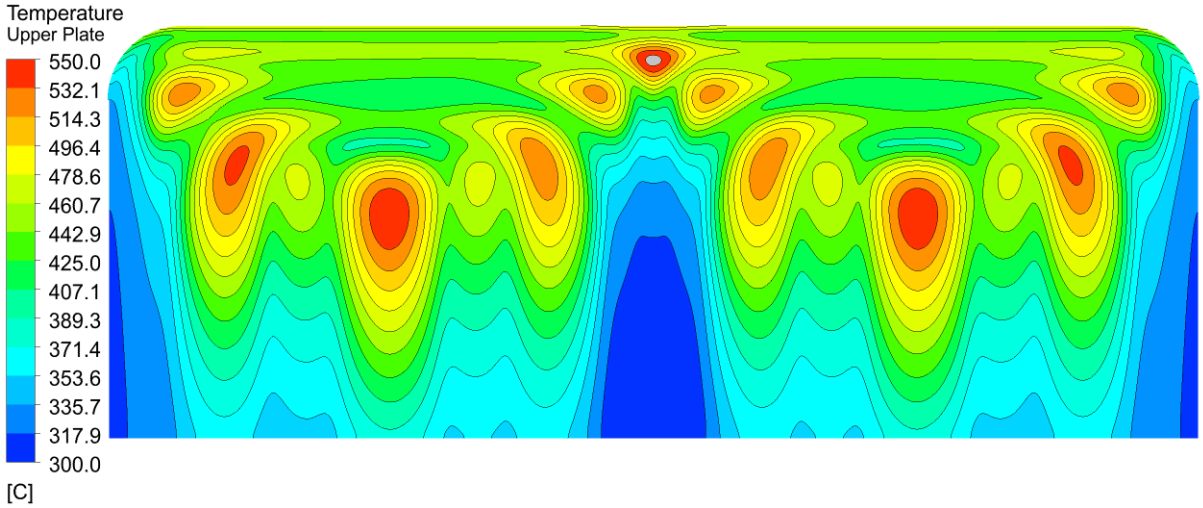

Fig. 4.41 – WCLL V0.6_FW4_R case #3 Eurofer upper plate temperature distribution

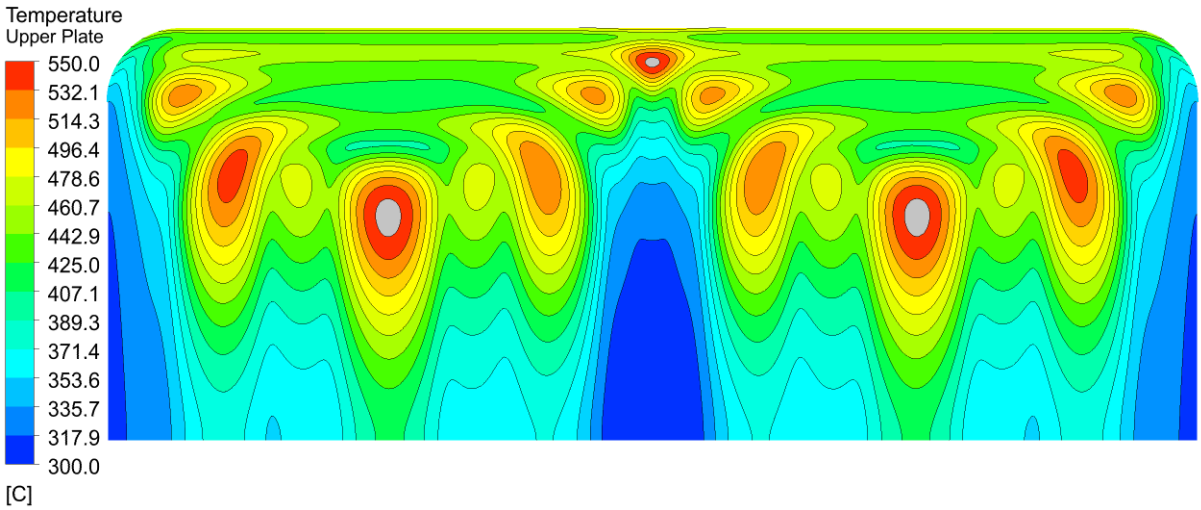

Fig. 4.42 – WCLL V0.6_FW4_R case #4 Eurofer upper plate temperature distribution

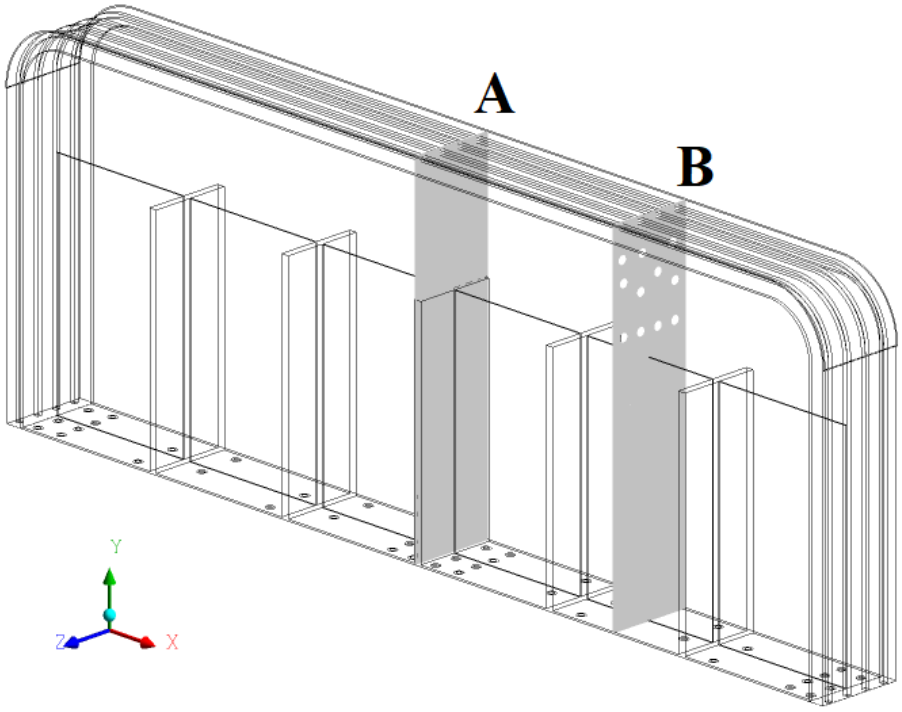

Fig. 4.43 – WCLL V0.6_FW4_R radial poloidal plane

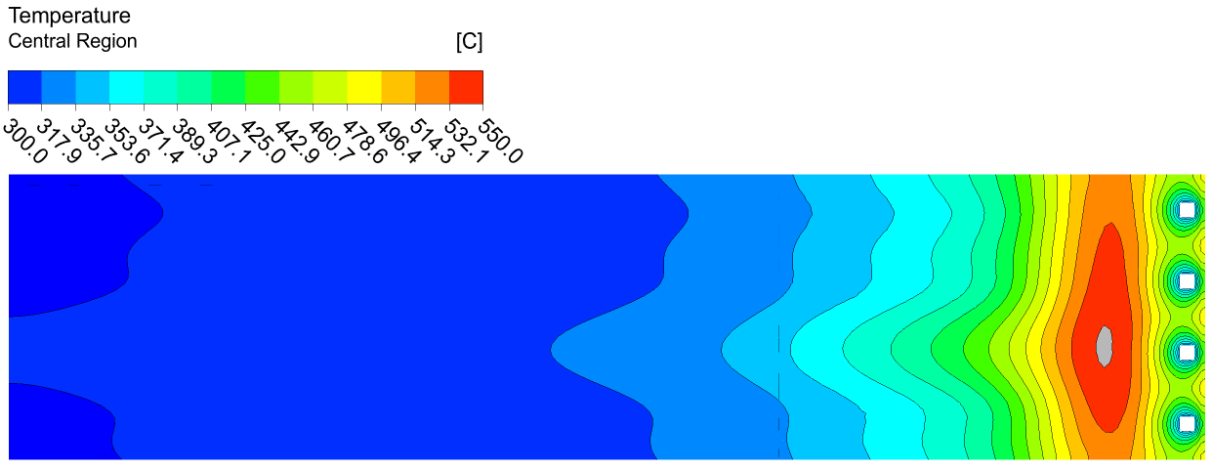
Temperature
Central Region
[C]
300.0
317.9
335.7
353.6
371.4
389.3
407.1
425.0
442.9
460.7
478.6
496.4
514.3
532.1
550.0

a) Run #1

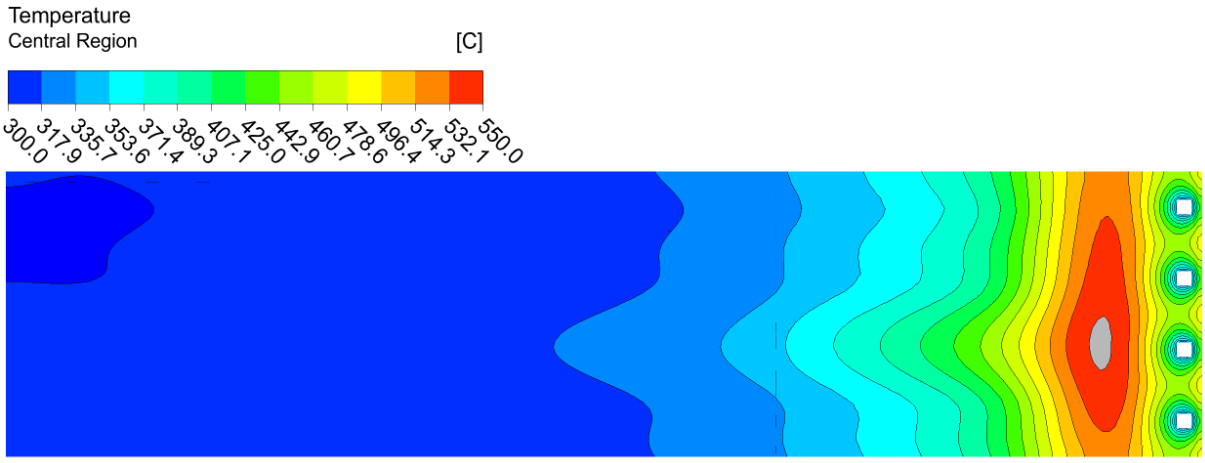
Temperature
Central Region
[C]
300.0
317.9
335.7
353.6
371.4
389.3
407.1
425.0
442.9
460.7
478.6
496.4
514.3
532.1
550.0

b) Run #2

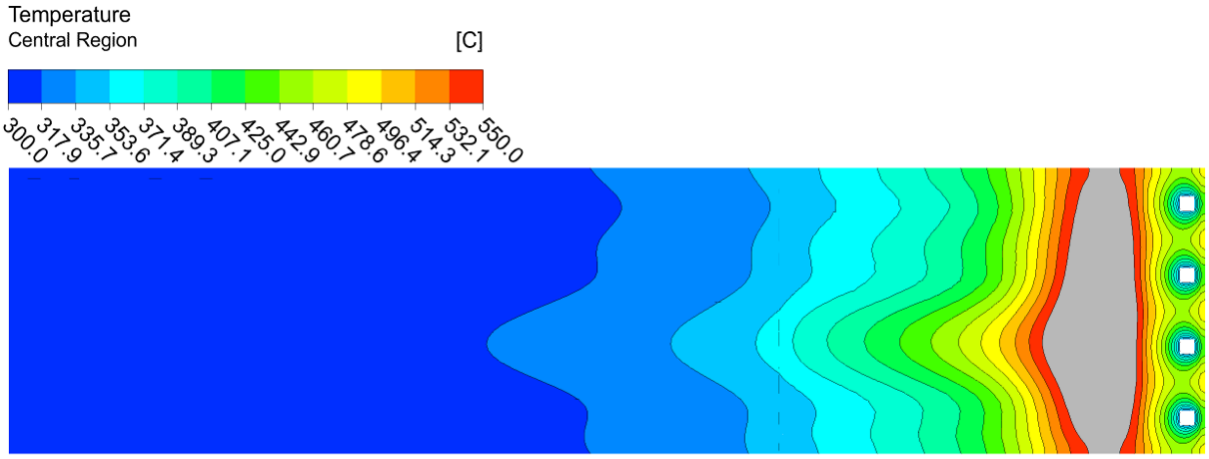

c) Run #3

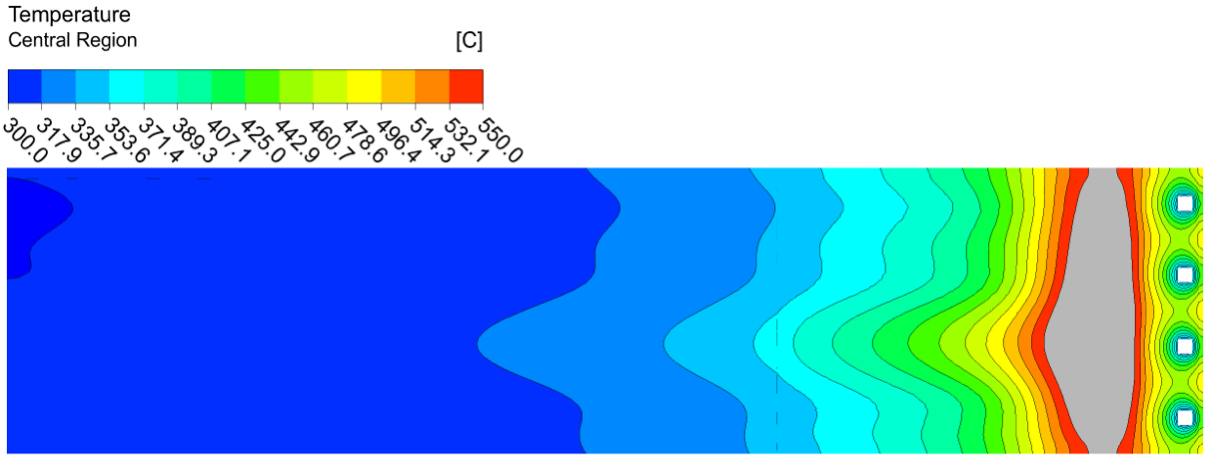

d) Run #4

Fig. 4.44 – Plane A temperature trend

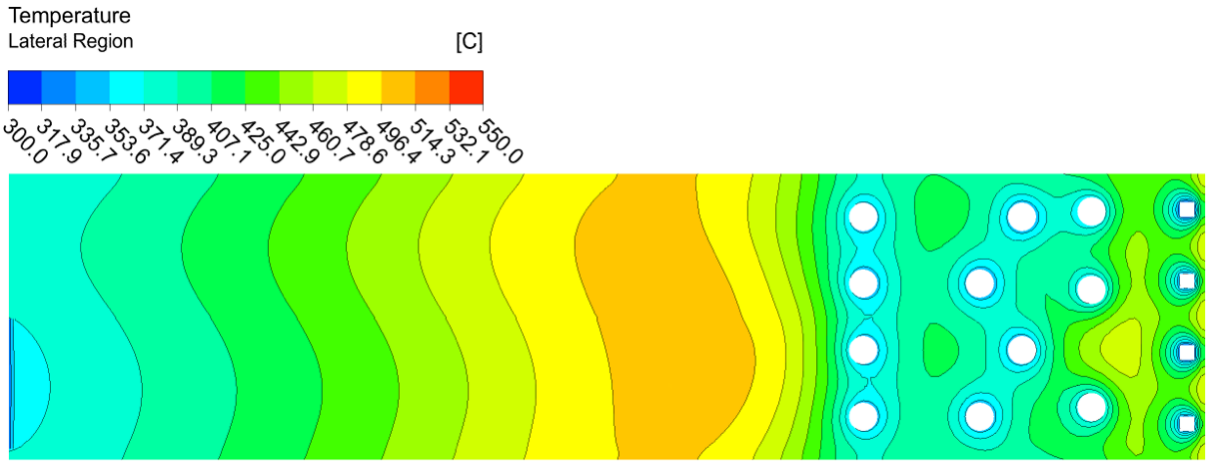
Temperature
Lateral Region
[C]
300.0
317.9
335.7
353.6
371.4
389.3
407.1
425.0
442.9
460.7
478.6
496.4
514.3
532.1
550.0

a) Run #1

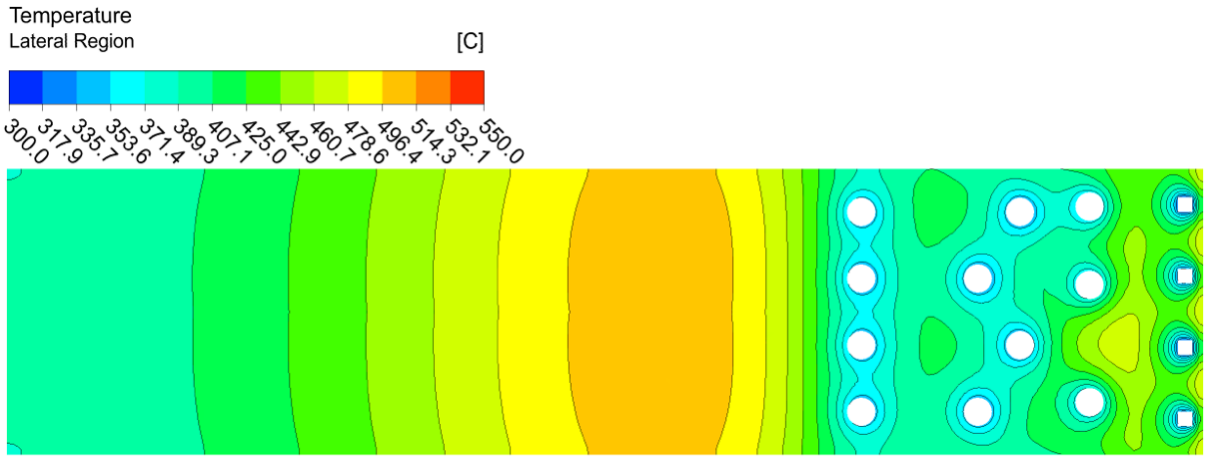
Temperature
Lateral Region
[C]
300.0
317.9
335.7
353.6
371.4
389.3
407.1
425.0
442.9
460.7
478.6
496.4
514.3
532.1
550.0

b) Run #2

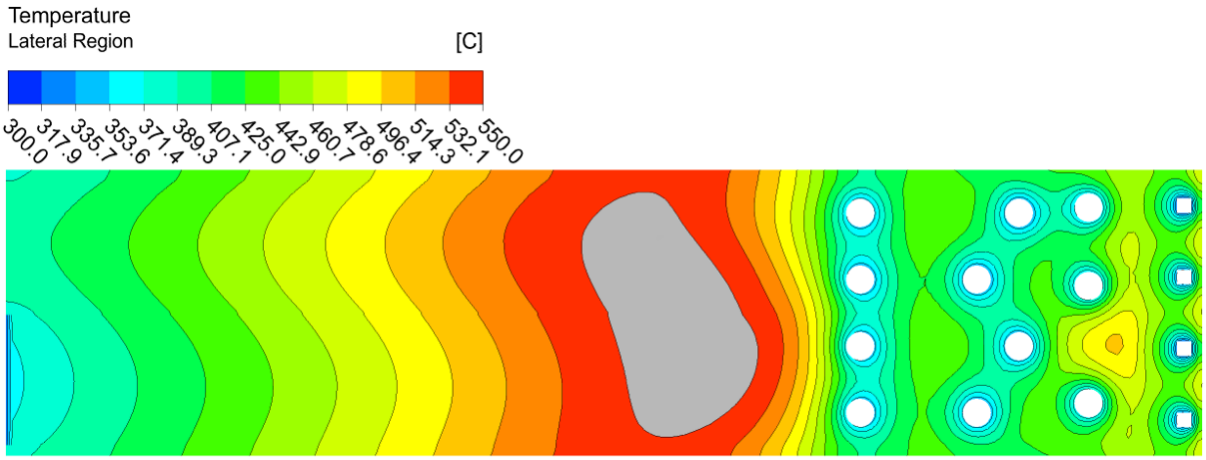

c) Run #3

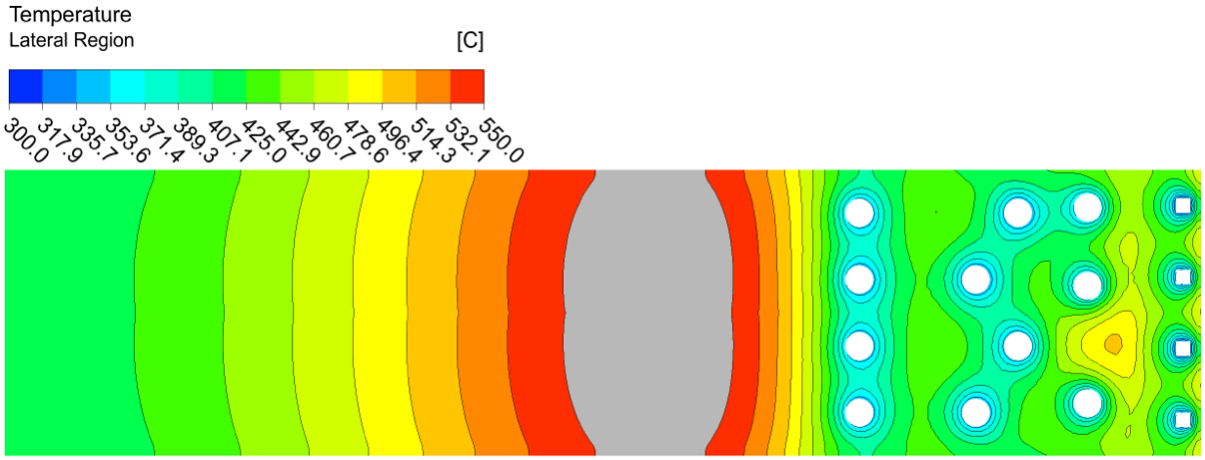

d) Run #4

Fig. 4.45 – Plane B temperature trend

4.6.3. Summary

The effects of the heat transfer modelling approach, in the assessment of WCLL thermal performances, have been evaluated firstly evaluate on the V0.6 and secondly on the V0.6_FW4_R layout.

The choice of the PbLi thermal conductivity correlation deeply affects the numerical predictions and, in particular, the Mogahed correlation returns a significantly lower thermal field than that obtained by means of the IAEA correlation. As a consequence of this, the Eurofer temperature meets the design requirements only whether predicted with the Mogahed correlation, exceeding the limit of 550°C in the case where IAEA correlation is adopted, no

matter of the numerical method followed for its calculation (FEM and/or FVM) or the PbLi state (fluid and/or solid). The V0.6, with its FW layout, is able to obtain a temperature range below the required limit at least in the upper plate and with PbLi modelled as fluid, albeit the baffle plate exceeds the limit. The new reference IAEA PbLi thermal conductivity correlation, adopted in the V0.6_FW4_R model, returns a thermal field that exceeds the limit temperature in both cases. The FW, with its 4 channels, has a less passive heat removal, which affects the frontal thermal field of the structures. In fact, in the V0.6_FW4_R models, the Eurofer exceeds the temperature limit in the plates even in the case of fluid PbLi. Comparing the two models, fluid with fluid, and solid with solid, more marked differences in the case of solid PbLi are noted. As a consequence of this, to perform a conservative analysis, solid PbLi should be adopted.

As to the impact of the numerical methods adopted for the thermal assessment, it can be stated that between the FEM and the FVM approach, whether adopted for a pure diffusive heat transfer analysis, even if there is no substantial variation in the results obtained, there is a strong difference in the requested computational effort, since FVM calculations take typically a longer computing time than the FEM ones. Therefore, as a first instance, it is advisable to use a FEM calculation to get an idea of the thermal field under examination. Moreover, it has been noted from the analyses that the simulation of PbLi as a solid domain reduces the calculation times in FVM analysis. A simplification that can be, hence, used to investigate some critical phenomena that might occur in the DWTs water or in the FW channels, such as critical heat flux occurrence or excessive flow velocities.

Regarding the approach adopted to model heat transfer occurring within water coolant and liquid breeder, it has been observed that the realistic simulation of coolant convection, instead of the assumption of convective boundary conditions, improves the prediction of the thermal field spatial distribution, slightly impacting its maximum values, while the proper simulation of PbLi flow with its convective-diffusive heat transfer process leads to greater changes in the predicted thermal field, both in terms of spatial distribution and maximum values, compared with the efforts obtained from the transition from purely conductive to water modelled. These larger changes are reputed to be such at least in the absence of buoyancy effects.

In conclusion, a further investigation is deemed appropriate to assess the effects of buoyancy forces and MHD effect on the PbLi thermal and fluid-dynamic performances.

Finally, as regards the V0.6_FW4_R layout, it can be stated that the BZ double-wall tubes have to be reshuffled to extinguish the hot spots onset, both in plates and baffle. With the new PbLi thermal conductivity as reference property, the Eurofer temperature requirement is no more achieved, exceeding the limit of 550°C, no matter of the PbLi modelling approach, fluid or solid. A further investigation is mandatory to carry out new DWTs arrangement to extinguish the hot spot onset into the Eurofer structures.

4.7. BZ system optimization – From V0.6 to V0.6_B

The main objective of this study is to optimize the DWTs layout of the COB equatorial elementary cell by modifying the layout of the tube to extinguish the hot spots in the Eurofer structures come out from Sect. 4.6.2, ensuring adequate refrigeration. Moreover, the analysis focuses on evaluating the water performance of the BZ and FW systems, in order to verify suitable thermodynamic conditions for the PHTS. For simplicity, the previous configuration V0.6_FW4_R will only be named as V0.6. The study is aimed to compare three specific different tubes arrangement of the BZ system: the V0.6, that is the reference configuration, the V0.6_A and V0.6_B, identifying and discussing advantages and key issues from the thermal-hydraulics point of view.

The analyses have been carried out using a CFD approach, adopting the commercial ANSYS CFX code. Thus a 3D finite volume model of each configuration has been developed. For each WCLL design, several steady-state analyses have been performed, to evaluate the Eurofer temperature field and the thermal-hydraulics performances under different cooling configuration, changing the position of the DWTs. In the present analysis, for completeness of information, some of the results already obtained for V0.6 (previous V0.6_FW4_R model with IAEA PbLi thermal conductivity) will be reported again.

4.7.1. Numerical models and mesh

As mentioned above, the COB elementary cell has a toroidal extension of 1500 mm and a radial dimension reduced to 567 mm, thus neglecting the section covering the manifold and back supporting structure, where heat loads are foreseen to be negligible. The poloidal dimension of the model is clipped to a height of 135 mm, limited by the plates, which is representative of a single elementary cell.

Three different models with different BZ tubes layout are evaluated for steady-state analyses, varying the position of the tube arrays. The first numerical model is based on the most updated layout, the V0.6. The second and the third configuration, V0.6_A and V0.6_B, respectively, present a different BZ tubes layout. The V0.6_A configuration foresees a radial lengthening to the FW of the first array of 5 mm, and a toroidal length reduction of 33 mm of the first and

second array to increase the side walls distancing. The V0.6_B changes further the first and second array toroidal length, by reducing 5 mm more from the V0.6_A layout; moreover, the layout of the pipes has been modified enhancing the radial extension of the second array by 5 mm, moving forward to the first array. Concerning the third array, it has been translated by 10 mm from the internal ribs, not modifying the overall tube length.

The main changes from the reference V0.6 have been reported in Fig. 4.46. The main geometrical parameters of the three BZ tubes layout are reported in Table 4.30.

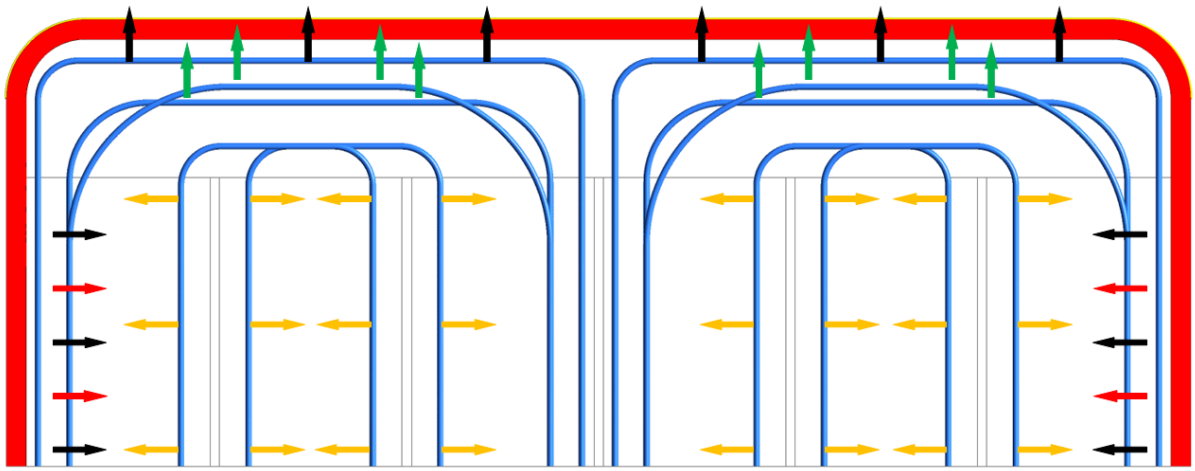

Fig. 4.46 – WCLL V0.6 tubes layout optimization (black arrows – V0.6_A; red, green and yellow arrows – V0.6_B)

Group [-]	Tube [-]	Curve radius [mm]	***V0.6***		***V0.6_A***		***V0.6_B***	
			FW dist [mm]	Tube Length [mm]	FW dist [mm]	Tube Length [mm]	FW dist [mm]	Tube Length [mm]
1st array	Tube 1	50	20.0	1672.58	15.0	1649.58	15.0	1644.58
	Tube 2	50	20.0	1672.58	15.0	1649.58	15.0	1644.58
	Tube 3	50	20.0	1672.58	15.0	1649.58	15.0	1644.58
2nd array	Tube 4	100	73.0	1443.66	73.0	1410.66	68.0	1415.66
	Tube 5	200	53.0	1397.82	53.0	1364.82	48.0	1369.82
	Tube 6	100	73.0	1443.66	73.0	1410.66	68.0	1415.66
	Tube 7	200	53.0	1397.82	53.0	1364.82	48.0	1369.82
3rd array	Tube 8	50	128.25	1010.08	128.25	1010.08	128.25	1010.08
	Tube 9	50	128.25	1010.08	128.25	1010.08	128.25	1010.08
	Tube 10	50	128.25	1010.08	128.25	1010.08	128.25	1010.08
	Tube 11	50	128.25	1010.08	128.25	1010.08	128.25	1010.08

Table 4.30 – WCLL V0.6 tubes layout optimization different models and geometrical parameters

To perform the analysis, an appropriate mesh has been defined, allowing accurate results and reasonable calculation time, in accordance with the mesh independence study performed and proved in Ref. [47]. Nevertheless, the model has further better defined with several bodies of FW, PbLi and stiffeners domains, to find the best geometry discretization optimizing the number of elements. The numerical model has been developed as a single part, to simulate the heat transfer between the multiple components, solids and fluids, using a conformal mesh. Hexahedral and tetrahedral elements were adopted in the models, considering the geometrical features of the domains, many and different local controls are inserted to define the complex geometry of the cell properly. For the resolution of the viscous sub-layer (y^+=1) of the water, the inflation layer has been set, based on a maximum water velocity of 7 m/s.

A mesh detail is shown in Fig. 4.47, and the mesh statistics of each numerical model are reported in Table 4.31.

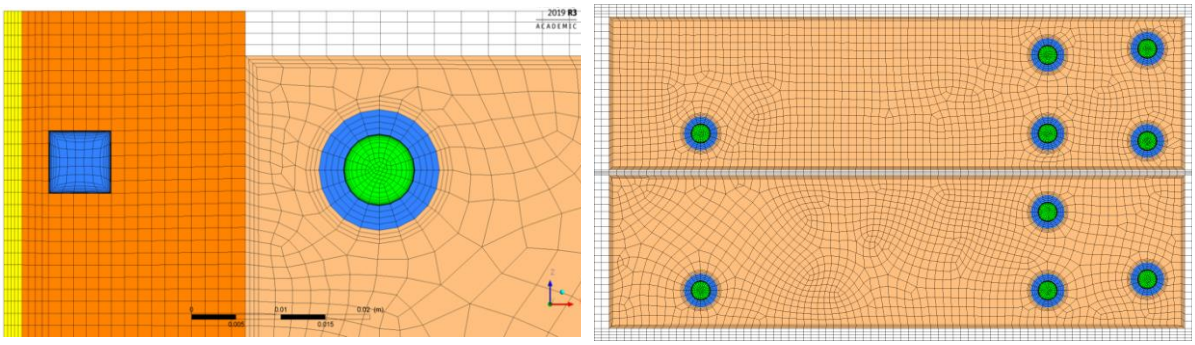

a) FW and BZ water domain b) PbLi and stiffeners domain

Fig. 4.47 – WCLL V0.6 tubes layout optimization mesh detail

Parameters	**Models**		
	V0.6	***V0.6_A***	***V0.6_B***
N° Nodes	14.65 M	15.97 M	15.02 M
N° Elements	19.76 M	19.38 M	19.41 M
Ave Orth Qual	0.842	0.852	0.852
Ave Skewness	0.180	0.180	0.179

Table 4.31 – WCLL V0.6 tubes layout optimization mesh statistics

4.7.2. Solver settings and boundary conditions

To evaluate the Eurofer temperature field and the thermal-hydraulic performances of the BZ and FW cooling systems, verifying the reliability to deliver the coolant at the design temperature of 328°C to the PHTS, and to properly refrigerate the Eurofer structures not exceeding the imposed limit of 550°C, different models of the elementary cell have been set up for the CFD analysis. The 3D finite volume models have been developed according to Sect. 4.7.1, using ANSYS CFX v18.2 code, to realistically reproduce the geometry and flow features of WCLL COB equatorial elementary cell and to obtain a complete and detailed temperature distribution, both in the fluid and the solid domains. In these analyses, fluid domains for BZ and FW water, and solid domains for Eurofer structures, FW Eurofer chase and Tungsten armor have been modelled. Regarding the PbLi domain, it has been modelled as a solid domain, as suggested from the main outcomes of Ref. [79] and Sect. 4.6.3, to perform a conservative analysis. The thermo-physical properties of the above-mentioned materials have been implemented in the CFX code by means of fixed value or polynomial fitting data functions

according to Sect. 4.1, where have been reported. It is recalled that, as regards the PbLi, a newer reference thermal conductivity, IAEA's correlation [66], is adopted.

To evaluate the thermal power deposition into the models under analysis, power deposition curves have been implemented representing the volumetric power density into materials and a nominal heat flux of 0.32 MW/m^2 have been applied onto the straight Tungsten armor surface with a linearly decreasing function to account the decrease in the normal component of the elbows. Both power contributions, power density and heat flux have been reported and discussed in Sect. 4.2.

As regards the imposed water mass flow rate, the total amount has been evaluated through the enthalpy balance, corresponding to 1.4868 kg/s. Since the total deposited power varies with the BZ tubes arrangement, it has deemed acceptable to set for all the models the V0.6 mass flow rate, due to a very low power deposition differences evaluated only in the V0.6_A model (Table 4.32), corresponding in a 0.02% of error. The BZ cooling system has an imposed water mass flow rate of 57.5%, firstly equally divided by the fourteen tubes of the first and second arrays and then equally divided by the eight tubes of the third array (Fig. 4.48 a). Thus, the FW water mass flow rate is the 42.5%, equally distributed on the four channels (Fig. 4.48 b).

The other boundary conditions adopted for all the models are:

- Periodic boundary conditions on the upper and lower surfaces of upper and lower stiffening plates, FW and Tungsten layer, in poloidal direction, to simulate the presence of adjacent elementary cell;
- Adiabatic condition to back walls of FW, stiffeners, Tungsten layer and FW side walls;
- Mass flow rate and static pressure imposed in the fluid domain at inlet and outlet sections, respectively;
- No-slip condition at the interface between coolant and the circuit steel walls;

The two equations k-ω Shear Stress Transport (SST) model has been set to simulate the water turbulence effects, as demonstrated in Refs. [69][81].

A detailed set of the imposed boundary conditions is reported in Fig. 4.48.

System	Region	Models			Unit
		V0.6	***V0.6_A***	***V0.6_B***	
BZ	*PbLi*	170.387	170.416	170.351	kW
	Tubes	3.214	3.212	3.250	kW
	Stiffeners	7.937	7.937	7.937	kW
	BZ Total	*181.538*	*181.565*	*181.538*	*kW*
FW	*FW*	34.656	34.656	34.656	kW
	Tungsten	6.694	6.694	6.694	kW
	Tung HF	56.160	56.160	56.160	kW
	Tung HF$_{SW}$	8.810	8.810	8.810	kW
	FW Total	*106.320*	*106.320*	*106.320*	*kW*
Total		***287.858***	***287.885***	***287.858***	***kW***

Table 4.32 – WCLL V0.6 tubes layout optimization power distribution divided by models and domains

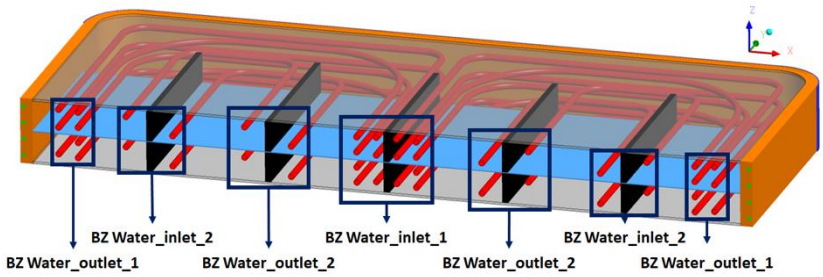

a) BZ Water inlet and outlet BCs

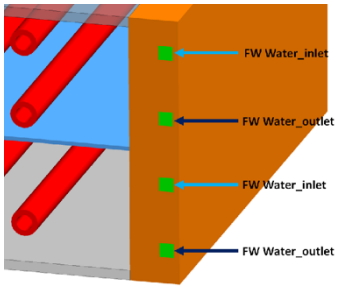

b) FW Water inlet and outlet BCs

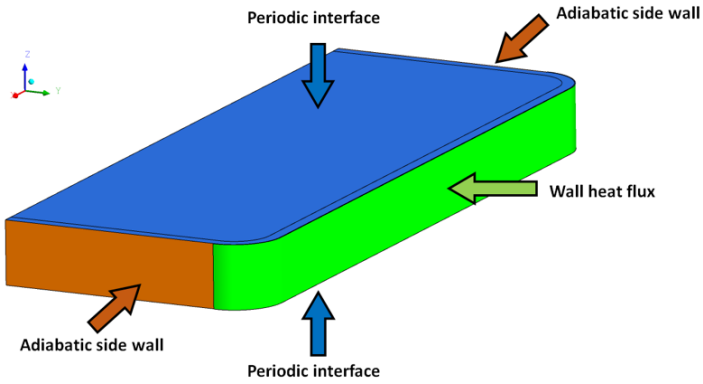

c) Different domain BCs

Fig. 4.48 – WCLL V0.6 tubes layout optimization equatorial elementary cell boundary conditions [81]

4.7.3. Results

The results of the three runs performed are discussed below. The models differ by the position of the BZ double-wall tubes. The analyses have been performed in steady-state conditions to optimize the layout of the tubes, obtaining a detailed temperature map of the Eurofer structures and evaluating the water thermal-hydraulic conditions.

The relevant parameters of the steady-state runs are reported in Table 4.33, where, it is clearly shown that the Eurofer temperature exceeds the maximum allowable value of 550°C in the V0.6 and V0.6_A configurations in all the plates, upper, lower and baffle. Concerning the V0.6_B layout, the Eurofer maximum temperature is below the limit for both plates, upper and lower; conversely, the baffle plate returns a maximum temperature of 552.1°C. The adopted recirculation manifold of the BZ water cooling system guarantees maximum water temperatures below the saturation temperature for the second and third arrays in all the cases, and slightly exceeds it in the first array. The BZ recirculation also ensures higher velocities, enhancing the cooling performances in all the arrays, obtaining comparable velocities in the first and second array and almost doubled in the third. The BZ pressure drops due to the recirculation are, however, reduced if compared with the FW cooling system, which turns out to be 5 times higher. All the three configurations provide as water average outlet temperature, for both BZ and FW cooling systems, of 328°C.

The obtained results are hereafter discussed, divided by models.

#	Parameters	Configuration			Unit
		V0.6	***V0.6_A***	***V0.6_B***	
1	Tungsten T_{max}	488.8	485.5	485.5	°C
2	FW T_{max}	513.9	505.0	504.8	°C
3	Upper Plate T_{max}	557.5	557.4	543.7	°C
4	Lower Plate T_{max}	557.7	557.6	543.9	°C
5	Baffle T_{max}	566.2	566.2	552.1	°C
6	PbLi T_{max}	600.7	587.6	584.7	°C
7	FW Water_outlet T_{ave}	328.2	328.3	328.4	°C
8	FW Water T_{max}	363.0	363.1	363.2	°C
9	BZ Water_outlet_2 T_{ave}	328.1	328.0	327.9	°C
10	BZ Water 1st array T_{max}	352.7	354.7	353.3	°C
11	BZ Water 2nd array T_{max}	342.3	338.2	337.8	°C
12	BZ Water 3rd array T_{max}	341.2	341.2	341.9	°C
13	FW Water_outlet v_{ave}	4.923	4.924	4.925	m/s
14	FW Water v_{max}	5.817	5.819	5.820	m/s
15	BZ Water_oulet_2 v_{ave}	3.294	3.293	3.292	m/s
16	BZ Water 1st array v_{max}	2.167	2.176	2.170	m/s
17	BZ Water 2nd array v_{max}	2.111	2.103	2.104	m/s
18	BZ Water 3rd array v_{max}	3.975	3.965	3.965	m/s
19	FW Water_inlet P drop	41.526	41.107	41.115	kPa
20	BZ Water_inlet_1 P drop	4.084	4.009	4.008	kPa
21	BZ Water_inlet_2 P drop	7.918	7.896	7.899	kPa

Table 4.33 – WCLL V0.6 tubes layout optimization main output parameters [81]

Regarding the reference layout V0.6, as reported, the Eurofer maximum temperature exceeds the imposed limit of 550°C. Given the results obtained in Sect. 4.6, where the two thermal conductivity of the PbLi Mogahed and IAEA are compared and where the latter reaches a Eurofer temperature field of the plates about 50 degrees higher than the Mogahed's one. This analysis has been performed with conservative boundary conditions allowing the BZ tubes optimization to extinguish the hot-spots onset into the Eurofer structures.

Regarding the structural materials, the V0.6 returns a symmetrical temperature field in toroidal direction and concerning the FW system also in the poloidal length, due to the opposite and alternate flow of the water and the constant poloidal pitch of the channels (Fig. 4.49 a). The configuration results below the required limit of 1300°C for the Tungsten layer, and regarding the Eurofer limit, only the FW chase satisfy the requirement reaching a maximum temperature of 513.9°C. In Fig. 4.49 (b), a radial-poloidal cut at the middle of the FW toroidal length shows that the internal part of the FW (FW-BZ interface) is warmer than the external region (FW-Tungsten interface). Comparing the FW system with that described in Ref. [71] and Sect. 4.4, Fig. 4.49 (b) shows a different temperature field. In the present analysis, (FW system with 4 water channels) a maximum temperature 50 degrees higher than the value previously reported is reached. The two plates slightly exceed the limit, as opposed to the baffle which exceeds it by 16.2 degrees. In order to evaluate the temperature distribution into the plates, the Eurofer lower plate temperature field has been reported in Fig. 4.50, where the grey regions exceed the maximum allowable temperature of 550°C. As shown, the FW chase is below the requirement, and two hot spot regions in the plate are shown. The first one is located in the frontal part near the BZ-FW interface, caused by the curvature of the first tube array and an FW detachment of 20 mm; the second hot region is at the end of the baffle plate, in the middle of the sub-unit of the cell, where the tubes of the third array are 20 mm distanced from the ribs structures and their influence on the central region is weak, thus causing the onset of a hot spot. Moreover, the side walls region is well cooled and stands around 350°C.

Considering the FW and BZ water coolant systems, as expected, the water outlet temperatures, averaged on the mass flow rate and the overall outlet tube sections, are very similar: 328.2°C and 328.1°C respectively. The first array and the FW channels exceed the saturation temperature value (344.8°C at 15.5 MPa), but they do not incur in thermal crisis, thanks to a large and safety margins from the CHF by 3.1 (CHF=3.42 MW/m^2) and 3.9 (CHF=2.76 MW/m^2) times lower for the FW channels and the first tubes array respectively.

Regarding the PbLi, in Fig. 4.43, two different radial poloidal cuts are presented. The Fig. 4.51 (a), in correspondence with the frontal hot spot (Plane A), shows how the curvature radius of the first tube array causes a hot column region above 550°C which impacts the two Eurofer plates. Moreover, it shows how the FW system contributes to cool down that region, limiting the hot spot radial extent. In the figure, it is also reported how the central rib is refrigerated by the DWTs inlet, returning a temperature distribution more than 200 degrees below the imposed limit. The Fig. 4.51 (b), located at the baffle plate hot spot (Plane B), shows a wider central hot spot column, where the third tubes array has no influence on the Eurofer structures.

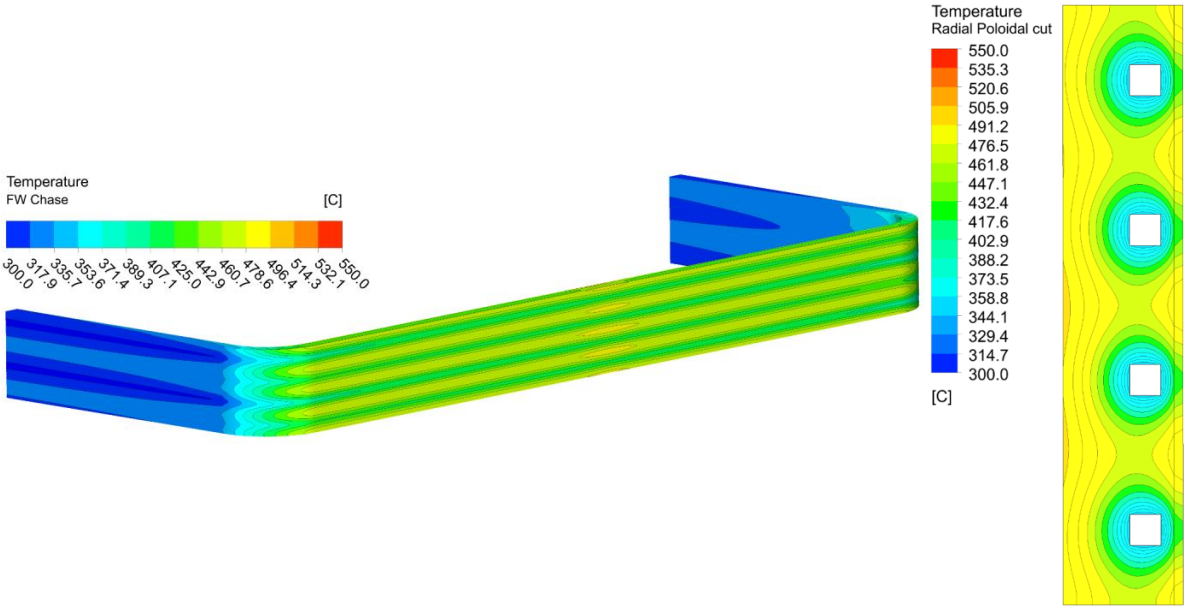

a) FW Eurofer chase temperature field

b) FW system radial poloidal view at half toroidal length

Fig. 4.49 – WCLL V0.6 elementary cell FW chase temperature distribution [81]

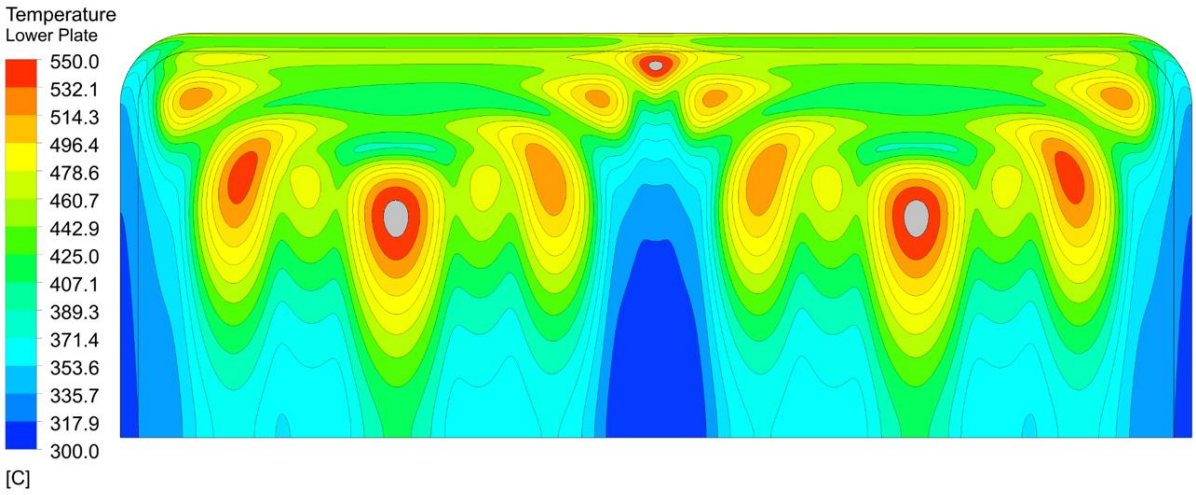

Fig. 4.50 – WCLL V0.6 elementary cell lower plate temperature distribution [81]

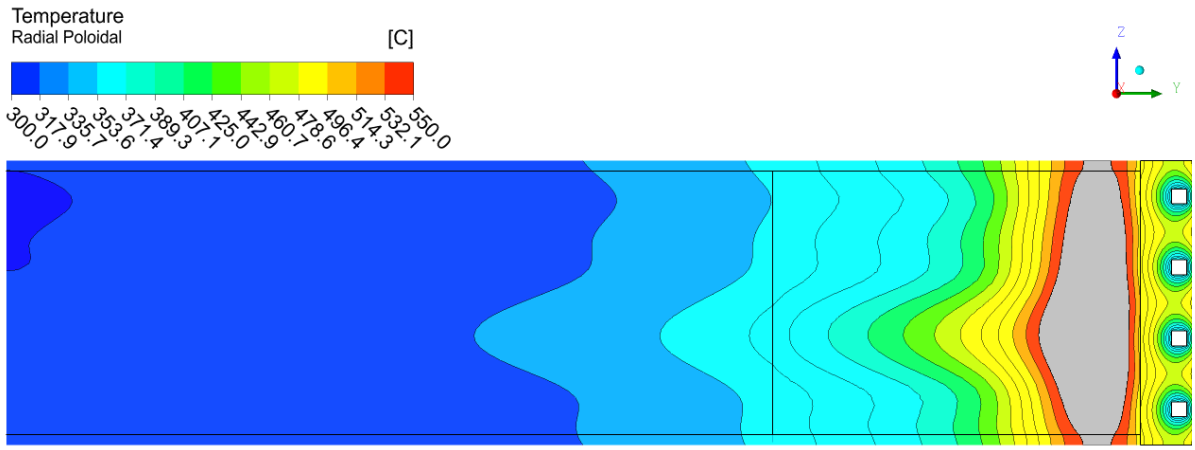

a) Radial poloidal view at Plane A

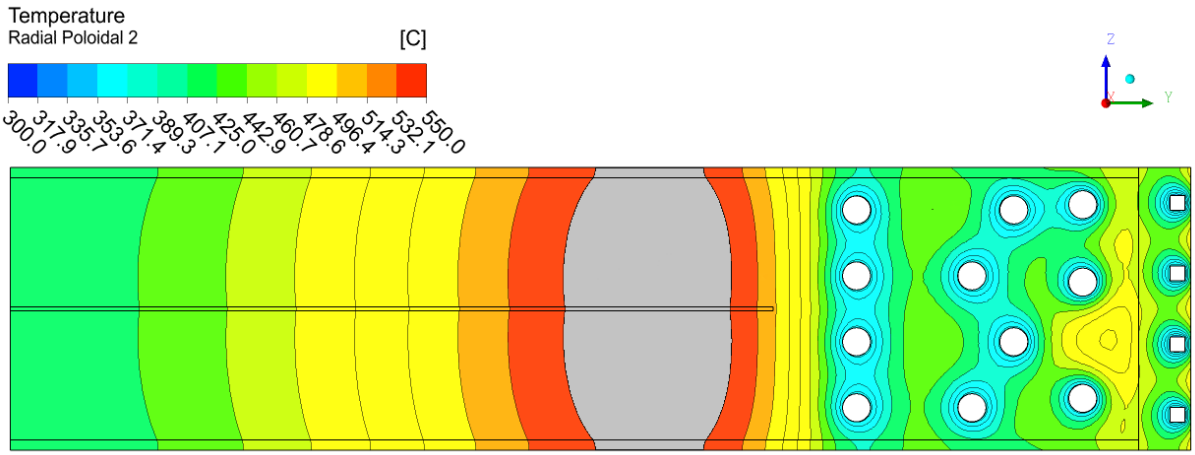

b) Radial poloidal view at Plane B

Fig. 4.51 – WCLL V0.6 elementary cell radial poloidal plane temperature distribution [81]

Regarding the V0.6_A optimization, which provides the reduction of the first tubes array detachment from the FW and the reduction of the toroidal length of the first and second arrays, it returns an improved, but still not entirely satisfactory temperature field. The Eurofer structures of the elementary cell V0.6_A, as in the previous case, have a symmetrical temperature field. The decrease of the distance between the first tubes array and the FW chase, achieves the refrigeration of the frontal hot spot, obtaining a temperature lower than the fixed limit of 550°C, as shown in Fig. 4.52. With the reduction of the toroidal tube length, the hot spot at the baffle plate is still present, as in the previous V0.6 case. As shown from the temperature field of the lower plate, it is clear that reducing the tubes toroidal length, the temperature field in the upper corner near the side walls bent increases, albeit within the limit.

The FW system benefits from the distance reduction between the first tubes array and FW chase, decreasing its maximum temperature by about 9 degrees. The maximum temperature of Tungsten is not affected by the variation of the BZ tubes: a slight decrease of only 2 degrees has been calculated. The temperature distribution of the two domains of the FW system is shown in Fig. 4.53. The Fig. 4.53 (b) shows how the FW internal part is affected by the first array movement, the isotherm of the internal part are flatten towards the water channels running into the concentric isotherm generated by the water channels. A different trend has been obtained in Ref. [71] and Sect. 4.4.3.1, where the isothermal lines, obtained from the water channels, show a symmetrical airfoil trend starting from the Tungsten up to the internal part of the FW. A greater balance between the passive heat supplied by the BZ system and that generated in the FW is noted.

As expected, the average outlet temperature in both FW and BZ cooling systems is 328.3 and 328°C, respectively. The power variation does not change the water outlet conditions. The CHF is evaluated, like in the previous cases, obtaining 3.42 for the FW and 2.76 MW/m^2 for the BZ, values to be compared with actual ones 2.9 and 4.0 times lower in the two systems, respectively. Therefore, the V0.6_A has higher margin to avoid the thermal crisis.

The radial-poloidal temperature profile is shown in Fig. 4.54. The (a) reports that the reduction of the FW detachment of the tubes from the FW has reduced the frontal hot spot region, concentrating entirely within the PbLi and greatly reducing its area, but in (b) is clear that this BZ tubes layout had no effect on the baffle plate region, even enhancing the side walls detachment.

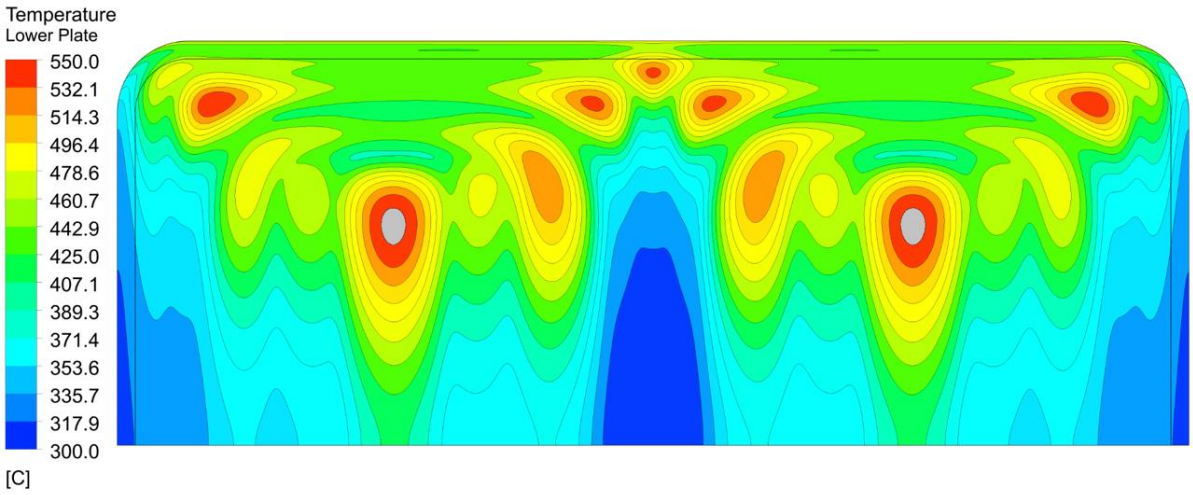

Fig. 4.52 – WCLL V0.6_A elementary cell lower plate temperature distribution [81]

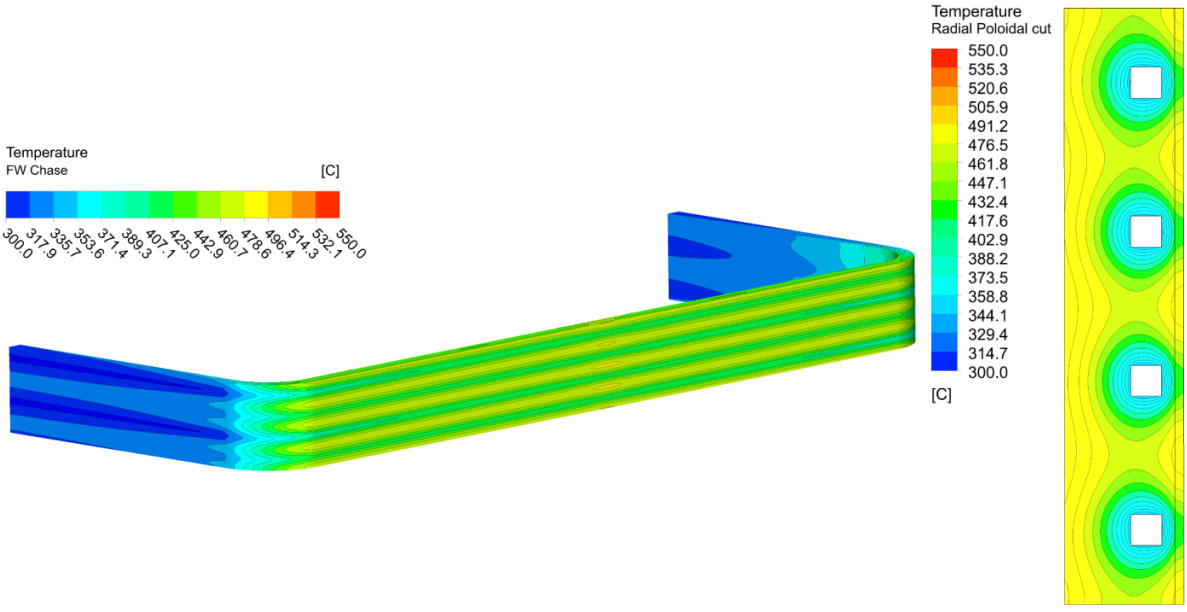

a) FW Eurofer chase temperature field

b) FW system radial poloidal view at half toroidal length

Fig. 4.53 – WCLL V0.6_A elementary cell FW system temperature distribution [81]

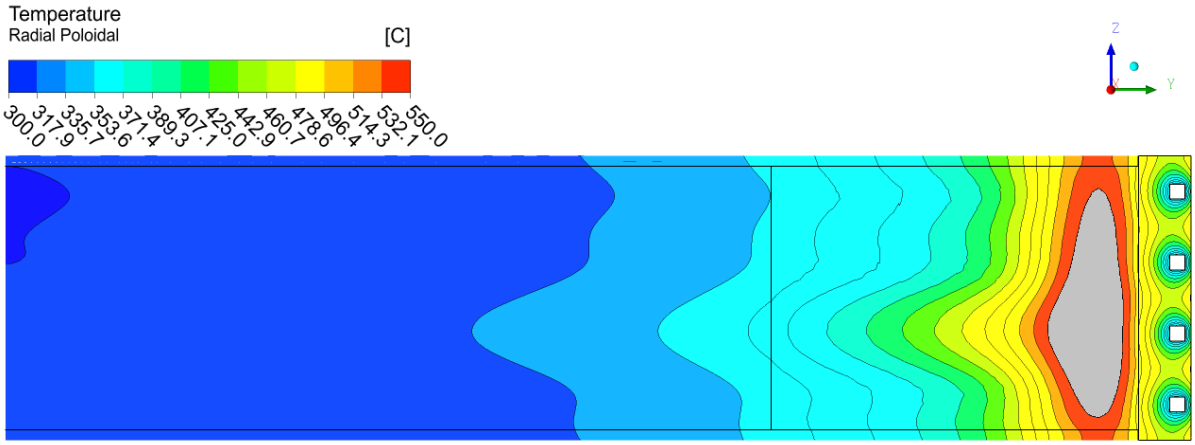

a) Radial poloidal view at Plane A

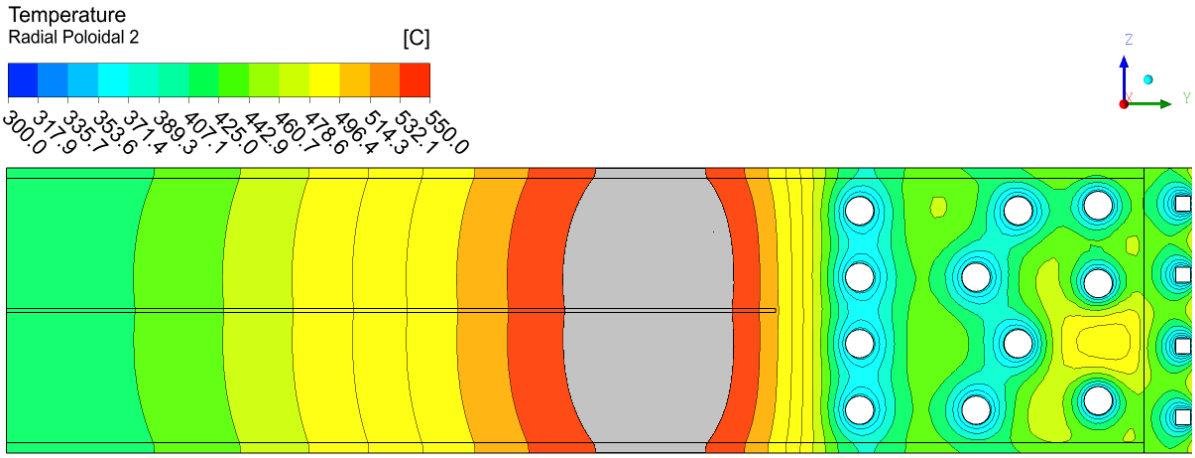

b) Radial poloidal view at Plane B

Fig. 4.54 – WCLL V0.6_A elementary cell radial poloidal plane temperature distribution [81]

The last analyzed BZ configuration V0.6_B, with a further toroidal length reduction of the first and second arrays, an increased radial path for the second tubes array and a rigid detachment from the ribs of the third array, as discussed in Sect. 4.7.1, returns a Eurofer temperature field below the imposed limit for the FW chase, upper and lower plates domains, as reported in Table 4.33; only the baffle plate exceeds by 2 degrees the temperature limit. The V0.6_B tubes layout extinguish all the hot spots presented into the plates, ensuring a maximum temperature, below the limit of 550°C, of about 7 degrees for both plates. The plates temperature field is toroidally symmetric, as in the previous analyses. The lower plate is shown in Fig. 4.55, where, the baffle plate hot spot region is not present; this implies that this BZ layout affects the baffle region of the previous version. Moreover, the hot spots in the upper corners near the sidewalls have reduced their area due to the radial length extensions of the second array that contributes to refrigerate those regions.

Regarding the FW system, the solid domain of FW chase and Tungsten present a maximum temperature of 504.8 and 485.5 °C, respectively. The maximum temperature value of the FW chase is higher than in the Tungsten layer, because of the BZ thermal interaction with the FW by passive heat exchange, heating the inside part of the latter (Fig. 4.56 a). Regarding the radial-poloidal temperature distribution, shown in Fig. 4.56 b, no significant variation compared with the V0.6_A has been evidenced.

As in the previous cases, the water mass flow rate was preliminarily evaluated to obtain the outlet conditions close to the design criteria (328°C) resulting 327.9 and 328.4, respectively for the BZ and FW cooling systems. The maximum temperature of the water reaches comparable values with the previous two cases, exceeding by about 19 degrees and 10 degrees the saturation temperature of the water at 15.5 MPa, in the FW and BZ system respectively. Since there was no variation in the imposed mass flow rate and inlet conditions, the CHF, of BZ first tubes array and FW channel, is the same of the previous version, obtaining in the present analysis maximum heat flux values of 0.68 and 1.18 MW/m^2, respectively.

To evaluate the presence of PbLi hot column, that can affect the structures temperature field, different radial poloidal cuts have been evaluated (Fig. 4.57): one (a) in the middle of the toroidal length; the second (b) and the third (c) in correspondence of the external and internal curvature path of the first and second arrays of tubes; the fourth (d) in the middle of the toroidal path of the third tubes array; and the fifth (e) cut placed in the hot region near the sidewall.

The temperature distribution of each single radial poloidal cut of the V0.6_B elementary cell is reported in Fig. 4.58. The first cut (Fig. 4.58 a) shows a temperature field very similar to the V0.6_A layout. This is because it is affected only by the first tubes array with its FW detachment and curvature radius that have not been modified. The second cut (Fig. 4.58 b) shows a hot region, above 550°C, inside the PbLi domain, distant from the Eurofer structures and located between the first and the second tubes array. As reported in (b), the hot regions into the Eurofer plates are in the range between 513 and 532°C, ensuring a large margin from the imposed limit of 550°C. The radial poloidal cut (c) shows a hot region located at the end of the baffle plate, which poloidally extends up to both plates, but within the limit. The fourth plane (d) returns a hot region above, both in the PbLi and in the baffle plate. The listed results Table 4.33 reports that the maximum temperature into the baffle plate is 552°C and Fig. 4.58 d shows that the region exceeding the limit (grey region) has been significantly reduced compared with the previous analyses. The last radial poloidal cut, near the sidewall, shows a hot spot region, above 550°C, within the PbLi domain. The hot spot has a grater elongation compared with the previous region and approaches, more than the others, the two plates. The plane (e) is near the end of the toroidal path of the BZ water, and this greatly influences the heat removal, as the water is warmer than in the previously analyzed regions. Having this area, however, Eurofer structures within the temperature limit.

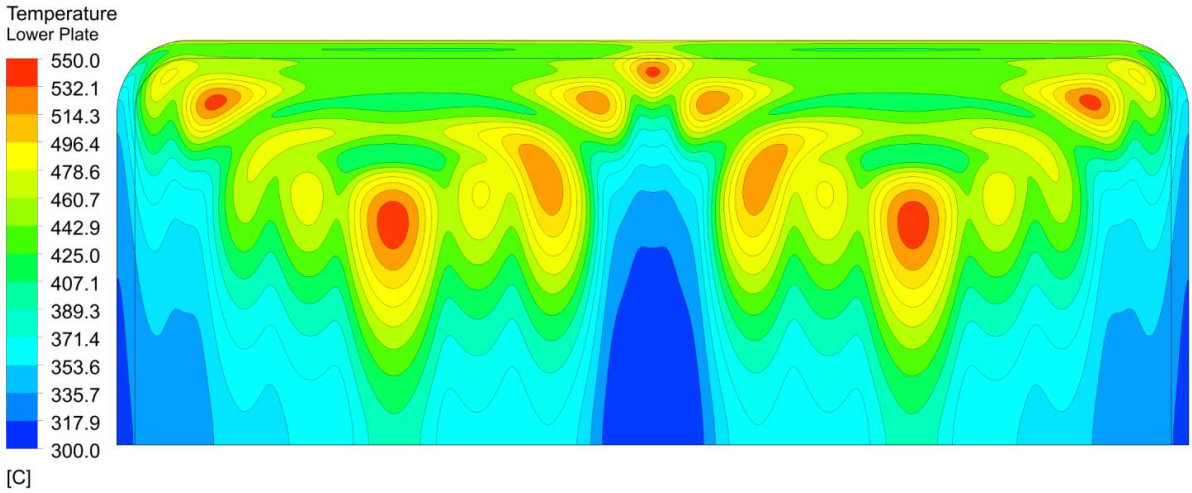

Fig. 4.55 – WCLL V0.6_B elementary cell lower plate temperature distribution [81]

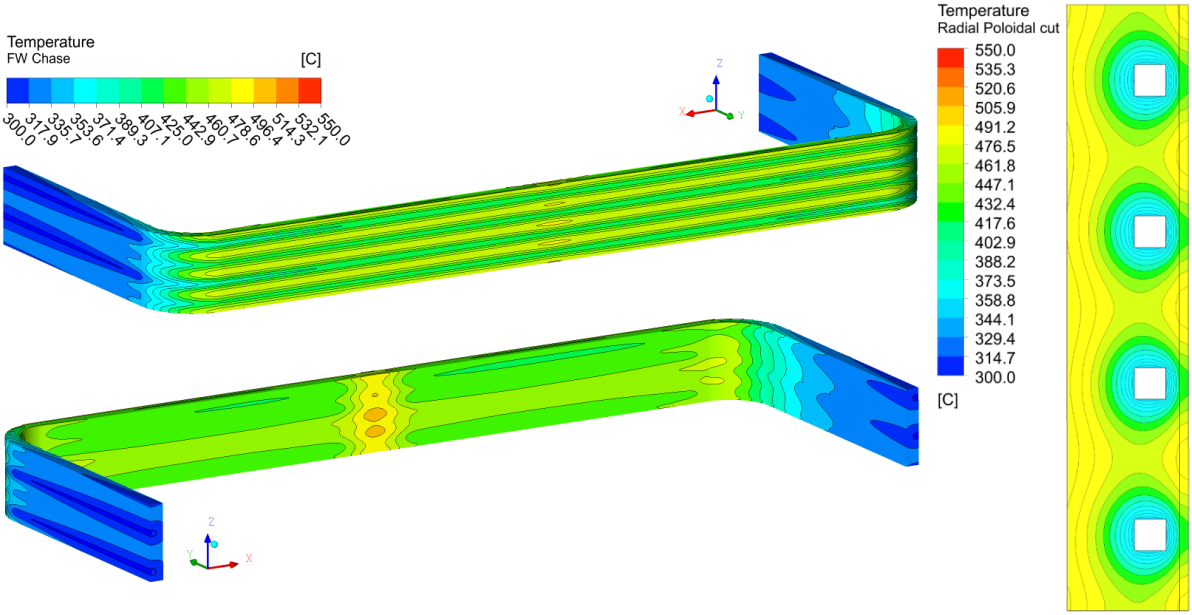

a) FW Eurofer chase temperature field

b) FW system radial poloidal view at half toroidal length

Fig. 4.56 – WCLL V0.6_B elementary cell FW system temperature distribution [81]

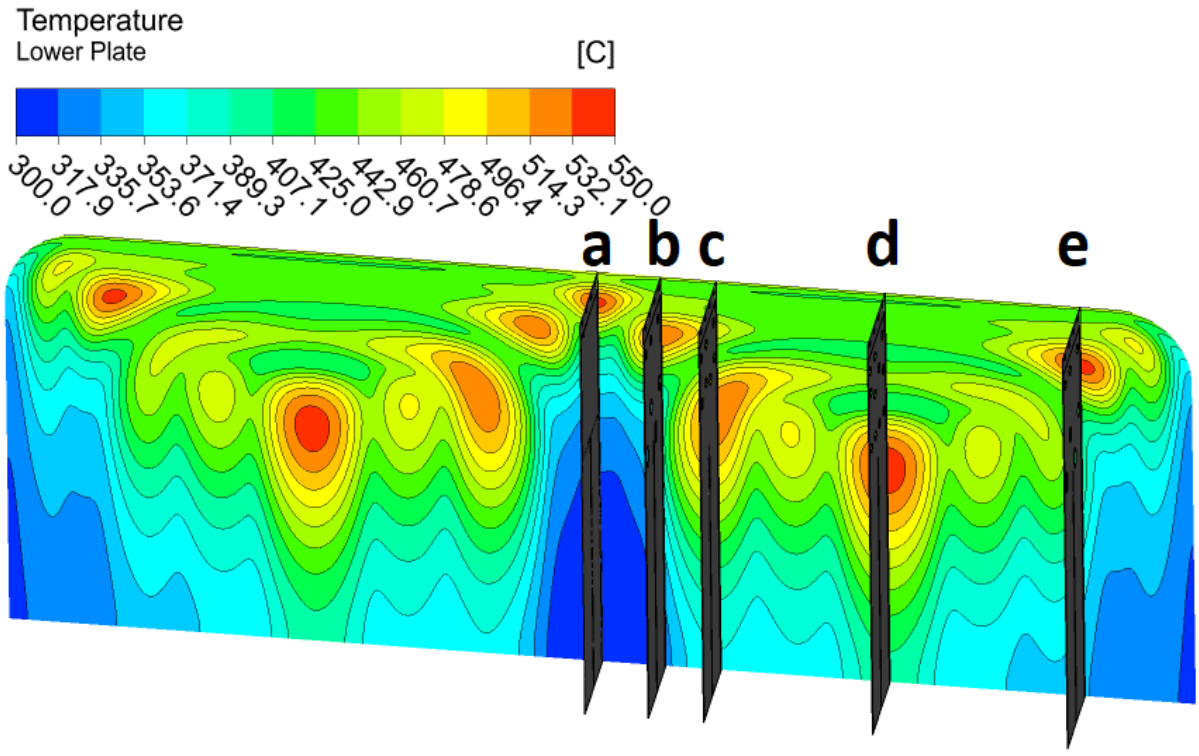

Fig. 4.57 – WCLL V0.6_B elementary cell lower plate temperature distribution with radial poloidal plane [81]

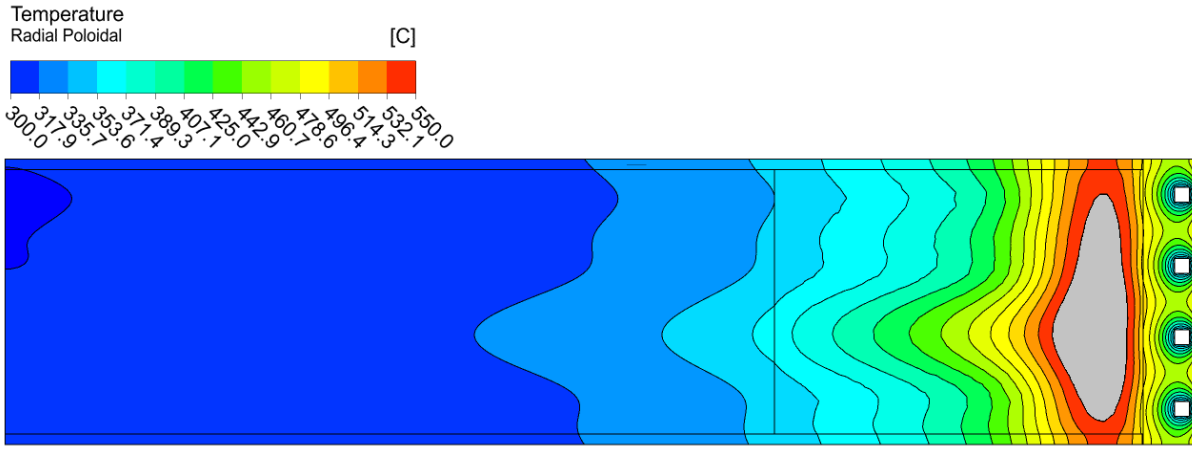

Plane a) Central toroidal cut

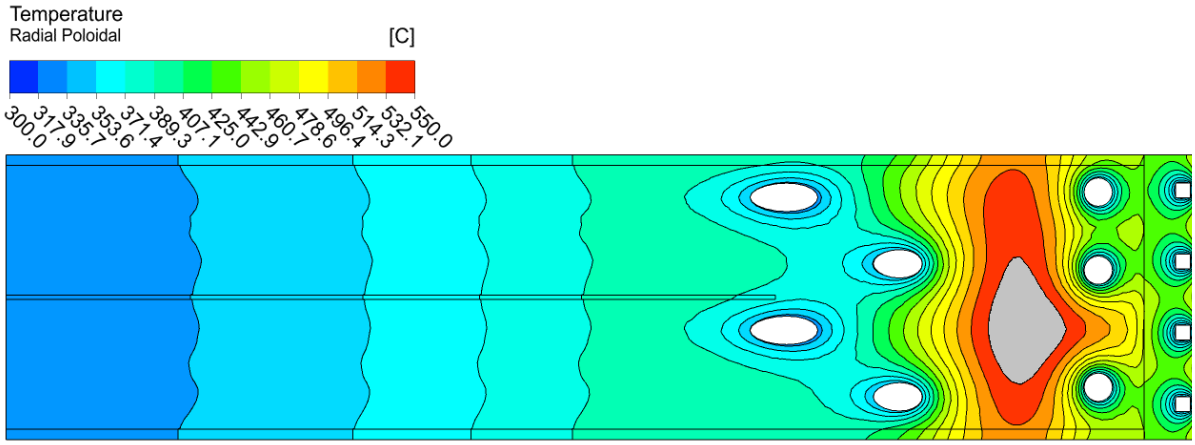

Plane b) Second array external curvature hot region cut

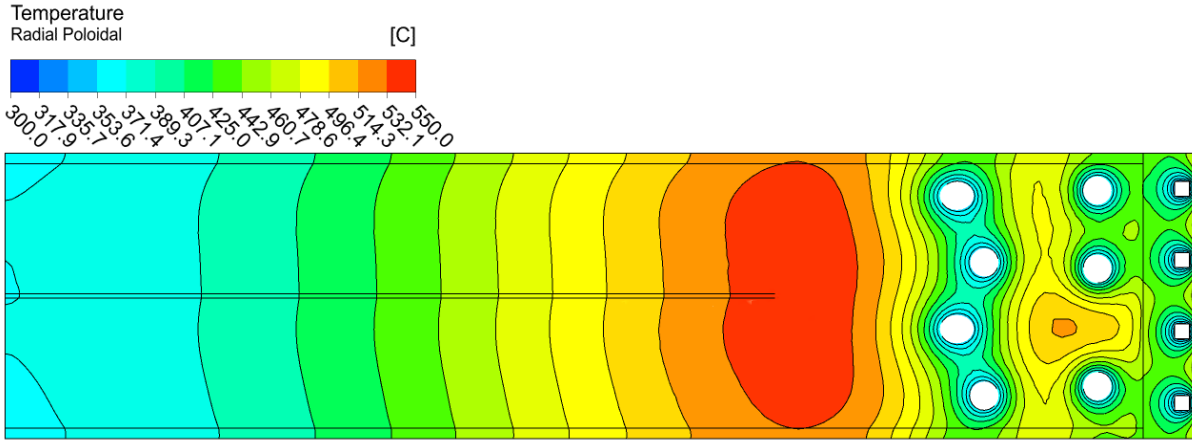

Plane c) First and second array toroidal hot region cut

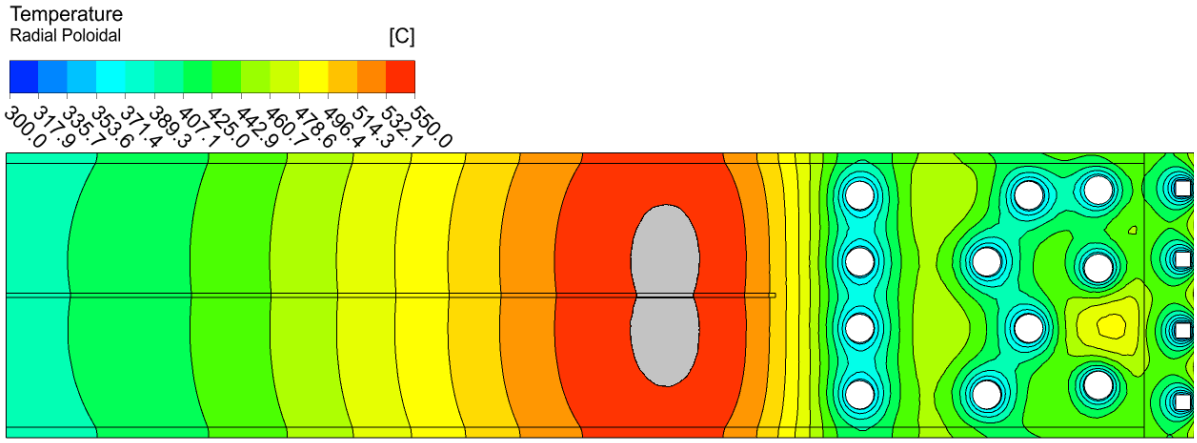

Plane d) Third array middle toroidal length hot region cut

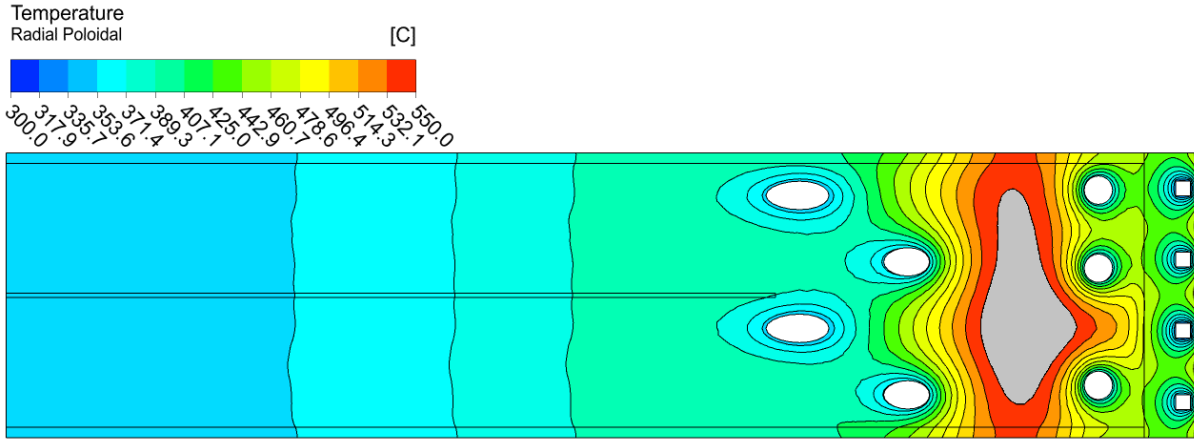

Plane e) Sidewall hot region cut

Fig. 4.58 – WCLL V0.6_B different radial poloidal cuts [81]

4.7.4. Summary

The cooling performance of the WCLL COB equatorial elementary cell has been investigated using a CFD approach, with the aim of its BZ tubes optimization. The analyses, based on the WCLL 2018 V0.6 design, focused on three different BZ tubes layout of the equatorial elementary cell: the reference layout V0.6; the V0.6_A, with a modified tubes arrangement of the first and second tubes arrays to extinguish onset of hot spots; the V0.6_B, to further extinguish the remaining hot spots of the V0.6_A model. Computational thermal and fluid-dynamic models of these elementary cells were developed using the commercial CFD code ANSYS CFX v18.2. The heat loads adopted for the analyses are based on the most updated data, to obtain the thermal field for the most recent design. In order to perform a conservative

analysis, optimizing the BZ tubes layout, the newer reference PbLi thermal conductivity from IAEA has been adopted, and, in addition, solid PbLi has been modelled, thus neglecting the convective contribution that affects the temperature field.

As stated, and proved, the BZ recirculation, with a double-flow pass, ensures large safety margins to avoid the arising of thermal crisis in each model, even if subcooled nucleate boiling is expected to occur in limited regions of the BZ first tube array. Furthermore, it enhances the thermal-hydraulic performances increasing the average water velocity of the arrays. The FW water also is subjected to subcooled nucleate boiling in limited regions of the channels; moreover, it is affected by the BZ first tubes array, which affects the temperature trend inside the FW chase. The analysis has demonstrated that the BZ and FW systems are related to each other, being there heat exchange between the PbLi and FW interface. The FW cooling system must have a 13% increase of water mass flow rate to ensure adequate water conditions at the outlet compared to the effective deposited power into the system, due to the BZ and FW systems heat exchange.

The present study has demonstrated that the V0.6_B configuration can withstand the imposed heat loads and meet the DEMO design requirements, ensuring an adequate temperature field on the Eurofer upper and lower plate, FW chase and Tungsten layer, even if the baffle plate slightly exceed the temperature limit by 2 degrees. This value, however, is deemed acceptable due to the conservative criteria adopted in the present analysis and its non-structural function. Both configurations, V0.6 and V0.6_A, are not able to keep the structural materials well below the temperature limit, exceeding 550°C in the Eurofer upper and lower plates. The reference layout V0.6 presents three different hot spots into both plates, as opposed to the V0.6_A that returns only two of them. The last configuration, the V0.6_B with its BZ tubes layout, returns a Eurofer plates temperature field without hot spots. It has been demonstrated that only the PbLi temperature rise over 550°C but with safety margins from the Eurofer structures. The V0.6_B BZ tubes layout can be considered as a promising improvement in the current design, suitable to fully withstands the steady-state thermal loads.

Further studies will be conducted with transient analysis to consider the real thermal inertia of the system and the large PbLi thermal conductivity. Moreover, analyses should be performed with transient simulation making vary the heat loads in order to evaluate the pulsed operating phase of the DEMO reactor and the response of the WCLL V0.6_B elementary cell under

operating conditions that can lead to temperatures above the limit in the Eurofer structures. In addition, modelling the eventual phase change, in order to evaluate the perturbation in the system due to possible subcooled boiling and the use of different turbulence models, would be a remarkable improvement.

4.8. Main achievements

Several thermal-hydraulics steady-state analyses have been performed on the central outboard segment equatorial elementary cell using a CFD approach, aimed to investigate the thermal-hydraulics behavior of the elementary cell. The analyses have been conducted to choose a design layout, of BZ and FW systems, which has to satisfy the following main requirements:

- Maximum temperature of Eurofer structural components below 550°C;
- DWTs minimum curvature radius equal to 3 times of the external diameter;
- Minimum distance between DWTs axes of 26 mm;
- Maximum number of DWTs curves limited to 2;
- Temperature toroidal symmetry into the BZ;
- No stiffeners crossing.

Moreover, a numerical evaluation about the effect of the modelling approach has been performed.

The V0.6 layout, carried out in the first bench of analyses, has set the minimum number of tubes, necessary to guarantee a Eurofer temperature below the imposed limit, equal to 22. This layout satisfies each above-mentioned requirement, returning a Eurofer temperature field widely below the limits, but, with low thermal-hydraulics water performances. In addition, through the water enthalpy balance, both BZ and FW systems, provides adequate outlet water conditions for the PHTS (i.e. water outlet temperature at 328°C), as required from the BoP requirement.

The FW optimization process has demonstrated that a 4 channels configuration can withstand the imposed thermal loads, with related benefits towards the BZ system. The channels reduction strongly enhances the FW water thermal-hydraulics performances, increasing the water velocity more than 50%, with a consequent increase in system pressure drops. The optimized FW layout decreases the volume of water in the first centimeters of the cell, a fundamental parameter for a good yield of the TBR. As a secondary effect, the passive heat removal from the FW to the BZ has been reduced by 20% in the V0.6_FW4 layout, making the two systems more independent.

The BZ recirculation manifold, evaluated in the V0.6_FW4_R model, is a useful solution to enhance the thermal-hydraulic performances of the BZ water. The double pass flow strongly enhances the water performance, and it also to reduces the temperature into the Eurofer plates. The higher velocities reached in the tubes increase the heat transfer coefficient reducing the maximum water temperature, which remains above the saturation temperature only in small area of the first tube array.

It has demonstrated that the choice of the modelling approach and PbLi thermal conductivity correlation deeply affects the numerical predictions. In particular, the Mogahed correlation returns a significantly lower thermal field than that obtained by means of the IAEA correlation, regardless of the adopted approach (FEM and/or FVM) or the modelling state for the PbLi (fluid and/or solid). The modelling approach instead, slightly impact on the numerical prediction, varying by around 3 degrees from the analyzed version, while the PbLi modelling state affects the Eurofer temperature results by around 5 degrees. The choice, as a reference, of the IAEA PbLi thermal conductivity causes a hot spots onset into the Eurofer structures exceeding the imposed temperature limits. As a consequence of this, the V0.6 layout has discarded as a suitable layout.

The newer V0.6_B, which adopts 4 FW channels and BZ recirculation, has demonstrated, with its updated BZ tubes layout, to be able to cope the imposed thermal loads, even in the most conservative observable conditions (IAEA PbLi thermal conductivity and PbLi modeled as solid domain). The V0.6_B design is considered a promising improvement in the current design, laying the basis for the finalization of the WCLL BB design.

Further studies will be performed with transient analysis on the V0.6_B layout, making vary the imposed heat loads, in order to evaluate the thermal behavior of the elementary cell under the DEMO operative conditions. The updated design should be able to ensure compliance with the multiple requirements. Moreover, providing to be able to operate in the different reactor phases.

5. THERMAL-HYDRAULIC ANALYSES IN TRANSIENT CONDITIONS

The main objectives of these analyses are to investigate the response of the cooling systems, FW and BZ, from the thermal-hydraulic point of view and to assess any critical issues in the reference design (i.e. thermal inertia, optimal outlet water conditions), during the operational phases of the reactor. Moreover, the analyses are also aimed at analyzing the capability of the V0.6_B model to provides adequate structures cooling and suitable water conditions for energy production, while the backgrounds conditions vary. In the present study, the pulsed nature of DEMO fusion reactor is investigated through transient CFD analyses, focusing on three main phases: the ramp-up, when the plasma is generated and the fuel is burnt producing energy; the ramp-down, when the CS is in recharge phase and the decay heat is removed; and the fluctuations, when the pellets injections produce plasma instabilities during the normal operation. These pioneering analyses, focused on global performances of the elementary cell, since local ones have been previously evaluated, are performed to assess whether the cell is suitable for DEMO operations.

The configuration V0.6_B has been analyzed and discussed as major outcomes during these studies, conducted in Section 4. Regarding the V0.6_B configuration, different analyses have been performed and the following goals have been successfully achieved:

- Temperature symmetry among the toroidal direction;
- No stiffeners crossing;
- 22 BZ tubes properly refrigerate the Eurofer structures;
- BZ water recirculation enhance the margin from the critical heat flux avoiding the thermal crisis;
- 4 FW water channels fully withstand the thermal loads;
- No thermal crisis occurs into BZ and FW systems;
- Eurofer temperature below the imposed limit of 550°C;
- Water coolant does not exceed the velocity of 7 m/s into both cooling systems.

The transient consists in varying the boundary conditions of the analyzed model, simulating the different operating phases of DEMO. Since the reactor phases have a different timescale, each

phase has its own characteristic curves as a function of time, which, from a steady-state condition, vary for a defined time, to then get back in a newer steady-state condition. In particular, during the transient and at the end of it, the analysis must respect the following main requirements:

- Temperature symmetry in toroidal direction;
- Eurofer temperature below the limit of 550°C;
- Water coolant velocity must not exceed 7 m/s;
- Adequate outlet water conditions for the PHTS.

For each transient analysis a 3D finite volume model has been set up according with the WCLL geometrical parameters. As regards the COB elementary cell, a toroidal length of 1500 mm, radial dimension of 1000 mm and poloidally enclosed between two horizontal stiffeners plate.

5.1. WCLL V0.6_B – Numerical model

To evaluate the temperature trend of the elementary cell and the thermal-hydraulic performances of the system, varying the boundary conditions during the operational phases of DEMO, a three-dimensional finite volume model has been set up, using the CFD commercial code ANSYS CFX v18.2. The numerical model has been conceived to faithfully reproduce and to obtain a complete and detailed temperature distribution both in fluid and solid domains. The model, based on the V0.6_B layout, has a toroidal dimension of 1500 mm, reduced radial dimension of 567 mm, which neglects the manifold region where the power contributions are negligible, and a poloidal height fixed at 135 mm. The V0.6_B geometry has been extensively discussed in Sect. 4.7, where all the geometric characteristics of the model are reported; for more information it is advisable to consult that Section. In Fig. 5.1 an isometric view of the V0.6_B model and both cooling schemes are shown.

In these analyses, fluid domains for BZ and FW water, and solid domains for PbLi, Eurofer structures, FW Eurofer chase and Tungsten armor have been modelled. Regarding the PbLi, due to: low velocity reached, which results in laminar flow (Re~30); low Prandtl number (Pr~0.02), which means that the heat conduction strongly prevails on convection; to the MHD effects, which strongly reduce the contribution of convection, suppressing the buoyancy forces; it has been modelled as a solid domain. This is a conservative assumption, as demonstrated in different numerical simulation reported in Refs. [54][79][81] and Sects. 4.6 and 4.7. Moreover, as demonstrated in [79] this assumption reduces the computational costs, thus, decreasing the number of equations to be solved in the PbLi domain.

The material thermo-physical properties are specified in terms of density, specific heat and thermal conductivity for solids domain, while fluids also require the dynamic viscosity. Temperature-dependent linear equations or fixed values have been implemented in the CFX code database. The complete lists of the adopted thermo-physical properties are collected in Sect. 4.1, in particular, Table 4.1, Table 4.2, Table 4.3 and Table 4.4 for Tungsten, Eurofer, PbLi and water materials respectively. As regards the PbLi, IAEA thermal conductivity has been adopted, since it has been set as new reference property.

Concerning the DEMO thermal loads, two main contributions have been considered for the analyses: the surface power density on the Tungsten layer, corresponding to a power heat flux with a maximum nominal value of 0.32 MW/m^2 onto the Tungsten straight surface, which linearly decrease along with the elbows; the volumetric power density into materials that radially decrease from the Tungsten to the backplate, represented with two different power curves, one for the PbLi and the other for the Eurofer and Tungsten structures. Both power contributions have been discussed in Sect. 4.2, where the linear HF decreasing equation and the volumetric power curves are shown.

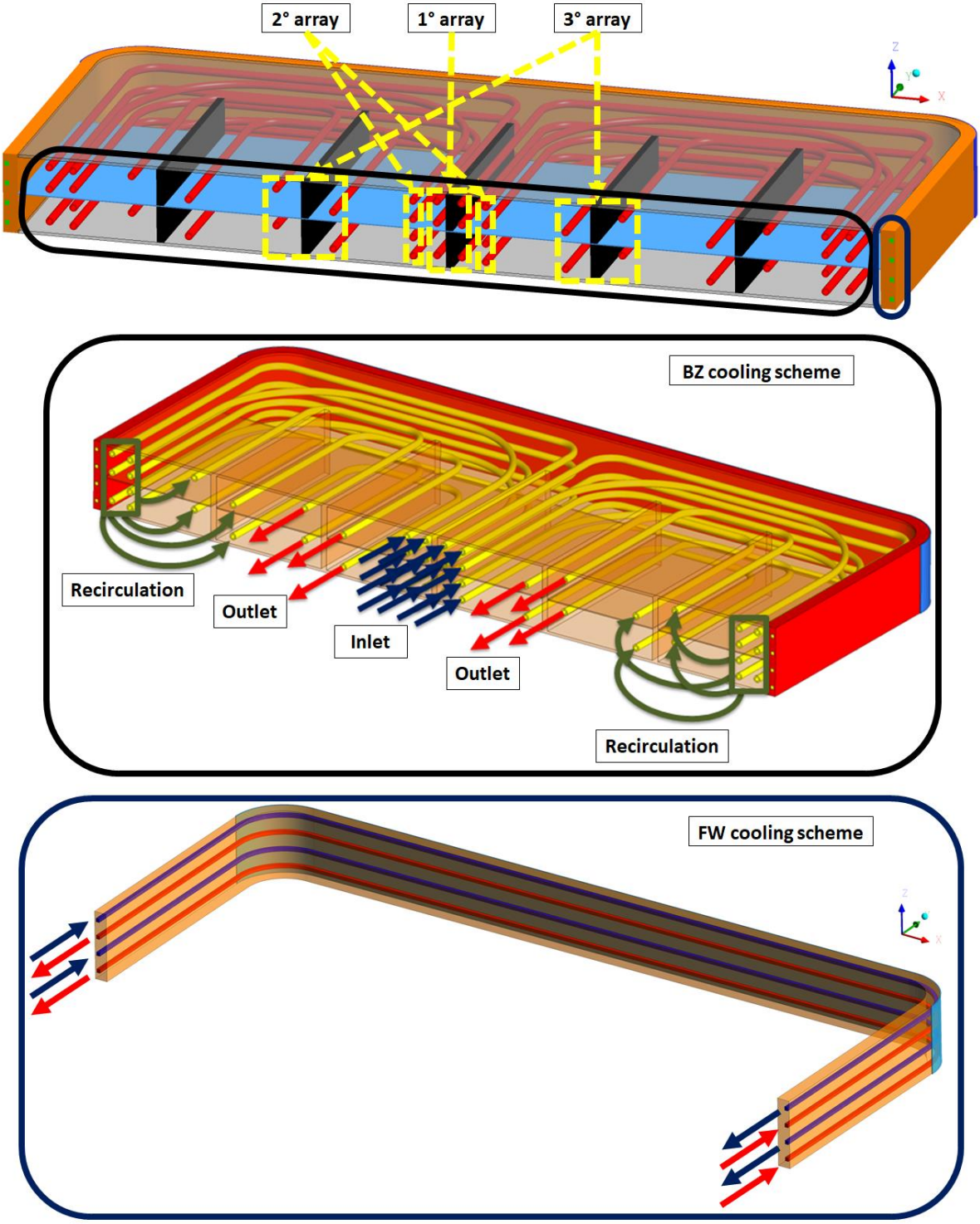

Fig. 5.1 – WCLL V0.6_B layout: isometric view; BZ cooling scheme; FW cooling scheme

5.2. Mesh independence analysis

To obtain results in a reasonable time a mesh independence analysis has been performed on the V0.6 tubes layout, that differs from the V0.6_B only for the BZ tubes geometrical position, to reduce the number of elements into the model, this because the computational costs of a transient analysis are definitely higher than in a steady-state analysis.

The objectives of these cases are not to obtain extremely accurate values at local level but to obtain reliable and accurate results at a global level (i.e. temperature trend, global outlet water temperature, characteristic time). The 3D FVM has been meshed using hexahedral and tetrahedral elements, considering the geometrical features of the domains, many and different local controls are inserted to define the complex geometry appropriately. For this purpose, different code tools are exploited, such as: sizing control, sweep method, mapped face. The inflation control near the solid walls for the resolution of the water viscous sub-layer has been imposed y^+=5, based on a maximum velocity of the BZ and FW water, 4 m/s and 6 m/s respectively, instead of 7 m/s in the previous analyses, this to significantly increase the first layer thickness of the fluid domains that influence the maximum Courant number, which influences the accuracy of the solution [82]. The latter diminishes with the increasing of the Courant number of the analysis. Even in this case, the numerical model has been developed as a single part, to simulate the heat transfer between the multiple components, solids and fluids, using a conformal mesh.

The mesh independence analysis is performed varying the sizing of the elements into the elementary cell. In particular, due to the radial power deposition trend, it was deemed appropriate to divide the cell in two main body groups: the front group where the deposited power trend has a much more relevant contribution and therefore a finer mesh is required; the back group where the power radial curve has an almost linear trend which contributes to a lesser extent to the deposited power and therefore a coarse mesh can be adopted, in Fig. 5.2 is reported the division of the bodies group.

The mesh sensitivity models and results are reported in Table 5.1, and the related results in Fig. 5.3 and Fig. 5.4, where the finest mesh is the BXX and the coarsest is B0A. The first mesh modification has been performed from the steady-state mesh (BXX), which has a uniform radial

spacing of the grid of 3 mm, doubling the size of the grid at back bodies group to 6 mm (B33). Then, the following models provide, alternatively, either the increase of the size of the grid in the rear part by 2 mm, or the increase of 1 mm in the front part, up to B11 model where the grid sizing is 5 mm in the front and 10 mm in the rear. The B00 and B0A models have an increase which is halved compared to the previous models, in fact, B00 has 5.5 and 11 mm and B0A has 6 and 12 mm, in the front and rear part respectively. The table returns global values which slightly differ from the finest to the coarsest. Unfortunately, the B0A mesh has been discarded due to a higher convergence criterion (residual magnitude above 10^{-4}); thus, the mesh adopted is the model B00. A detail of the adopted mesh into the V0.6_B model is shown in Fig. 5.5. As regards the transient analysis, the model, in addition to the boundary conditions, which are discussed below (Sect. 5.4), requires the initial conditions. To obtain these conditions, it was considered more appropriate to use the finest mesh, in order to provide more accurate values. Both related mesh statistics are reported in Table 5.2.

Fig. 5.2 – WCLL V0.6_B mesh independence cell bodies group division (orange finer mesh, blue coarse mesh)

ID	N° of Nodes	N° of Elements	Eurofer T_{max} [°C]	PbLi T_{max} [°C]
B0A	4.30 M	6.64 M	521.7	551.4
B00	5.05 M	7.56 M	523.5	551.5
B11	5.43 M	8.04 M	523.7	551.5
B12	6.10 M	8.91 M	524.3	551.6
B22	6.39 M	9.17 M	524.4	551.6
B23	7.59 M	10.8 M	524.8	551.7
B33	8.06 M	11.3 M	524.9	551.7
BXX	14.7 M	19.8 M	525.8	551.8

Table 5.1 – WCLL V0.6 mesh independence statistics and results divided by ID

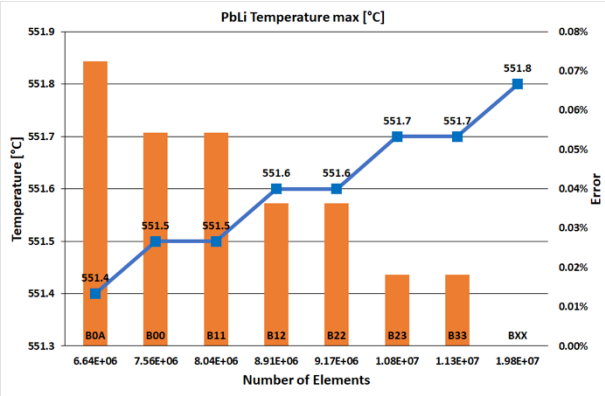

Fig. 5.3 – WCLL V0.6 mesh independence PbLi temperature results with error bar

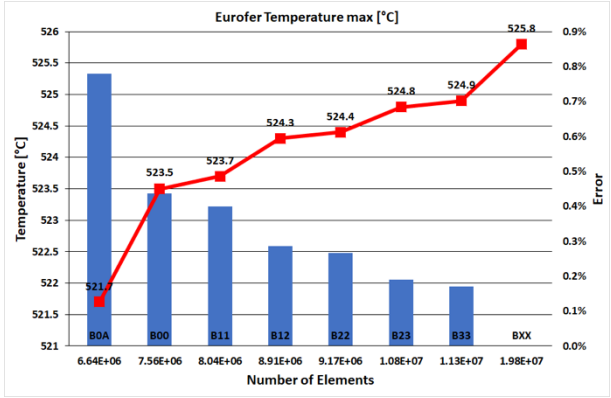

Fig. 5.4 – WCLL V0.6 mesh independence Eurofer temperature results with error bar

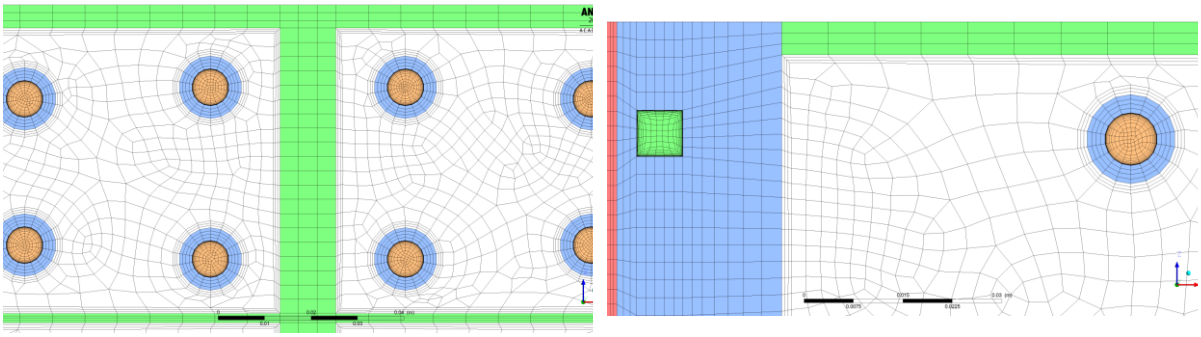

a) BZ system b) FW system and BZ upper corner

Fig. 5.5 – WCLL V06_B layout mesh B00 detail

Parameters	**Value**	
	B00	***BXX***
N° Nodes	4.58 M	15.02 M
N° Elements	6.91 M	19.41 M
Ave Orth Qual	0.823	0.852
Ave Skewness	0.206	0.179

Table 5.2 – WCLL V0.6_B transient analysis B00 and BXX mesh statistics

5.3. WCLL Transient thermal loads

Due to the pulsed nature of DEMO machine, the breeding blanket thermal loads vary according to plasma operation [83][84], as shown in Fig. 5.6. For this reason, it is necessary to identify a stationary case, where steady-state thermal loads are foreseen (i.e. full power, dwell); and transitional cases where the heat loads are varied in time. The transient thermal loads postulated in normal operation are identified with three major cases: ramp-up, when the heat loads pass from the dwell state to the pulsed phase; ramp-down, when from the full power condition, it goes to the dwell phase; controlled power fluctuations, when during the pulsed phase the pellet injection cause peaks of overpower or underpower. In addition, off-normal transients have been postulated to characterize the DEMO electromagnetic loads generated inside the tokamak acting on the BB structures, identified as: plasma disruptions, loss of confinements and vertical plasma displacement (Refs. [85][86][87]). Moreover, accidental events have also been characterized, defining the possible scenarios and supporting the mitigation, those have been identified as: in-box Loss Of Coolant Accident (LOCA) or Loss Of Flow Accident (LOFA) (Refs. [88][89][90][91]).

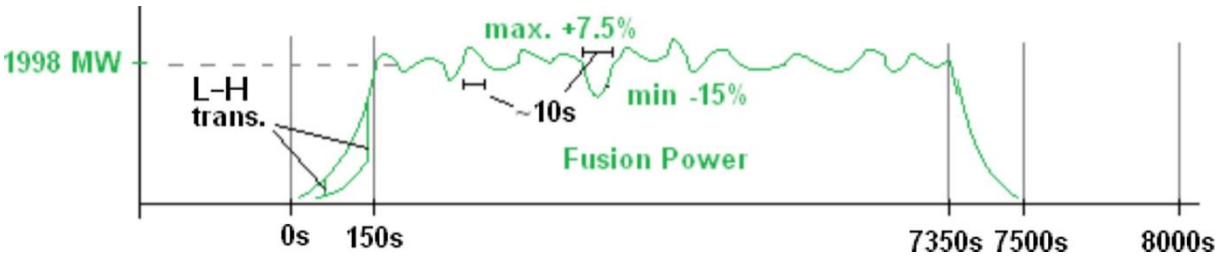

Fig. 5.6 – DEMO plasma operations [83][84]

In the present analysis the transient normal operations have been investigated, through time-dependent linear functions which provide the nuclear heating trend of the WCLL breeding blanket. These transient trend concern both thermal loads, the volumetric deposited power and the heat flux on the Tungsten layer, having the same time-dependent trends.

From the figure above, two types of ramp-up are identified: one milder ramp, which has a first vertical power step and then an exponential growth; one higher, which has a parabolic trend for most of the transient duration and then sudden rise up to the nominal power in the few last seconds of the ramp. The first is named “slow ramp-up” and the second as “fast ramp-up”. The latter, from the thermal point of view, provides high thermal loads to the blanket in a few

seconds and for this reason it is analyzed. As regards the ramp-down, the power decreases exponentially in about 40 seconds reaching the 16% of the nominal power, after which it continues with a decreasing logarithmic trend, due to the decay heat, reaching about the 0.9% of the nominal power after 150 s, remaining with that power until the beginning of a new cycle. Concerning the controlled power fluctuations during the full power, caused by the pellet injection, peaks of overpower and underpower occur, increasing and/or decreasing the nominal power for a defined time (around 30 seconds). From a thermal-hydraulic point of view, they create instabilities inside the BB (i.e. temperature build up, thermal crisis) and for this have been evaluated.

The transient thermal loads equations are reported in ANNEX B: Steady-state and transient thermal loads.

5.3.1. Ramp-up and ramp-down

In order to assess the WCLL behaviour during a pulse-dwell phases, transient thermal loads have been considered to simulate the power deposition during these phases. Time-dependent curves have been implemented in CFX, that varies with the above discussed power contributions of heat flux and deposited power as reported in Sect. 4.2.

To obtain a realistic time-trend of the power, and, of boundary conditions, it was necessary to perform specific analyses on the entire reactor. As performed for similar analysis (Ref. [92]), which provides the transient modelling of the balance of plant for the WCLL blanket, a thermal-hydraulic system code analysis has been performed through the RELAP5/Mod3.3 code [65][68]. These analyses have been performed by the DIAEE Nuclear Section of “Sapienza” University of Rome, in the framework of the EUROfusion BoP activities. The system code model has been conceived on the most updated BB layout [93] and relies on a scaled BoP model, concerning the BB and the PHTS. This latter analysis provides a pulse length of 7200 s (2 hours) and a dwell period of 600 s (10 minutes). In Fig. 5.7 the RELAP5/Mod3.3 of the reduced BoP model is shown. The RELAP5 model has been set-up with appropriate time-dependent power curves, provided by the most updated reference data given by Refs. [94] and [95].

The RELAP5 simulation was necessary to provide the CFX model with all the thermal-hydraulic variables required to set boundary conditions, as water mass flow rate and inlet temperature. Since, in Refs. [83] and [84], the water inlet temperature is foreseen variable. The RELAP5 model, which represents the entire reactor, returns the trend of the water temperature necessary to remove the total deposited power, given that the water mass flow remains constant.

During the RELAP analysis setup, the normalized power curves have been carried out (Fig. 5.8 a). These curves have been implemented in both codes, RELAP5 and CFX, in order to obtain comparable output values. In the RELAP 5 code table function every 2 second has been inserted and in CFX time-dependent function. In particular, for the CFX commercial code, to realistically reproduce the time-dependent power deposition, during the ramp-up and ramp-down phases, multiple curves have been created, obtaining appropriate trends of the different transient cases. Two different sets of equations have been implemented in the model, which represent the fast ramp-up (Fig. 5.8 b) and the ramp-down (Fig. 5.8 c) power deposition trend. Concerning the fast ramp-up, for both codes, the initial parabolic trend foreseen in Refs. [94] and [95], has been neglected due to a very low power contribution reducing the timing of the ramp-up transient. The fast ramp-up, which would last 150 s, has been reduced to 55 s, neglecting the first 95 seconds where the power increase is foreseen negligible. This assumption is however considered conservative since the power contribution is provided to the system in a shorter time. As regards the ramp-down the decay heat has been stopped after 150 s from the start of the transient, this is to simplify the analysis, since it contributes less than 2% of the total power after that time due to the very slow power decrease of the decay heat.

As previously mentioned, the RELAP5 model was mostly necessary to provide the trend of the inlet water temperatures during the two different phases, since, as required from the BoP department, DEMO must guarantee adequate water conditions for the electricity production. The system code model has carried out the FW and BZ water coolant inlet conditions, which vary during both transients and both cooling systems. This implies that the foreseen water inlet temperatures for fast ramp-up and dwell vary in a proper manner, depending on the considered system. In Fig. 5.9 and Fig. 5.10 are shown the BZ and FW water transient temperatures, respectively. As regards the two CFD simulations, four different curves have been created to reproduce the water inlet temperatures trends, two for the fast ramp-up and two for the ramp-down, BZ and FW respectively, and are shown in Fig. 5.11.

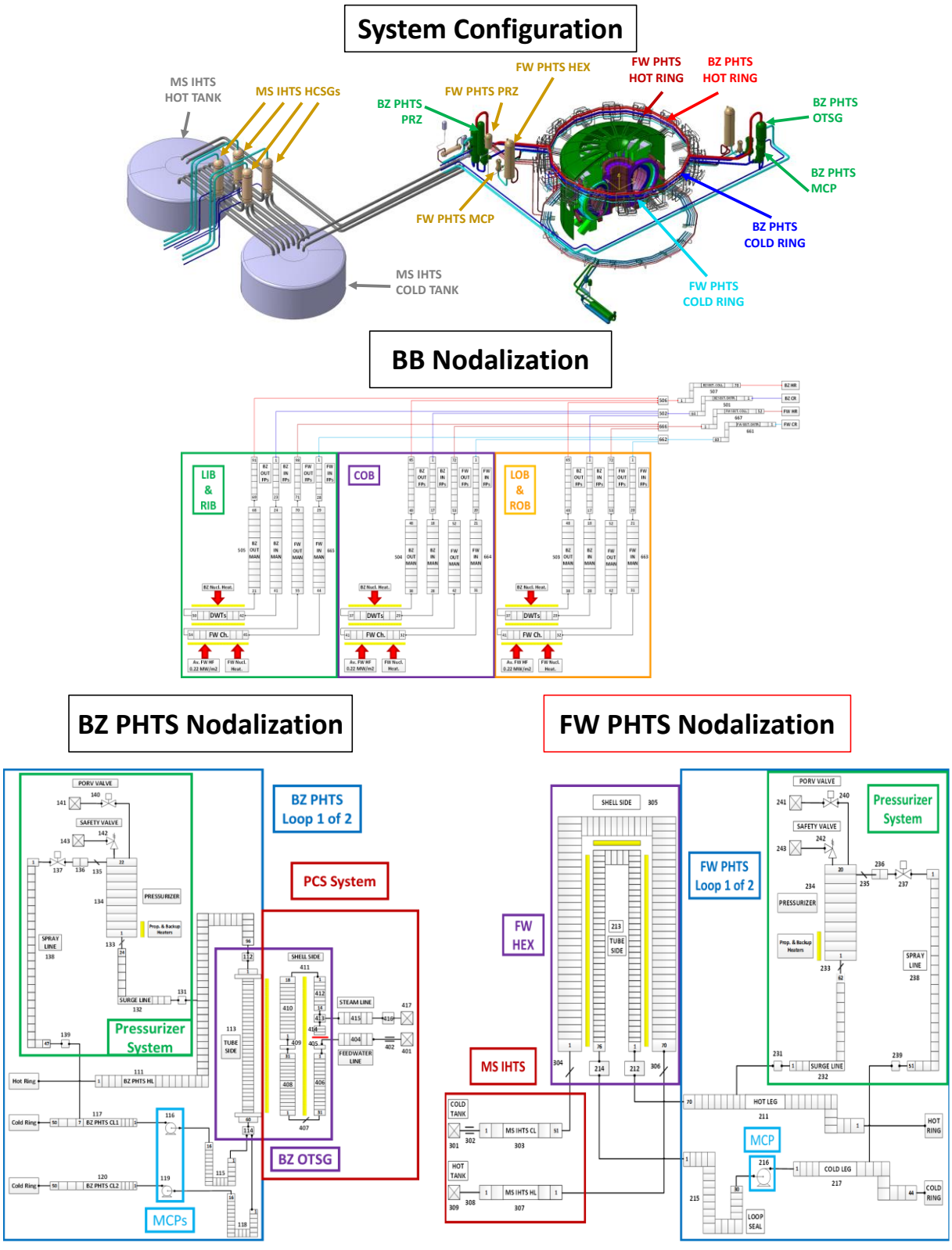

Fig. 5.7 – WCLL Breeding Blanket RELAP5/Mod3.3 nodalization [91]

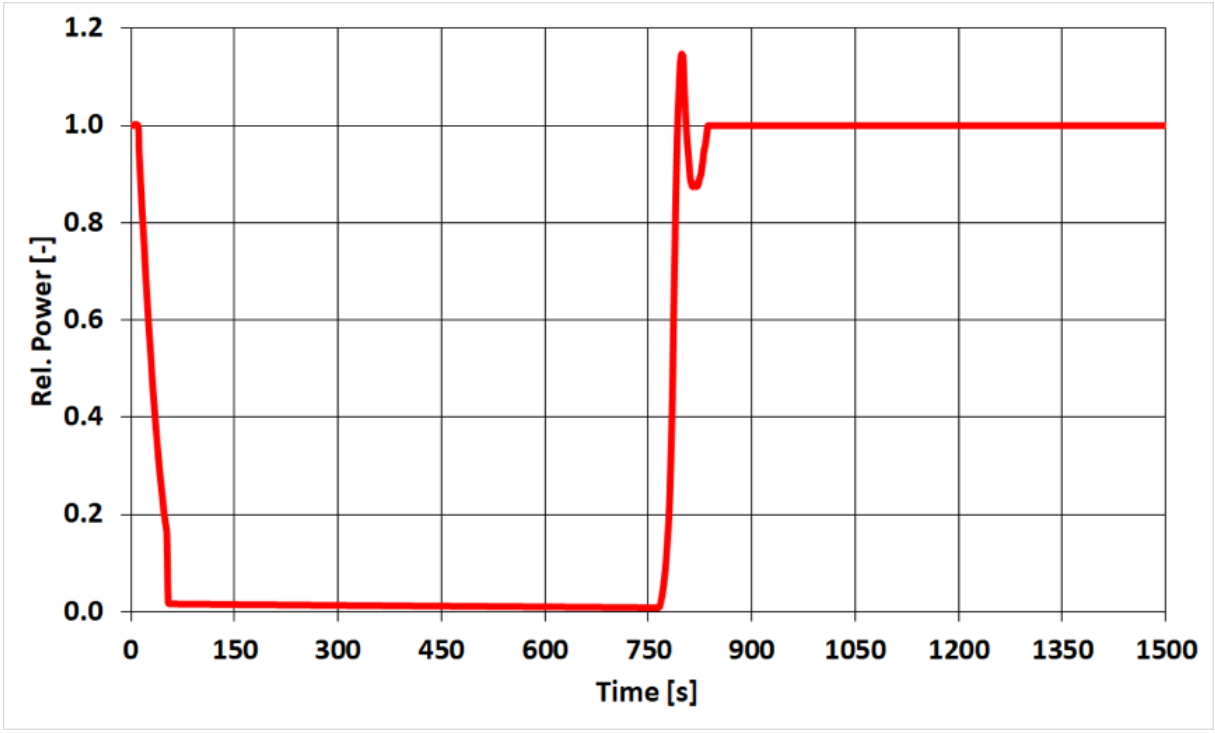

a) Full transient normalized power trend

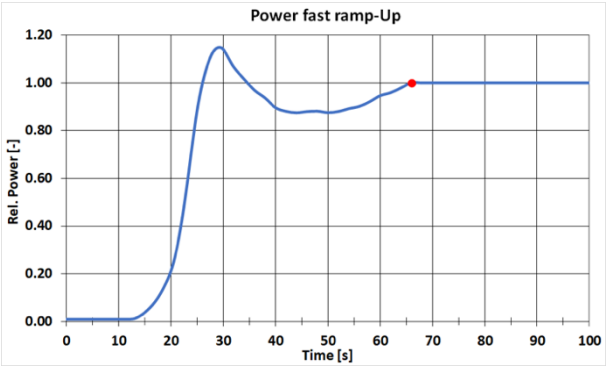

b) Ramp-up normalized power trend

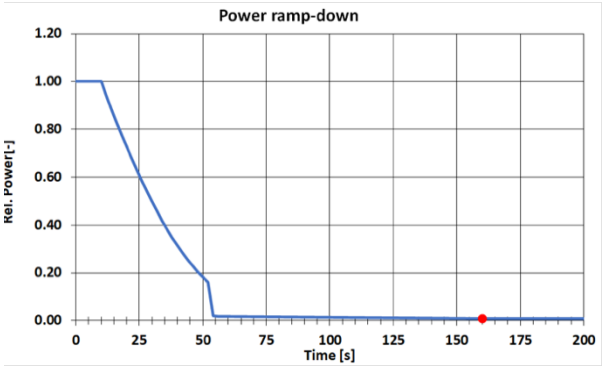

c) Ramp-down normalized power trend

*Point ●: Starts of the steady-state conditions

Fig. 5.8 – WCLL BB normalized power transient trends: one cycle; fast ramp-up; ramp-down

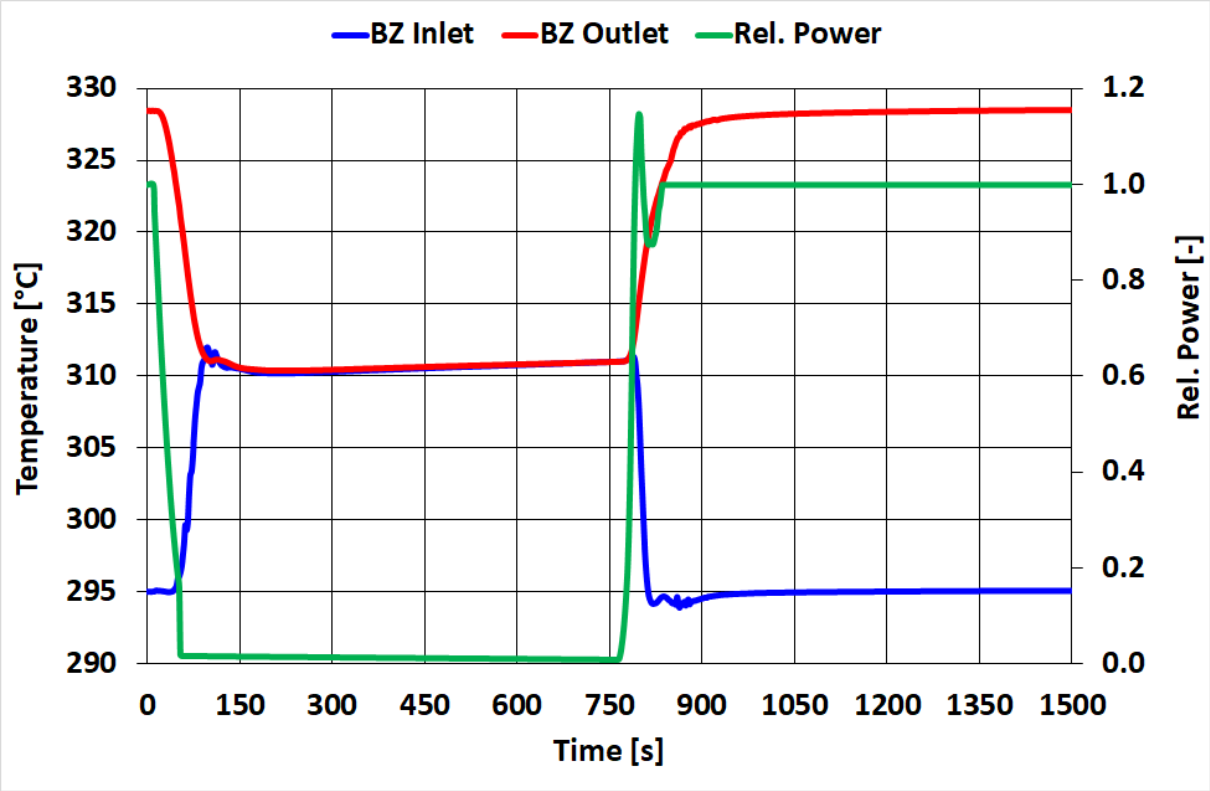

Fig. 5.9 – WCLL BZ water temperatures transient trends

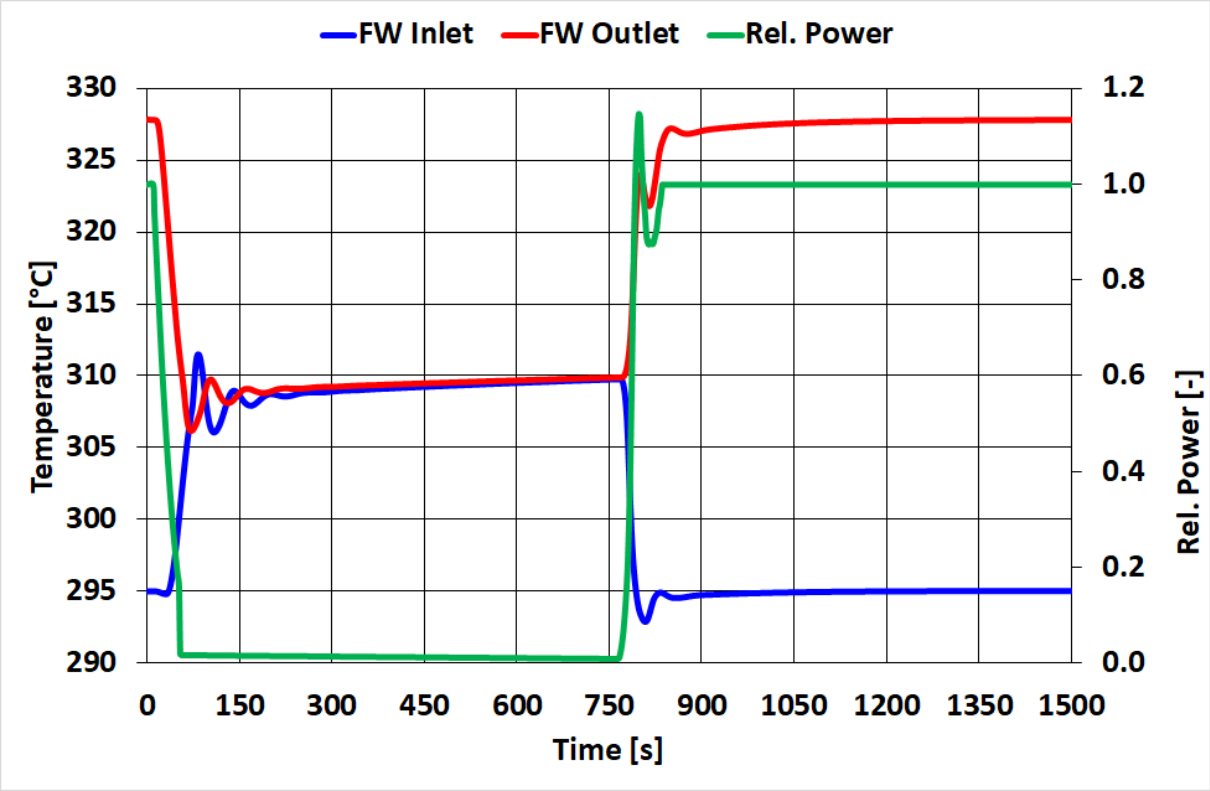

Fig. 5.10 – WCLL FW water temperatures transient trends

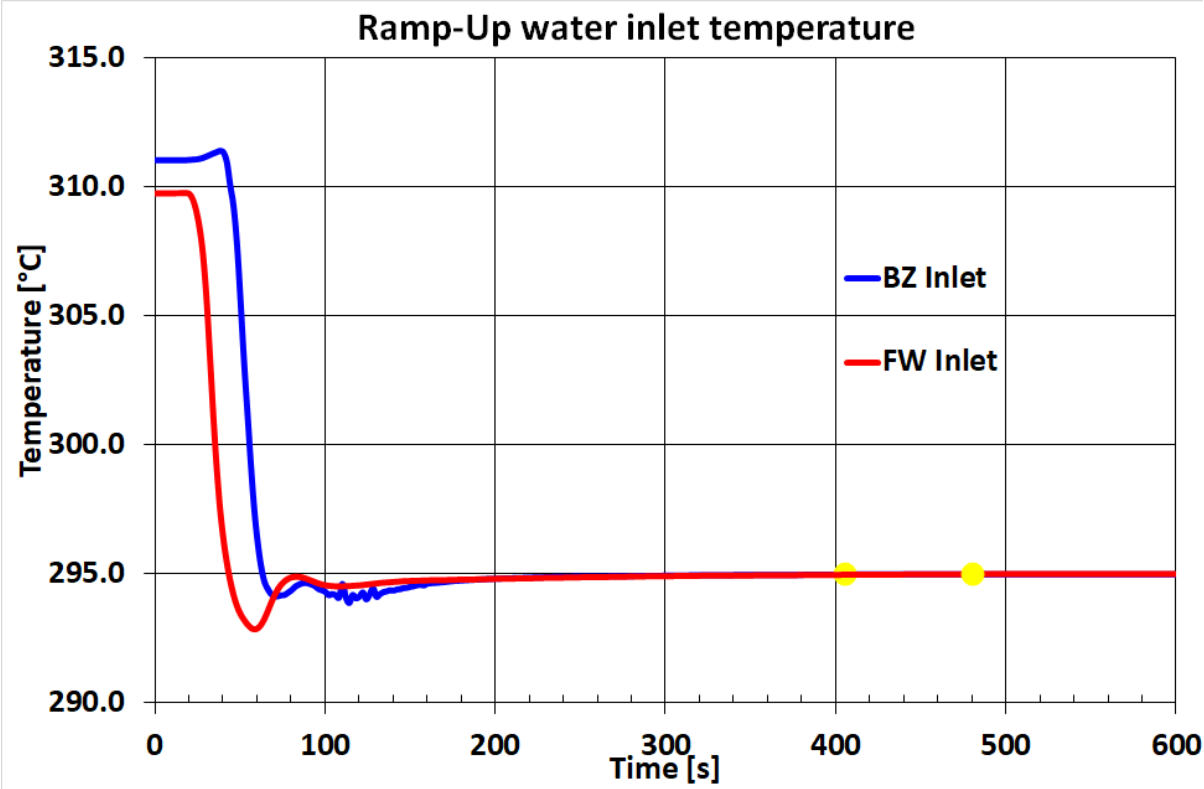

a) Fast ramp-up water inlet temperatures

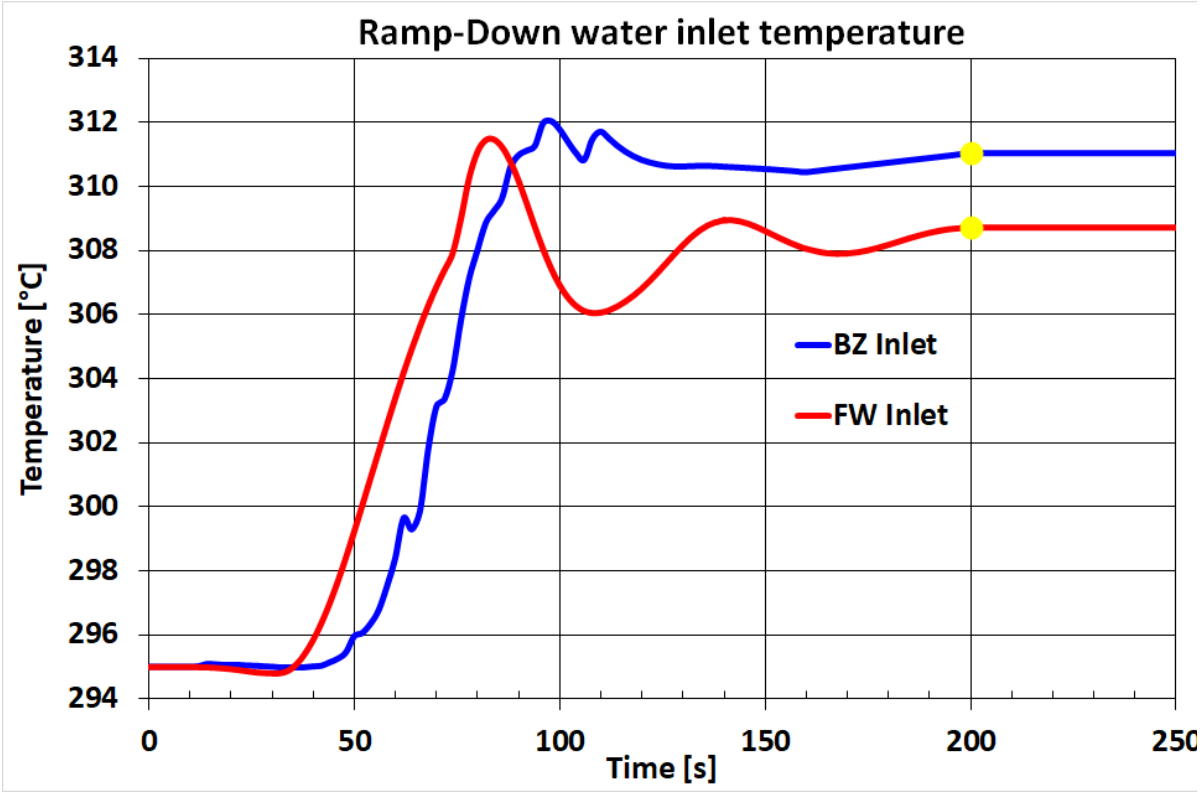

b) Ramp-down water inlet temperatures

*Point ● : Starts of the steady-state conditions

Fig. 5.11 – WCLL water inlet temperatures transient trends: fast ramp-up and ramp-down

5.3.2. Power fluctuations

To evaluate the WCLL thermal behaviour during the pulsed phase, since the plasma produces power fluctuations as reported in Ref. [84], transient analyses have been performed reproducing a full power condition, characterized by power fluctuations.

To represents this phase, time-dependent curves have been implemented in CFX, that varies with the above discussed power contributions of heat flux and deposited power as reported in Sect. 4.2. These curves vary the nominal power with overpower and underpower peaks. Two different analyses have been considered, where the first reproduces three positive power fluctuation in a row, and even the second is characterized by three power fluctuation in a row but, a positive-negative-positive is foreseen.

These power oscillations are represented by Gaussian curves, where the cycle has been imposed at 30 s, after which the second oscillation starts, and the amplitude is reached after 15 seconds. In the first case, named low power fluctuations, the overpower peaks have been imposed at 2.81% of nominal power. In the second case, named high power fluctuations, overpower peak represents an increase of 10% of the nominal power, and the underpower peak represents a decrease of 7.5% of the nominal power. Since it represents the pulsed phase, the water inlet temperatures of BZ and FW coolant systems is kept constant at 295°C, throughout the whole transient. To represents both simulation, two different set of curves are shown in Fig. 5.12.

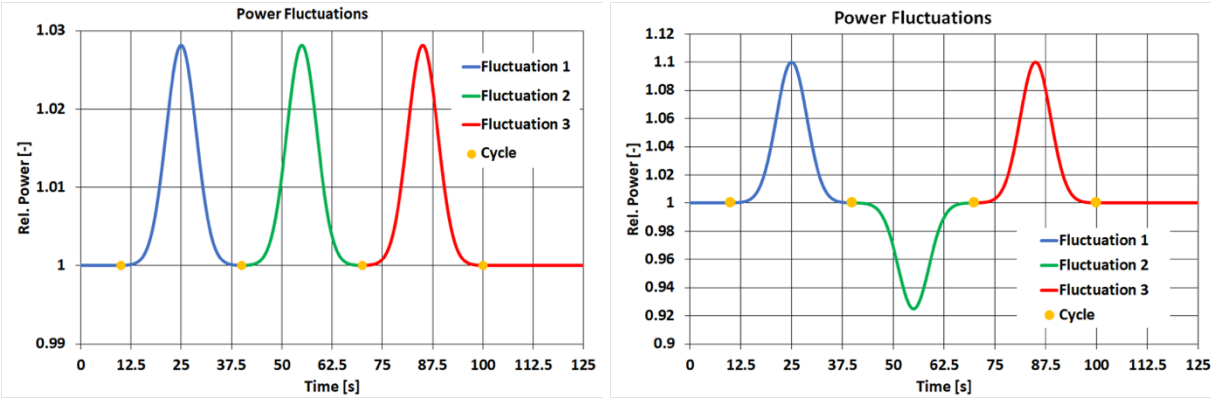

a) Low power fluctuations b) High power fluctuations

Fig. 5.12 – WCLL BB normalized power fluctuations transient trends

5.3.3. PbLi thermal inertia

To evaluate the effect of the high PbLi thermal inertia, which is a typical feature of the heavy liquid metals, a transient analysis has been conducted with a step-down ramp. This analysis does not reflect any operational phases of DEMO, but it was deemed important to identify a characteristic PbLi cooling timing.

A time-dependent curve has been implemented in CFX, varying the DEMO thermal loads (Sect. 4.2) from the nominal power to zero, in one second as shown in Fig. 5.13. The BZ and FW systems have been set up with a constant inlet temperature of 295°C, providing the lowest asymptotic value. The power remains at zero for 1000 seconds after steady state conditions began, in order to obtain asymptotic value at the end of the transient.

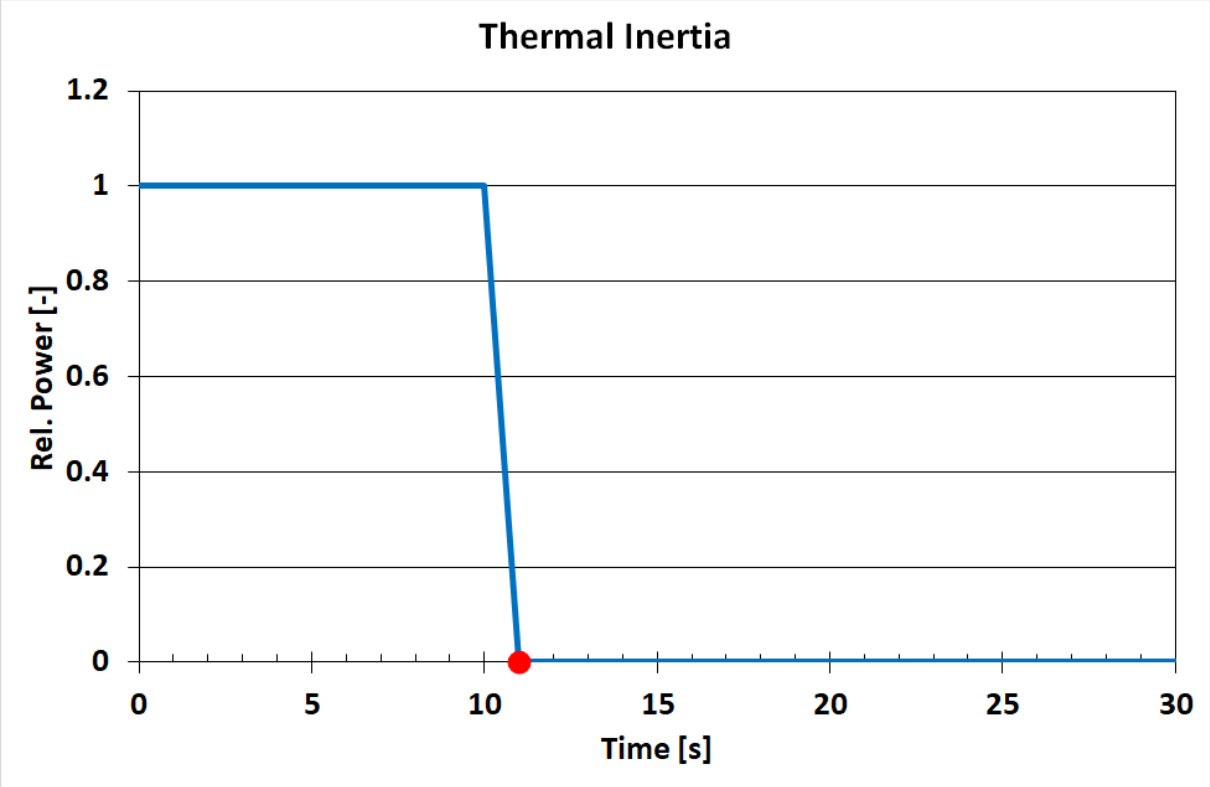

Fig. 5.13 – WCLL normalized power step-down ramp transient trend: thermal inertia analysis

5.4. Solver settings and boundary conditions

To evaluate the temperature trend of the elementary cell and the thermal-hydraulic performances of the system, the 3D model has been set up, using the CFD commercial code ANSYS CFX v18.2. The analyses have been performed to verify the reliability to deliver the coolant at the design temperature, where for the ramp-up and fluctuations is foreseen at 328°C and for the ramp-down have been provided by the RELAP5/Mod3.3 system code, and to properly refrigerate the Eurofer structures not exceeding the imposed limit of 550°C. In addition, an unrealistic analysis has been performed to evaluate the thermal inertia of the system. This analysis has a step-down ramp from the pulsed phase, where, in just 1 second reaches a 0-power condition.

The complete list of the performed runs is reported in Table 5.3.

#	Model	Transient case	Transient variables	Note
1	V0.6_B	Fast ramp-up	• Thermal loads • Water inlet temperatures	BCs provided by the SYS-TH code
2	V0.6_B	Ramp-down	• Thermal loads • Water inlet temperatures	BCs provided by the SYS-TH code
3	V0.6_B	Low fluctuations	• Power	
4	V0.6_B	High fluctuations	• Power	
5	V0.6_B	Thermal inertia	• Power	

Table 5.3 – WCLL V0.6_B transient analysis: performed run

The V0.6_B model has been reproduced and meshed as described in Sects. 5.1 and 5.2, to realistically reproduce the geometry and flow features of WCLL COB equatorial elementary cell and to obtain a detailed temperature trend, both in the fluid and the solid domains, due to the related thermo-physical properties.

Depending on the analysis, different time-dependent thermal loads have been set-up to simulate power deposition. Each phase has been represented with time-dependent curves that have been implemented in CFX. These curves, widely described in Sect. 5.3, vary the above-mentioned power contributions of heat flux and deposited power during the simulation (Sect. 4.2). In

addition, also the water inlet temperatures may vary, both for BZ and FW systems, according with the performed analysis. Different curves have been implemented in CFX to reproduce the water inlet temperature variations trend, or fixed value of 295°C where no change in temperature is expected during the transient.

As regards the imposed water mass flow rate, the total amount has been previously evaluated through the enthalpy balance, corresponding to 1.4868 kg/s, respectively divided into 57.5% and 42.5% for the BZ and FW systems. The water is distributed into tubes and channels according with the main outcomes of Sect. 4.7 (see Fig. 4.48), where, recirculation is adopted for the BZ, and equal channel distribution is set for the FW.

Different total time duration has been set for each analysis, in order to obtain steady state conditions at the end of the transient. For all the analysis, from 0 to 10 seconds of time interval, steady-state conditions have been imposed to stabilize the system before the transient starts. This time interval has been analytically evaluated on the water velocity, since the longest path is around 3 meters (1^{st} array plus 3^{rd} array) and the maximum water velocity in the related system is around 4 m/s, obtaining around 10 cycle before the transient starts. The time parameters of the performed runs have been reported in Table 5.4.

Run	Time interval	Total Time [s]
Fast ramp-up	1) 0 [s] <= t < 10 [s] dwell phase – 0.887% nominal power 2) 10 [s] <= t < 66 [s] fast ramp-up 3) t >= 66 [s] pulse phase – nominal power	1000
Ramp-down	1) 0 [s] <= t < 10 [s] pulse phase – nominal power 2) 10 [s] <= t < 160 [s] ramp-down 3) t >= 160 [s] dwell phase – 0.887% nominal power	760
Low fluctuations	1) 0 [s] <= t < 10 [s] pulse phase – nominal power 1) 10 [s] <= t < 40 [s] first fluctuation – overpower 2) 40 [s] <= t < 70 [s] second fluctuation – overpower 3) 70 [s] <= t < 100 [s] third fluctuation – overpower 4) t >= 100 [s] pulse phase – nominal power	125
High fluctuations	1) 0 [s] <= t < 10 [s] pulse phase – nominal power 2) 10 [s] <= t < 40 [s] first fluctuation – overpower 3) 40 [s] <= t < 70 [s] second fluctuation – underpower 4) 70 [s] <= t < 100 [s] third fluctuation – overpower 5) t >= 100 [s] pulse phase – nominal power	125
Thermal inertia	1) 0 [s] <= t < 10 [s] pulse phase – nominal power 2) 10 [s] <= t < 11 [s] step-down ramp 3) t >= 11 [s] zero power	1011

Table 5.4 – WCLL V0.6_B transient analysis: power time interval and total time

Since the power variations deeply affect the numerical model equation resolution, three different time steps have been selected in all the models, where: 10^{-2} seconds has been imposed for the initial 10 seconds where steady-state conditions are imposed; a range of values from 10^{-3} to 10^{-4} seconds during the power variation, depending on the residual magnitude convergence criterion; 10^{-2} seconds for the remaining total time.

For each run, a steady-state analysis has been previously performed to provide the initial conditions of the transient. These two steady-state runs concern the pulse and the dwell phase, performed with fixed value or radial-dependent linear functions as boundary conditions. As discussed above, the adopted model, to perform these both phases, is the V0.6_B with the BXX

mesh. A complete list of the imposed boundary conditions for the steady-state performed analyses is shown in Table 5.5.

The other boundary conditions adopted for all the models are:

- Periodic boundary conditions on the upper and lower surfaces of upper and lower stiffening plates, FW and Tungsten layer, in poloidal direction, to simulate the presence of adjacent elementary cell;
- Adiabatic condition to back walls of FW, stiffeners, Tungsten layer and FW side walls;
- Mass flow rate and static pressure imposed in the fluid domain at inlet and outlet sections, respectively;
- No-slip condition at the interface between coolant and the circuit steel walls.

The two equations k-ω Shear Stress Transport (SST) model has been set to simulate the water turbulence effects, as demonstrated in Refs. [69][81]; the Second Order Backward Euler implicit time-stepping transient scheme has been adopted for the transient terms.

A complete list of the boundary conditions adopted for the performed transient analyses is shown in Table 5.6.

#	**Parameters**	**Value**		**Unit**
		Pulse	***Dwell***	
1	FW HF	$q''(y)_p$	$q''(y)_d$	MW/m^2
2	q’’’	$q'''(y)_p$	$q'''(y)_d$	MW/m^3
3	BZ Water T_{inlet}	295.0	311.04	°C
4	FW Water T_{inlet}	295.0	309.73	°C
5	Water (BZ-FW) Press	15.5	15.5	MPa
6	FW MFR	0.63189	0.63189	kg/s
7	BZ MFR	0.85491	0.85491	kg/s
8	Total MFR	1.4868	1.4868	kg/s
*$q''(y)_p$: heat flux at 100% *$q'''(y)_p$: power at 100%		*$q''(y)_d$: heat flux at 0.887% *$q'''(y)_d$: power at 0.887%		

Table 5.5 – WCLL V0.6_B steady-state analysis: boundary conditions

#	Parameters	Value					Unit
		Fast ramp-up	***Ramp-down***	***Low Fluct***	***High Fluct***	***Thermal Inertia***	
1	FW HF	f(t)·q''(y)	f(t)·q''(y)	f(t)·q''(y)	f(t)·q''(y)	f(t)·q''(y)	MW/m^2
2	Q'''	f(t)·q'''(y)	f(t)·q'''(y)	f(t)·q'''(y)	f(t)·q'''(y)	f(t)·q''(y)	MW/m^3
3	Water (BZ-FW) T_{inlet}	f(t)	f(t)	295.0	295.0	295.0	°C
4	Water (BZ-FW) Press	15.5	15.5	15.5	15.5	15.5	MPa
5	FW MFR	0.63189	0.63189	0.63189	0.63189	0.63189	kg/s
6	BZ MFR	0.85491	0.85491	0.85491	0.85491	0.85491	kg/s
7	Total MFR	1.4868	1.4868	1.4868	1.4868	1.4868	kg/s

Table 5.6 – WCLL V0.6_B transient analysis: boundary conditions

5.5. Results

5.5.1. Steady-state

The steady-state analyses of the COB equatorial elementary cell have been performed referring to the V0.6_B model. These analyses recreate the pulse and the dwell phases, in order to obtain reliable and accurate outputs values for the transient initial conditions. One model represents the dwell steady-state conditions, where the total power is 0.887% of the nominal power, while the other, represents the pulse steady-state conditions, where the total power is the nominal one.

A brief description of the obtained dwell steady-state results is reported below, while the pulse steady-state has been widely discussed in Sect. 4.7. The main outputs parameters of both runs have been reported in Table 5.7.

#	Parameters	Value		Unit
		Pulse	***Dwell***	
1	Tungsten T_{max}	485.5	311.5	°C
2	FW T_{max}	504.8	311.9	°C
3	Upper Plate T_{max}	543.9	313.5	°C
4	Lower Plate T_{max}	543.7	313.5	°C
5	Baffle T_{max}	552.1	313.6	°C
6	PbLi T_{max}	584.7	313.8	°C
7	FW water $T_{ave\ out}$	327.9	310.1	°C
8	BZ water $T_{ave\ out\ 1}$	319.3	311.2	°C
9	BZ water $T_{ave\ out\ 2}$	328.4	311.3	°C
10	FW water $v_{ave\ out}$	4.925	4.579	m/s
11	BZ water $v_{ave\ out\ 1}$	1.816	1.767	m/s
12	BZ water $v_{ave\ out\ 2}$	3.292	3.093	m/s

Table 5.7 – WCLL V0.6_B steady state analysis: relevant results

The Fig. 5.14 shows the Eurofer upper plate temperature distribution and, according with Fig. 4.43, two radial poloidal planes of the elementary cell are shown in Fig. 5.15 and Fig. 5.16. As shown in all the figure, the temperature thermal field is below 314°C, where the hotter zones

are located in the PbLi in the Plane A, and in the middle of the radial length in the Plane B. The domains averaged volume temperatures return comparable values with the related cooling system, since the FW and the BZ water enter at 309.7°C and 311°C, while the Tungsten and FW have both 310.9°C and the PbLi and stiffeners reach 312°C.

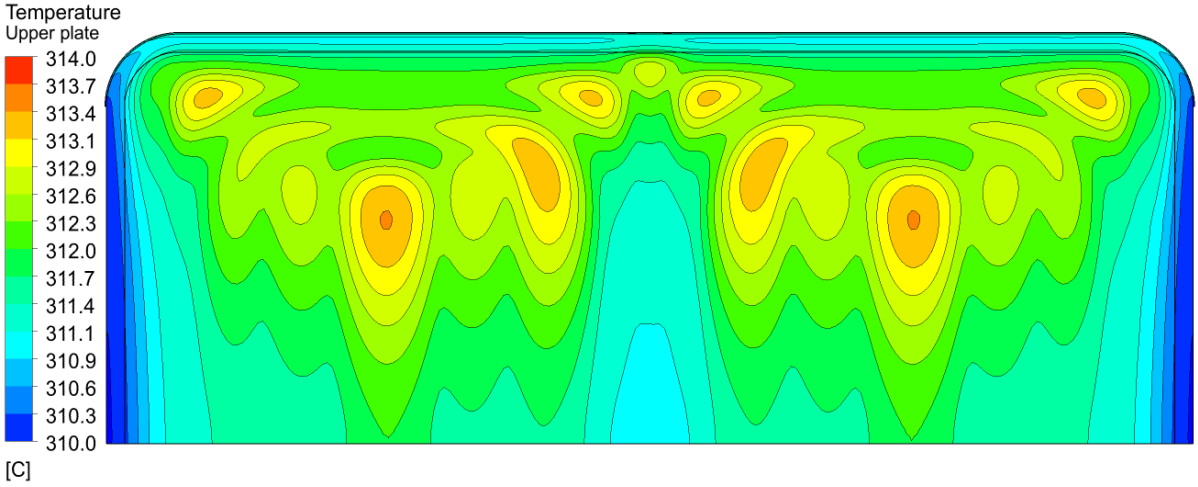

Fig. 5.14 – WCLL V0.6_B dwell steady-state analysis: upper plate temperature distribution

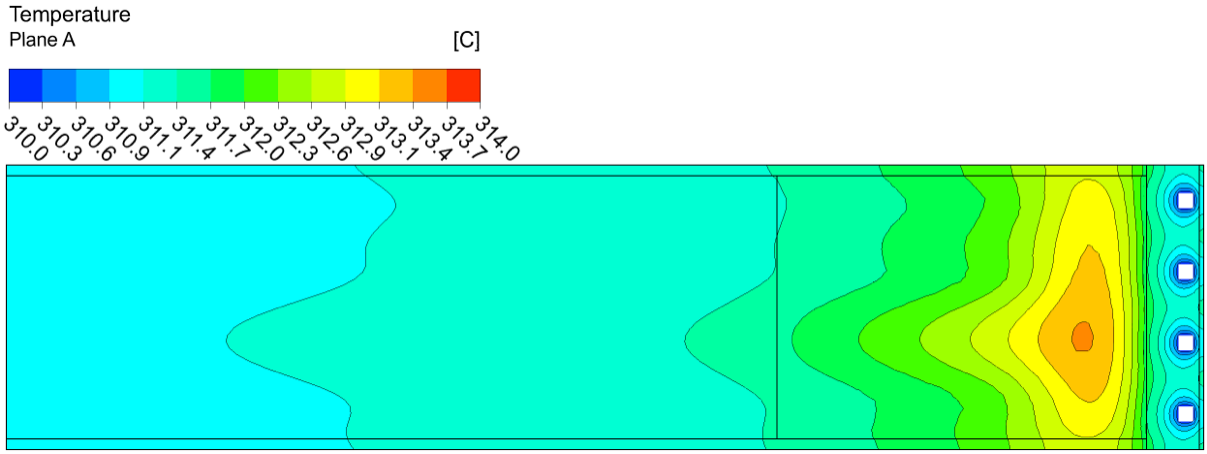

Fig. 5.15 – WCLL V0.6_B dwell steady-state analysis: Plane A temperature distribution

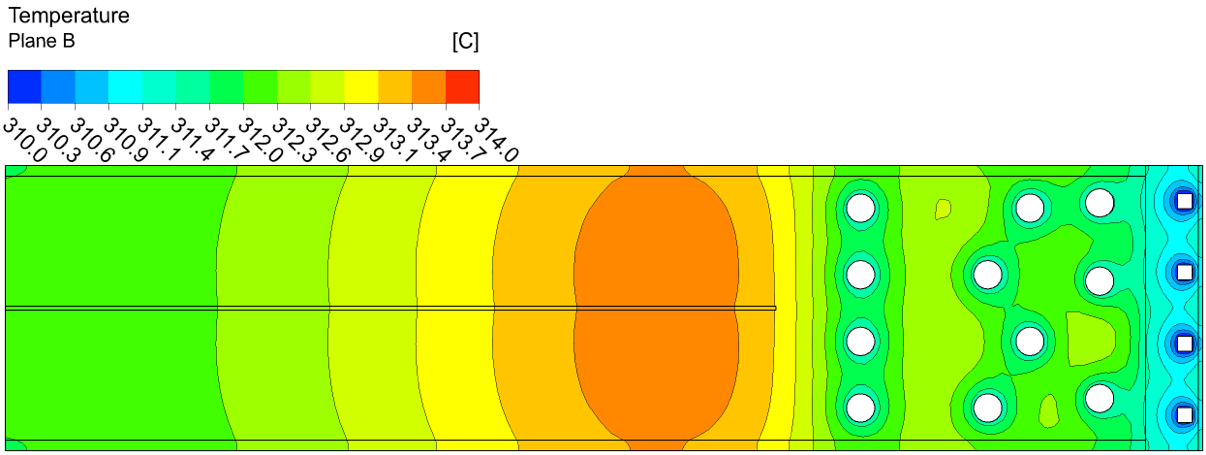

Fig. 5.16 – WCLL V0.6_B dwell steady-state analysis: Plane B temperature distribution

5.5.2. Transient

5.5.2.1. Fast ramp-up

The first transient analysis concerns the dwell-pulse phase. This operational phase has been represented with the fast ramp-up power, where starting from the dwell phase, with an imposed power of 0.887% of the nominal, in 56 seconds reaches the full power. During this transient, also the water inlet conditions vary for both systems, reaching steady-state conditions of inlet temperatures only after 405 and 480 seconds for BZ and FW respectively. The analysis has been performed to evaluate the maximum Eurofer temperature during the transient, since a spike of around the 15% of overpower is foreseen after 20 seconds from the starts of the ramp; and to verify if the water outlet conditions, of the BZ and FW systems, are suitable with the requirements. The relevant temperatures of the performed analysis are shown in Table 5.8.

Parameters	**Value**		**Unit**
	$t_{initial}$	t_{final}	
Tungsten T_{max}	311.5	488.2	°C
FW T_{max}	311.9	507.7	°C
Upper Plate T_{max}	313.5	540.9	°C
Lower Plate T_{max}	313.5	542.6	°C
Baffle T_{max}	313.6	543.5	°C
PbLi T_{max}	313.8	586.3	°C
FW Water $T_{ave\ out}$	310.1	328.2	°C
BZ Water $T_{ave\ out}$	311.3	327.7	°C

Table 5.8 – WCLL V0.6_B fast ramp-up transient initial and final temperature

The total time of the transient simulation has been set at 1000 s, in order to guarantee adequate steady-state conditions at the end of it, trying to recreate the pulsed phase. The analysis of the transient timesteps also provides the timing within which the reactor returns to normal operation, verifying if the data declared in the Sect. 5.3 are truthful and comparable.

In Fig. 5.17 are reported the BZ Eurofer structures maximum temperatures trend during the whole transient. It can be stated that no temperatures exceed the imposed limit of 550°C and also that these results are comparable with the steady-state obtained results of Table 5.7,

confirming that the system has returned to a stationary condition of full power. Regarding the baffle plate, a slight temperature differentiation is noted, where, in the steady-state analysis returns a temperature beyond the limit and in this case below it. This is probably attributable to the mesh, which, especially in the back part of the model where this value is obtained, is coarser, affecting the numerical prediction of the results. In addition, due to the large thermal inertia of the PbLi, it seems that after 1000s the baffle plate still has to grow its maximum temperature, not presenting a completely isothermal trend.

As regards the PbLi, the maximum temperature has a trend which reaches the stability after around 460 s. In the first 120 s, the PbLi temperature rises up very fast with an almost vertical growth, increasing its temperature by about 200 degrees. From 120 to 320 seconds the trend begins to flatten towards the value of 584°C, afterwards it continues to grow very slowly until reaching 586°C after 460 s, but to obtain the final and constant value of 586.3°C it takes 800 seconds. The PbLi maximum temperature trend is shown in Fig. 5.18.

Regarding the FW system temperatures trend, shown in Fig. 5.19, the Tungsten domain reaches a stability condition just after 320 s. This domain shows a growth comparable with the transient thermal loads in the first 40 seconds, after which, the effects of the cooling water begin to affect the domain by modifying its trend. Even if the FW water has a constant inlet temperature after the 480 seconds, the Tungsten domain does not seem to be affected by this delay. The FW chase instead, reaches a stationary condition much later, due to the water that determines its timing, stabilizing after 500 seconds.

In Fig. 5.20 are reported the BZ water average temperatures at inlet and outlet. The outlet water temperature has a very slow response to the system change, while the inlet water steady temperature condition is reached after 405 s, the outlet temperature steady-state condition is obtained more than twice as long, at around 900 seconds. This pronounced delay is closely related to the PbLi timing, as the tubes are immersed in the breeder. The PbLi thermal inertia deeply affects this system, greatly delaying the achievement of stationary conditions. The FW water, even if the steady inlet temperature is obtained 75 seconds after the BZ, suddenly after 480 seconds reaches an outlet steady-state temperature. As shown in Fig. 5.21, two parallel isothermal lines are represented after 500 s. The initial part of the transient instead, in the first 60 seconds, the temperature returns an identical trend of the power ramp-up, then in 150 seconds already reaches optimal conditions with a temperature above 325°C, promptly ensuring

and providing adequate water conditions to the PHTS. To obtain similar conditions for the BZ, around 350 s are needed.

A further assessment has performed comparing the water outlet temperatures obtained by CFD and RELAP5/Mod3.3 model. The COB equatorial cell is the one experiencing the highest BZ thermal loads (in terms of nuclear heating). For this reason, it is also the one provided with the largest DWT heat transfer surface. This design parameter, as well as the tube layout, is available only for this breeding cell. Although, both these design features vary along the poloidal coordinate. Hence, in the RELAP5 model, the BZ cooling system heat transfer capability is overestimated. On the contrary, the material inventories are strictly maintained. With the system code, during the full power state, the mean PbLi temperature obtained (378°C) is the average one related to the whole BB component, not to the COB equatorial cell (higher since this specific cell is more thermally stressed). During the transient, the overestimation of the BZ heat transfer surface inside the breeding cells of the whole reactor led to a faster system response (compared with CFD) due to the lower thermal inertia (the ΔT from pulse to dwell for the system code is reduced). This misalignment between code results is reduced for the FW, since no PbLi is present in this system and the structural temperatures are mainly driven by the water coolant. The time difference to reach stationary conditions is a consequence: the CFD model takes 900 seconds, the RELAP5 model shows stationary conditions shortly after the stationarity of the inlet temperature at around 500 seconds. Thus, the PbLi thermal inertia deeply affects the temperature rising, since the CFD model takes almost the double of the time. Obviously CFD considers all the local thermal effects of the model. The thermal-hydraulic system code roughly approximates the viscous sub-layer effects, while the CFD provides more accurate values at local level, despite having $y^+=5$, that affect the heat transfer. In particular, in Fig. 5.22, a BZ outlet temperature spike is noted at around 50 s, this is due to the increase of the inlet temperature at 40 seconds as imposed from boundary condition, that, combined with the almost full power contribution, returns a spike of around 8 degrees. The system code, instead, absolutely jumps over, showing a linear growth at that time. Thus, the PbLi thermal inertia deeply affects the temperature rising in both codes playing a key role.

The FW water coolant comparison shows a similar trend for both codes. Nonetheless, the CFD model shows a less "nervous" trend, reaching an outlet temperature of 327°C in a softer way. Both codes after 250 seconds have an identical trend. Regardless to the adopted code, the FW water system promptly reacts to changes as shown in Fig. 5.23. As shown in the figure, the

CFD model reaches the first peak at almost 320°C, while the RELAP5 model returns a higher temperature by 4.5 degrees, this is also due to the modellization differences between one cell and the entire reactor. Moreover, in the CFD analysis the PbLi thermal inertia affects the FW system with continuous heat exchange in the frontal part of the model, providing a significant contribution to the heat exchange. On the contrary, the RELAP5 code returns the average temperature of the whole reactor which is subjected to higher heat fluxes compared to that of the equatorial elementary cell.

To have a better understanding of the delay due to PbLi on FW, in Ref. [71] a transient case has been performed with transient thermal load and water inlet temperature condition very similar. Comparing the two FW water temperatures trends, normalized on the time of the inlet temperature, since in this model the steady inlet temperature is reached at 480 s instead of 300 s of the stand-alone system described in Ref. [71], the latter, immediately obtain stationary output values. In comparison, a delay of around 20 seconds is noted in the present analysis.

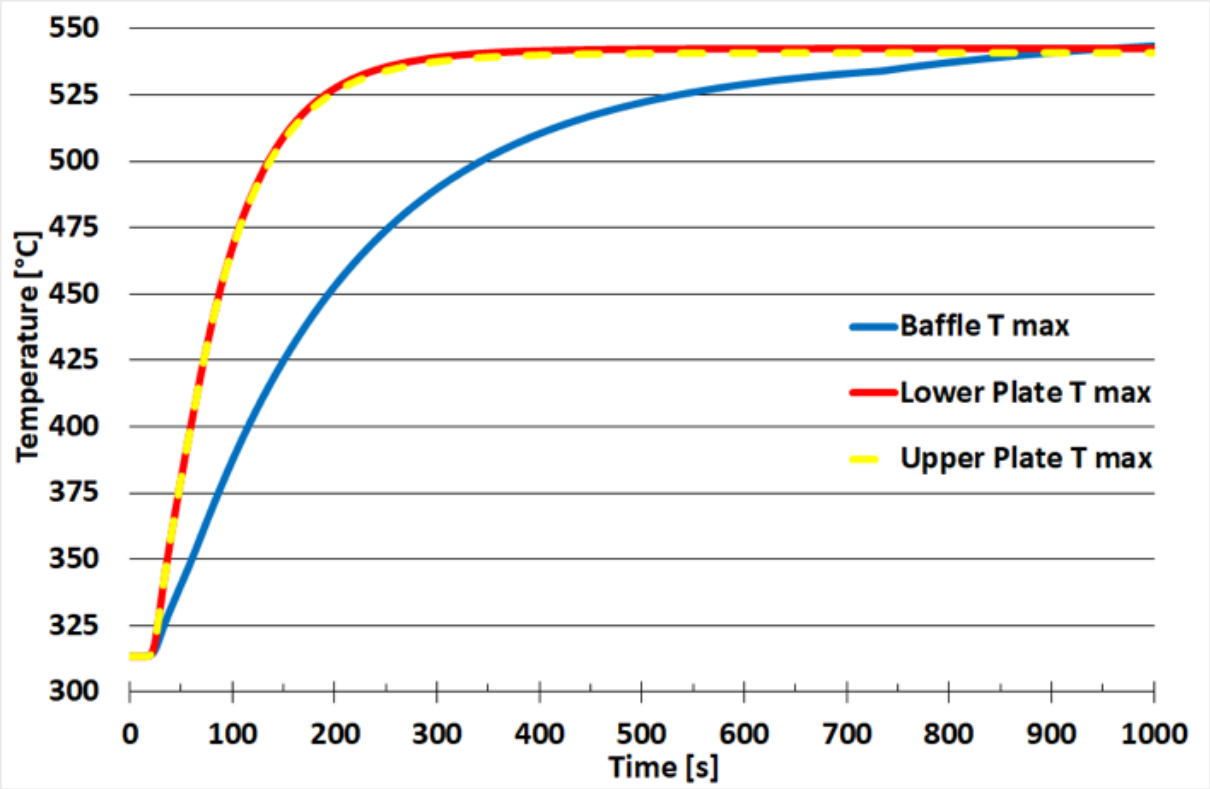

Fig. 5.17 – WCLL V0.6_B fast ramp-up transient maximum BZ Eurofer temperatures trend

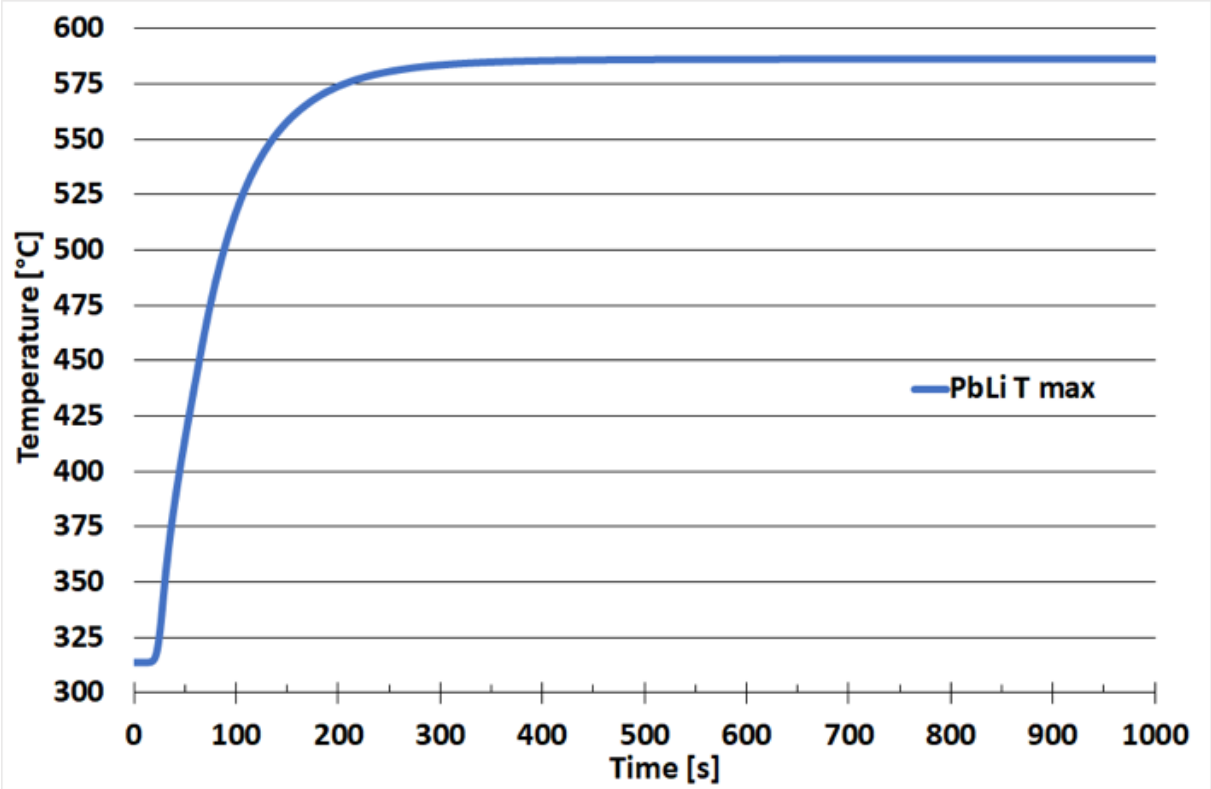

Fig. 5.18 – WCLL V0.6_B fast ramp-up transient PbLi maximum temperature trend

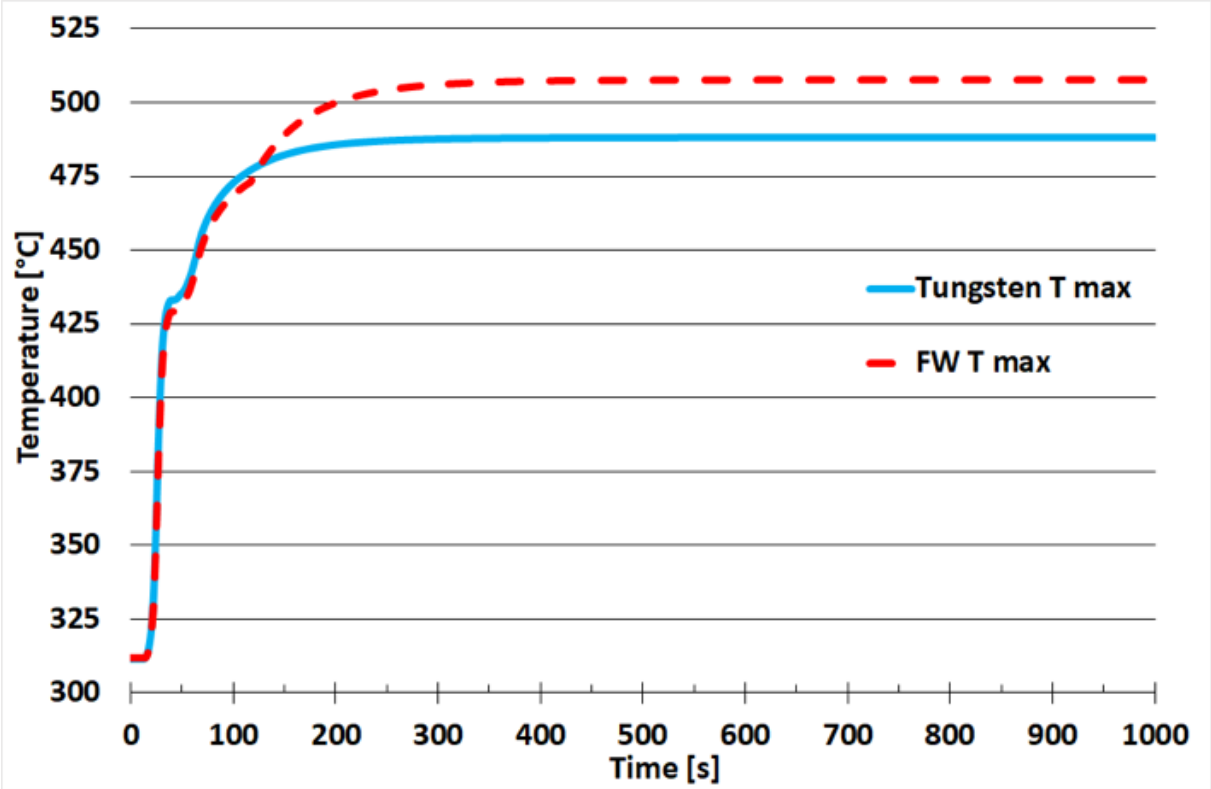

Fig. 5.19 – WCLL V0.6_B fast ramp-up transient maximum Tungsten and FW temperatures trend

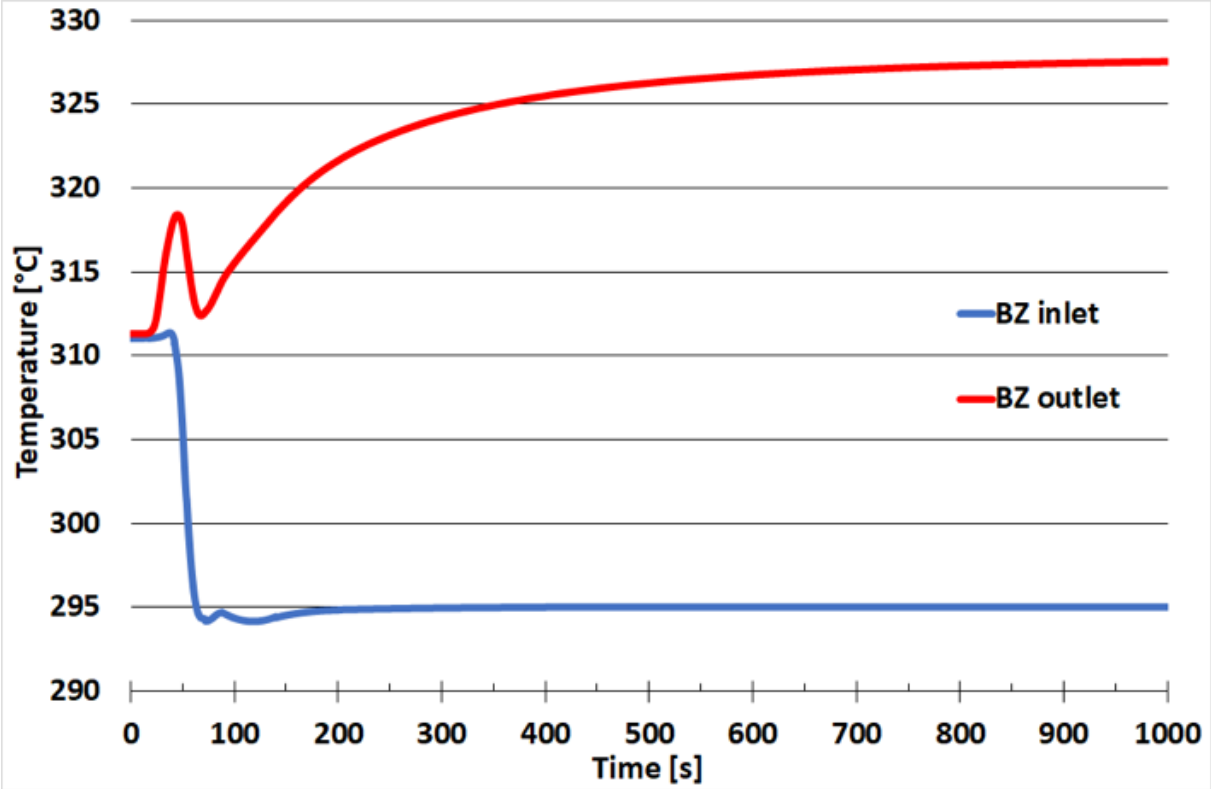

Fig. 5.20 – WCLL V0.6_B fast ramp-up transient BZ water average inlet and outlet temperatures trend

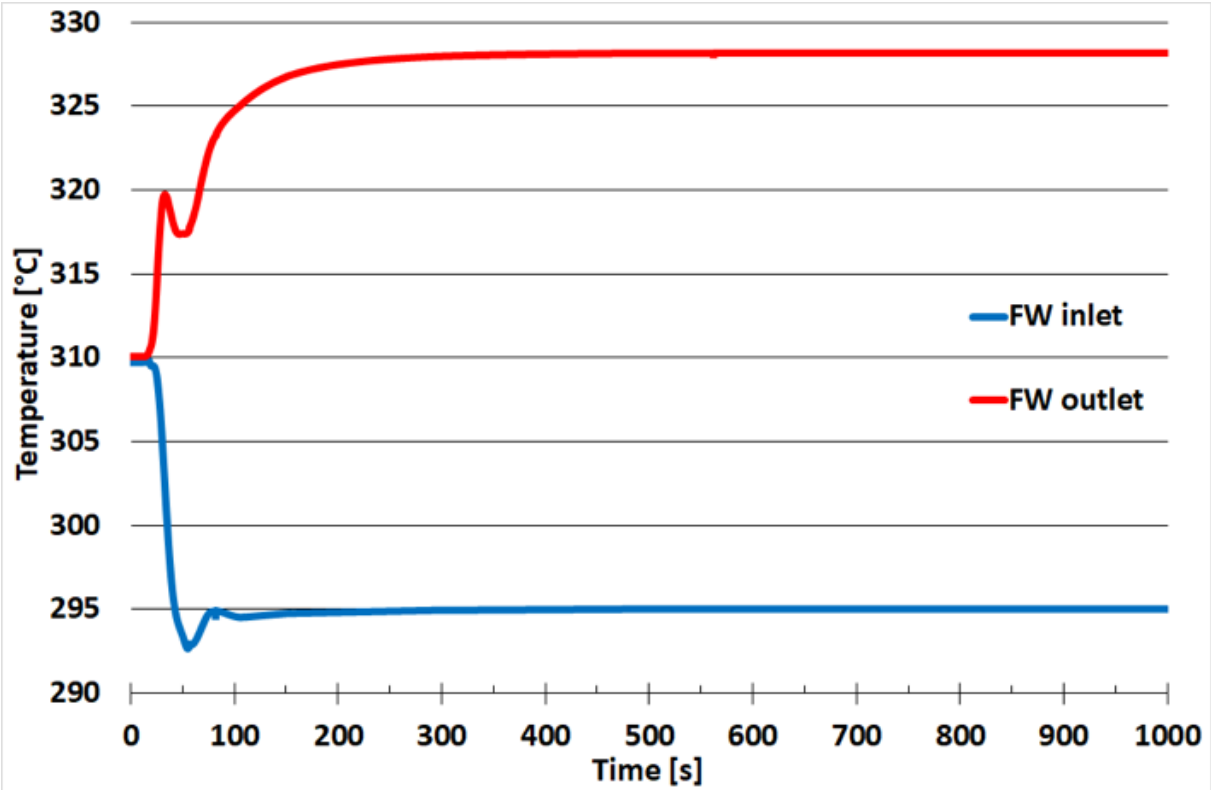

Fig. 5.21 – WCLL V0.6_B fast ramp-up transient FW water average inlet and outlet temperatures trend

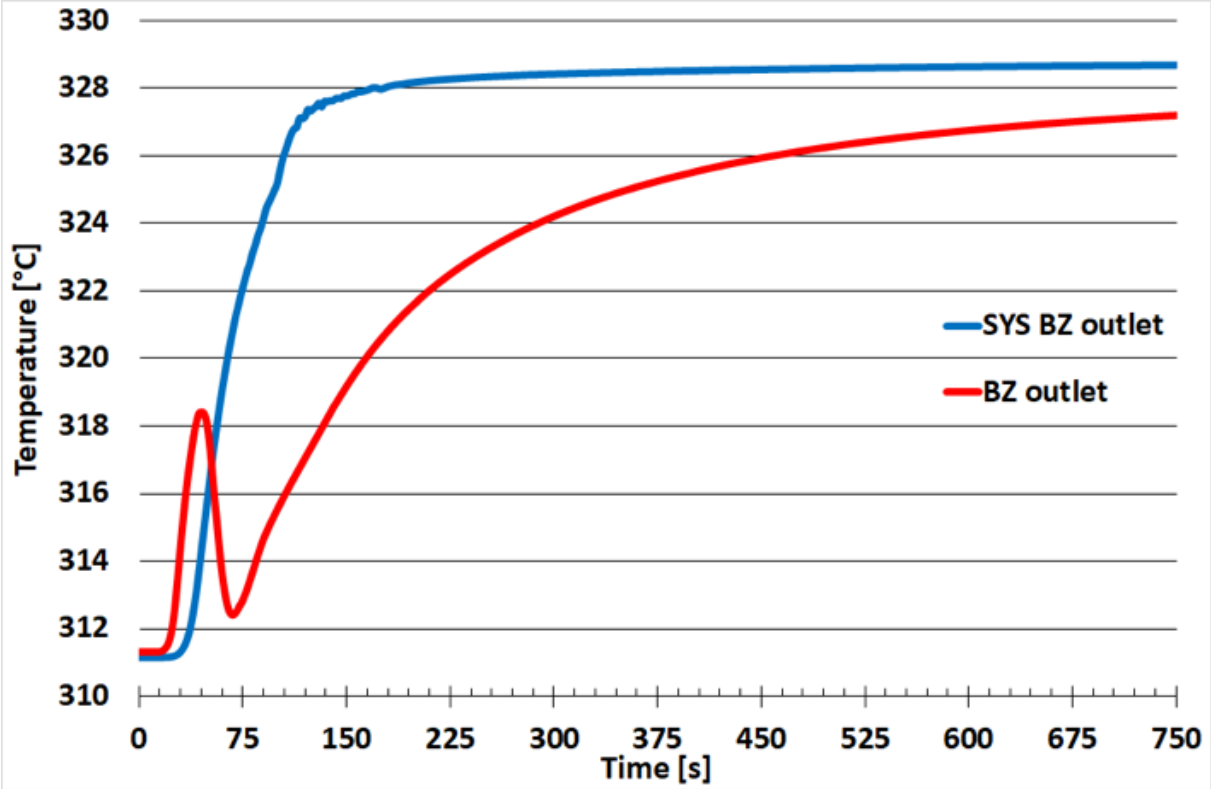

Fig. 5.22 – WCLL V0.6_B fast ramp-up transient BZ water average outlet temperatures comparison trend

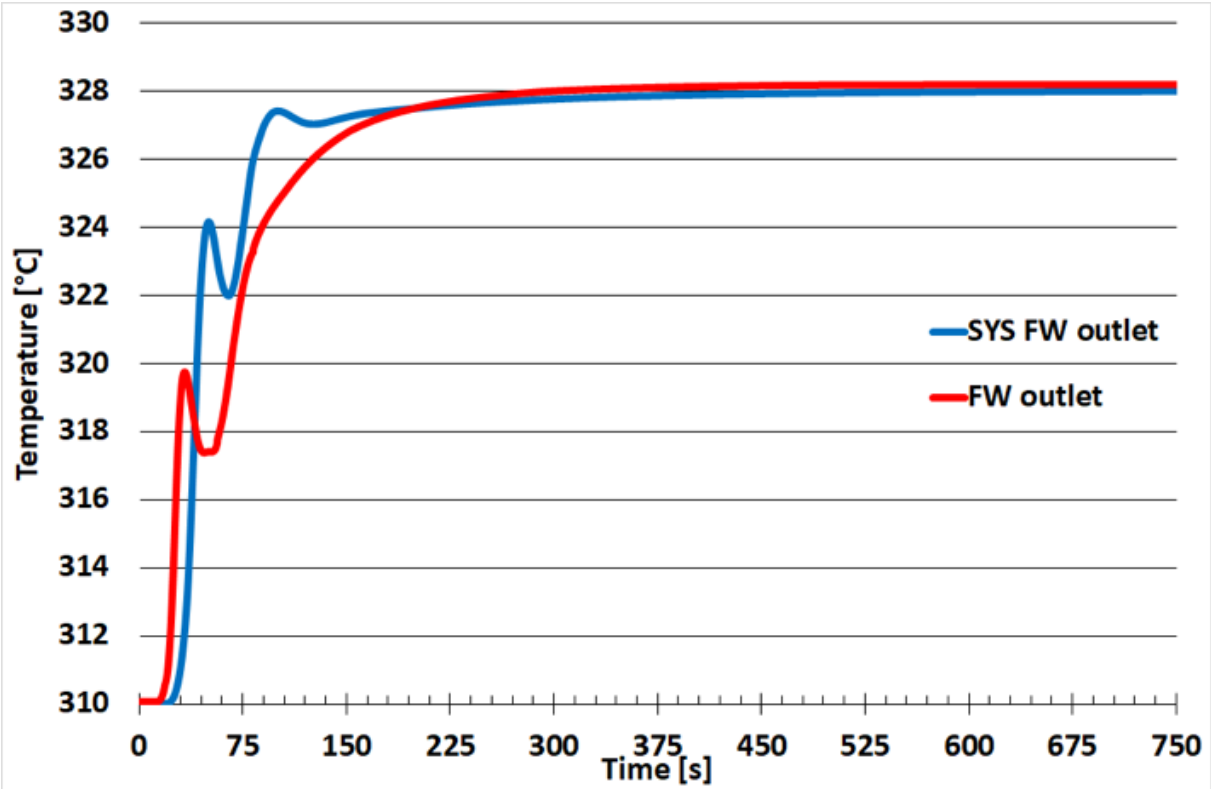

Fig. 5.23 – WCLL V0.6_B fast ramp-up transient FW water average outlet temperatures comparison trend

5.5.2.2. Ramp-down

The second analyzed transient concerns the pulse-dwell phase. This operational phase has been represented with the ramp-down power curves, where, starting from the pulsed phase of full power, in an interval time of 150 seconds reaches the dwell state, with the 0.887% of the nominal power imposed. During this transient also, the water inlet conditions vary for both systems, reaching a dwell steady-state conditions of inlet temperatures only after 200 seconds for both cooling systems, BZ and FW respectively. The analysis has been performed to evaluate the maximum Eurofer temperature trend, in order to verify if the elementary cell returns to an isothermal dwell condition in the expected 650 seconds; and to verify if the water outlet conditions, of the BZ and FW systems, are suitable with the requirements. The relevant output temperatures of initial and final conditions are shown in Table 5.9.

Parameters	**Value**		**Unit**
	$t_{initial}$	t_{final}	
Tungsten T_{max}	488.2	311.5	°C
FW T_{max}	507.7	311.9	°C
Upper Plate T_{max}	541.1	343.2	°C
Lower Plate T_{max}	542.6	343.2	°C
Baffle T_{max}	549.5	342.4	°C
PbLi T_{max}	586.3	343.2	°C
FW Water $T_{ave\ out}$	328.2	310.1	°C
BZ Water $T_{ave\ out}$	327.8	312.1	°C

Table 5.9 – WCLL V0.6_B ramp-down transient initial and final temperatures

The total time of the transient simulation has been set at 760 s, this to take into account the initial 10 seconds of pulsed phase and guaranteeing an additional 100 seconds in order to evaluate, if and when, the system returns to stationary conditions before a new cycle begins.

The thermal-hydraulic analysis has demonstrated that the BZ system of the elementary cell under analysis does not reach an equilibrium condition at the end of the transient. In particular, the BZ return a maximum temperature with a parabolic decreasing trend both in Eurofer structures and PbLi, shown in Fig. 5.24 and Fig. 5.25 respectively. All these four domains have an identical trend, where, the only one difference occurs in the PbLi domain before the first 60

seconds, where the curve has a different slope, after then, it follows the identical trend of the Eurofer structures. In fact, after 52 seconds, the volumetric deposited power curve no longer has a decreasing exponential tendency, but, starting from 54 seconds, it follows a trend due to the decay heat which is more linear. Already at 75 seconds, the four curves have the same maximum temperature of 520°C, to then arrive in 750 seconds at about 340°C with a still considerable slope, which suggests that as many seconds would be necessary to reach a condition of equilibrium. This phenomenon is of considerable importance, as it does not guarantee the complete "discharge" of the temperatures before the start of a new cycle, even if an additional 100 seconds were considered. Further problems caused by temperature build-up could arise in the system, due to the huge thermal inertia of the PbLi.

As seen in the previous case, the FW system provides a faster response compared with the BZ. The system, after 400 seconds from the beginning of the transient, starts to reach an asymptotic value of the steady-state conditions (around 313°C for both domains), when finally, at 650 seconds reaches the steady-state conditions obtaining the maximum temperatures of 311.9°C and 311.5°C for FW and Tungsten respectively, which are the identical values shown in Table 5.7. During the additional 100 seconds, the system remains in a steady state. From the figure, a faster trend is noted in the Tungsten domain, since it is not affected by the PbLi thermal inertia, which delays the FW.

As regards the cooling systems, the ramp-down analysis has returned a different trend for each system. Concerning the BZ, in Fig. 5.27 it can be seen how, in the first 120 seconds, there is a damped downward trend, caused by the steep upward ramp of the inlet temperature and the slow descent of the PbLi temperature. As soon as the inlet temperature of about 311°C (120 seconds) is reached, the outlet temperature begins to decrease with an asymptotic trend towards this temperature. The system, as seen previously, is strongly dependent by the PbLi temperature, causing it to slowly descend. From the final result, at the end of the transient, the BZ average outlet temperature reaches 311.2°C, which is the same of the dwell steady-state simulation, varying by only 0.1. However, even if the temperatures are the same, the graph clearly shows that the outlet temperature has not reached a steady state yet.

The FW water returns two converging trends at 310°C for both inlet and outlet temperatures. Both curves show the same peaks, increasingly reducing the gap between inlet and outlet temperatures with the time progress, as ideally required by the BoP. The water system is able

to guarantee adequate water conditions just before 300 seconds from the simulation starts, obtaining an average outlet temperature of 310°C, which is the same as the dwell steady-state analysis. In this specific case, it would seem that the water is not affected by the PbLi heat exchange, indeed, the phenomenon is due to the fact that the inlet temperature rises so fast that it closes the temperature gap between FW and BZ, which causes the passive heat removal, obtaining an earliest steady-state conditions. The FW water inlet and outlet temperatures are shown in Fig. 5.28.

Even in this transient case, the comparison between the obtained data from CFD and system code, show water temperatures trends considerably different in the BZ and almost similar in the FW, as discussed in the fast ramp analysis due to the modellization effects. As analysed in the previous case, the PbLi in the CFD model drastically increases the timing of temperature drop, of the present analysis, in contrast with the system code which show a decreasing trend reaching around 311°C meanwhile the power ramp-down ends (150 s) for both cooling systems, as shown in Fig. 5.29 and Fig. 5.30. Unlike the previous case, all the four temperatures of a single system are plotted, this to highlight the trend convergence to the average value of the water thermodynamic cycle (311.5°C).

As the BZ water system shows, the RELAP5 model at 90 seconds, return two temperatures that meet at 312°C, stabilizing over the next 90 seconds at the temperature of approximately 311.5°C. Otherwise, in the CFD model the water outlet temperature never joins the inlet curve, since the PbLi thermal inertia slowly flattens the curve.

As regards the comparison of the FW water, the RELAP5 model shows that the inlet and outlet temperatures trend crossing, resulting in inlet water that exits from the system colder than it entered. This occurs from 90 to 200 seconds when the curves show a damped oscillatory trend, crossing four times. Differently from what was seen in the CFD model, in this case, the FW water is the "slow system", reaching a steady-state conditions after 225 seconds. The response of the CFD model shows how the two temperatures tend to the same value, recreating the same trend between inlet and outlet.

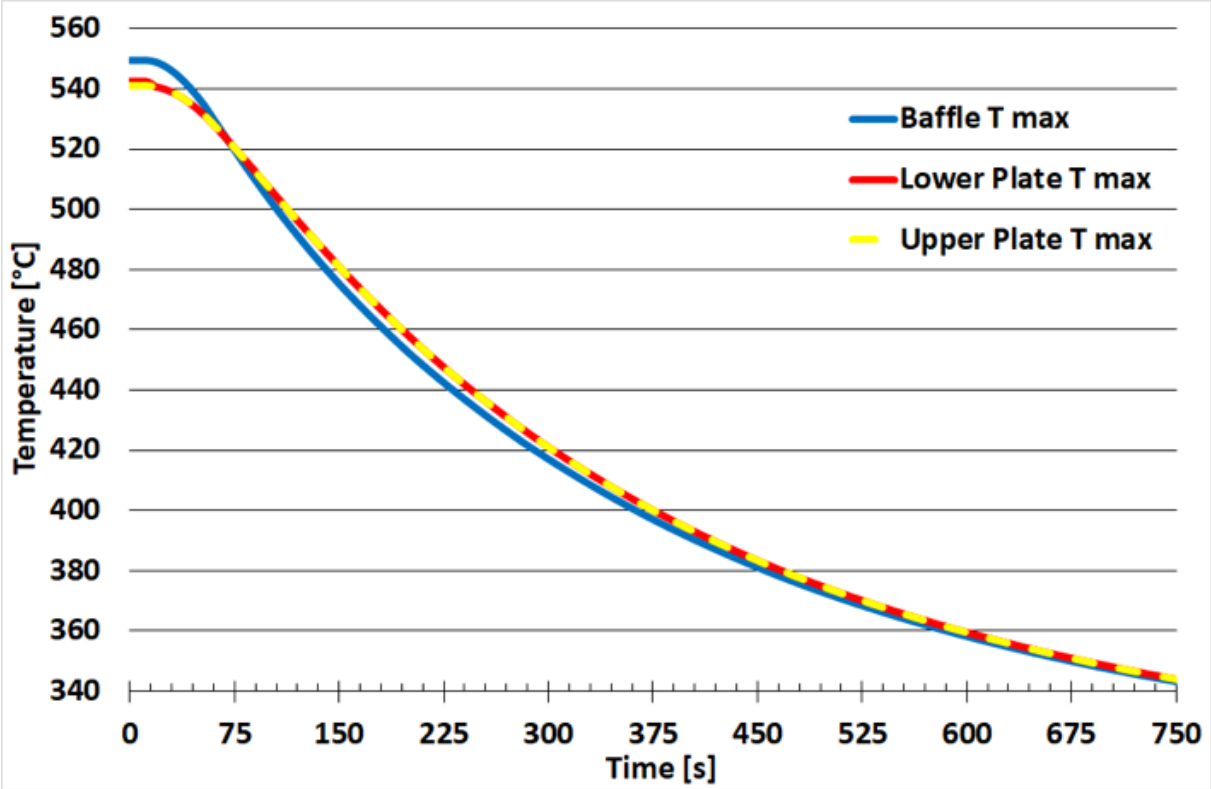

Fig. 5.24 – WCLL V0.6_B ramp-down transient maximum BZ Eurofer temperatures trend

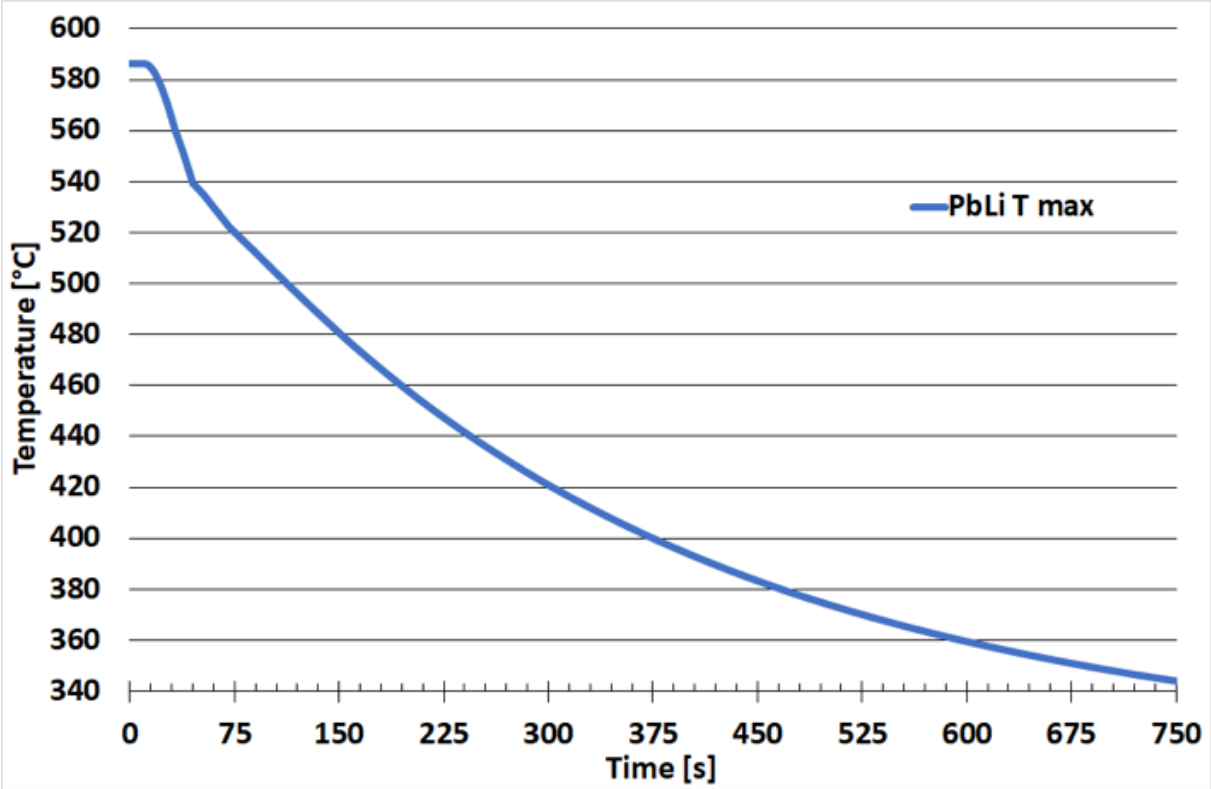

Fig. 5.25 – WCLL V0.6_B ramp-down transient PbLi maximum temperature trend

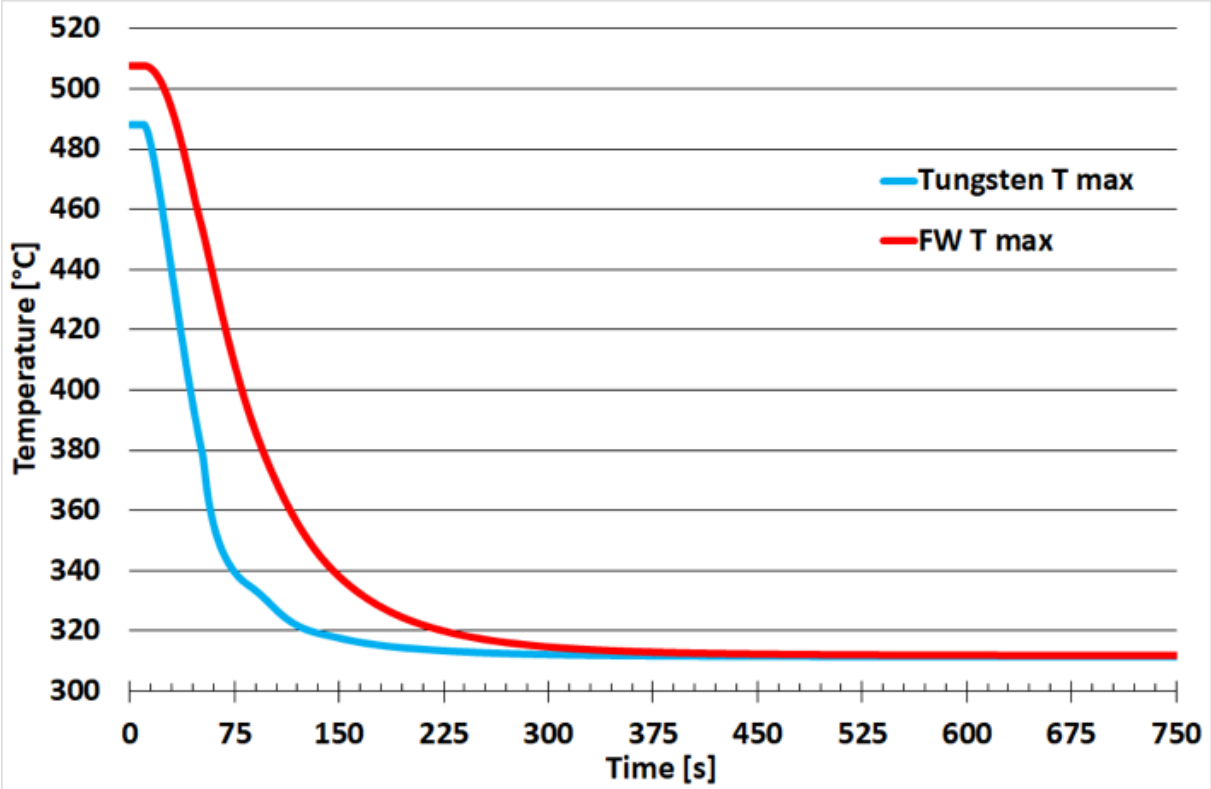

Fig. 5.26 – WCLL V0.6_B ramp-down transient maximum Tungsten and FW temperatures trend

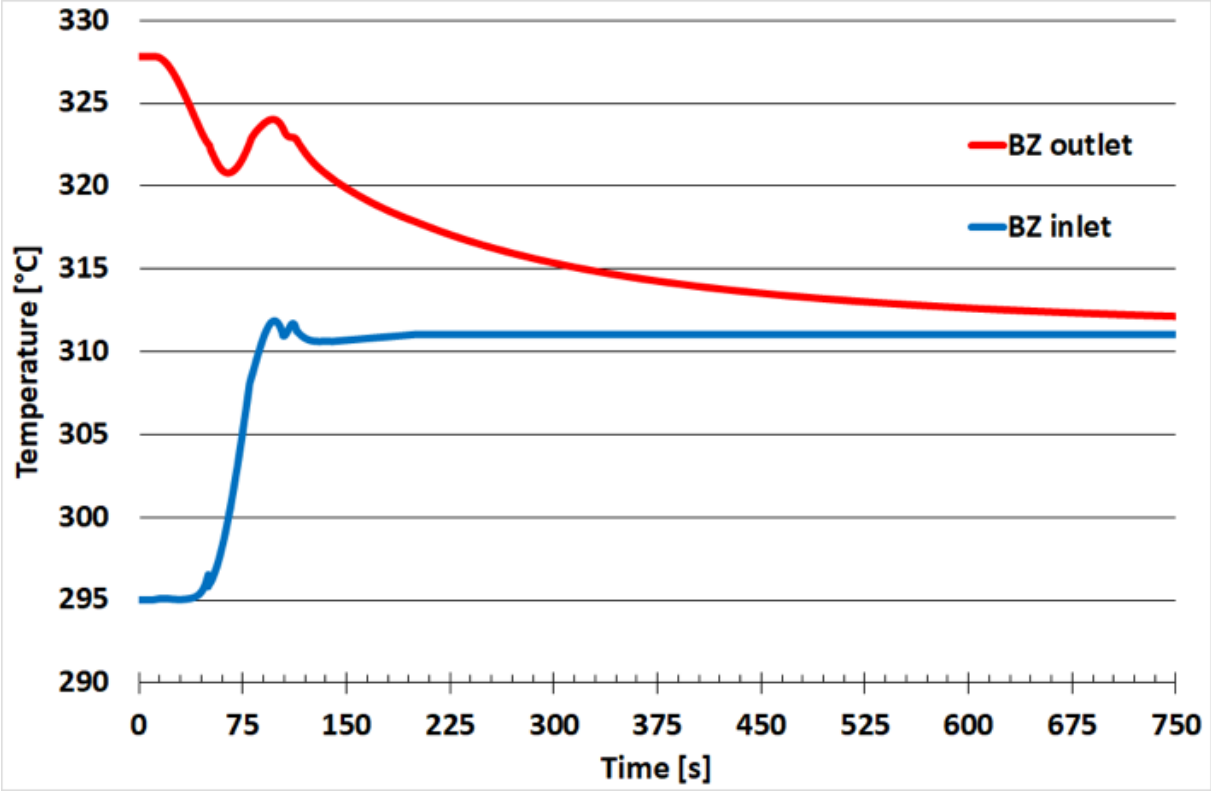

Fig. 5.27 – WCLL V0.6_B ramp-down transient BZ water average inlet and outlet temperatures trend

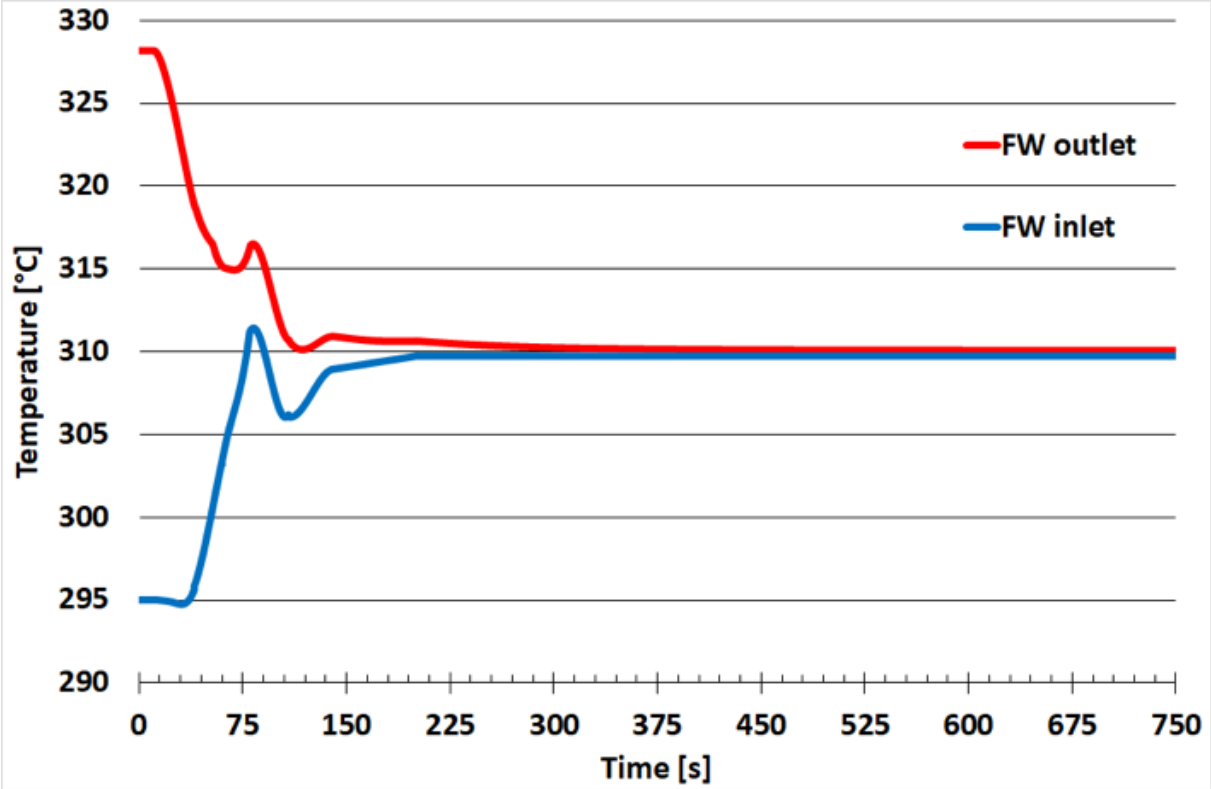

Fig. 5.28 – WCLL V0.6_B ramp-down transient FW water average inlet and outlet temperatures trend

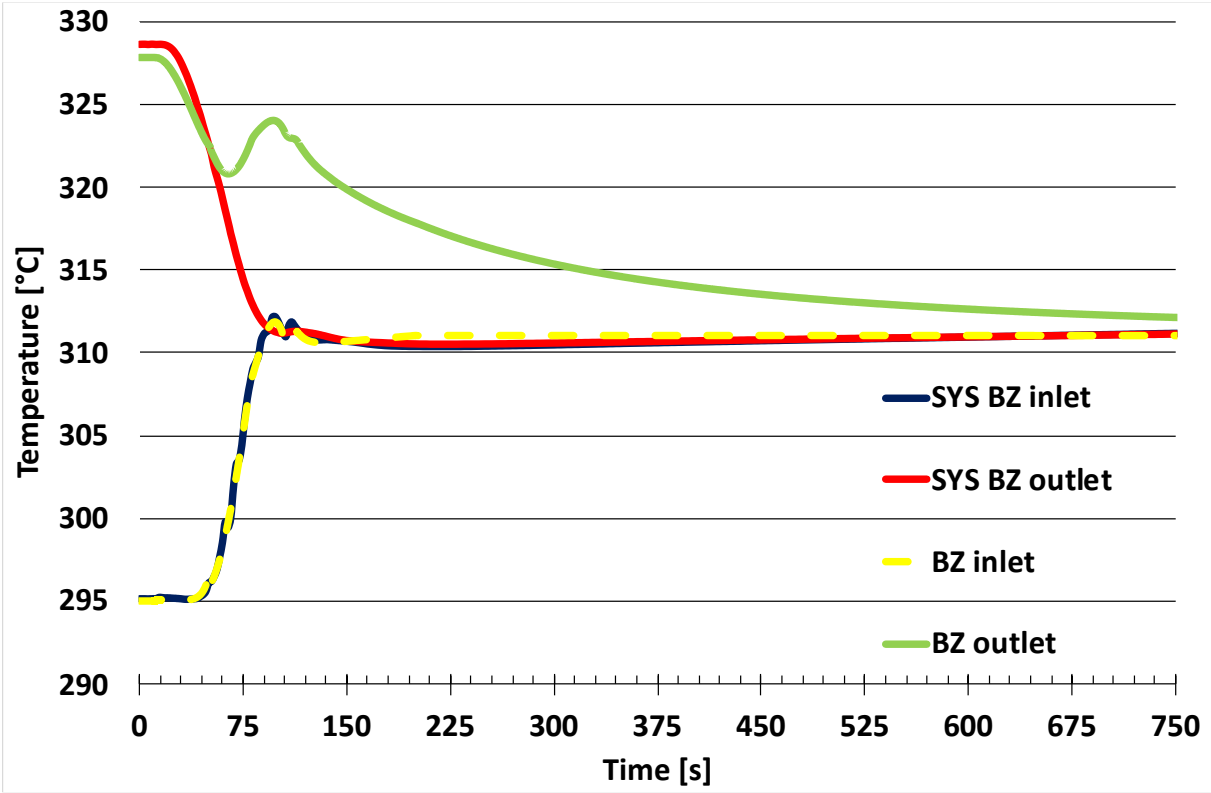

Fig. 5.29 – WCLL V0.6_B ramp-down transient BZ water temperatures comparison trend

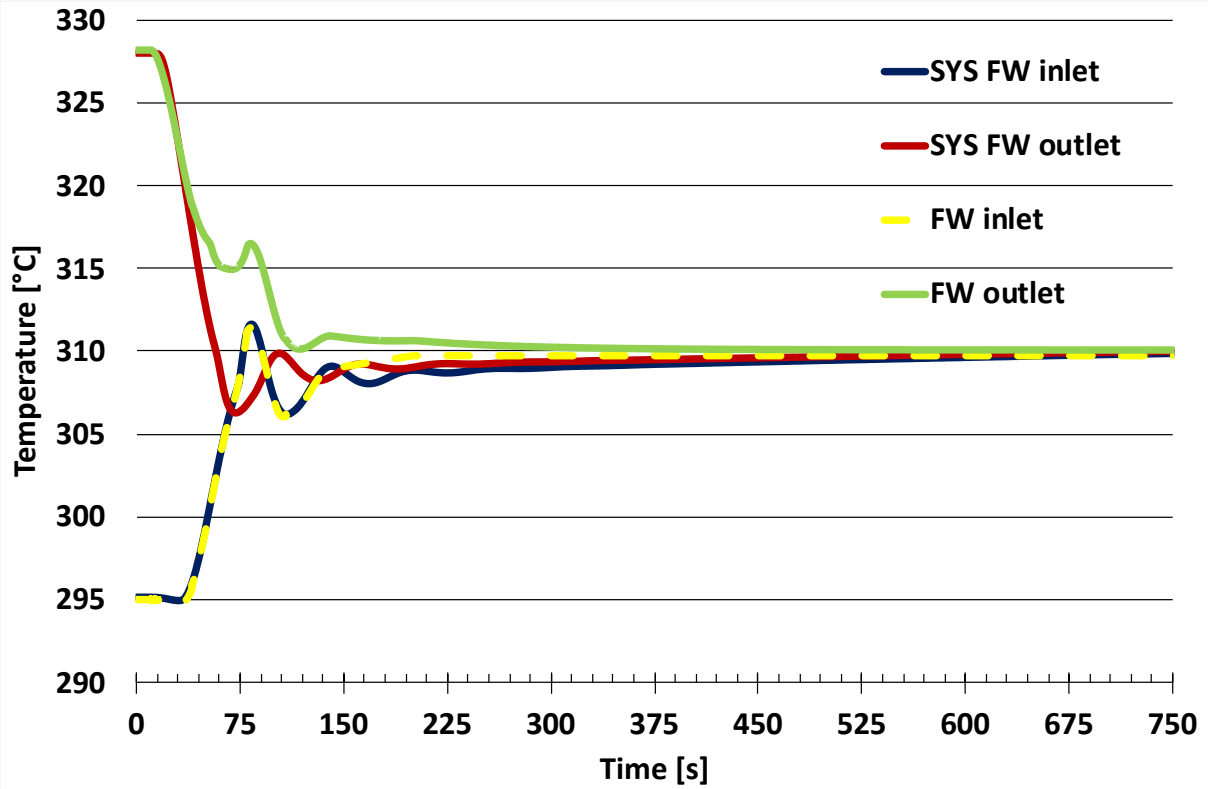

Fig. 5.30 – WCLL V0.6_B ramp-down transient FW water temperatures comparison trend

5.5.2.3. Low fluctuations

The transient analysis, that concerns low overpower fluctuations during the pulsed phase, starts from the steady-state condition of full power (pulse). The analysis has been performed to evaluate the Eurofer temperature field, evaluating the possibility of an increasing build-up temperature and the water outlet conditions of the BZ and FW cooling systems, during this transient phase. The relevant temperatures at initial and final conditions have been reported in Table 5.10.

Parameters	**Value**		**Unit**
	$t_{initial}$	t_{final}	
Tungsten T_{max}	488.2	488.9	°C
FW T_{max}	507.7	507.8	°C
Upper Plate T_{max}	540.4	540.4	°C
Lower Plate T_{max}	540.6	540.6	°C
Baffle T_{max}	549.5	549.5	°C
PbLi T_{max}	586.1	586.5	°C
FW Water $T_{ave\ out}$	328.2	328.3	°C
BZ Water $T_{ave\ out}$	327.8	327.8	°C

Table 5.10 – WCLL V0.6_B low fluctuations transient initial and final temperatures

The simulation has a fixed total time of 125 s, to guarantee and adequate steady-state conditions at the end of the transient, attempting to obtain the pulsed phase main outputs parameters of the steady-state analysis.

In Fig. 5.31 are reported the maximum BZ Eurofer temperature trend during the whole transient, it can be affirmed that no Eurofer structures exceed the imposed limit and also that these results are comparable with the results obtained in Table 5.7. Only one value stands out, which is the maximum baffle temperature, as in the previous case of the fast ramp-up, returns a value below the limit of 550°C. This has been considered attributable to the mesh, which affects the numerical prediction of the results. Moreover, is also caused to the large thermal inertia of the PbLi that leaps over the fluctuations. Nevertheless, the BZ Eurofer structures have no variation, from the initial steady-state conditions of the transient analysis, caused by the fluctuation peaks. Form the figure it can be seen that both stiffeners and the maximum baffle temperature do not

show any significant slope, staying almost isothermal. This means that the system in analysis "absorbs" these power oscillations and the BZ Eurofer structures are not significantly affected.

As regards the PbLi maximum temperature trend, three different steps have been carried out, with around 4 seconds of delay from the related peaks. For each peak, a maximum temperature grow is noted, followed by a plateau of around 20 seconds. The temperature starts to grow in correspondence of each peak (25 s, 55 s and 85 s) with a linear ramp for around 4 seconds (the noted delay). Since PbLi has a large thermal inertia the transient ending temperature is slightly above the initial temperature, but with an increase of 0.4 degrees, which is considered negligible. The PbLi maximum temperature trend is shown in Fig. 5.32.

The Tungsten domain, as shown in Fig. 5.33, clearly returns the power fluctuation trend with three similar Gaussian curves of the maximum temperature. The first peak, located at 25 s, returns a maximum temperature, which in that time, is 489.9°C, but, from the outputs post processing, the Tungsten temperature continue to grows up to 490.3°C, which corresponds a transient time of around 27 s, presenting a delay-time of about 2 s. This phenomenon has also been found in the second and the third peak, where, in the last peak (85 s) the temperature reaches 490.3°C, but the temperature still grows for 2 seconds, reaching 490.6°C which is the highest reached temperature. From the initial to the final condition, a temperature build-up occurs, that correspond to 0.8 degrees. In Fig. 5.33 is also shown the FW domain maximum temperature trend, which is presented as an isothermal line. The maximum temperature increase has been evaluated 0.05 degrees, assumed negligible. This temperature trend differs from the Tungsten layer domain because it is strongly affected by the continuous heat exchange with PbLi.

Regarding the cooling water, shown in Fig. 5.34, the FW systems shows a trend comparable with the Tungsten layer, where three Gaussian curves have been reproduced, due to the reduced distance from the latter instead of FW-PbLi interface. As evaluated in the Tungsten, the higher temperature is reached with a delay respect to the fluctuation peaks. The first temperature peak reaches 328.35°C at 29.25 s, the second 328.37 at 58.22 s, and the last peak reaches the maximum average outlet temperature of 328.38 at 88.54 s, with 4.25, 3.22 and 3.54 seconds of delay respectively. The BZ cooling systems presents an almost isothermal trend, slightly above 327.8°C. Although the trend shows an isothermal line, analyzing the output data, small increases with a logarithmic trend of 30 seconds of period are noted. The temperature grow

starts 5 seconds after each peak. This delay is caused by the thermal inertia of the PbLi which completely absorbs the oscillations, not causing significant variations in the average water outlet temperature.

To have an idea of the variation of the temperature field, two radial-poloidal planes have been chosen to show the temperature trend in the hot-spots zone (Fig. 4.43) at different characteristics times. The specific time are five: the initial condition (t=0 s), 1st fluctuation peak (t=25 s), 2nd fluctuation peak (t=55 s), 3rd fluctuation peak (t=85 s), and the end of the transient (t=125 s). From both planes, shown in Fig. 5.36 and Fig. 5.37, A and B respectively, is it clear that globally no substantial changes are showed in the temperature field of Eurofer structures and PbLi, since the thermal inertia of the latter absorbs completely the power variation during the transient in each selected plane.

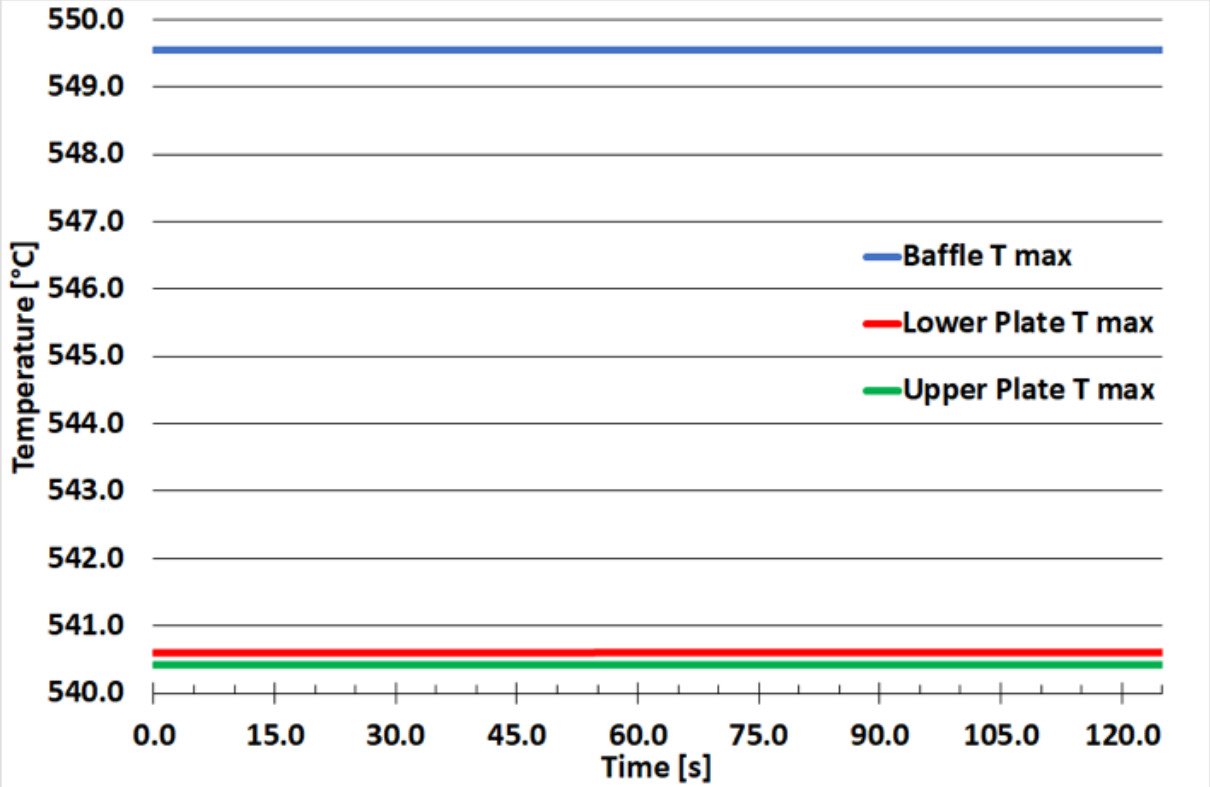

Fig. 5.31 – WCLL V0.6_B low fluctuations transient maximum BZ Eurofer temperature trend

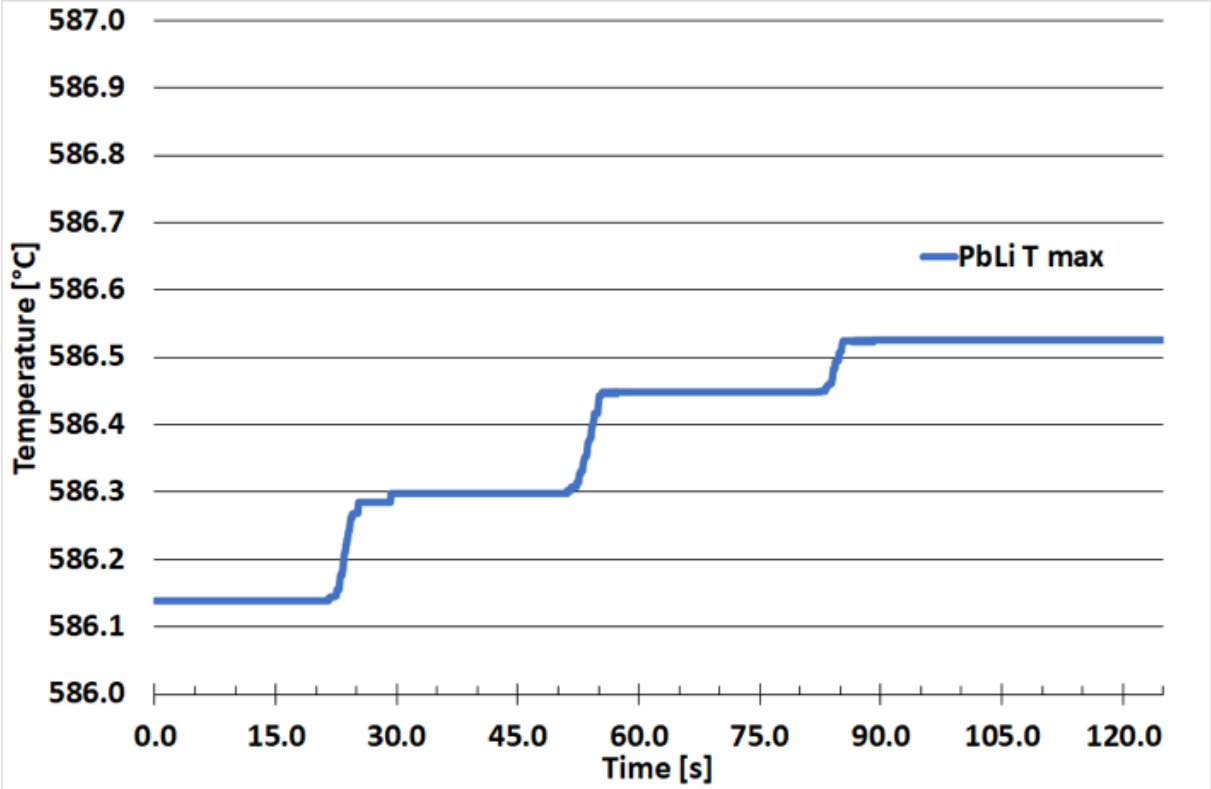

Fig. 5.32 – WCLL V0.6_B low fluctuations transient PbLi maximum temperature trend

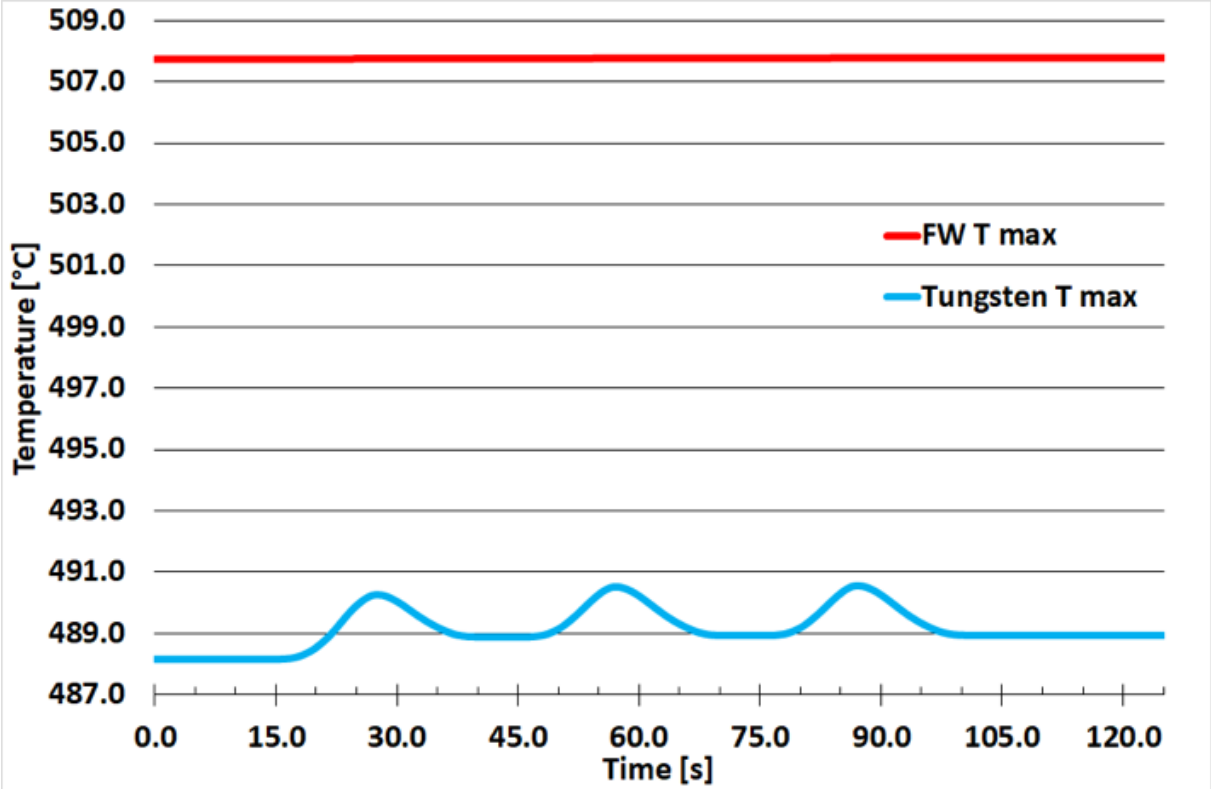

Fig. 5.33 – WCLL V0.6_B low fluctuations transient Tungsten and FW maximum temperatures trend

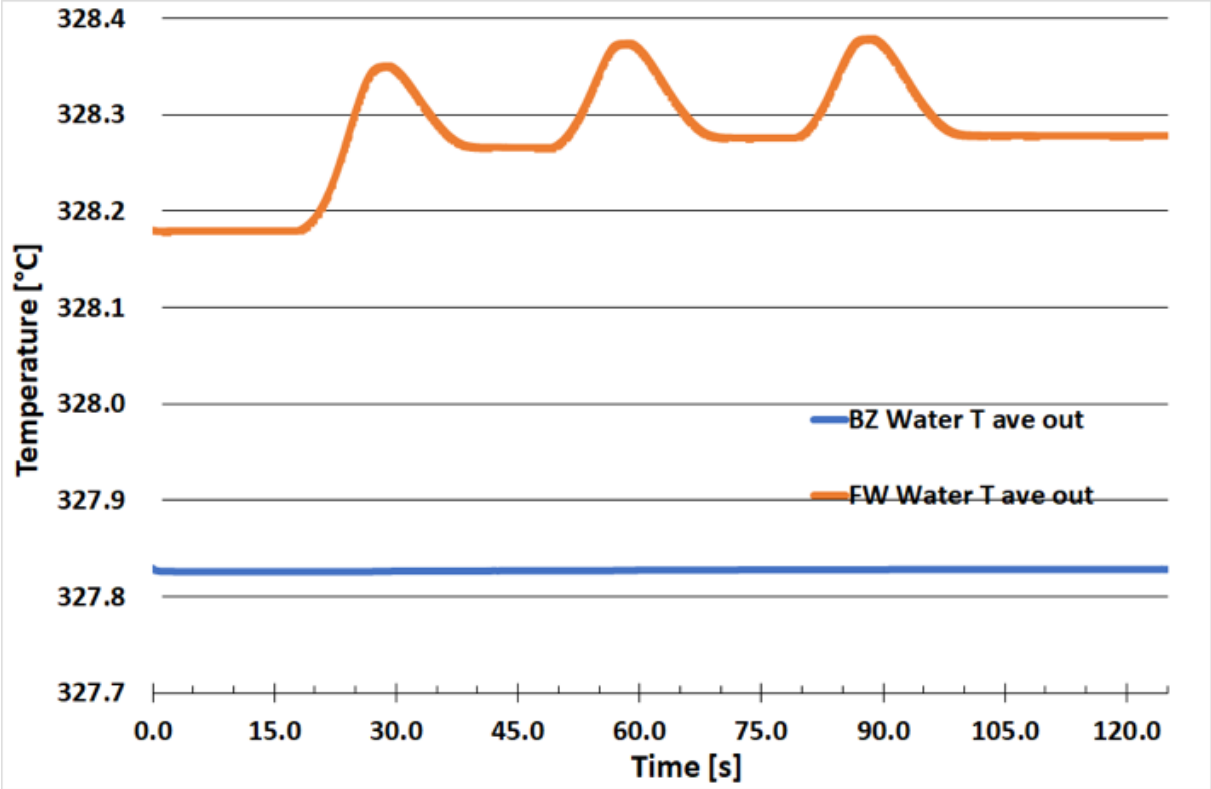

Fig. 5.34 – WCLL V0.6_B low fluctuations transient water average outlet temperatures trend

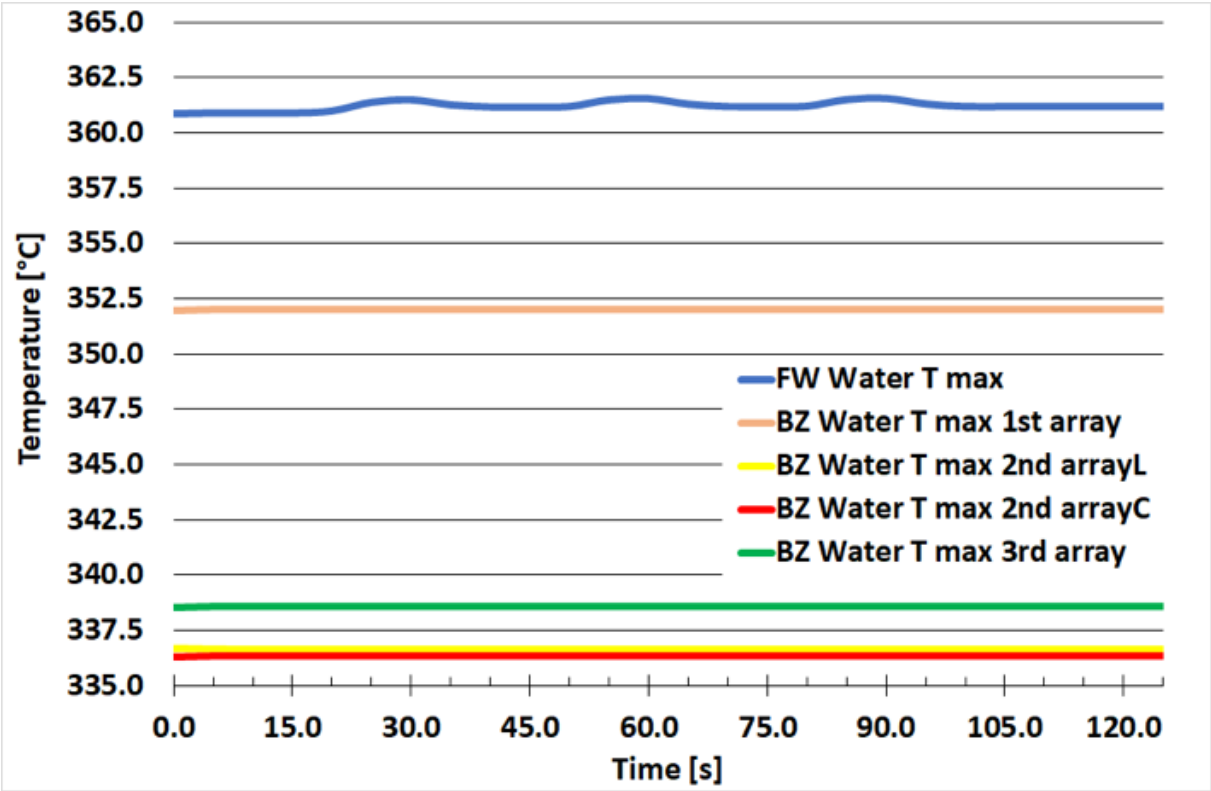

Fig. 5.35 – WCLL V0.6_B low fluctuations transient water maximum temperatures trend

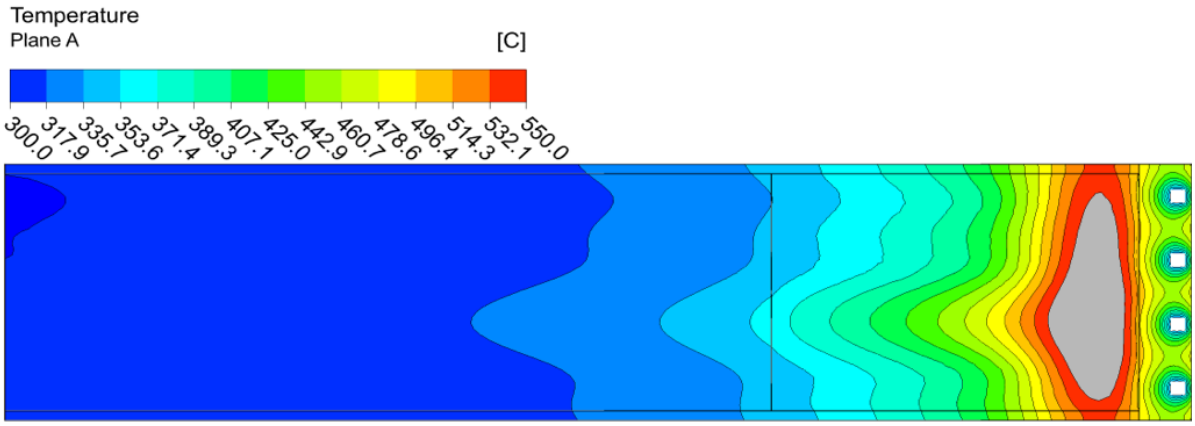

a) t = 0 s

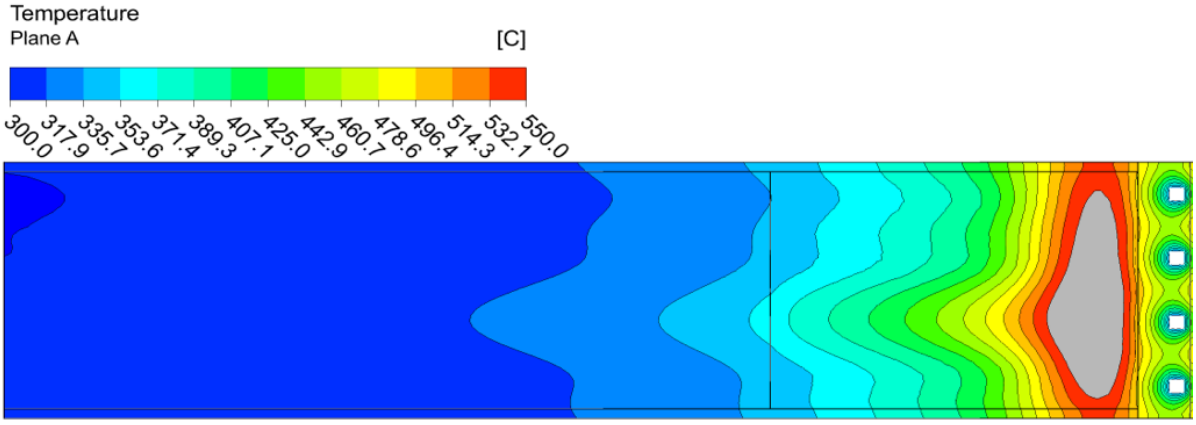

b) t = 25 s

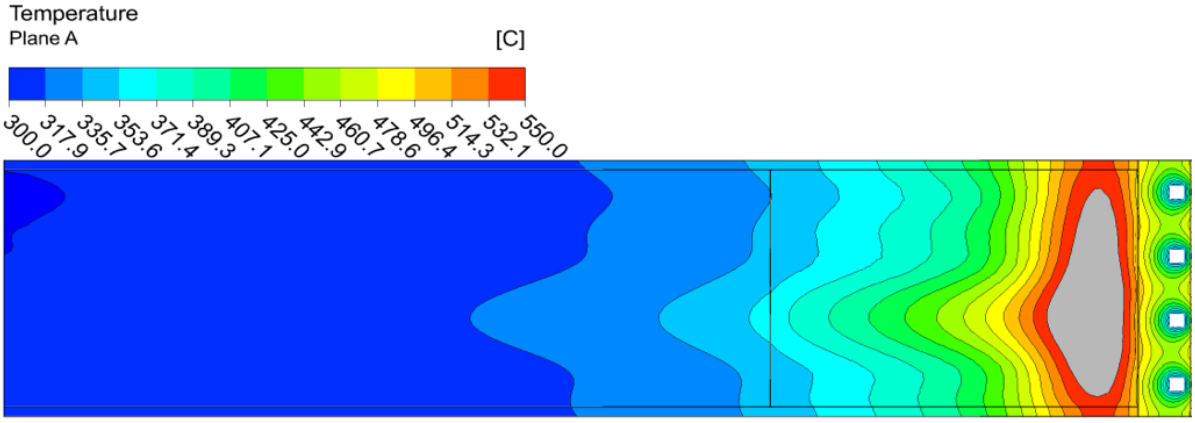

c) t = 55 s

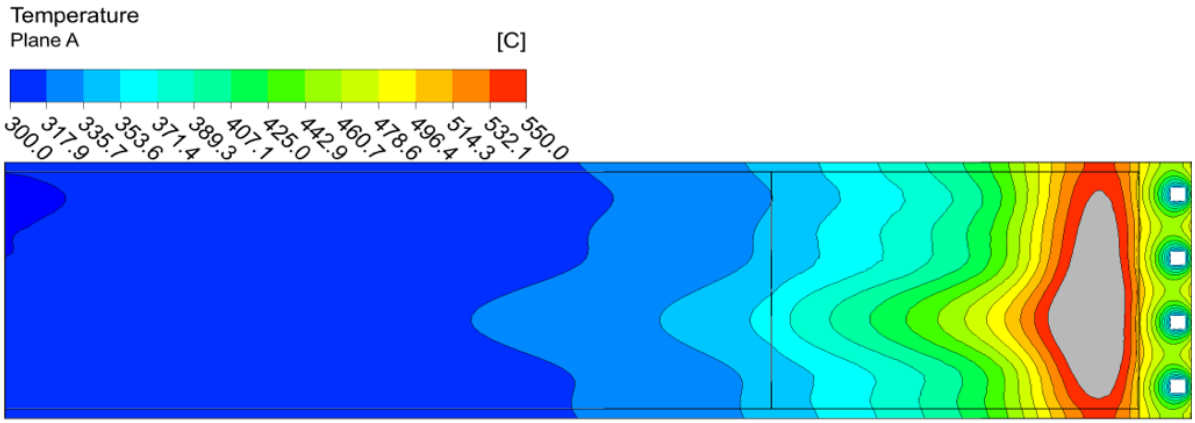

d) t = 85 s

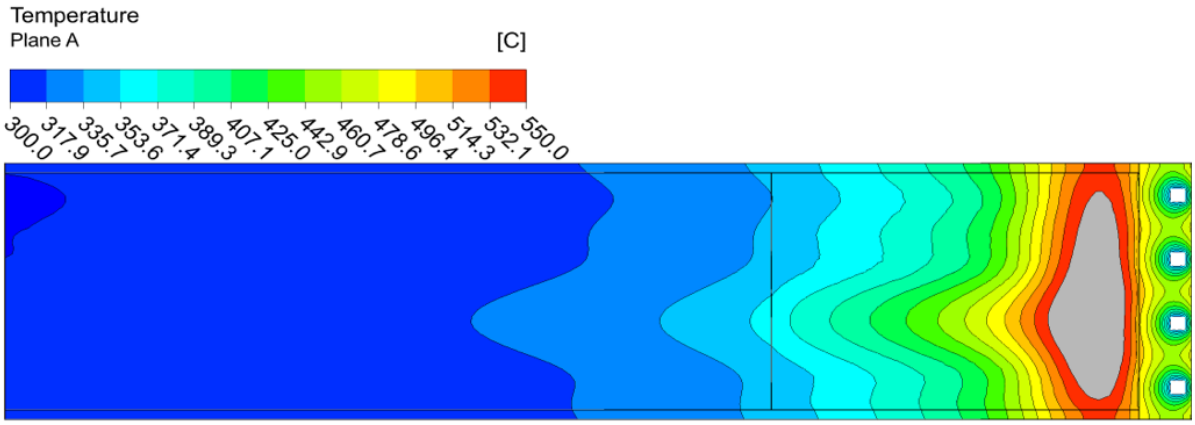

e) t = 125 s

Fig. 5.36 – WCLL V0.6_B low fluctuations Plane A at different time step

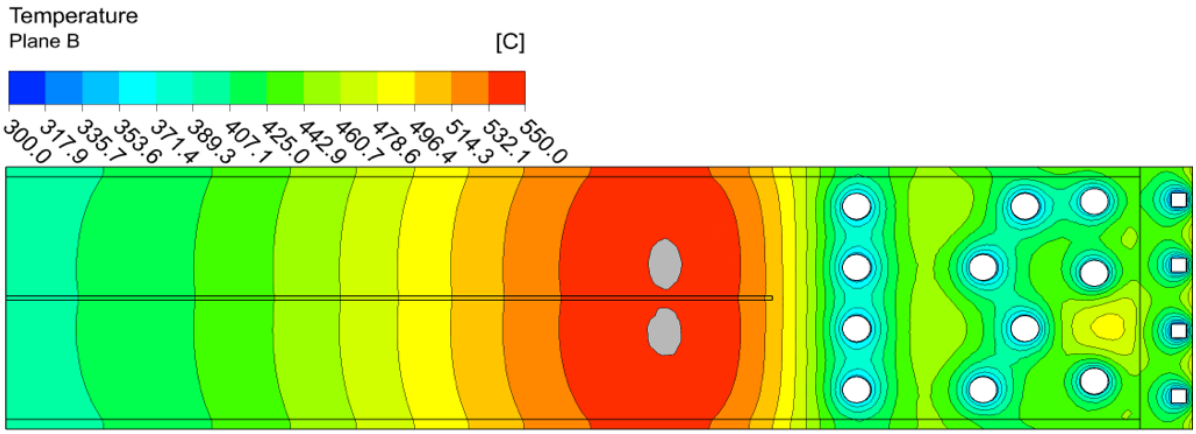

a) t = 0 s

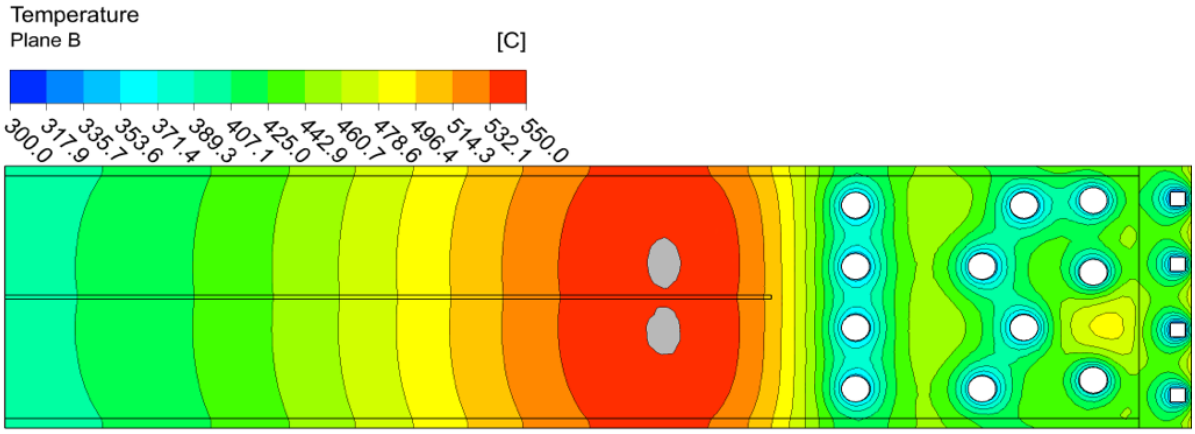

b) t = 25 s

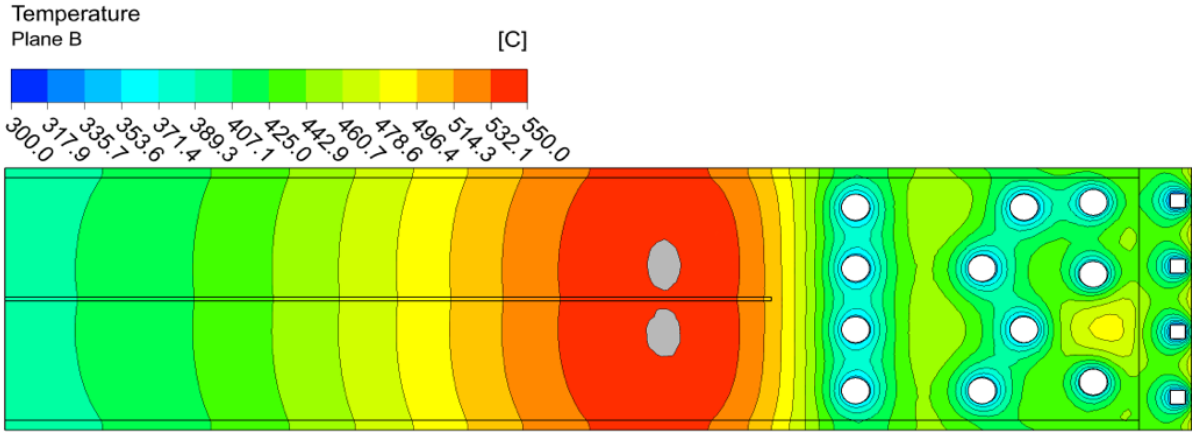

c) t = 55 s

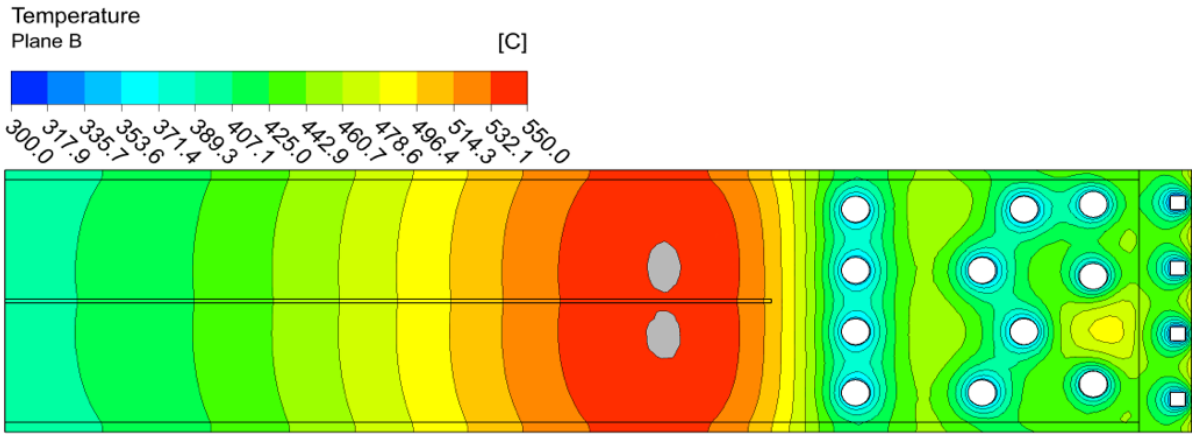

d) t = 85 s

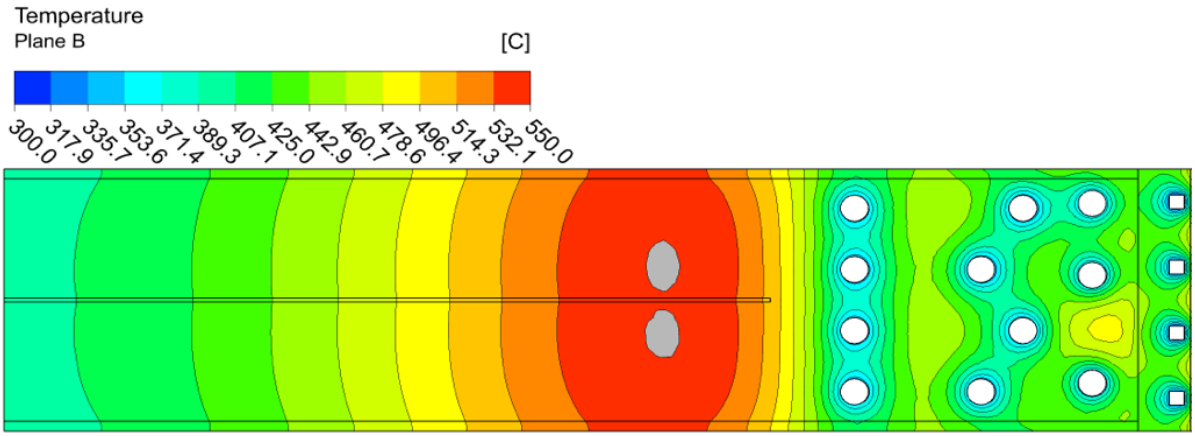

e) t = 125 s

Fig. 5.37 – WCLL V0.6_B low fluctuations Plane B at different time step

5.5.2.4. High fluctuations

The transient analysis, that recreates the high power fluctuations during the pulsed phase, starts from the steady-state condition of full power (pulse). The analysis has been performed to evaluate the Eurofer thermal field, and the water outlet conditions of the BZ and FW cooling systems, during this transient phase. The high fluctuations transient temperatures at initial and final timestep are shown in Table 5.11.

Parameters	**Value**		**Unit**
	$t_{initial}$	t_{final}	
Tungsten T_{max}	488.2	489.3	°C
FW T_{max}	507.7	510.0	°C
Upper Plate T_{max}	540.4	541.6	°C
Lower Plate T_{max}	540.6	542.7	°C
Baffle T_{max}	549.5	549.6	°C
PbLi T_{max}	586.1	589.5	°C
FW Water $T_{ave\ out}$	328.2	328.4	°C
BZ Water $T_{ave\ out}$	327.8	328.0	°C

Table 5.11 – WCLL V0.6_B high fluctuations transient initial and final temperatures

The transient has a total time of 125 s, to guarantee adequate steady state conditions at the end of it, trying to obtain the pulsed phase parameters of the full power steady-state analysis. In Fig. 5.38 the maximum BZ Eurofer temperature trend during the whole transient is reported; it can be stated that no Eurofer structures exceed the imposed limit. The plates show a temperature variation caused by the peaks, where, in their correspondence, the temperature reaches its maximum or minimum. Moreover, a plateau of around 20 s is reported, this is caused by the large thermal inertia of the PbLi. At the end of the transient, both plates have comparable temperature with the steady state conditions, even if a slight build-up occurs. As in the previous analyses, the baffle temperature doesn't have a significant variation, and its final temperature is slightly below the limit of 550°C. This temperature value, which however remains comparable with the more accurate steady state results, is due to the large thermal inertia of the PbLi that cuts fluctuations. In addition, all the Eurofer structures return the maximum temperatures of around 2 degrees less than in the steady-state analysis; this is attributable to the coarser mesh, which slightly affects the numerical prediction.

The PbLi maximum temperature shows a very similar trend with the previously discussed upper and lower plate temperature, presenting a plateau after the peaks with an extension of around 15 s. The maximum reached temperature is around 3.5 degrees over the steady condition. The temperature ramp delay has been evaluated of 5 s, and it is located where the first plateau begins. Regarding the negative fluctuation, the temperature starts to decrease 5 seconds after the fluctuation starts and reaches the plateau after a total time of 60 s, 5 seconds after the peak and stays in the plateau for more than 15 s. The last positive fluctuation increases the maximum temperature again up to 589.5°C stabilizing until the end of the transient. This turns out to be 3.5 degrees higher than the steady state condition, due to the large PbLi thermal inertia. In Fig. 5.39, the PbLi maximum temperature trend is shown.

The Tungsten and FW domains temperature trends, as shown in Fig. 5.40, clearly return the fluctuation trend in the Tungsten domain, and in the FW domain a similar trend of the above discussed domain of Eurofer and PbLi. The Tungsten shows three different peaks with maximum, minimum and maximum, recreating almost the Gaussian trend; peaks reached with a delay of around 2 seconds. Regarding the FW domain, it does not represent the trend as shown in the Tungsten layer, this because the FW system is affected by the continuous heat exchange with the PbLi domain, and since the latter has a large thermal inertia, the FW does not show the Gaussian trend seen in the Tungsten layer. In addition, at the end of the transient, both domains show a slight build-up, reaching temperature few degrees over the initial conditions, but still comparable with the steady state results of the nominal full power condition.

Regarding both cooling systems, the average water outlet temperature trends during the transient are reported in Fig. 5.41. As shown, the FW water has a trend comparable with the Tungsten layer, where three different peaks are reproduced, this phenomenon is caused by the geometric proximity with the Tungsten that affects the FW water temperature field. As obtained for the Tungsten the temperature, peaks are reached with around 2 seconds of delay respect to the power peaks. Concerning the BZ water, it shows an average outlet temperature trend comparable with that in the Pbli and Eurofer structures, because the DWTs are deeply affected by the PbLi thermal field. As reported in Fig. 5.41, the BZ average outlet temperature shows the characteristic plateau seen in the previously analyzed domains, and with it also the characteristic 5 seconds of temperature delay compared with the power fluctuations peak. Both systems present an average outlet temperature build-up of 0.2 degrees. The maximum water temperatures shown in Fig. 5.42, in both systems, have been evaluated above the saturation

temperature (344.8°C at 15.5 MPa), and as reported in the steady-state analysis, since there is no variation in the imposed mass flow rate and inlet temperature, the CHF, of the BZ first tubes array and FW water channels is the same of the steady state analysis, 2.76 and 3.42 MW/m^2 respectively. What varies, however, is the wall heat flux, that increasing and decreasing the power, directly affect its trend during the transient. Since the overpower is the 10% of the nominal power, both resulting maximum heat fluxes, to which the FW channel and the BZ 1st tube array are subjected respectively, have no substantial variations and no thermal crisis occur, also thanks to the large margins previously evaluated around 3 times from the CHF for both system.

To have an idea of the temperature variations, according with Fig. 4.43, two radial-poloidal planes have been set to show the temperature field at different time. The characteristic times are five: the initial condition (t=0 s), 1st peak positive fluctuation (t=25 s), 2nd peak negative fluctuation (t=55 s), 3rd peak positive fluctuation (t=85 s), and the end of the transient (t=125 s). Analyzing Fig. 5.43 and Fig. 5.44, where the two planes are reported and divided by time-step, is it clear that the fluctuations do not provide substantial changes in the temperature field of Eurofer structures and PbLi. The large thermal inertia of the PbLi almost completely absorb and pass over the power variation, causing only a slight temperature variation of the order of few degrees in the hot spot zones.

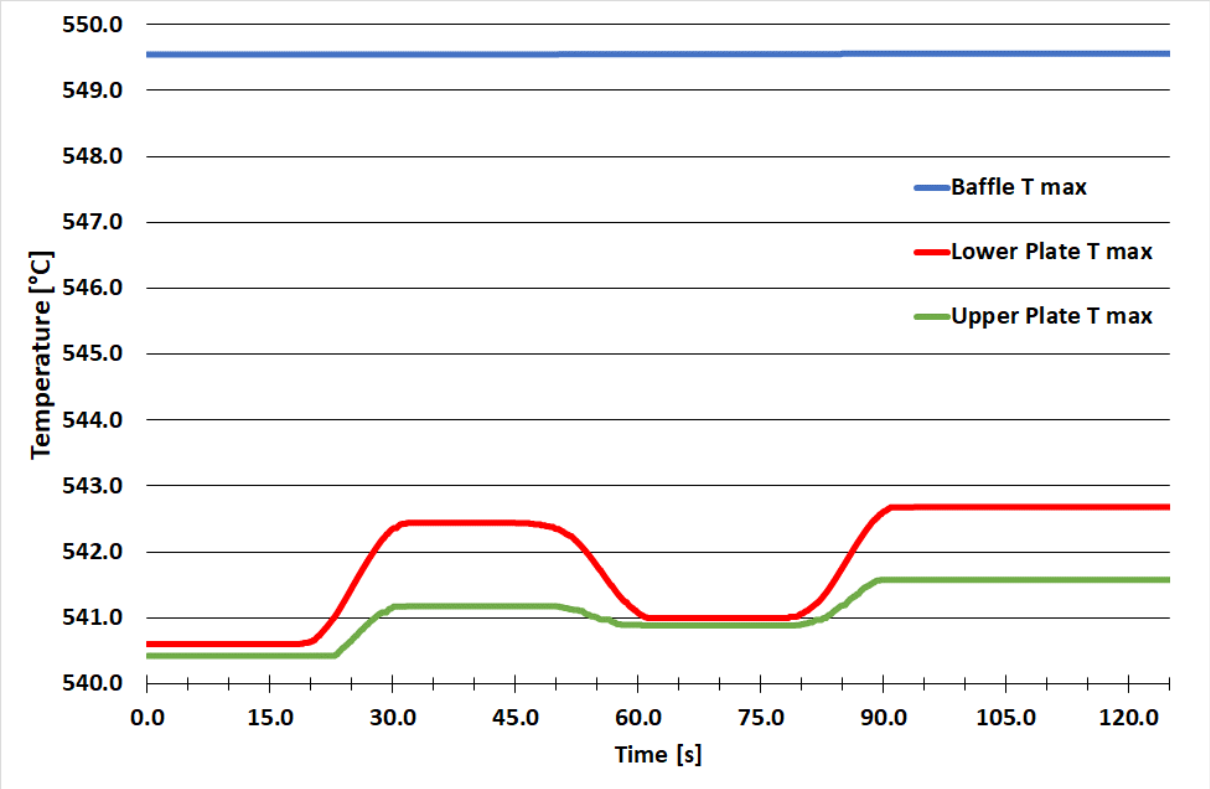

Fig. 5.38 – WCLL V0.6_B high fluctuations transient maximum BZ Eurofer temperatures trend

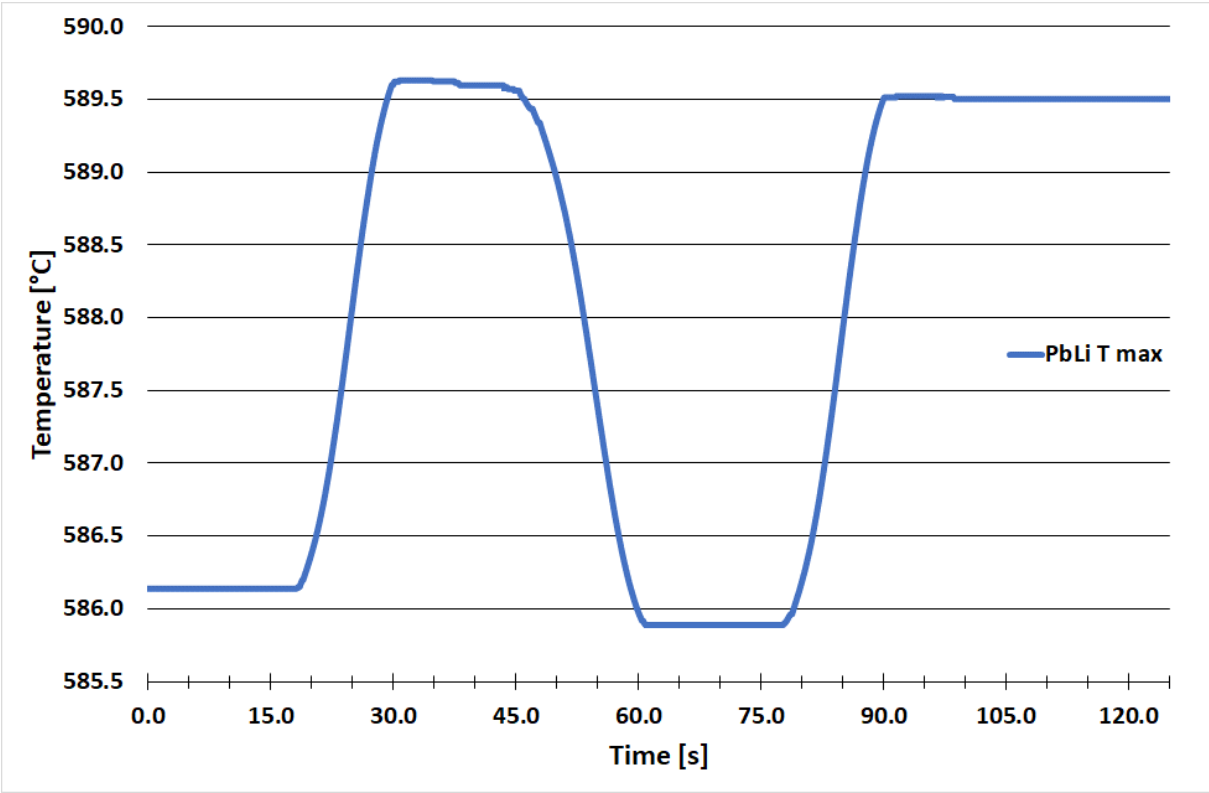

Fig. 5.39 – WCLL V0.6_B high fluctuations transient PbLi maximum temperature trend

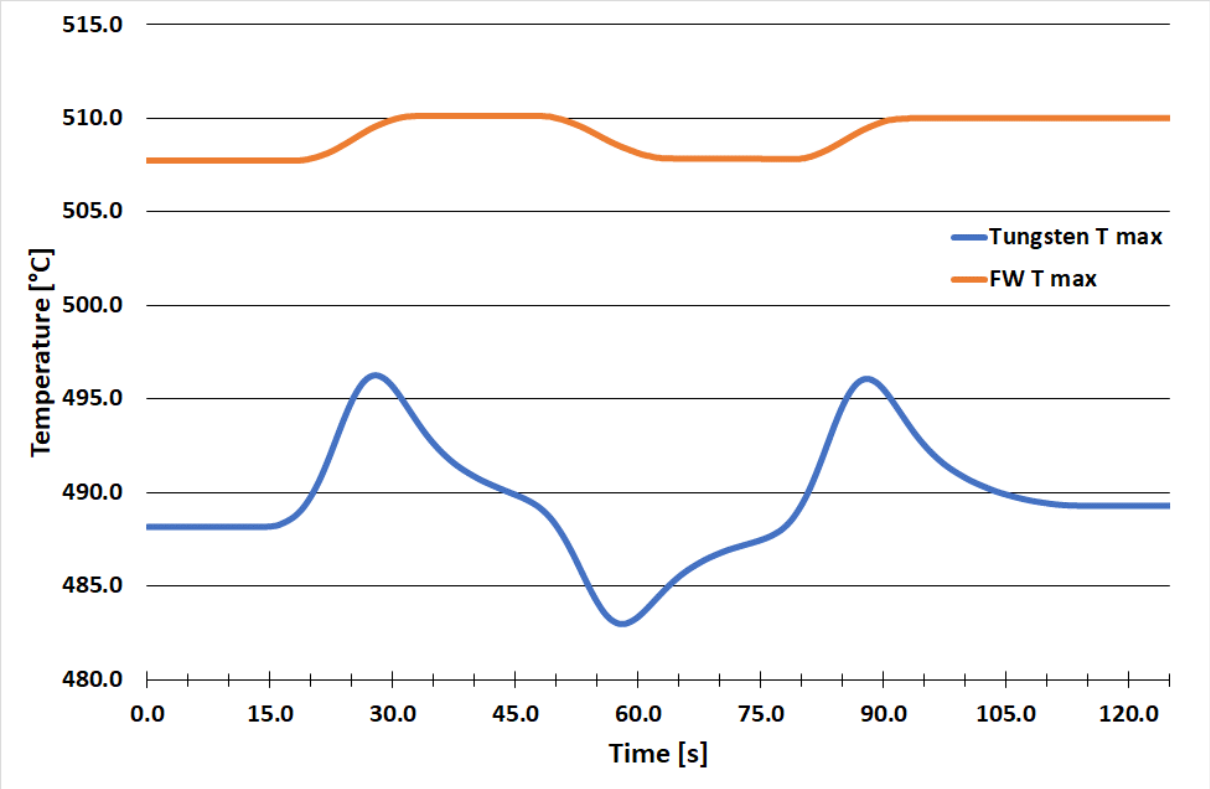

Fig. 5.40 – WCLL V0.6_B high fluctuations transient Tungsten and FW maximum temperatures trend

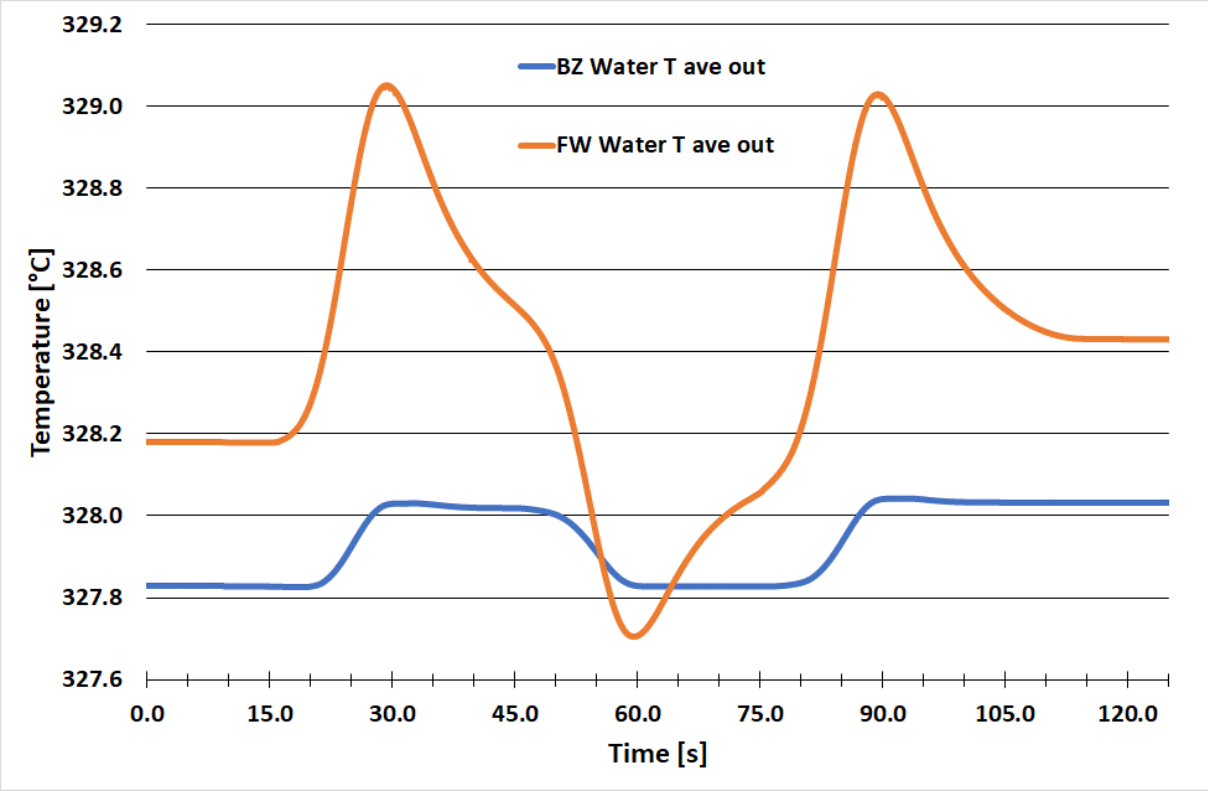

Fig. 5.41 – WCLL V0.6_B high fluctuations transient water average outlet temperatures trend

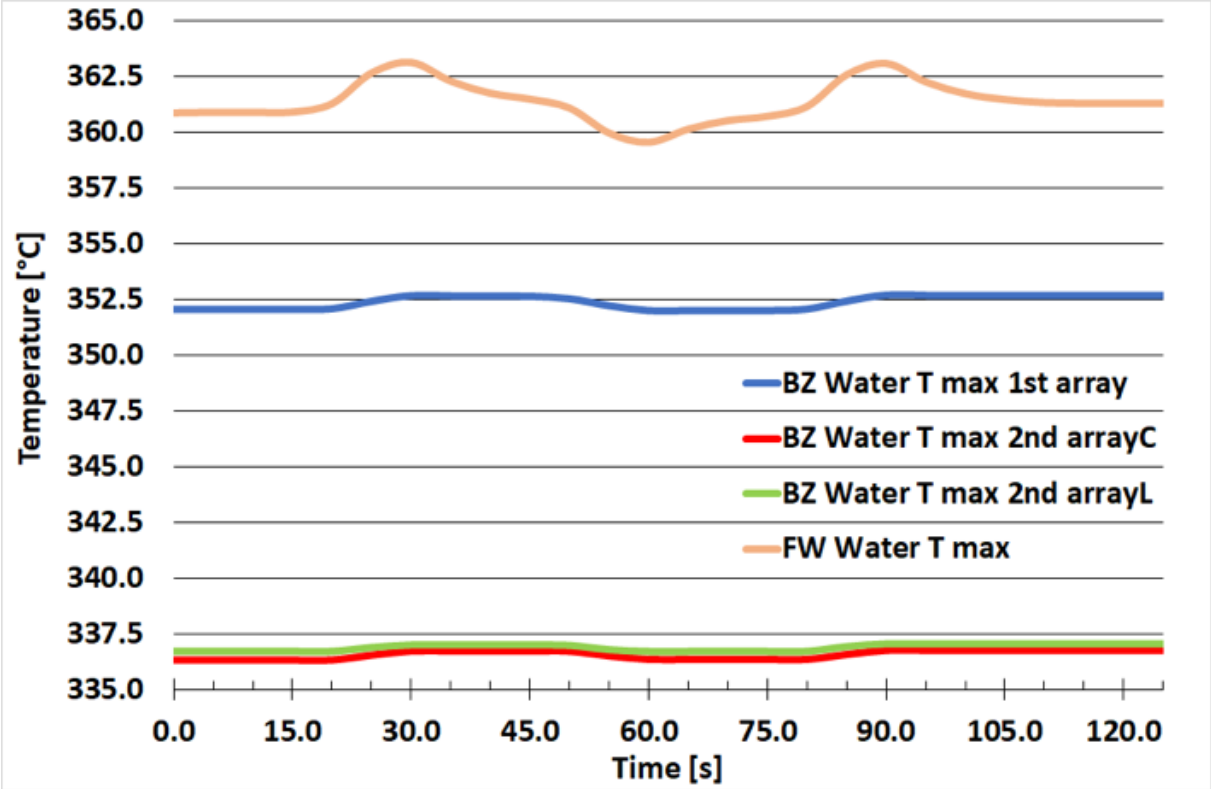

Fig. 5.42 – WCLL V0.6_B high fluctuations transient water maximum temperatures trend

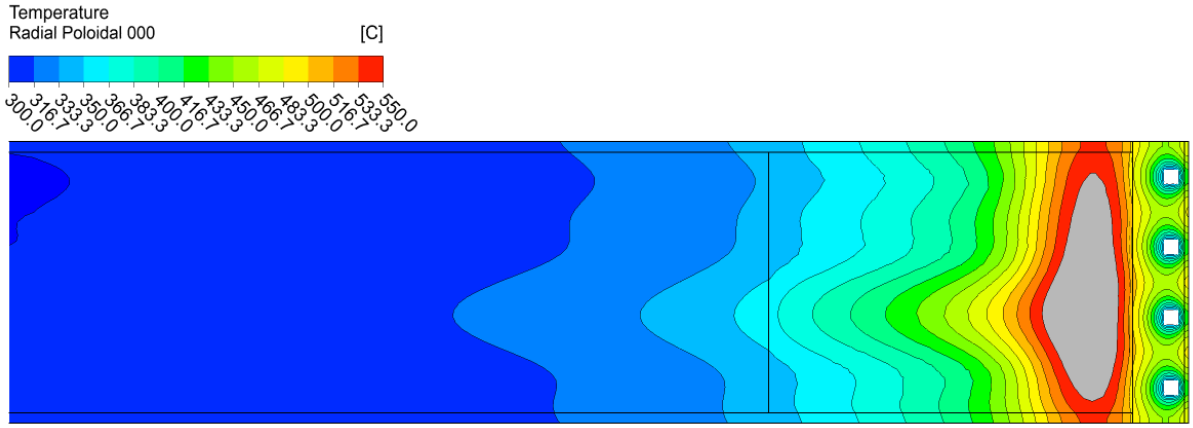

a) t = 0 s

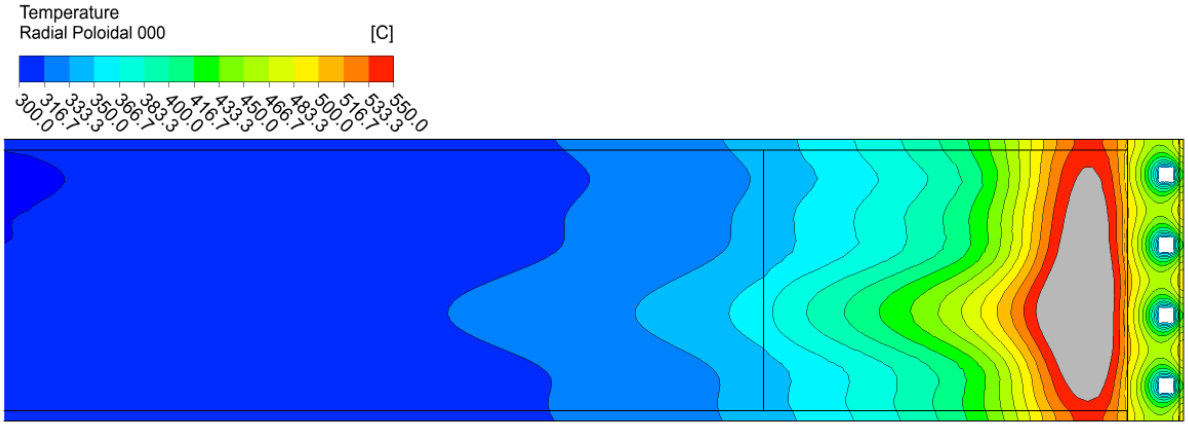

b) t = 25 s

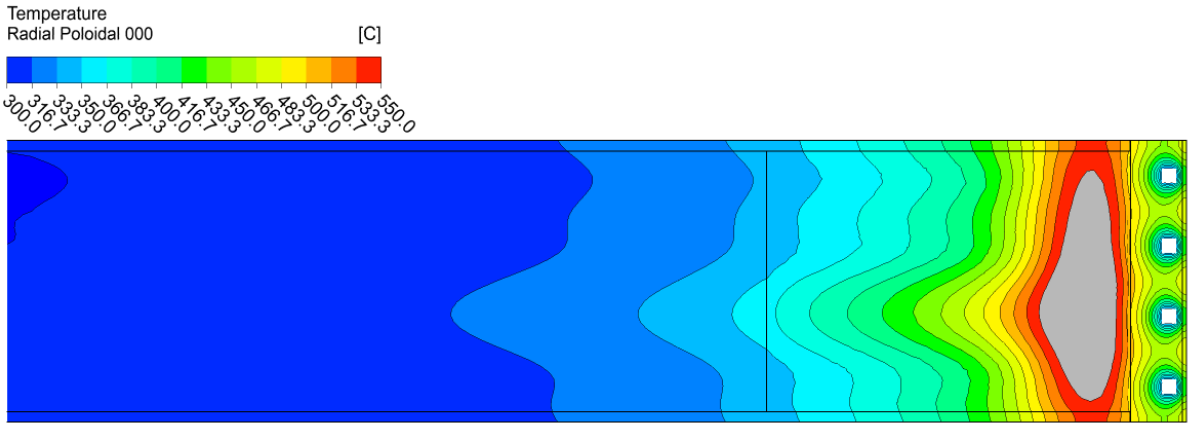

c) t = 55 s

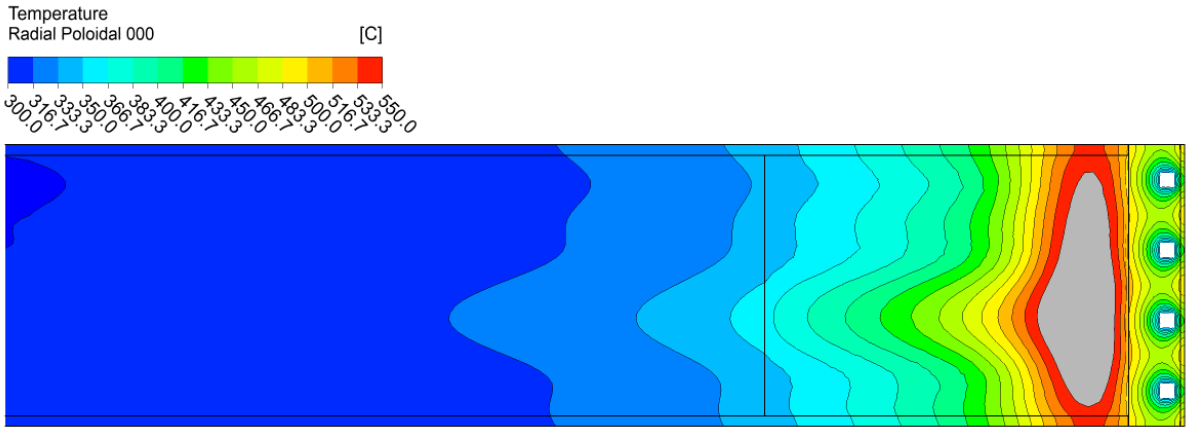

d) t = 85 s

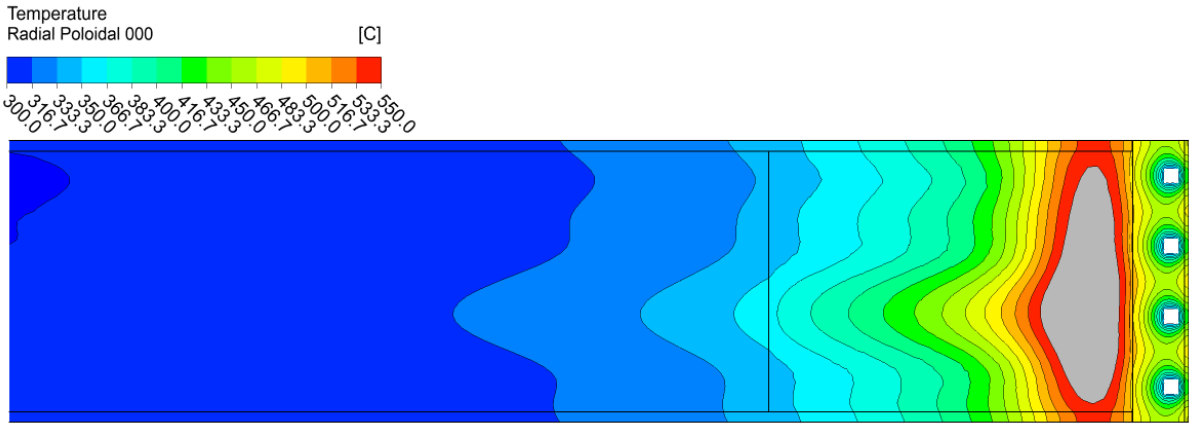

e) t = 125 s

Fig. 5.43 – WCLL V0.6_B high fluctuations Plane A at different time step

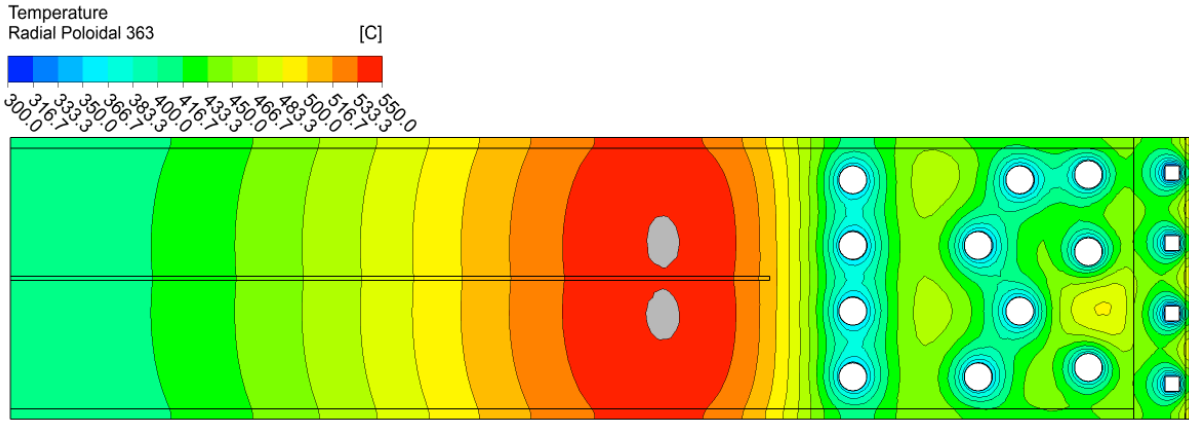

a) t = 0 s

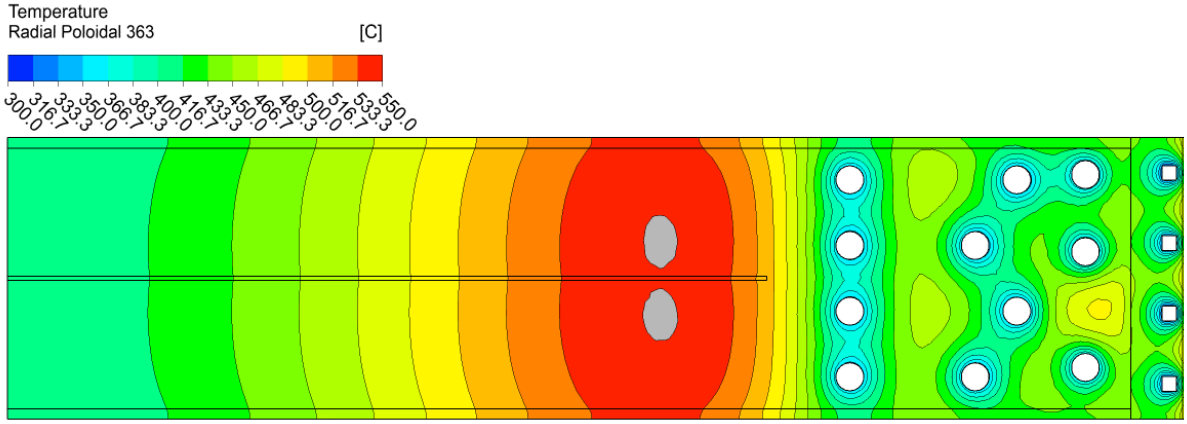

b) t = 25 s

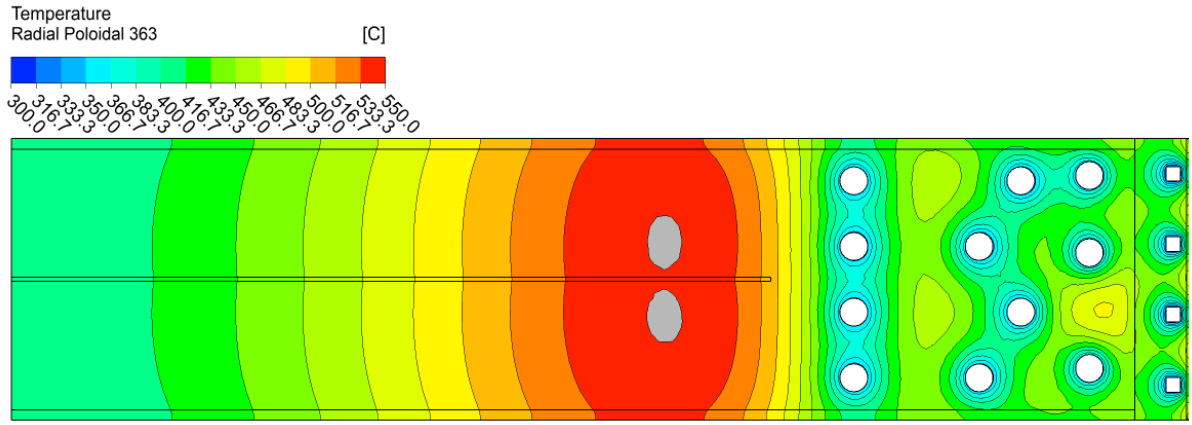

c) t = 55 s

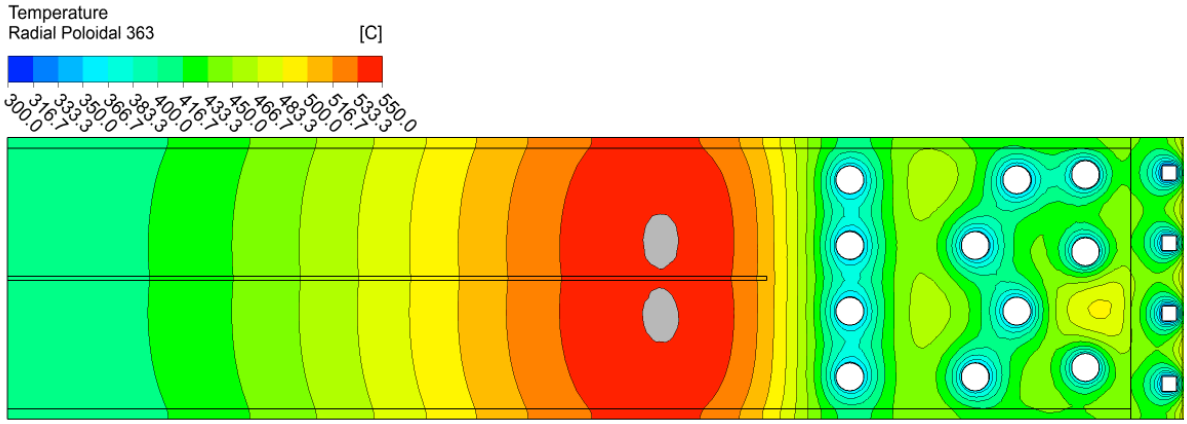

d) t = 85 s

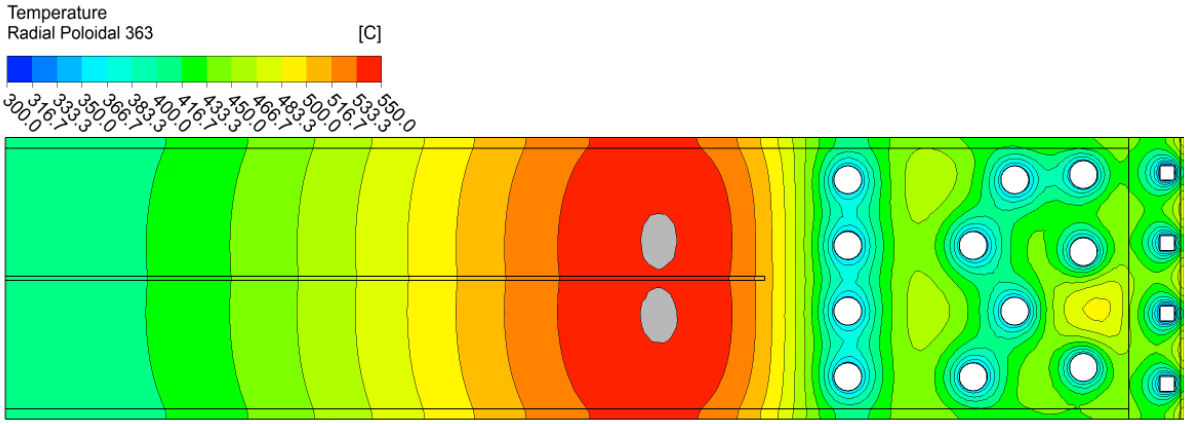

e) t = 125 s

Fig. 5.44 – WCLL V0.6_B high fluctuations Plane B at different time step

5.5.2.5. Thermal inertia

The last transient analysis has been performed to evaluate the thermal inertia of the elementary cell. This has been pursued through a step-down ramp analysis, simulating an instant power cut-off, reaching the zero-power condition in just one second. The asymptotic condition to which the model should converge is provided by both cooling systems, BZ and FW, since the water inlet temperature is maintained at 295°C for the whole transient duration. The analysis of the results shows that the whole system tends to the isothermal condition of 295°C, according to the Newton's law of cooling [96]. A complete list of the initial and final temperature divided by domain is shown in Table 5.12, while the obtained results are hereafter discussed.

Parameters	**Value**		**Unit**
	$t_{initial}$	t_{final}	
Tungsten T_{max}	437.7	295.8	°C
FW T_{max}	506.7	296.0	°C
Upper Plate T_{max}	540.3	312.9	°C
Lower Plate T_{max}	540.3	312.9	°C
Baffle T_{max}	548.2	312.5	°C
PbLi T_{max}	575.3	312.9	°C

Table 5.12 – WCLL V0.6_B thermal inertia transient initial and final temperatures

The total transient time has been imposed at 1011 seconds in order to fully evaluate 1000 seconds of natural cooling, since the zero-power condition begins at 11 seconds.

In Fig. 5.45, the BZ Eurofer structures are shown, the maximum baffle and plates temperatures trends have been reported, in addition, the Eurofer temperature averaged on the volumes of the structures is shown. All the three domains return an identical maximum temperature trend, settling just below 320°C at the end of the transient. The average BZ Eurofer temperature returns a trend that at first is well below the maximum temperatures (around 404.8°C), but, as the system cools down with increasing simulation time, the difference becomes smaller, passing from an initial value of 144.5, 136.9 and 136.1 to 13.4, 13.8 and 13.8, for baffle, lower plate and upper plate respectively. As regards the PbLi domain, the Fig. 5.46 shows a comparable trend with the Eurofer structures. As well as the maximum and average temperatures approach with increasing time with a similar Eurofer trend, the gap is also similar, obtaining 174.1

degrees at the initial time and 14.5 at the end of the transient. From these values it can be seen that the PbLi, although it has a greater gap between the average temperature and the maximum temperature, closes the gap faster than the Eurofer. This is because the BZ tubes are immersed in it, contributing to its faster cooling.

A completely different timing-trend occurs in the FW system. As shown in Fig. 5.47, the two domains trend of both maximum and average temperatures is steeper compared with the BZ system. The average Tungsten and FW temperatures very quickly reach 300°C in about 135 and 165 seconds respectively. The BZ, on the other hand, takes about 940 and 880 seconds for Eurofer and PbLi respectively, to reach the average temperature of 300°C. The FW maximum temperature has a slightly different trend since the FW hottest region is located in the inner part of the system at the interface with PbLi. This causes a difference of about 150 seconds between Tungsten and FW in reaching a similar temperature for both models and both temperatures, maximum and average. After 300 seconds, four curves are obtained with a trend tending to the asymptotic value of 295°C.

Based on these results, a preliminary evaluation on the time coefficient affecting the cooling trend has been performed. This coefficient has been evaluated through the Newton's cooling law, according to Ref. [96]. The Newton's cooling law provides the temporal trend of a body temperature in contact with a colder body, the equation is: $T(t) = T(t_\infty) + \big(T(t_0) - T(t_\infty)\big) \cdot e^{-k \cdot t}$, where the coefficient "*k*" determines the trend of the cooling curve, where, higher *k* will tend the curve towards the asymptotic value earlier than a lower *k*. The term $T(t_\infty)$ represents the temperature that would be obtained in the system for an infinite time, that in this case is 295°C. To obtain k, a system of equations is set-up imposing $T(t_0) = T_0$ and $T(t_1) = T_1$, where T_0 and T_1 are the initial and final obtained average temperatures of each domain. Solving the equation system with the obtained data, it returns $k = (-1/t_1) \cdot \ln(T_1 - T_\infty / T_0 - T_\infty)$. The Eurofer and PbLi domains have k=0.0033 and k=0.0035 s^{-1}, confirming the fact that PbLi decreases slightly faster than Eurofer. While, for FW and Tungsten the obtained k values are 0.0057 and 0.0051 s^{-1} respectively, obtaining a cooling rate of the FW which is almost double that of the BZ Eurofer structures. Finally, the marked (0.002) difference confirms a fast pace curves in the FW system than in the BZ.

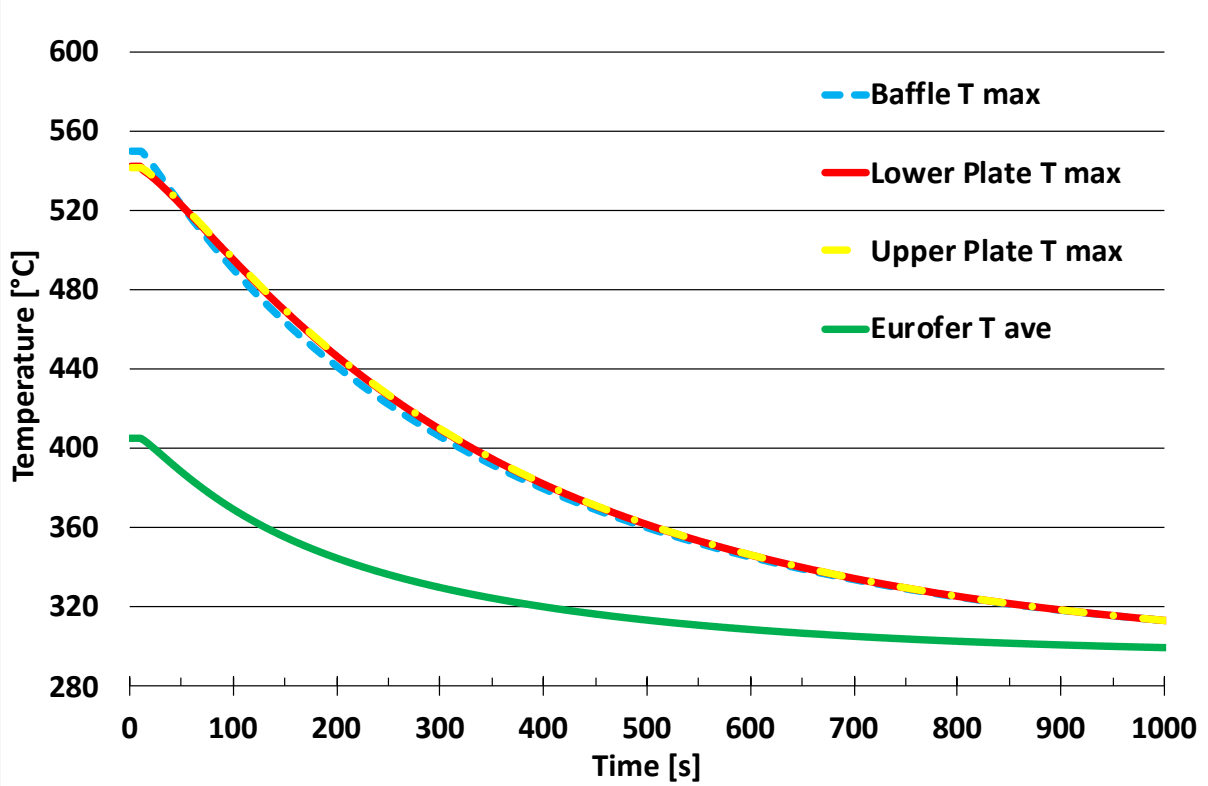

Fig. 5.45 – WCLL V0.6_B thermal inertia transient BZ Eurofer temperatures trend

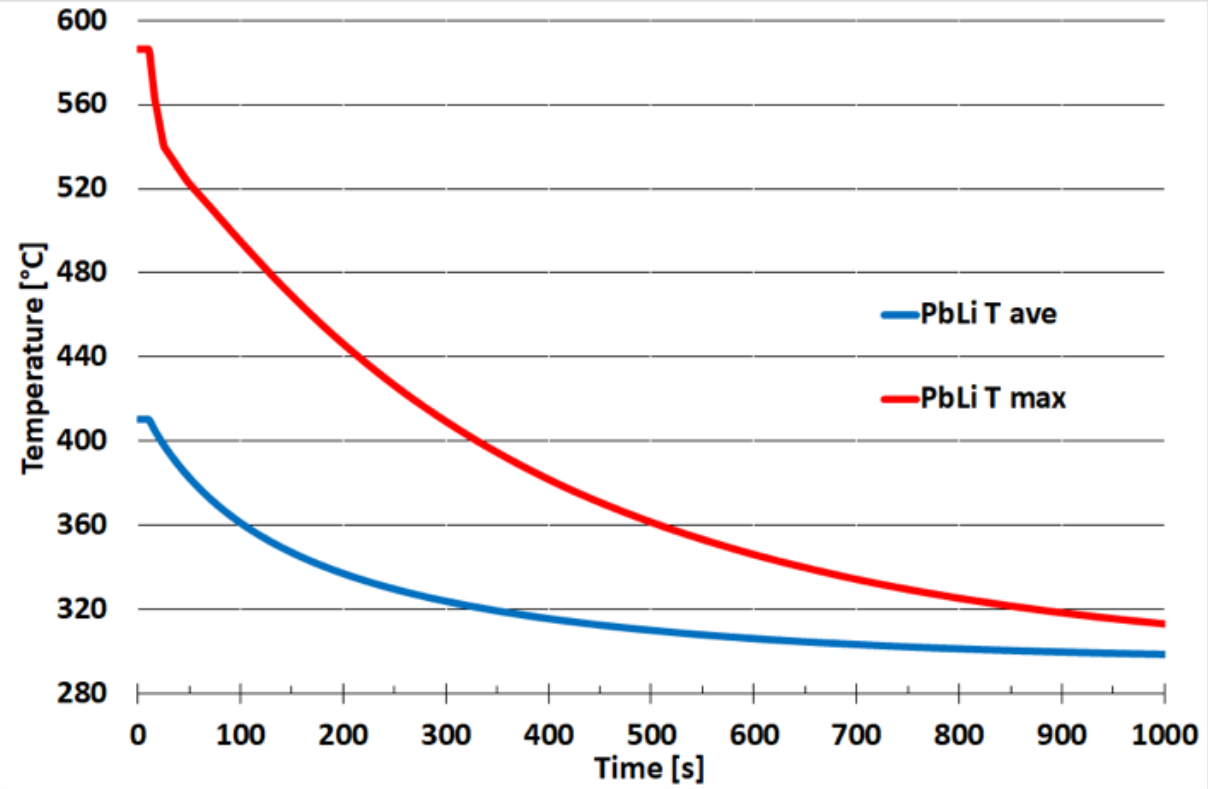

Fig. 5.46 – WCLL V0.6_B thermal inertia transient PbLi maximum temperature trend

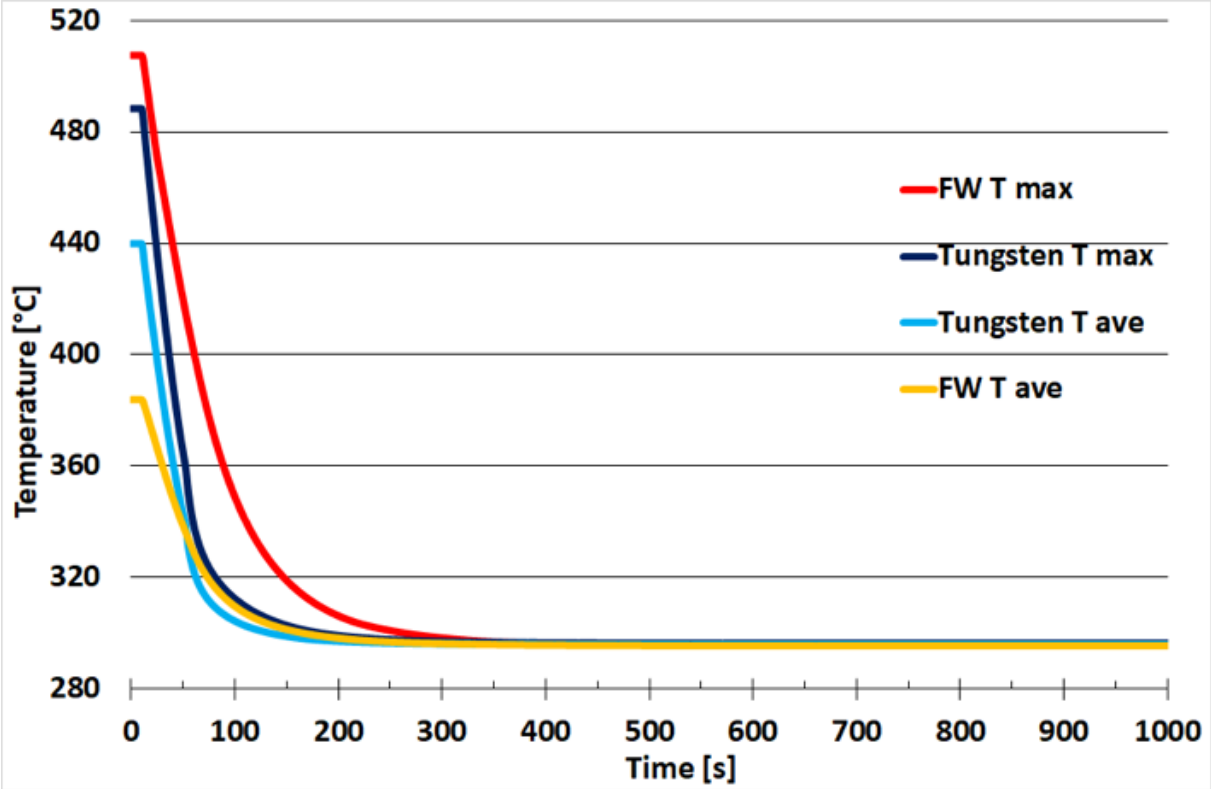

Fig. 5.47 – WCLL V0.6_B thermal inertia transient maximum Tungsten and FW temperatures trend

5.6. Summary and main achievements

Several thermal-hydraulics transient analyses have been performed on the central outboard segment equatorial elementary cell using a CFD code ANSYS CFX v18.2, aimed to investigate the operational thermal-hydraulics behavior of the elementary cell during the operating phases of pulse and dwell of the DEMO reactor. The analyses have been conducted to evaluate the response of the thermal system during the transient operations, evaluating the possibility of an issue; and to consider the adopted geometry as able to face the transient conditions of the DEMO reactor. Different operational scenarios have been analyzed, verifying if the V0.6_B elementary cell model is able to withstand and faces the transient thermal loads in each transient case. Moreover, the analyses are aimed to investigate the cooling water outlet conditions verifying if both cooling systems, FW and BZ, are able to provide adequate and suitable water to the PHTS, since the DEMO reactor has the main task to demonstrate the feasibility of the electricity production.

The transient heat loads adopted for the analyses are based on the most updated data, to properly recreate the power trends of the operational phases and to return the thermal field trend for the most recent design.

Four different analyses have been performed to widely covers the operating scenarios of the DEMO reactor: fast ramp-up, ramp-down, low fluctuations and high fluctuations. In each analysed case, the intent is to obtain stationary conditions at the transitory end. The obtained results from the transient analyses are compared with the steady-state outputs, of dwell or pulse phase, verifying if the model has returned to a comparable condition of the steady-state analysis of the related state. Moreover, a water outlet comparison with the RELAP5/Mod3.3 system code has been carried out regarding the fast ramp-up and the ramp-down analysis. In addition, a fifth analysis has been conducted to evaluate the thermal inertia of the system through a step-down ramp. This latter analysis provides the cooling characteristics trend of the two independent systems, FW and BZ.

The V0.6_B layout, has returned optimal transient results, no Eurofer structures exceed the allowable temperature during the fast ramp-up. Furthermore, all the obtained data at the end of the transient are comparable with the pulsed steady-state analysis performed with the V0.6_B

model. The only one parameter that arouses a bit suspicious is the maximum baffle temperature, which in the present transient analysis, result below the imposed temperature limit, while in the steady-state is beyond the limit for 2.5 degrees. This difference is however negligible, given the only 3 degrees from the steady-state run. In addition, this gap is attributable to the coarser mesh adopted into the model, which affects the numerical predictions. From the ramp-up analysis, it should be noted that the model slowly reaches the steady condition of full power. In particular, splitting the model in two independent systems, FW and BZ, it is clear that the FW system promptly react to the power variation of the fast ramp-up tending to the steady operative conditions in a faster way (500 s) compared with the BZ. This latter instead, takes around 800 seconds to provides almost steady output values, despite the baffle needs more than 900 seconds to reaches stationary values. The PbLi undoubtedly characterizes the timing of the model, where, in the BZ significantly slows down the growth of temperatures. The FW, even if has continuous heat exchange with this latter system, also slows down the ramp, but still manages to return in a shorter time to the nominal full power values. Even the trends of the water outlet temperatures are different for both systems, the FW is able to provide an adequate temperature even before the inlet temperature stabilizes. On the contrary, the BZ has a very long ramp, taking almost all the time of the transient (900 s) to reaches around 328°C. This means that almost the 15% of the pulsed time is employed to return to the full power conditions. This data is strongly dependent on the high thermal inertia of PbLi.

As regards the ramp-down transient analysis, the model has partly demonstrated the achievement of the dwell condition in the defined time. The FW system reaches a steady condition before the end of the transient in all its domain, in addition, it provides water with adequate thermal-hydraulic characteristics in 300 seconds. The BZ system instead, does not reach an equilibrium state. The slow drop in temperature of the PbLi causes a big delay in all systems closely connected to it. Although the final temperatures are comparable with the data obtained from the dwell steady-state analysis, the BZ system still shows curves with a considerable slope. This could actually generate two aspects, with the start of a new cycle the model should be more “reactive” to increase its temperature, given its higher average temperature and the water inlet temperature set by the PHTS and with a significant delay compared with the power ramp-up, may causes a temperature build-up as effect of the huge PbLi thermal inertia. This effect, if repeated cycle after cycle, will tend to reach higher and higher temperatures with a divergent trend. Meanwhile, hot spots could arise into the structures

exceeding the Eurofer limit compromising the Eurofer thermo-mechanical characteristics property, thus, the structural integrity of the blanket.

Comparing the two models, CFD and RELAP5 system code, it can be stated that the CFD temperature ramps in both cooling systems are much longer in time. In fact, the system code, not taking into account the local effects into the model and overestimating the heat exchange surfaces, shows steeper ramps reducing the required times to obtain nominal values. In fact, this comparison has highlighted that the system code roughly models the PbLi thermal effect on the elementary cell compared with the CFD simulation. In addition, the rapid reaction of the system, could be a source of error for the CFD water inlet temperature boundary conditions, modifying the proper structures temperature trend inside the cell. Nevertheless, the BZ system shows very different temperature trend, regardless of the considered ramp but with a final temperature comparable with the steady-state analyses. On the other hand, the FW water is able to provide temperatures trends almost similar, in both ramps, to that of the system code. Despite the influence of the PbLi on it, it still manages to give a response in slightly longer times than the system code, but much shorter than the BZ.

It can be stated that, from the two transient analyses of fast ramp-up and ramp-down, the V0.6_B model fully withstands the transient thermal loads and is able to provide adequate water conditions to the PHTS for both systems, as required from BoP. Furthermore, a CFD with a full ramp-down-ramp-up transient analysis should be performed to evaluate the possibility of temperature build-up during this phase.

The power fluctuations analyses, low and high, have demonstrated that the V0.6_B model fully withstands these transient thermal loads, ensuring excellent performances. It can be assumed that these oscillations, positive in row and/or positive-negative-positive in row, have almost no effect on the cell, since the PbLi completely absorbs these fluctuations avoiding that the temperature of the system widely increases. Moreover, it can be stated that the response of the system is directly proportional to the radial distance, thus, the Tungsten is the structure that best reproduces the trend of the power peaks in both analyses; on the contrary, the PbLi does not show any trend attributable to the peaks, returning a temperature plateau where it remains for almost the entire duration of the pulse power. In particular, regarding the low fluctuations, only the FW system shows a slight increase in temperature in Tungsten and water domains, however negligible since are less than 1 degree. Concerning the high fluctuations, in all domains, the

temperatures slightly vary between the initial and the final condition. The variations are however to be considered negligible since the maximum gap has been evaluated 3.5 degrees in the PbLi. Given the BoP requirements, the response of both water systems, during the power variations, is considered optimal, since the water temperatures do not undergo significant changes that may affect the PHTS conditions. Finally, it can be affirmed that, once the full power steady-state conditions of the system are reached, it will remain in an almost undisturbed state, unless very high-power fluctuations or variations occur.

In the last transient analysis, the V0.6_B model thermal inertia has been evaluated. From the results it stands out that the two cooling systems tend to cool down, with different timing. The numerical analysis has confirmed the assumptions made in the previous calculations of fast ramp-up and ramp-down. Indeed, the resolution of the Newton's cooling law equation has carried out two different time-coefficient, where, the BZ requires about twice as long as the FW to reach an isothermal equilibrium condition. As regards the resolution of the Newton's cooling law, it has returned for Eurofer and PbLi domains respectively, k=0.0033 and k=0.0035 s^{-1}, while for FW and Tungsten, k=0.0057 and k=0.0051 s^{-1} respectively. In addition, the FW could be even faster if it were really an independent adiabatic system. Thus, it can be affirmed that the PbLi thermal inertia deeply affect the temperatures trends of the entire model.

To evaluate the reliability of the elementary cell under all the operating conditions of DEMO, normal and off-normal, further transitory analyses should be performed. Since the cell has demonstrated its capability to withstand the normal operations thermal loads, the analyses should be performed to evaluate the off-normal scenarios. It will allow to verify if the model is also able to withstand such high thermal loads (i.e. plasma disruption) or high stress conditions (i.e. LOFA, in-box LOCA). In addition, modelling the eventual phase change, in order to evaluate the perturbation in the system due to possible subcooled boiling and the use of different turbulence models, would be a remarkable improvement.

6. CONCLUSIONS AND PERSPECTIVES

The Ph.D. work, conducted in collaboration with ENEA Brasimone Research Center, was carried out in the framework of the European Power Plant and Physics Technological Programme, under the coordination of the EUROfusion Consortium in the task of the Work Package Breeding Blanket.

This Ph.D. thesis work aimed to contribute to the development of the conceptual design of the DEMO Water Cooled Lithium Lead breeding blanket, in order to design an efficient and reliable system, demonstrating its capability to fully withstands the DEMO main requirements in normal and off-normal conditions.

The activity has been focused on the thermal-hydraulic of the system; in particular, on the optimization of the elementary cell cooling systems, FW and BZ. Specifically, the analyses were performed on one single elementary cell of the central outboard segment, that compose the WCLL due to its periodicity. To perform realistic analyses, multiple factors have taken into account: engineering aspects, neutronic, thermo-mechanic and magneto-hydrodynamic. This has been pursued through the engineering approach and with the application of the numerical CFD code ANSYS CFX v18.2 to represent the behaviors of the different analyzed models.

The research activity has led to the development of a complete and optimized conceptual design of the WCLL breeding blanket elementary cell. The goal was pursued by means of thermal-hydraulic analyses aimed at optimizing the BZ and FW independent cooling systems, as well as, their mutual interaction was evaluated. Moreover, an evaluation on the impact of the heat transfer modelling approach on the numerical prediction has contributed to identify the final optimized layout. Finally, to confirm the choice made, different transient analyses have been performed verifying the reliability and performances of the optimized layout, in particular, if the selected design was able to face the operational phases of the DEMO reactor.

The main achievements of the research activities are hereafter discussed.

The first part of the activity had the task of identify an innovative WCLL breeding blanket layout evaluating the thermal and fluid dynamic behavior of the equatorial elementary cell

through numerical simulation. The process was completed by means of a succession of progressive optimizations on the layout of BZ and FW. Thus, for each analysis, a 3D finite volume model was set-up, using the CFD commercial code ANSYS CFX v18.2. The several models, which include solid and fluid domains, have been reproduced according with the most updated geometrical parameters obtained from the milestones of the previously performed analyses. Moreover, to realistically reproduce the thermo-fluid-dynamic behavior of the elementary cell thermal loads and material thermo-physical properties have been implemented in the CFX commercial code by means of a set of different equations.

The analyses aimed to investigate and optimize both systems, FW and BZ, have highlighted several advantages. The studies have led, step by step, to the finalization of the V0.6_B layout, where the main achieved key points are listed and commented below:

- Achieved temperature symmetry in the toroidal direction into the BZ system due to the arrangement of the horizontal tubes;
- Simplified BZ tubes layout, C-shaped tubes so as not to cross the stiffeners, also thanks to the radial-poloidal stiffeners arrangement, selected as reference, since the other arrangement cause high PbLi pressure drops;
- Minimum number of BZ tubes set to 22, divided in 3 arrays with different curvature radius, radial extension and toroidal dimension; this to provide the highest thermal removal into the BZ, avoiding the onset of hot-spots;
- Achieved temperature symmetry in the poloidal direction into the FW system due to a constant channels pitch and the alternate and opposite water flow;
- FW system with 4 channels is able to keep structural materials well below the temperature limit, withstanding the imposed thermal loads of heat flux and deposited power;
- Decreased volume of water in the first centimeters of the cell, which positively affect the TBR performances due to the FW channels reduction;
- Alternative BZ recirculation manifold to enhance the water thermal-hydraulic performances, which provides a water double-pass flow, reducing the maximum water temperature into all the tubes arrays;
- BZ recirculation and 4 channels FW strongly enhanced the water thermal-hydraulic performances, ensuring large and safety margins from thermal crisis; the water velocity was doubled in the BZ and more than tripled in the FW, while respecting the maximum

water velocity of 7 m/s; furthermore, a reduced passive heat removal from FW to BZ by around the 20% has been evaluated;

- Optimal BZ and FW water performances achieved, since water mass flow rate has been evaluated through the enthalpy balance in order to obtain 328°C at both cooling systems outlets, providing adequate water conditions for the PHTS.

In addition, the analysis carried out to investigate the impact of the heat transfer modelling approach on the numerical prediction has stood out these main aspects:

- The choice of the PbLi thermal conductivity deeply affects the numerical prediction regardless to the model approach FEM and/or FVM, with a variation in the obtained results of about 15% in the worst case;
- The pure diffusive method with FEM and FVM approach returns comparable output values; the main difference resides in the computational effort, since FVM requires higher computational time and costs;
- The water modelization into the numerical model, instead of an imposed heat transfer coefficient, produces significant improvement into the numerical predictions, providing more accurate data and reducing the maximum temperatures of the model;
- The PbLi modelled as solid domain, strongly reduces the FVM computational costs, and compared with the fluid PbLi model, does not provide significant improvements in the obtained results; this assumption is valid for a forced convection model.

The last part of this research activity has been focused on the feature verifications of the V0.6_B elementary cell model during the DEMO normal operations. Since DEMO is a pulsed reactor, the elementary cell is subjected to different operational behaviors. The DEMO operational phases, which affects the WCLL breeding blanket, have been investigated through CFD transient analyses, recreating the fast ramp-up, ramp-down, low fluctuations and high fluctuations, covering the most part of the normal operation phases. In addition, a numerical evaluation on the thermal inertia of the WCLL V0.6_B model has been performed through a step-down ramp, evaluating the differences of the cooling time trend between the two systems, FW and BZ.

From the transient analyses, several positive features have been demonstrated. The major ones are pointed out below:

- The V0.6_B model, in all cases, reaches outputs values comparable with the related steady-state analysis of the phenomena, regardless if dwell or pulsed phases;
- The PbLi deeply affect the temperature time trend of the BZ system, and slightly affect the FW, causing a short delay in reaching the steady-state conditions of the latter system;
- The whole system takes about 1000 s to reach steady-state conditions after ramp-up, this means that almost the 15% of its operational phase is used to reach the steady-state conditions reducing its expected operational time;
- The BZ system takes almost double time, compared to the FW, to reaches steady-state conditions, since the large thermal inertia of the PbLi strongly increase the required time to obtain constant temperature into the model;
- The system, during the pulse phase, does not undergo significant temperature variations, providing adequate thermal-hydraulic water conditions, as required by the PHTS; a fundamental parameter for the electricity production;
- The comparison between CFD ANSYS CFX v18.2 and RELAP5/Mod3.3 code has demonstrated the system code limits, providing significantly faster results in response to the variation of the imposed boundary conditions; while the CFD returns longer times in the FW system, but comparable, and far longer into the BZ;
- The evaluation of the PbLi thermal inertia has shown that the BZ system cools down with a time trend which is almost doubled compared to the FW system.

In conclusion, the future perspectives are listed, which come out from the open issues or points of uncertainty of the carried out analyses.

The research activity has conceptualized a preliminary design of WCLL BB elementary cell and has also verified its reliability and performances during the normal operation phases, confirming the results obtained in the stationary analyses. Further analyses are needed to fully evaluate all the DEMO operating scenarios, verifying the WCLL reliability also under the off-normal operations. Furthermore, in collaboration with the Work Package Balance of Plant, it will be necessary to uniquely establish the quantities of water foreseen in the WCLL, in order to perform further analyses with a water mass flow rate no longer based on the enthalpy balance but on the real characteristic of the refrigeration circuit.

A short list of future analyses can be listed below:

- CFD transient analyses of off-normal operation, verifying the accident scenarios as LOCA, LOFA or plasma disruption, these phenomena will considerably stress the blanket, from a thermal point of view;
- CFD steady-state analyses with a water mass flow rate evaluation on the BoP parameters, to realistically evaluate the water outlet temperature from BZ and FW system;
- CFD steady-state analyses on the lateral outboard segment and inboard segment to provide an adequate BZ tubes arrangement in the whole sector;
- CFD steady-state analyses on different poloidal positions to evaluate the cooling performances in different poloidal positions, since the heat loads vary among the poloidal distribution.

ANNEX A: Materials properties

Eurofer

The structural material of WCLL breeding blanket is a Reduced Activation ferritic/Martensitic steel (RAFM) developed and produced in Europe (designated Eurofer). The physical and mechanical properties are those given in Ref. [97] and listed for different temperature in Table A.1.

T [°C]	a_m [10^{-6} K^{-1}]	E [Gpa]	r [kg m^{-3}]	C_p [J $kg^{-1}K^{-1}$]	l [W m^{-1} K^{-1}]	W [10^{-6} W m]	$S_{y,min}$ [MPa]	$S_{u,min}$ [MPa]
20		217	7750	448	28.3	0.50	516	637
100	10.7	212	7728	486	29.2	0.60	480	595
200	11.0	207	7699	522	30.7	0.74	457	555
250		205		537		0.80	449	537
300	11.2	203	7666	551	30.2	0.87	442	517
350		200		566		0.93	431	495
400	11.7	197	7633	584	29.3	1.00	416	468
450		194		612		1.07	393	434
500	12.0	189	7596	655	29.5	1.13	360	392
550		184		721		1.20	316	340
600	12.3	178	7558	801	31.2	1.7	257	277
650		170				1.33	181	200
700	12.5	161					87	107

T: temperature; a_m: Ave. coef. of thermal expansion; E: Young's module; r: density; C_p: specific heat; l: thermal conductivity; W: electrical resistivity; $S_{y,min}$: minimum yield strength; $S_{u,min}$: ultimate tensile strength

Table A.1 – Thermo-physical properties of Eurofer [97]

Water

The coolant is water at typical PWR conditions. The thermo-dynamic properties used are those in reference [67]. The properties relevant for calculations are reported in Table A.2, listed per temperature.

P [MPa]	T [K]	T [°C]	n [m^3/kg]	r [kg m^{-3}]	h [J kg^{-1}]
15.50	558.0	285.0	1.32E-03	755.97	1.258E+06
15.50	563.0	290.0	1.34E-03	746.77	1.284E+06
15.50	*568.0*	*295.0*	*1.36E-03*	*737.08*	*1.310E+06*
15.50	593.0	320.0	1.47E-03	680.60	1.452E+06
15.50	598.0	325.0	1.50E-03	666.84	1.484E+06
15.50	*601.0*	*328.0*	*1.52E-03*	*657.76*	*1.503E+06*
15.50	603.0	330.0	1.53E-03	651.85	1.517E+06
P: pressure; T: temperature; n: specific volume; r: density; h: specific enthalpy					

Table A.2 – Thermo-physical properties of Water [67]

Tungsten

The Tungsten is adopted as FW armor. The fixed values have been imposed from an evaluation of the properties reported in Ref. [98] and listed for different temperature reported in Table A.3.

T [K]	a_m [10^{-6} K^{-1}]	E [Gpa]	r [kg m^{-3}]	C_p [J $kg^{-1}K^{-1}$]	l [W m^{-1} K^{-1}]
300	5.248	407.80	19300.0	132.00	174.00
400	5.305	404.66	19300.0	137.00	159.00
473	5.350	402.00	19300.0	138.44	150.12
600	5.419	396.61	19300.0	142.00	137.00
800	5.533	386.42	19300.0	145.00	125.00
873	5.550	382.00	19300.0	146.67	121.60
1000	5.646	374.36	19300.0	148.00	118.00
1073	5.760	370.00	19300.0	149.68	115.33
1200	5.700	360.69	19300.0	152.00	113.00
1273	5.800	355.00	19300.0	152.74	111.43
1473	5.920	340.00	19300.0	156.17	108.39
1500	5.931	337.74	19300.0	157.00	107.00
2000	6.215	295.17	19300.0	167.00	100.00

T: temperature; a_m: Ave. coef. of thermal expansion; E: Young's module; r: density; C_p: specific heat; l: thermal conductivity;

Table A.3 – Thermo-physical properties of Tungsten [98]

ANNEX B: Steady-state and transient thermal loads

Structural Material Power Deposition

The volumetric power deposition of the Eurofer/Tungsten domain according to the radial dimension is provided in Ref. [58]; the nuclear heating for different radial dimension (y) of the CFX model are reported in Table B.1.

Eurofer			
Region	***y CFX [m]***	***Nuclear Heating [MW m^{-3}]***	***Function [MW m^{-3}]***
W	0.027	2.6770E+01	$q'''(y) = (9185.7 \cdot y) - 221.25$
W/FW	0.025	8.3986E+00	
BZ	-0.025	4.0715E+00	$q'''(y) = (1483.1 \cdot y^3) + (574.96 \cdot y^2) + (85.614 \cdot y) + 5.8757$
BZ	-0.075	2.0631E+00	
BZ	-0.125	1.2609E+00	
BZ	-0.175	8.0651E-01	$q'''(y) = (253.5 \cdot y^4) + (296.81 \cdot y^3) + (142.72 \cdot y^2) + (35.202 \cdot y) + 3.9488)$
BZ	-0.225	5.2273E-01	
BZ	-0.275	3.3903E-01	
BZ	-0.325	2.2291E-01	
BZ	-0.375	1.4800E-01	$q'''(y) = (14.777 \cdot y^3) + (22.088 \cdot y^2) + (11.52 \cdot y) + 2.1412$
BZ	-0.425	1.0041E-01	
BZ	-0.475	6.9053E-02	
BZ	-0.525	4.7872E-02	$q'''(y) = (3.3608 \cdot y^3) + (6.6985 \cdot y^2) + (4.5994 \cdot y) + 1.1026$
BZ/Manifold	-0.575	3.3717E-02	
Manifold	-0.625	2.4068E-02	
Manifold	-0.675	1.7451E-02	$q'''(y) = (-0.6183 \cdot y^3) - (0.878 \cdot y^2) - (0.2249 \cdot y) + 0.0755)$
Manifold	-0.725	1.2706E-02	
Manifold	-0.775	1.0295E-02	
Manifold	-0.825	1.3408E-02	$q'''(y) = (-0.8364 \cdot y^2) - (1.4006 \cdot y) - 0.5727)$
Manifold	-0.875	1.2338E-02	

Table B.1 – Eurofer/Tungsten volumetric power deposition [58]

PbLi Power Deposition

The volumetric power deposition of the PbLi domain according to the radial dimension are available in Ref. [58]; the nuclear heating for different radial dimension (y) of the CFX model are reported in Table B.2.

PbLi			
Region	***y CFX [m]***	***Nuclear Heating [MW m^{-3}]***	***Function [MW m^{-3}]***
BZ	0	9.5968E+00	$q'''(y) = (98.962 \cdot y) + 9.5968)$
BZ	-0.05	4.6486E+00	
BZ	-0.1	3.1738E+00	$q'''(y) = (365.35 \cdot y^4) + (443.1 \cdot y^3) + (215 \cdot y^2) + (54.376 \cdot y) + 6.8797$
BZ	-015	2.2617E+00	
BZ	-0.2	1.6474E+00	
BZ	-0.25	1.2200E+00	
BZ	-0.3	9.0846E-01	
BZ	-0.35	6.7833E-01	
BZ	-0.4	5.2164E-01	
BZ	-0.45	4.0103E-01	$q'''(y) = (-24.012 \cdot y^4) + (-44.926 \cdot y^3) + (-26.442 \cdot y^2) + (-3.0862 \cdot y) + 1.2574$
BZ	-0.5	3.0456E-01	
BZ/Manifold	-0.55	2.3365E-01	
Manifold	-0.6	1.8173E-01	
Manifold	-0.65	1.4304E-01	
Manifold	-0.7	1.1163E-01	$q'''(y) = (-20.587 \cdot y^3) + (-41.042 \cdot y^2) + (-26.626 \cdot y) - 5.4774$
Manifold	-0.75	9.1167E-02	
Manifold	-0.8	9.7098E-02	
Manifold	-0.85	8.1890E-02	$q'''(y) = (0.311 \cdot y) + 0.346$
Manifold	-0.9	6.6000E-02	

Table B.2 – PbLi volumetric power deposition [58]

Fast Ramp-Up Power

The normalized power values of the fast ramp-up are given by the Refs. [94][95], where the listed values divided by time interval are shown in Table B.3.

Time [s]	Rel. Power [-]	Equation
0.0	0.0089	F(t) = 0.00887
12.0	0.0089	
13.0	0.0111	$F(t) = 1.9902E\text{-}04 \cdot t^4 - 1.1433E\text{-}02 \cdot t^3 + 2.4813E\text{-}01 \cdot t^2 - 2.3962 \cdot t + 8.6621$
16.0	0.0573	
17.0	0.0830	$F(t) = 8.7450E\text{-}05 \cdot t^4 - 5.9979E\text{-}03 \cdot t^3 + 1.5801E\text{-}01 \cdot t^2 - 1.8608 \cdot t + 8.2185$
20.0	0.2111	
21.0	0.2919	$F(t) = -7.3498E\text{-}04 \cdot t^3 + 6.4311E\text{-}02 \cdot t^2 - 1.6291 \cdot t + 12.9480$
23.0	0.5573	
24.0	0.7249	$F(t) = -5.5853E\text{-}03 \cdot t^2 + 4.3013E\text{-}01 \cdot t - 6.3809$
25.0	0.8814	
26.0	0.9957	$F(t) = -1.5016E\text{-}02 \cdot t^2 + 8.7749E\text{-}01 \cdot t - 11.6697$
30.0	1.1409	
32.0	1.0664	$F(t) = 1.5963E\text{-}03 \cdot t^2 - 1.3387E\text{-}01 \cdot t + 3.7191$
38.0	0.9367	
40.0	0.8961	$F(t) = 3.0822E\text{-}03 \cdot t^2 - 2.6069E\text{-}01 \cdot t + 6.3921$
42.0	0.8802	
44.0	0.8746	$F(t) = -1.8500E\text{-}04 \cdot t^3 + 2.5475E\text{-}02 \cdot t^2 - 1.1669 \cdot t + 18.6615$
50.0	0.8750	
52.0	0.8793	$F(t) = 2.4550E\text{-}04 \cdot t^2 – 2.0352E\text{-}02 \cdot t + 1.2757$
66.0	1.0000	
68.0	1.0000	F(t) = 1.0

Table B.3 – Fast ramp-up normalized power trend [94][95]

FW Water Fast-Ramp-up inlet temperature

The FW water inlet temperature values of the fast ramp-up are given by the RELAP5/Mod3.3 analysis: the time-dependent equations adopted, listed by time interval, are shown in Table B.4.

Time [s]	Temperature [K]	Equation
0.0	582.88	$Y(t) = 582.88$
10.0	582.88	$Y(t) = 1.0000E\text{-}03 \cdot t + 5.8287E+02$
18.0	582.89	
20.0	582.66	$Y(t) = 2.4121E\text{-}07 \cdot t^6 - 5.5342E\text{-}05 \cdot t^5 + 5.1084E\text{-}03 \cdot t^4 - 2.4098E\text{-}01 \cdot t^3 + 6.0801 \cdot t^2 - 7.7870E+01 \cdot t + 9.8016E+02$
56.0	566.04	
58.0	566.02	$Y(t) = -3.8911E\text{-}04 \cdot t^3 + 7.9915E\text{-}02 \cdot t^2 - 5.3303 \cdot t + 6.8226E+02$
82.0	568.06	
84.0	568.05	$Y(t) = 4.3390E\text{-}05 \cdot t^3 - 1.2102E\text{-}02 \cdot t^2 + 1.1022 \cdot t + 5.3513E+02$
110.0	567.68	
112.0	567.69	$Y(t) = 5.5188E\text{-}03 \cdot t + 5.6707E+02$
154.0	567.92	
156.0	567.91	$Y(t) = 1.2691E\text{-}03 \cdot t + 5.6771E+02$
290.0	568.08	
295.0	568.08	$Y(t) = 3.9838E\text{-}04 \cdot t + 5.6796E+02$
480.0	568.15	
481.0	568.15	$Y(t) = 568.15$

Table B.4 – Fast ramp-up FW water inlet temperature trend

BZ Water Fast Ramp-up inlet temperature

The BZ water inlet temperature values of the fast ramp-up are provided by the RELAP5/Mod3.3 analysis, and the time-dependent equations used, listed by time interval, are shown in Table B.5.

Time [s]	Temperature [K]	Equation
0.0	584.19	$Y(t) = 584.19$
12.0	584.19	
14.0	584.21	$Y(t) = -5.8486E\text{-}08 \cdot t^6 + 8.6079E\text{-}06 \cdot t^5 - 5.1571E\text{-}04 \cdot t^4 + 1.6093E\text{-}02 \cdot t^3 - 2.7494E\text{-}01 \cdot t^2 + 2.4316 \cdot t + 5.7552E+02$
42.0	584.11	
44.0	583.22	$Y(t) = 1.0985E\text{-}03 \cdot t^4 - 2.0855E\text{-}01 \cdot t^3 + 1.4762E+01 \cdot t^2 - 4.6247E+02 \cdot t + 6.0007E+03$
54.0	574.48	
56.0	572.54	$Y(t) = -6.0825E\text{-}05 \cdot t^4 + 1.4224E\text{-}02 \cdot t^3 - 1.2012 \cdot t^2 + 4.2504E+01 \cdot t + 5.9376E+01$
72.0	567.31	
74.0	567.31	$Y(t) = -3.1460E\text{-}04 \cdot t^3 + 7.5862E\text{-}02 \cdot t^2 - 6.0455 \cdot t + 7.2675E+02$
88.0	567.82	
90.0	567.77	$Y(t) = 5.9728E\text{-}04 \cdot t^2 - 1.4120E\text{-}01 \cdot t + 5.7564E+02$
140.0	567.58	
142.0	567.56	$Y(t) = -1.1616E\text{-}04 \cdot t^2 + 4.6824E\text{-}02 \cdot t + 5.6325E+02$
200.0	567.97	
205.0	568.00	$Y(t) = -3.2412E\text{-}06 \cdot t^2 + 2.6588E\text{-}03 \cdot t + 5.6759E+02$
400.0	568.14	
401.0	568.15	$Y(t) = 568.15$

Table B.5 – Fast ramp-up BZ water inlet temperature trend

Ramp-Down Power

The normalized power values of the ramp-down are given by the Refs. [94][95]; the listed values divided by time interval are shown in Table B.6.

Time [s]	Rel. Power [-]	Equation
0.0	1.0000	F(t) = 1.0
10.0	1.0000	
12.0	0.9426	$F(t) = 0.00023549 \cdot t^2 - 0.03465661 \cdot t + 1.32555436$
52.0	0.1616	
54.0	0.0190	$F(t) = -0.07131074 \cdot t + 3.86973975$
160.0	0.0089	
161.0	0.0089	F(t) = 0.00887

Table B.6 – Ramp-down normalized power trend [94][95]

FW Water Ramp-down inlet temperature

The FW water inlet temperature values of the ramp-down were obtained thorough the RELAP5/Mod3.3 analysis; the derived time-dependent equations, listed by time interval, are shown in Table B.7.

Time [s]	Temperature [K]	Equation
0.0	568.15	$Y(t) = 568.15$
10.0	568.15	
12.0	568.16	$Y(t) = -2.6166E\text{-}08 \cdot t^6 + 4.0436E\text{-}06 \cdot t^5 - 2.4167E\text{-}04 \cdot t^4 + 7.2584E\text{-}03 \cdot t^3 - 1.1694E\text{-}01 \cdot t^2 + 9.5769E\text{-}01 \cdot t + 5.6504E+02$
40.0	568.86	
42.0	569.52	$Y(t) = -3.1546E\text{-}04 \cdot t^3 + 5.1244E\text{-}02 \cdot t^2 - 2.3498 \cdot t + 6.0119E+02$
60.0	576.54	
62.0	577.37	$Y(t) = 8.5950E\text{-}04 \cdot t^3 - 1.7558E\text{-}01 \cdot t^2 + 1.2252E+01 \cdot t + 2.8784E+02$
80.0	584.35	
82.0	584.56	$Y(t) = 8.7973E\text{-}04 \cdot t^3 - 2.4886E\text{-}01 \cdot t^2 + 2.3116E+01 \cdot t - 1.2266E+02$
108.0	579.34	
110.0	579.20	$Y(t) = -1.8317E\text{-}04 \cdot t^3 + 6.8783E\text{-}02 \cdot t^2 - 8.4719 \cdot t + 9.2265E+02$
140.0	582.09	
142.0	582.11	$Y(t) = -3.7913E\text{-}03 \cdot t + 5.8262E+02$
200.0	582.88	
201.0	582.88	$Y(t) = 582.88$

Table B.7 – Ramp-down FW water inlet temperature trend

BZ Water Ramp-down inlet temperature

The BZ water inlet temperature values of the ramp-down were obtained through the RELAP5/Mod3.3 analysis; the derived time-dependent equations, listed by time interval, are shown in Table B.8.

Time [s]	Temperatures [K]	Equation
0.0	568.15	$Y(t) = 568.15$
10.0	568.15	
12.0	568.18	$Y(t) = 9.7624E\text{-}09 \cdot t^6 - 1.5490E\text{-}06 \cdot t^5 + 9.8119E\text{-}05 \cdot t^4 - 3.1200E\text{-}03 \cdot t^3 + 5.1178E\text{-}02 \cdot t^2 - 3.9717E\text{-}01 \cdot t + 5.6929E+02$
50.0	568.98	
52.0	569.26	$Y(t) = -1.1993E\text{-}04 \cdot t^3 + 3.1462E\text{-}02 \cdot t^2 - 2.1339 \cdot t + 6.1201E+02$
80.0	581.25	
82.0	581.83	$Y(t) = -4.4051E\text{-}04 \cdot t^3 + 1.0973E\text{-}01 \cdot t^2 - 8.8195 \cdot t + 8.1008E+02$
104.0	584.19	
106.0	584.19	$Y(t) = -5.1559E\text{-}03 \cdot t^3 + 1.6703 \cdot t^2 - 1.8020E+02 \cdot t + 7.0587E+03$
114.0	584.38	
116.0	584.24	$Y(t) = -9.6526E\text{-}05 \cdot t^3 + 3.8610E\text{-}02 \cdot t^2 - 5.1455 \cdot t + 8.1224E+02$
140.0	583.76	
142.0	583.79	$Y(t) = 6.9948E\text{-}03 \cdot t + 5.8279E+02$
200.0	584.19	
201.0	584.19	$Y(t) = 584.19$

Table B.8 – Ramp-down BZ water inlet temperature trend

Low Power Fluctuations

The normalized power values of the low fluctuations are given by the Refs. [83][84], where the listed equations divided by time interval are shown in Table B.9.

Time [s]	Rel. Power [-]	Equation
0.0	1.0	F(t) = 1.0
10.0	1.0	
11.0	1.0	F(t) = 1 + (0.2641 ((1/9.3975) $e^{(- ((t - 25)^2)/(28.125))}$)
25.0	1.0281	
40.0	1.0	
41.0	1.0	F(t) = 1 + (0.2641 ((1/9.3975) $e^{(- ((t - 55)^2)/(28.125))}$)
55.0	1.0281	
70.0	1.0	
71.0	1.0	F(t) = 1 + (0.2641 ((1/9.3975) $e^{(- ((t - 85)^2)/(28.125))}$)
85.0	1.0281	
100.0	1.0	
101.0	1.0	F(t) = 1.0

Table B.9 – Low power fluctuations normalized power trend [83][84]

High Power Fluctuations

The normalized power values of the high fluctuations are given by the Refs. [83][84], and the listed equations divided by time interval are shown in Table B.10.

Time [s]	Rel. Power [-]	Equation
0.0	1.0	F(t) = 1.0
10.0	1.0	
11.0	1.0	F(t) = 1 + (0.94 ((1/9.3975) $e^{(- ((t - 25)^2)/(28.125))}$)
25.0	1.10	
40.0	1.0	
41.0	1.0	F(t) = 1 – (0.70475 ((1/9.3975) $e^{(- ((t - 55)^2)/(28.125))}$)
55.0	0.925	
70.0	1.0	
71.0	1.0	F(t) = 1 + (0.94 ((1/9.3975) $e^{(- ((t - 85)^2)/(28.125))}$)
85.0	1.10	
100.0	1.0	
101.0	1.0	F(t) = 1.0

Table B.10 – High power fluctuations normalized power trend [83][84]

Thermal Inertia step-down ramp power

The normalized power values of the step-down ramp are those shown in Table B.11.

Time [s]	Rel. Power [-]	Equation
0.0	1.0	F(t) = 1.0
10.0	1.0	
11.0	0.0	F(t) = 0.0
12.0	0.0	

Table B.11 – Step-down ramp normalized power trend

BIBLIOGRAPHY

[1] F. Romanelli, et al., *Fusion Electricity – A Roadmap to the Realization of Fusion Energy*, EFDA Report, ISBN 978-3-00-040720-8T, 2012

[2] https://www.euro-fusion.org

[3] A. J. H. Donné, et al., *European Research Roadmap to the realization of fusion energy*, EUROfusion (2018), ISBN 978-3-00-061152-0

[4] G. Federici, et al., *Overview of the design approach and prioritization of R&D activities towards an EU DEMO*, Fus. Eng. and Des., 109–111 (2016) 1464–1474

[5] S. M. Weston, *Fusion: An Introduction to Physics and Technology of Magnetic Confinement Fusion*, Physics Textbook, Wiley-VCH Verlag GmbH &Co., 2010

[6] K. Miyamoto, *Plasma physics and controlled nuclear fusion*, vol. 38. Springer Science & Business Media, 2006

[7] C. M. Braams and P. E. Stott, *Nuclear fusion: half a century of magnetic confinement fusion research*, CRC Press, 2002

[8] www.iter.org

[9] J. Wesson, *The Science of JET*, JET-R(99)13, (http://www.euro-fusionscipub.org/wp-content/uploads/2014/11/JETR99013.pdf)

[10] G. Federici, et al., *An overview of the EU breeding blanket design strategy as an integral part of the DEMO design effort*, Fus. Eng. and Des., 2019, Vol. 141, pp 30-42, https://doi.org/10.1016/j.fusengdes.2019.01.141

[11] S. Ciattaglia, et al., *The European DEMO fusion reactor: Design status and challenges from balance of plant point of view*, 2017 IEEE International Conference on Environment and Electrical Engineering and 2017 IEEE Industrial and Commercial Power Systems Europe (EEEIC/I&CPS Europe), Milan, 2017, pp. 1-6, https://doi.org/10.1109/EEEIC.2017.7977853

[12] C. Bachmann, et al., EFDA_D_2KVWQZ, DEMO Plant Description Document, v1.9, EUROfusion, 2020 (Available online for the EUROfusion member at https://idm.euro-fusion.org/?uid=2kvwqz)

[13] G. Federici, et al., *DEMO design activity in Europe: Progress and updates*, Fus. Eng. and Des., 2018, https://doi.org/10.1016/j.fusengdes.2018.04.001

[14] F. Cismondi, et al., *Progress of the conceptual design of the European DEMO breeding blanket, tritium extraction and coolant purification systems*, Fus. Eng. and Des., 2020, Vol. 157, https://doi.org/10.1016/j.fusengdes.2020.111640

[15] L. Barucca, et al., *Status of EU DEMO heat transport and power conversion systems*, Fus. Eng. and Des., Vol. 136, 2018, pp. 1557-1566, https://doi.org/10.1016/j.fusengdes.2018.05.057

[16] F. Cismondi, et al., *Progress in EU Breeding Blanket design and integration*, Fus. Eng. and Des., Vol. 136, Part A, 2018, pp. 782-792, https://doi.org/10.1016/j.fusengdes.2018.04.009

[17] C. Bachmann, et al., Critical design issues in DEMO and solution strategies, Fus. Eng. and Des., Vol. 146, Part A, 2019, pp. 178-181, https://doi.org/10.1016/j.fusengdes.2018.12.013

[18] C. Bachmann, et al., *Key design integration issues addressed in the EU DEMO pre-concept design phase*, Fus. Eng. and Des., Vol. 156, 2020, 111595, https://doi.org/10.1016/j.fusengdes.2020.111595

[19] M. Abdou, et al., *Blanket/first wall challenges and required R&D on the pathway to DEMO*, Fus. Eng. and Des., Vol. 100, 2015, pp. 2-43, https://doi.org/10.1016/j.fusengdes.2015.07.021

[20] U. Fischer, et al., *Required, achievable and target TBR for the European DEMO*, Fus. Eng. and Des., Vol. 155, 2020, 111553, https://doi.org/10.1016/j.fusengdes.2020.111553

[21] L. V. Boccaccini, et al., *Objectives and status of EUROfusion DEMO blanket studies*, Fus. Eng. and Des., Vol. 109–111, Part B, 2016, pp. 1199-1206, https://doi.org/10.1016/j.fusengdes.2015.12.054

[22] G. Bongiovi, et al., *Multi-Module vs. Single-Module concept: comparison of thermomechanical performances for the DEMO water-cooled lithium lead breeding blanket*, Fus. Eng. and Des., Vol. 136, Part B, 2018, pp. 1472-1478, https://doi.org/10.1016/j.fusengdes.2018.05.037

[23] J. Aubert, et al., *Status of the EU DEMO HCLL breeding blanket design development*, Fus. Eng. and Des., Vol. 136, Part B, 2018, pp. 1428-1432, https://doi.org/10.1016/j.fusengdes.2018.04.133

[24] I. Fernández-Berceruelo, et al., *Remarks on the performance of the EU DCLL breeding blanket adapted to DEMO 2017*, Fus. Eng. and Des., Vol. 155, 2020, 111559, https://doi.org/10.1016/j.fusengdes.2020.111559

[25] F. A. Hernández, et al., *An enhanced, near-term HCPB design as driver blanket for the EU DEMO*, Fus. Eng. and Des., Vol. 146, Part A, 2019, pp. 1186-1191, https://doi.org/10.1016/j.fusengdes.2019.02.037

[26] F. A. Hernández, et al., *Consolidated design of the HCPB Breeding Blanket for the pre-Conceptual Design Phase of the EU DEMO and harmonization with the ITER HCPB TBM program*, Fus. Eng. and Des., Vol. 157, 2020, 111614, https://doi.org/10.1016/j.fusengdes.2020.111614

[27] M.H.H. Kolb, et al., *Li_4SiO_4based breeder ceramics with Li_2TiO_3, $LiAlO_2$ and Li_xTiO_3 additions, part I: Fabrication*, Fus. Eng. and Des., Vol. 115, 2017, pp. 39-48, https://doi.org/10.1016/j.fusengdes.2016.12.033

[28] O. Leys, et al., *Ceramic pebble production from the break-up of a molten laminar jet*, Proceedings of the 29th ILASS-Europe, Paris (2019)

[29] R. Gaisin, et al., *Synthesis of Be12Ti compound via arc melting or hot isostatic pressing*, Journal of Alloys and Compounds, Vol. 818, 2020, 152919, https://doi.org/10.1016/j.jallcom.2019.152919

[30] F. A. Hernández, et al., *Advancements in the helium cooled pebble bed breeding blanket for the EU DEMO: holistic design approach and lessons learned*, Fusion Sci. and Technol., Vol. 75, 2019, pp. 352-364, https://doi.org/10.1080/15361055.2019.1607695

[31] F. A. Hernández, et al., EFDA_D_2NKC7G, *HCPB Design and Integration Studies 2019*, v1.0, EUROfusion, 2020 (Available online for the EUROfusion member at https://idm.euro-fusion.org/?uid=2nkc7g)

[32] P. A. Davidson, *An introduction to magnetohydrodynamics*, Vol. 25, Cambridge university press, 2001

[33] R. J. Moreau, *Magnetohydrodynamics*, Vol. 3, Springer Science & Business Media, 2013

[34] U. Müller and L. Bühler, *Magnetofluiddynamics in channels and containers*, Springer Science & Business Media, 2013

[35] A. Tassone, *Study on liquid metal magnetohydrodynamic flows and numerical application to a water-cooled blanket for fusion reactors*, PhD thesis, Sapienza University of Rome, 2019, https://doi.org/10.13140/RG.2.2.15262.38720

[36] E. Martelli, *Thermal Hydraulic design of DEMO Water Cooled Lithium Lead Breeding Blanket and integration with primary system and balance of plant*, PhD thesis, Sapienza University of Rome, February 2018 (Available at https://iris.uniroma1.it/retrieve/handle/11573/1070504/610931/Tesi%20dottorato%20Martelli)

[37] A. Tassone, el al., *Recent progress in the WCLL breeding blanket design for the DEMO fusion reactor*, IEEE Transaction on Plasma Science, Vol. 46, no. 5, pp. 1446-1457, 2018, https://doi.org/10.1109/TPS.2017.2786046

[38] F. Tavassoli, *Eurofer steel, development to full code qualification*, Procedia Engineering, Vol. 55, pp. 300-308, 2013, https://doi.org/10.1016/j.proeng.2013.03.258

[39] A. Del Nevo, et al., *WCLL breeding blanket design and integration for DEMO 2015: status and perspectives*, Fus. Eng. and Des., Vol. 124, 2017, pp. 682-686, https://doi.org/10.1016/j.fusengdes.2017.03.020

[40] L. Giancarli, et al., *Status of the European breeding blanket technology*, Fus. Eng. and Des., Vol. 36, 1997, pp. 69-79

[41] L. Giancarli, et al., Candidate blanket concepts for a Europea fusion power plants, Fus. Eng. and Des., Vol.49-50, 2000, pp. 445-456

[42] P. Sardin, et al., *Power plant conceptual study – WCLL concept*, Fus. Eng. and Des., Vol. 69, 2003, pp. 769-774

[43] D. Maisonnier, et al., *The European power plant conceptual study*, Fus. Eng. and Des., Vol. 75-79, 2005, pp. 1173-1179

[44] J. Aubert, et al., Development of the water cooled lithium lead blanket for DEMO, Fus. Eng. and Des., Vol. 89, 2014, pp. 1386-1391

[45] E. Martelli, et al., Advancements in DEMO WCLL breeding blanket design and integration, Int. J. Energy Res., 2017, https://doi.org/10.1002/er.3750

[46] E. Martelli, et al., *Study of EU DEMO WCLL breeding blanket and primary heat transfer system integration*, Fus. Eng. and Des., Vol. 136, Part B, 2018, pp. 828-833, https://doi.org/10.1016/j.fusengdes.2018.04.016

[47] E. Martelli, et al., *Thermo-hydraulic analysis of EU DEMO WCLL breeding blanket*, Fus. Eng. and Des., Vol. 130, 2018, pp. 48-55, https://doi.org/10.1016/j.fusengdes.2018.03.030

[48] E. Martelli, et al., EFDA_D_2MYHNE, *WCLL Design Report 2017*, v1.0, EUROfusion, 2018 (Available online for the EUROfusion member at https://idm.euro-fusion.org/?uid=2myhne)

[49] G. A. Spagnuolo, et al., *A multi-physics integrated approach to breeding blanket modelling and design*, Fus. Eng. and Des., Vol. 143, 2019, pp. 35-40, https://doi.org/10.1016/j.fusengdes.2019.03.131

[50] P.A. Di Maio, et al., *On the effect of stiffening plates configuration on the DEMO Water Cooled Lithium Lead Breeding Blanket module thermo-mechanical behaviour*, Fus. Eng. and Des., Vol. 146, Part B, 2019, pp. 2247-2250, https://doi.org/10.1016/j.fusengdes.2019.03.163

[51] R. Mozzillo, et al., *Alternative design of DEMO Water Cooled Lithium Lead internal structure*, Fus. Eng. and Des., Vol. 146, Part A, 2019, pp. 1056-1059, https://doi.org/10.1016/j.fusengdes.2019.02.001

[52] A. Del Nevo, et al., *Recent progress in developing a feasible and integrated conceptual design of the WCLL BB in EUROfusion project*, Fus. Eng. and Des., Vol. 146, Part B, 2019, pp. 1805-1809, https://doi.org/10.1016/j.fusengdes.2019.03.040

[53] A. Del Nevo, et al., EFDA_D_2NUPDT, *WCLL Design Report 2018*, v1.1, EUROfusion, 2019 (Available online for the EUROfusion member at https://idm.euro-fusion.org/?uid=2nupdt)

[54] A. Tassone, et al., *MHD mixed convection flow in the WCLL: Heat transfer analysis and cooling system optimization*, Fus. Eng. and Des., Vol. 146, Part A, 2019, pp. 809-813, https://doi.org/10.1016/j.fusengdes.2019.01.087

[55] F. Edemetti, et al., *DEMO WCLL breeding zone cooling system design: Analysis and discussion*, Fus. Eng and Des., Vol. 146, Part B, 2019, pp. 2632-2638, https://doi.org/10.1016/j.fusengdes.2019.04.063

[56] Q. Ling, G. Wang, *A research and development review of water-cooled breeding blanket for fusion reactors*, Annals of Nuclear Energy, Vol. 145, 2020, 107541, https://doi.org/10.1016/j.anucene.2020.107541

[57] R. Forte, et al., *On the effects of the Double-Walled Tubes lay-out on the DEMO WCLL breeding blanket module thermal behavior*, Fus. Eng. and Des., Vol. 146, Part A, 2019, pp. 883-886, https://doi.org/10.1016/j.fusengdes.2019.01.105

[58] S. Noce, et al., *Nuclear analysis of the Single Module Segment WCLL DEMO*, Fus. Eng. and Des., Vol. 147, 2019, 111207, https://doi.org/10.1016/j.fusengdes.2019.05.026

[59] M. Utili, et al., *Status of Pb-16Li technologies for European DEMO fusion reactor*, Fus. Eng. and Des., Vol. 146, Part B, 2019, pp. 2676-2681, https://doi.org/10.1016/j.fusengdes.2019.04.083

[60] AFCEN, *RCC-MRx: Design and Construction Rules for Mechanical Components in high-temperature structures, experimental reactors and fusion reactors*, Standard, 2015

[61] A. Tassone, et al., *MHD pressure drop estimate for the WCLL in-magnet PbLi loop*, Fus. Eng. and Des., Vol. 160, 2020, 111830, https://doi.org/10.1016/j.fusengdes.2020.111830

[62] F. Maviglia, et al., *Wall protection strategies for DEMO plasma transients*, Fus. Eng. and Des., Vol. 136, Part A, 2018, pp. 410-414. https://doi.org/10.1016/j.fusengdes.2018.02.064

[63] F. Maviglia, et al., *Overview of DEMO Technology and Scenario Design activities in Europe*, 2nd Asia-Pacific Conference on Plasma Physics (AAPPS-DPP 2018), Kanazawa, Japan, 12.11.2018 – 17.11.2018

[64] D. Martelli et al., *Literature review of lead-lithium thermophysical properties*, Fus. Eng. and Des., Vol. 138, 2019, pp. 183-195, https://doi.org/10.1016/j.fusengdes.2018.11.028

[65] E. A. Mogahed, G. L.Kulcinski, *Bibliography of a Promising Tritium Breeding Material – Pb83Li17*, Fusion Technology Institute, University of Wisconsin, UWFDM-994, 1995

[66] Thermophysical Properties of Materials For Nuclear Engineering: A Tutorial and Collection of Data, IAEA, Vienna, 2008, ISBN 978–92–0–106508–7

[67] ISL Inc, *RELAP5/MOD3.3 Code Manual Volume I: Code Structure, System Models, and Solution Methods*, Nuclear Safety Analysis Division, July 2003

[68] F. Giannetti, T. D'Alessandro, C. Ciurluini, *Development of a RELAP5 mod3.3 version for FUSION applications*, DIAEE Sapienza Technical Report D1902_ENBR_T01 Rev. 01

[69] I. Di Piazza and M. Ciofalo, *Numerical prediction of turbulent flow and heat transfer in helically coiled pipes*, International Journal of Thermal Sciences, Vol. 49, Issue 4, 2010, pp. 653-663, https://doi.org/10.1016/j.ijthermalsci.2009.10.001

[70] Ansys inc., *Ansys CFX reference guide*, release 18.2, USA.

[71] F. Edemetti, et al., *Optimization of the first wall cooling system for the DEMO WCLL blanket*, Fus. Eng. and Des., Vol. 161, 2020, 111903, https://doi.org/10.1016/j.fusengdes.2020.111903

[72] E. Martelli, et al., *Thermal-hydraulic modeling and analyses of the water-cooled EU DEMO using RELAP5 system code*, Fus. Eng. and Des., Vol. 146, Part A, 2019, pp. 1121-1125, https://doi.org/10.1016/j.fusengdes.2019.02.021

[73] M. Shah, *A general correlation for critical heat flux in horizontal channels*, International Journal of Refrigeration, 2015, https://doi.org/10.1016/j.ijrefrig.2015.06.027

[74] L.S. Tong, *A phenomenological study of critical heat flux*, ASME Paper 75-HT-68, 1975

[75] I. Catanzaro, et al., *Parametric study of the influence of double-walled tubes layout on the DEMO WCLL breeding blanket thermal performances*, Fus. Eng. and Des., Vol. 161, 2020, 111893, https://doi.org/10.1016/j.fusengdes.2020.111893

[76] P. Arena et al., *Parametric thermal analysis for the optimization of Double Walled Tubes layout in the Water Cooled Lithium Lead inboard blanket of DEMO fusion reactor*, J. Phys.: Conf. Ser., 1224, 2019, https://doi.org/10.1088/1742-6596/1224/1/012031

[77] E. Rodríguez López and D. Alonso, EFDA_D_2NY8VX, *Thermal-mechanical analysis in support of WCLL BB: ESTEYCO contribution*, v1.0, EUROfusion, 2019 (Available online for the EUROfusion member at https://idm.euro-fusion.org/?uid=2ny8vx)

[78] I.E. Idelchik, *Handbook of Hydraulic Resistance*, CRC Begell House, 1994

[79] F. Edemetti, et al., *On the impact of the heat transfer modelling approach on the prediction of EU-DEMO WCLL breeding blanket thermal performances*, Fus. Eng. and Des., paper under review, in: ISFNT 2019 – 14th International Symposium on Fusion Nuclear Technology.

[80] D. Taler and J. Taler, *Simple heat transfer correlations for turbulent tube flow*, 2017, E3S Web of Conferences 13, 02008, https://doi.org/10.1051/e3sconf/20171302008

[81] F. Edemetti, et al., *Thermal-hydraulic analysis of the DEMO WCLL elementary cell: BZ tubes layout optimization*, Fus. Eng. and Des., Vol. 160, 2020, 111956, https://doi.org/10.1016/j.fusengdes.2020.111956

[82] Y. Liu, et al., *Influence of time step length and sub-iteration number on the convergence behavior and numerical accuracy for transient CFD*, Ollivier-Gooch, C. (Ed.), 11th annual conference of the CFD Society of Canada (CFD 2003) Proceedings, 2003, Canada: CFD Society of Canada.

[83] G. A. Spagnuolo, et al., EFDA_D_2NLL6N, *Breeding Blanket Load Specifications Document*, v1.1, EUROfusion, 2019, (Available online for the EUROfusion member at https://idm.euro-fusion.org/?uid=2nll6n)

[84] G. A. Spagnuolo, et al., *Development of load specifications for the design of the breeding blanket system*, Fus. Eng. and Des., Vol. 157, 2020, 111657, https://doi.org/10.1016/j.fusengdes.2020.111657

[85] F. Maviglia, et al., *Optimization of DEMO geometry and disruption location prediction*, Fus. Eng. and Des., Vol. 146, Part A, 2019, pp. 967-971, https://doi.org/10.1016/j.fusengdes.2019.01.127

[86] F. Giorgetti, et al., *Dynamic behaviour of DEMO vacuum vessel during plasma vertical displacement events*, Fus. Eng. and Des., Vol. 159, 2020, 111876, https://doi.org/10.1016/j.fusengdes.2020.111876

[87] I. A. Maione, et al., *Analysis of EM loads on DEMO WCLL breeding blanket during VDE-up*, Fus. Eng. and Des., Vol. 136, Part B, 2018, pp. 1523-1528, https://doi.org/10.1016/j.fusengdes.2018.05.048

[88] M. D'Onorio, et al., *In-Box LOCA accident analysis for the European DEMO water-cooled reactor*, Fus. Eng. and Des., Vol. 146, Part A, 2019, pp. 732-735, https://doi.org/10.1016/j.fusengdes.2019.01.066

[89] M. Eboli, et al., Experimental activities for in-box LOCA of WCLL BB in LIFUS5/Mod3 facility, Fus. Eng. and Des., Vol. 146, Part A, 2019, pp. 914-919, https://doi.org/10.1016/j.fusengdes.2019.01.113

[90] A. Del Nevo, et al., *Addressing the "In-Box LOCA" safety issue of the WCLL Breeding Blanket and Test Blanket Module*, proceedings of the 31st Symposium on Fusion Technology (31st SOFT), 20th – 25th September 2020, Virtual Edition

[91] C. Ciurluini, et al., *Analysis of the thermal-hydraulic behavior of the EU-DEMO WCLL Breeding Blanket systems during a Loss Of Flow Accident*, proceedings of the 31st Symposium on Fusion Technology (31st SOFT), 20th – 25th September 2020, Virtual Edition

[92] C. Harrington, et al., EFDA_D_2MG38N, *WCLL BB Extended thermodynamic modelling activities with Apros for simulating DEMO with IHTS & ESS*, v1.0, EUROfusion, 2019 (Available online for the EUROfusion member at https://idm.euro-fusion.org/?uid=2mg38n)

[93] A. Del Nevo, et al., EFDA_D_2P5NE5, *WCLL BB design and integration studies 2019 activities*, v1.0, EUROfusion, 2020, (Available online for the EUROfusion member at https://idm.euro-fusion.org/?uid=2p5ne5)

[94] F. Palermo, et al., EFDA_D_2NB66G, *Ramp-Up and Ramp-Down investigation*, v1.0, EUROfusion, Feb 2020 (Available online for the EUROfusion member at https://idm.euro-fusion.org/?uid=2nb66g)

[95] F. Palermo, et al., EFDA_D_2NJ85C, *Reference Ramp-Up and Ramp-Down trajectories for EU-DEMO and database of plasma perturbations*, v1.0, EUROfusion, Jul 2020 (Available online for the EUROfusion member at https://idm.euro-fusion.org/?uid=2nj85c)

[96] R. H. S. Winterton, *Newton's law of cooling*, Contemporary Physics, 1999, Vol. 40:3, pp. 205-2015, https://doi.org/10.1080/001075199181549

[97] F. Tavassoli, Fusion DEMO Interim Structural Design Criteria (DISDC)/Appendix A Material Design Limit Data/A3, S18E Eurofer Steel, EFDA TSKTW4-TTMS-005-D01, CEA Report DMN/DIR/NT2004-02/A, December 2004

[98] F. P. Incropera et al., Principles of heat and mass transfer, 7th edition.

ACKNOWLEDGMENTS

I just want to say a few words to thank the people who accompanied and helped me during these three years.
I would like to thank Prof. Gianfranco Caruso and Prof. Fabio Giannetti that gave me the opportunity to work on this innovative field. Their support allowed me to conclude this experience, I hope in the best way. Thanks also to department colleagues and Master's students, with whom I spent this experience. A special thanks to Emanuela and Alessandro my two "work mentors".
I'd like to thank also Ing. Alessandro Del Nevo and the ENEA Brasimone colleagues, with whom I've closely worked every day.
I wish to thank my both reviewers, Ing. Ivan Di Piazza and Dr. Iván Fernández-Berceruelo, who took the time to review this PhD thesis. Your advice and suggestions were greatly appreciated.
Thanks also to all my friend for allowing me to be by your side, each of you has played a key role at various times, and for this I thank you guys and girls. Among all, I want to acknowledge one in particular, my brother and friend Federico.
My family is the one that for sure deserves a huge thank, their support was fundamental during these three years, their love and support gave me stability and self-confidence to conclude this path. A special thanks goes to Mamma and Valentino, you have had an arduous task.
Finally, thank you Silvia. You perfectly know why. I have shared every success, difficulty, project and doubt in these three years and before, and this is how I want to continue. Thanks for your love.

This work has been carried out within the framework of the EUROfusion consortium and has received funding from the Euratom research and training programme 2014-2018 and 2019-2020 under grant agreement No 633053. The views and opinions expressed herein do not necessarily reflect those of the European Commission.